

**DEVELOPMENT OF A PORTAL DOSE IMAGE
PREDICTION ALGORITHM FOR ARBITRARY
DETECTOR SYSTEMS**

by

BOYD MATTHEW CLARK MCCURDY

A Thesis

Submitted to the Faculty of Graduate Studies

In Partial Fulfillment of the Requirements

For the Degree of

DOCTOR OF PHILOSOPHY

Department of Physics

UNIVERSITY OF MANITOBA

Winnipeg, Manitoba, Canada

© Boyd M. C. McCurdy, 2001



**National Library
of Canada**

**Acquisitions and
Bibliographic Services**

**395 Wellington Street
Ottawa ON K1A 0N4
Canada**

**Bibliothèque nationale
du Canada**

**Acquisitions et
services bibliographiques**

**395, rue Wellington
Ottawa ON K1A 0N4
Canada**

Your file Votre référence

Our file Notre référence

The author has granted a non-exclusive licence allowing the National Library of Canada to reproduce, loan, distribute or sell copies of this thesis in microform, paper or electronic formats.

L'auteur a accordé une licence non exclusive permettant à la Bibliothèque nationale du Canada de reproduire, prêter, distribuer ou vendre des copies de cette thèse sous la forme de microfiche/film, de reproduction sur papier ou sur format électronique.

The author retains ownership of the copyright in this thesis. Neither the thesis nor substantial extracts from it may be printed or otherwise reproduced without the author's permission.

L'auteur conserve la propriété du droit d'auteur qui protège cette thèse. Ni la thèse ni des extraits substantiels de celle-ci ne doivent être imprimés ou autrement reproduits sans son autorisation.

0-612-62655-5

Canada

**THE UNIVERSITY OF MANITOBA
FACULTY OF GRADUATE STUDIES

COPYRIGHT PERMISSION PAGE**

Development of a Portal Dose Image Prediction Algorithm for Arbitrary Detector Systems

BY

Boyd Matthew Clark McCurdy

**A Thesis/Practicum submitted to the Faculty of Graduate Studies of The University
of Manitoba in partial fulfillment of the requirements of the degree
of
Doctor of Philosophy**

BOYD MATTHEW CLARK MCCURDY © 2001

Permission has been granted to the Library of The University of Manitoba to lend or sell copies of this thesis/practicum, to the National Library of Canada to microfilm this thesis/practicum and to lend or sell copies of the film, and to Dissertations Abstracts International to publish an abstract of this thesis/practicum.

The author reserves other publication rights, and neither this thesis/practicum nor extensive extracts from it may be printed or otherwise reproduced without the author's written permission.

ABSTRACT

Portal imaging was originally developed for geometric treatment verification of photon beams used in cancer radiotherapy. More recently, portal imaging systems have been successfully used in dosimetric treatment verification applications. Many of the proposed dosimetric applications involve the accurate calculation of a predicted portal dose image, including both primary and scatter dose components emerging from the patient. This thesis presents the development of a two step model that predicts dose deposition in arbitrary portal image detectors. The algorithm requires patient computed tomographic data, source-detector distance, and knowledge of the incident photon beam fluence. The first step predicts the photon fluence entering a portal imaging detector located behind the patient. Primary fluence is obtained through simple ray tracing techniques, while scatter fluence prediction requires a library of scatter fluence kernels generated by Monte Carlo simulation. These kernels allow prediction of basic radiation transport parameters characterizing the scattered photons, including fluence and energy. The second step of the algorithm involves a superposition of Monte Carlo-generated pencil beam kernels, describing dose deposition in a specific detector, with the predicted incident fluence of primary and scattered photons. This process is performed separately for primary and scatter fluence at high and low spatial resolutions respectively, and yields a predicted planar dose image.

This algorithm is tested on a variety of phantoms including simple slab phantoms and anthropomorphic phantoms. Other clinical parameters were varied over a wide range of interest, including 6, 18, 23 MV photon beam spectra and 10-80 cm air gap between

phantom and portal imaging detector. Both low and high atomic number detectors were used to verify the algorithm, including a linear array of fluid ionization chambers and a solid state, amorphous silicon detector. Agreement between predicted and measured portal dose is better than 5% in areas of low dose gradient ($<30\%/cm$) and better than 5 mm in areas of high dose gradient ($>30\%/cm$) for the variety of situations tested here. It is concluded that this portal dose prediction algorithm is fast, accurate, allows separation of primary and scatter dose, and can model dose image formation in arbitrary detector systems.

ACKNOWLEDGEMENTS

I would like to take this opportunity to thank the people who have contributed to this project in many unique ways.

I would like to thank my supervisor and mentor, Dr. Stephen Pistorius. Stephen leads our Medical Physics Department by example, being an excellent scientific researcher with great insight and innovative approaches to problem solving, as well as a wonderful teacher who provides his students with sound instruction. From the beginning of this project, Stephen has been committed to providing me with the best learning experience possible. I look forward with great anticipation to continuing our productive relationship as we expand this departments' research and academic programs and work towards making this the best cancer treatment facility in Canada.

I would like to thank my advisory committee for their valuable advice throughout this project. The members include Professor Norm Davison, Dr. Ray Somerjai, Dr. Ahmet Leylek, and Dr. John Lewis. In particular I would like to thank John for many thoughtful comments during manuscript preparation.

I would also like to thank my friends and colleagues Drs. Richard Lee, Jeff Bews, David Viggars, Satyapal Rathee, Keith Furutani, and Yuri Mandelzweig, as well as Anita Berndt, Collins Yeboah, Steve Miller, Kishalay Kundo, Cathy MacGillivray, Cathy Neath, Cristina Spanu, James Beck, and Kyle Malkoskie.

I would like to especially thank my friend and colleague Kurt Luchka, currently working at the British Columbia Cancer Agency, Vancouver Centre. Kurt sponsored my measurement efforts involving an amorphous silicon portal imaging detector (as presented in chapter six) during a one week whirlwind visit in May of 2000. He

sacrificed all of his nights that week and portions of his daytime, in order to assist my research efforts. In addition, Kurt was extremely accommodating whenever I required any additional measurements with the detector (which meant extra work for him!), and provided editorial help for chapter six of this thesis.

I have also had excellent technical support provided to me throughout this research project. The Medical Devices staff (including Ian Paul, Bob Miller, Chad Harris, Georgette Land, Sean Billing, and Andy Egtberts) have provided many useful gadgets to assist my experimental activities. I would like to thank Brian Myslicki of the Nuclear Electronics section for answering my constant barrage of technical questions related to electronic portal imaging. I would like to thank Janet Martin (formerly of Treatment Planning) for providing assistance in acquiring CT data. Special thanks are extended to Randy Roels, Kelly Francey, Brad Versluis, and Khay Khan for providing me with substantial computer support.

I would like to gratefully acknowledge financial support for this project provided by the University of Manitoba, CancerCare Manitoba, the Manitoba Health Research Council, and Siemens Medical Systems (Concord, CA).

I would like to thank my brother Wayne, my sister Kate, and especially my parents, Helen and Larey, for fostering my curiosity, instilling a respect for education, and always supporting my choices in life.

Finally, I would like to express my deepest gratitude to my wife Kerri, for her incredible support, encouragement, and patience throughout this long journey. Words cannot express how important she has been in this endeavour, as in all other aspects of my life.

PUBLICATIONS

The majority of the content of this thesis has been (or is in the process of being) published by myself and Dr. Stephen Pistorius. Chapters three, four, and five are mainly based on [Mc00a], [Mc00b], and [Mc00c] of the references respectively. Chapter six is based on a manuscript which is in press in the *Medical Physics Journal*, with Kurt Luchka (of the British Columbia Cancer Agency, Vancouver Centre) as coauthor. Appendix A is primarily contained in [Mc99] of the references. Appendix C summarizes work presented at the 5th International Workshop on Electronic Portal Imaging [Mc98a].

TABLE OF CONTENTS

ABSTRACT	ii
ACKNOWLEDGEMENTS	iv
PUBLICATIONS	vi
TABLE OF CONTENTS	vii
TABLE OF FIGURES	xii
CHAPTER ONE: RATIONALE	
1.1 Description of treatment process	1
1.2 Tissue response to radiation	3
1.3 Uncertainties in radiotherapy treatment	6
1.4 Rationale for treatment verification in radiotherapy	8
CHAPTER TWO: INTRODUCTION	
2.1 Current Methods of Treatment Verification	9
2.1.1 Record and verify systems	9
2.1.2 Geometric treatment verification	10
2.1.3 Dosimetric treatment verification	12
2.2 Potential of Portal Imaging Systems for Dosimetric Treatment Verification ..	15
2.2.1 Portal Imaging Systems	15
2.2.1.1 Camera/screen systems	15
2.2.1.2 Liquid ionisation matrix	17
2.2.1.3 Solid state detectors – linear arrays	17
2.2.1.4 Solid state detector arrays – area arrays	18
2.2.2 Proposed applications/implementations for portal image dosimetry ...	19
2.2.2.1 Comparison of predicted image to measured image	19
2.2.2.2 Adjustment of patient CT data	20
2.2.2.3 Exit dosimetry	20
2.2.2.4 Transit dosimetry	21
2.2.2.5 Recalculating patient dose distribution	22
2.2.2.6 Verifying dynamic treatment beams	23
2.3 Current Methods of Predicting Portal Dose Images	25
2.3.1 Problems to be addressed	25
2.3.2 Use of treatment planning algorithms	27
2.3.3 Three-dimensional superposition	28
2.3.4 Two-dimensional superposition	30
2.3.4.1 Experimental scatter kernels	31
2.3.4.2 Monte Carlo simulation of scatter kernels	32
2.4 The Need for a General Approach to Portal Dose Image Prediction	33
2.4.1 Summary of limitations of current approaches	33
2.4.2 Required features of a general approach	33

2.5	A Brief Overview of Monte Carlo Techniques for Radiation Transport	35
2.5.1	Monte Carlo technique	35
2.5.2	The EGS4 radiation transport code	36
2.5.3	Selection of random numbers	38
2.5.4	Accuracy of EGS4	38
2.6	Equivalent Fields	40
2.7	Thesis Overview	41

CHAPTER THREE: PHOTON SCATTER IN PORTAL IMAGES: PHYSICAL CHARACTERISTICS OF PENCIL BEAM KERNELS GENERATED USING THE EGS MONTE CARLO CODE

3.1	Introduction	45
3.2	Materials and Methods	47
3.2.1	Simulation geometry for ideal pencil beams	47
3.2.2	Monte Carlo simulation	49
3.2.3	Scatter fraction, full width at half maximum, and modulation transfer function	50
3.3	Results and Discussion	52
3.3.1	Comparison of singly scattered fluence with analytical calculation ...	52
3.3.2	Influence of air gap on pencil beam scatter kernels	61
3.3.3	Influence of phantom thickness on pencil beam scatter kernels	62
3.3.4	Scatter fraction	65
3.3.5	Full width at half maximum of scatter fluence	73
3.3.6	Modulation transfer function	76
3.5	Summary and Conclusion	79

CHAPTER FOUR: PHOTON SCATTER IN PORTAL IMAGES: ACCURACY OF A FLUENCE BASED PENCIL BEAM SUPERPOSITION ALGORITHM

4.1	Introduction	82
4.2	Materials and Methods	86
4.2.1	Monte Carlo simulation of radiation transport	86
4.2.2	Generating ideal pencil beams using Monte Carlo simulation	86
4.2.3	Pencil beam algorithm to predict scatter fluence	88
4.2.4	Monte Carlo simulation using phantoms	90
4.2.5	Experimental validation of Monte Carlo simulations	94
4.2.6	Assessment of accuracy	95

4.3	Results and Discussion	98
4.3.1	Experimental validation of Monte Carlo simulations	98
4.3.2	Accuracy of pencil beam algorithm in predicting fluence	100
4.3.2.1	Effect of field size	100
4.3.2.2	Effect of air gap	102
4.3.2.3	Effect of generating scatter kernels in a semi-infinite slab geometry	106
4.3.2.4	Errors due to use of the EHP concept	108
4.3.2.5	Sampling resolution of incident beam	114
4.3.3	Accuracy of pencil beam algorithm in predicting mean energy and mean angle	117
4.4	Conclusion	119

CHAPTER FIVE: A TWO STEP ALGORITHM FOR PREDICTING PORTAL DOSE IMAGES IN ARBITRARY DETECTORS

5.1	Introduction	120
5.2	Materials and Methods	125
5.2.1	Predicting fluence reaching the portal imager	125
5.2.2	Converting fluence to dose in the detector	129
5.2.3	Off-axis spectrum softening	133
5.2.4	Experimental validation	134
5.3	Results and Discussion	136
5.3.1	Dose kernels	136
5.3.2	Effects of the flattening filter	139
5.3.3	Experimental validation of portal dose prediction algorithm	141
5.4	Discussion and Conclusions	148

CHAPTER SIX: DOSIMETRIC INVESTIGATION AND PORTAL DOSE IMAGE PREDICTION USING AN AMORPHOUS SILICON ELECTRONIC PORTAL IMAGING DEVICE

6.1	Introduction	150
6.2	Materials and Methods	154
6.2.1	Flat panel detector characteristics	154
6.2.1.1	Detector description	154
6.2.1.2	Energy response	155
6.2.1.3	Linearity	157
6.2.1.4	Glare	158
6.2.2	Portal dose prediction algorithm	160
6.2.3	Experimental validation	163

6.3	Results and Discussion	165
6.3.1	Flat panel detector characteristics	165
6.3.1.1	Energy response	165
6.3.1.2	Linearity	172
6.3.1.3	Glare	174
6.3.2	Experimental validation of dose algorithm	181
6.3.2.1	Scatter fluence kernels	181
6.3.2.2	Comparison of predicted and measured images	189
6.4	Conclusions	201

CHAPTER SEVEN: SUMMARY

7.1	Conclusion	203
7.2	Future Work	209

APPENDIX A: DETERMINATION OF EQUIVALENT PHOTON FIELDS THROUGH INTEGRATED 1D CONVOLUTION KERNELS

A.1	Introduction	213
A.2	Theory	215
A.2.1	Integrated 1D kernels for dose calculation	215
A.2.2	Equivalent Fields	218
A.3	Methods	220
A.3.1	Generating scatter kernels using Monte Carlo simulation	220
A.3.2	Deriving equivalent fields through conservation of energy	222
A.3.3	Application to equivalent fields concepts	223
A.4	Results and Discussion	226
A.4.1	Validation of integrated 1D kernel dose calculation technique	226
A.4.2	Deriving equivalent field relationships through conservation of energy	228
A.4.3	Energy independence of equivalent fields	231
A.4.4	Generating equivalent field relationships for rectangular fields	231
A.4.5	Validity of the equivalent fields concept	233
A.4.6	Modifying depth dose matching by using truncated kernels	237
A.4.7	Investigating the equivalent fields concept away from the central axis	237
A.5	Conclusions	241

APPENDIX B:	CONVERTING DIVERGENT BEAM SCATTER FRACTION DATA INTO A PARALLEL GEOMETRY	243
-------------	--	-----

APPENDIX C: ANALYTICAL PREDICTION OF FIRST SCATTER ENERGY FLUENCE INTO A PORTAL IMAGING DEVICE	
C.1 Introduction	246
C.2 Materials and Methods	247
C.3 Results	249
C.4 Discussion and Conclusions	251
APPENDIX D: UNCERTAINTY ESTIMATES	252
REFERENCES	257

TABLE OF FIGURES AND TABLES

CHAPTER ONE: RATIONALE

Figure 1.1: Example of a dose response curve for tumour control and normal tissue complication.	4
--	---

CHAPTER TWO: INTRODUCTION

No figures or tables.

CHAPTER THREE: PHOTON SCATTER IN PORTAL IMAGES: PHYSICAL CHARACTERISTICS OF PENCIL BEAM KERNELS GENERATED USING THE EGS MONTE CARLO CODE

Figure 3.1: Geometry of pencil beam simulation. Scattered photon fluence, mean energy, and mean angle were scored within the radial bins as a function of air gap, phantom thickness, and photon history.	48
--	----

Figure 3.2: Scattered photon fluence normalized to the incident fluence ($\times 10^{-6} \text{ cm}^{-2}$) due to an incident (a) 6 MV, (b) 24 MV, (c) 2 MeV, and (d) 10 MeV pencil beam behind a 20 cm thick water slab, at various air gaps. Solid lines represent singly scattered photon fluence, dashed lines represent multiply scattered photon fluence, and dotted lines represent bremsstrahlung and positron annihilation photons. Gray lines represent results of an analytical singly scattered fluence calculation. Background shading indicates dominance of the singly scattered photon fluence while no shading indicates dominance of the multiply scattered fluence component <i>except</i> in (d), where no shading indicates dominance of the bremsstrahlung and positron annihilation photons.	54
--	----

Figure 3.3: Mean energy (MeV) of scattered photon fluence due to an incident (a) 6 MV, (b) 24 MV, (c) 2 MeV, and (d) 10 MeV pencil beam behind a 20 cm thick water slab, at various air gaps. Solid lines represent mean energy of singly scattered photons, dashed lines represent mean energy of multiply scattered photon fluence, and dotted lines represent mean energy of bremsstrahlung and positron annihilation photons. Gray lines represent results of an analytical singly scattered fluence calculation.	56
--	----

Figure 3.4: Scattered photon fluence normalized to the incident fluence ($\times 10^{-6} \text{ cm}^{-2}$) due to an incident (a) 6 MV, (b) 24 MV, (c) 2 MeV, and (d) 10 MeV pencil beam at a 30 cm air gap, behind various thickness' of water phantom. Solid lines represent singly scattered photon fluence, dashed lines represent multiply scattered photon fluence, and dotted lines represent bremsstrahlung and positron annihilation	
---	--

photons. Gray lines represent results of an analytical singly scattered fluence calculation. Background shading indicates dominance of the singly scattered photon fluence while no shading indicates dominance of the multiply scattered fluence component *except* in (d), where no shading indicates dominance of the bremsstrahlung and positron annihilation photons. 58

Figure 3.5: Mean energy (MeV) of scattered photon fluence due to an incident (a) 6 MV, (b) 24 MV, (c) 2 MeV, and (d) 10 MeV pencil beam at a 30 cm air gap, behind various thicknesses of water phantom. Solid lines represent mean energy of singly scattered photons, dashed lines represent mean energy of multiply scattered photon fluence, and dotted lines represent mean energy of bremsstrahlung and positron annihilation photons. Gray lines represent results of an analytical singly scattered fluence calculation. 60

Figure 3.6(a): Total scatter fraction as a function of air gap and phantom thickness, for a 27×27 cm² field. Solid lines represent results using a 6 MV spectrum, dotted lines represent results using a 24 MV spectrum. The dashed line locates the cross section plotted in Figures 3.6 (b) and 3.6 (c). 68

Figure 3.6(b): Cross section of the 6 MV results corresponding to dashed line in Figure 3.6(a). The solid line represents scatter fraction due to singly scattered photons, the short dashed line represents scatter fraction due to multiply scattered photons, the dotted line represents scatter fraction due to bremsstrahlung and positron annihilation photons, and the long dashed line represents the total scatter fraction. 68

Figure 3.6(c): Cross section of the 24 MV results corresponding to dashed line in Figure 3.6(a). Line legend as in 3.6(b) description. 68

Figure 3.7(a): Total scatter fraction as a function of phantom thickness and field size, for a 30 cm air gap. Solid lines represent results using a 6 MV spectrum, dotted lines represent results using a 24 MV spectrum. The dashed line locates the cross section plotted in Figures 3.7(b) and 3.7(c). 70

Figure 3.7(b): Cross section of the 6 MV results corresponding to dashed line in Figure 3.7(a). The solid line represents scatter fraction due to singly scattered photons, the short dashed line represents scatter fraction due to multiply scattered photons, the dotted line represents scatter fraction due to bremsstrahlung and positron annihilation photons, and the long dashed line represents the total scatter fraction. 70

Figure 3.7(c): Cross section of the 24 MV results corresponding to dashed line in Figure 3.7(a). Line legend as in 3.7(b) description. 70

- Figure 3.8(a): Total scatter fraction as a function of field size and air gap, for a 20 cm thick water phantom. Solid lines represent results using a 6 MV spectrum, dotted lines represent results using a 24 MV spectrum. The dashed line locates the cross section plotted in Figures 3.8(b) and 3.8(c). 72
- Figure 3.8(b): Cross section of the 6 MV results corresponding to dashed line in Figure 3.8(a). The solid line represents scatter fraction due to singly scattered photons, the short dashed line represents scatter fraction due to multiply scattered photons, the dotted line represents scatter fraction due to bremsstrahlung and positron annihilation photons, and the long dashed line represents the total scatter fraction. 72
- Figure 3.8(c): Cross section of the 24 MV results corresponding to dashed line in Figure 3.8(a). Line legend as in 3.8(b) description. 72
- Figure 3.9: Full width at half maximum data (in cm) as a function of air gap and phantom thickness for scattered photon fluence pencil beams representing (a) singly scattered photons, (b) multiply scattered photons, and (c) bremsstrahlung and positron annihilation photons. Solid lines represent 6 MV spectrum and dotted lines represent 24 MV spectrum. 75
- Figure 3.10: Modulation transfer function of point spread functions using (a) 6 MV, and (b) 24 MV pencil beam through a 20 cm thick water phantom, for various air gaps. 77
- Figure 3.11: Modulation transfer function of point spread functions using (a) 6 MV, and (b) 24 MV pencil beam, at an air gap of 30 cm for various phantom thickness'. 78

CHAPTER FOUR: PHOTON SCATTER IN PORTAL IMAGES: ACCURACY OF A FLUENCE BASED PENCIL BEAM SUPERPOSITION ALGORITHM

- Figure 4.1: Scatter fluence kernels per incident particle, scored at an air gap of 30 cm behind a 20 cm thick water slab due to incident polyenergetic pencil beam representing 6 MV (thin lines) and 24 MV (thick lines) spectra. 87
- Figure 4.2: Phantom cross sections, with all dimensions in centimeters. Incident beam edges are indicated by dotted arrows. Density is colour coded as ■ $\rho=1.9 \text{ g/cm}^3$, ◼ $\rho=1.0 \text{ g/cm}^3$, ◻ $\rho=0.2 \text{ g/cm}^3$, ◻ $\rho=0.0012 \text{ g/cm}^3$ 93
- Figure 4.3: A comparison of scatter fractions measured by Jaffray *et al* [Ja94] using an ionization chamber (6 MV, 17 cm PMMA slab), and estimated with Monte Carlo techniques including a model of detector response (6 MV, 20 cm water slab).

Monte Carlo estimates were converted [Mc00a] from a parallel geometry to a diverging geometry. Four field sizes are shown. 99

Figure 4.4: Cross section through centre of scoring plane showing predicted total scatter fluence per incident beam fluence for phantom 1 at 30 cm air gap for 10×10 cm², 20×20 cm², 30×30 cm² incident fields with a 6 MV energy spectrum. 101

Table 4.1: Maximum difference between predicted and simulated scatter fluence as a percentage of total fluence on central axis at scoring plane, for phantom 1 and a 6 MV energy spectrum, as a function of air gap and incident field size. 101

Table 4.2: Maximum difference between predicted and simulated scatter fluence as a percentage of total fluence on central axis at scoring plane, for phantoms 1-9 (P1-P9), as a function of air gap and incident energy spectra. A negative value indicates an underestimate relative to the Monte Carlo simulation results. All field sizes are 10×10 cm², except for phantom 7 (8×14 cm²) and phantom 8 (30×30 cm²). 104

Figure 4.5: Maximum error between predicted scatter fluence and DOSXYZ output as a percentage of total fluence on the central axis, as a function of air gap, 10×10 cm² field. Results shown are for (a) phantom 2 with a 6 MV beam, and (b) phantom 6 with a 24 MV beam. 105

Figure 4.6: Cross section through centre of scoring plane (y = 20 cm) showing predicted scatter fluence per incident beam fluence by photon history component. Symbols represent DOSXYZ output, while lines signify pencil beam algorithm prediction. Results are for phantom 9 at a 30 cm air gap using a 24 MV energy spectrum. The orientation of the phantom and incident field are depicted at the top of the figure. 107

Figure 4.7: Cross section through centre of scoring plane (y = 20 cm) showing predicted scatter fluence per incident beam fluence by photon history component. Total scatter fluence is represented by *, singly scattered fluence by +, multiply scattered fluence by Δ, and bremsstrahlung and positron annihilation fluence by □. Symbols represent DOSXYZ output, while lines signify pencil beam algorithm prediction. Results are for phantom 2 at a 30 cm air gap using a 6 MV beam (a), and phantom 6 at 30 cm air gap using a 24 MV beam (b). 111

Figure 4.8: Error in pencil beam algorithm predicted scatter fluence per incident beam fluence, as a percentage of total fluence on the central axis, for phantom 8 using a 6 MV beam and 30×30 cm² field, for air gaps of (a) 0 cm, (b) 10 cm, (c) 20 cm, and (d) 40 cm. 113

Figure 4.9: Dependence of maximum percentage error of pencil beam algorithm scatter fluence estimate on spatial resolution of incident pencil beam grid. The dotted line represents the estimate of worst performance. 116

Figure 4.10: Cross section through scoring plane ($y = 20$ cm) showing predicted mean energy (a and c), and mean angle with respect to the incident pencil beam (b and d), by photon history component. Results for single scatter are represented by +, multiple scatter by Δ , and bremsstrahlung and positron annihilation fluence by \square . Symbols represent DOSXYZ output, while lines signify pencil beam algorithm prediction. Results in (a) and (b) are for phantom 2 at a 30 cm air gap using a 6 MV, 10×10 cm² field, while those for (c) and (d) are for phantom 6 at a 30 cm air gap using a 24 MV, 10×10 cm² field. 118

CHAPTER FIVE: A TWO STEP ALGORITHM FOR PREDICTING PORTAL DOSE IMAGES IN ARBITRARY DETECTORS

Figure 5.1: Cross section illustrating geometry of dose kernels for a portal imaging detector consisting of two layers of material. 131

Figure 5.2: Detector response (normalized at 10 MeV) for eight portal imaging detectors obtained by integrating energy deposited over entire detection layer. Detectors include a high resolution storage phosphor [Ba91], ST storage phosphor with 0.8 mm lead buildup [Ba91], film sandwiched between two 0.8 mm lead sheets [Ba87], linear array (LA48) with 3.5 cm PMMA buildup, LA48 with 0.2 cm brass buildup, Siemens Beamview^{Plus} detector, and a Philips SRI-100 with an additional 0.1 cm of steel buildup [Pa98a]. 137

Figure 5.3: Difference between monoenergetic and pseudo-polyenergetic approach for modeling scatter dose kernels illustrated with the metal/phosphor Beamview^{Plus} detector, for a slab of PMMA, 15×15 cm², 6 MV field, at 20 cm air gap. 138

Figure 5.4: Demonstration of improvement in comparison with measured data obtained by modeling primary energy fluence hardening through the flattening filter (FF). Data is acquired using an incident 6 MV, 15×15 cm² field, with the LA48 detector with PMMA buildup, 29 cm thick PMMA slab phantom, at an air gap of 80 cm. Comparison is done at large air gap to reduce the scatter dose contribution to a small uniform value. 140

Figure 5.5: Predicted total portal dose images at 10 cm air gap behind a slab phantom (a), a simple lung phantom (b), thorax of anthropomorphic phantom (c), pelvis of anthropomorphic phantom (d). Beam energy and field size are 6 MV, 15×15 cm² for (a), (b), and (c), and 23 MV, 10×10 cm² for (d). Position of measured profiles presented in Figure 5.6 correspond to horizontal white lines. 143

Figure 5.6: Sample predicted and measured profiles behind all phantoms tested here. Beam energy and field size are 6 MV, 15×15 cm² for (a), (b), and (c), and 23 MV, 10×10 cm² for (d). Both small and large air gaps are demonstrated (with normalization performed to maximum point of total dose at small air gap, to keep

relative magnitudes at different air gaps preserved). Calculated scatter dose is also illustrated. Detector configurations are LA48 with PMMA buildup in (a) and (b), and LA48 with brass buildup in (c) and (d). Error in the measured data points is estimated at $\pm 1.3\%$ (see section 5.2.4 for explanation). 145

Figure 5.7: Analysis of measured and predicted total dose comparison, using categories proposed by Van Dyk *et al* [Va93]. 147

CHAPTER SIX: DOSIMETRIC INVESTIGATION AND PORTAL DOSE IMAGE PREDICTION USING AN AMORPHOUS SILICON ELECTRONIC PORTAL IMAGING DEVICE

Figure 6.1: (a) Dose kernels for the aS500 detector in configuration A (solid line) and B (dotted line), for 1 MeV and 10 MeV incident photon energy. (b) All dose kernels for the aS500 detector in configuration A (solid lines) and B (dotted lines), as a function of radius and incident photon energy. Dose contours are labeled in units of Gy/incident particle. 166

Figure 6.2: (a) Detector response for the aS500 detector in configuration A (solid lines) and B (dotted lines). (b) Relative detector response normalized to 10 MeV for the aS500 detector in configuration A (solid line) and B (dotted line), and a water detector (dashed line). (c) Percentage of total deposited energy which is attributable to scattered photons arising in the detector itself, for the aS500 detector in configuration A (solid line) and B (dotted line), and a water detector (dashed line). 168

Figure 6.3: (a) Detector response of various layers of phosphor in the aS500, configuration A. Entrance layer (dashed line), middle layer (dotted line), and exit layer (solid line) are presented. (b) Detector response of various layers of phosphor in the aS500, configuration B. Entrance layer (dashed line), middle layer (dotted line), and exit layer (solid line) are presented. 171

Figure 6.4: (a) Linearity of aS500 detector in configuration A with frame integration, using images of an open, $15 \times 15 \text{ cm}^2$ field for 6 MV (circles) and 18 MV (squares) beams. (b) Linearity of aS500 in configuration A with dose rate, using images of an open, $15 \times 15 \text{ cm}^2$, 6 MV field. Two ROI's are examined in the images, one on the central axis (circles) and one $\sim 4 \text{ cm}$ outside the field edge (squares). 173

Figure 6.5: (a) Profiles of images acquired using the aS500 detector in configuration A, for an open, $15 \times 15 \text{ cm}^2$, 6 MV field. SDD's include 120 cm (solid line), 150 cm (dotted line), and 180 cm (dashed line). (b) Profiles of images acquired using the aS500 detector in configuration A, for an open, $15 \times 15 \text{ cm}^2$, 18 MV field. SDD's include 120 cm (solid line), 150 cm (dotted line), and 180 cm (dashed line). 176

- Figure 6.6: (a) Profiles of images acquired using the aS500 detector in configuration A, for an open, $15 \times 15 \text{ cm}^2$, 6 MV field. Profiles are normalized to central axis, and SDD's include 120 cm (solid line), 150 cm (dotted line), and 180 cm (dashed line). (b) Profiles of images acquired using the aS500 detector in configuration A, for an open, $15 \times 15 \text{ cm}^2$, 18 MV field. Profiles are normalized to central axis, and SDD's include 120 cm (solid line), 150 cm (dotted line), and 180 cm (dashed line). 177
- Figure 6.7: (a) Glare kernel used to model the glare effect. The initial kernel estimate is represented by solid circles, while the dotted line represents the final glare kernel. (b) Normalized profiles of a predicted portal dose image of an open, $15 \times 15 \text{ cm}^2$, 6 MV field (solid line), the result of convolving this image with the glare kernel (dotted line), and the measured data using the aS500 in configuration A (dashed line). 180
- Figure 6.8: (a) Scattered photon fluence normalized to the number of incident particles ($\times 10^{-6} \text{ cm}^{-2}$) due to an incident 6 MV pencil beam of photons, behind a 20 cm thick water slab with radius 17.5 cm, at a range of air gaps. Solid lines represent singly scattered photon fluence, dashed lines represent multiply scattered photon fluence, and dotted lines represent bremsstrahlung and positron annihilation photons. Gray lines represent results of an analytical singly scattered fluence calculation. Locations α and β are used in further analysis presented in (b, c, d) on next page. 183
- Figure 6.8: (b) Scattered fluence energy spectrum in location α . (c) Scattered fluence energy spectrum in location β . (d) Comparison of Monte Carlo scored (solid lines) and analytically calculated (dotted lines) singly scattered photon energy fluence, at locations α and β 185
- Figure 6.9: (a) Scattered photon fluence normalized to the number of incident particles ($\times 10^{-6} \text{ cm}^{-2}$) due to an incident 18 MV pencil beam of photons, behind a 20 cm thick water slab with radius 17.5 cm, at a range of air gaps. Solid lines represent singly scattered photon fluence, dashed lines represent multiply scattered photon fluence, and dotted lines represent bremsstrahlung and positron annihilation photons. Gray lines represent results of an analytical singly scattered fluence calculation. Locations α and β are used in further analysis presented in (b, c, d) on next page. 186
- Figure 6.9: (b) Scattered fluence energy spectrum in location α . (c) Scattered fluence energy spectrum in location β . (d) Comparison of Monte Carlo scored (solid lines) and analytically calculated (dotted lines) singly scattered photon energy fluence, at locations α and β 188
- Figure 6.10: (a) Measured and predicted image profiles through isocentre at 150 cm SDD for a $15 \times 15 \text{ cm}^2$, 6 MV field incident on a 26 cm thick, homogeneous, water equivalent slab using the aS500 in configuration A. Included are the measured

- data (solid line), predicted dose convolved with glare (dotted line), predicted dose without glare (dashed line), and scattered dose (dash-dot line). (b) Analysis of comparison of measured and predicted images in (a). Figure 6.10 continued on next page. 192
- Figure 6.10 (continued): (c) Measured and predicted image profiles through isocentre at 120 cm SDD for a $15 \times 15 \text{ cm}^2$, 18 MV field incident on a 26 cm thick, homogeneous, water equivalent slab using the aS500 in configuration B. Line labeling as in (a). (d) Analysis of comparison of measured and predicted images in (c). 193
- Figure 6.11: (a) Measured image at 130 cm SDD for a $15 \times 15 \text{ cm}^2$, 6 MV field incident on the chest of the Rando phantom. (b) Associated predicted image for configuration in (a). (c) Difference image using (a) and (b), 50% relative dose difference indicated by black, 0% relative dose difference indicated by white. Figure 6.11 continued on next page. 194
- Figure 6.11 (continued): (d) Profiles taken transversely through the images in the location indicated by the white line in (a) and (b). Included are the measured data (solid line), predicted dose convolved with glare (dotted line), predicted dose without glare (dashed line), and scatter dose component (dash-dot line). (e) Analysis of comparison of measured and predicted images presented in (a) and (b). 195
- Figure 6.12: (a) Measured image at 130 cm SDD for a $15 \times 15 \text{ cm}^2$, 6 MV field incident on the pelvis of the Rando phantom. (b) Associated predicted image for configuration in (a). Note that a contrast enhancement function was applied equally to each image, strictly for improved visual clarity and not for analysis. (c) Difference image using (a) and (b), 50% relative dose difference indicated by black, 0% relative dose difference indicated by white. Figure 6.12 continued on next page. 196
- Figure 6.12 (continued): (d) Profiles taken transversely through the images in the location indicated by the white line in (a) and (b). Included are the measured data (solid line), predicted dose convolved with glare (dotted line), predicted dose without glare (dashed line), and scatter dose component (dash-dot line). (e) Analysis of comparison of measured and predicted images presented in (a) and (b). 197
- Figure 6.13: (a) Measured image at 130 cm SDD for a $15 \times 15 \text{ cm}^2$, 6 MV field laterally incident on the head of the Rando phantom. (b) Associated predicted image for configuration in (a). (c) Difference image using (a) and (b), 50% relative dose difference indicated by black, 0% relative dose difference indicated by white. Figure 6.13 continued on next page. 198

Figure 6.13 (continued): (d) Profiles taken transversely through the images in the location indicated by the white line in (a) and (b). Included are the measured data (solid line), predicted dose convolved with glare (dotted line), predicted dose without glare (dashed line), and scatter dose component (dash-dot line). (e) Analysis of comparison of measured and predicted images presented in (a) and (b).	199
---	-----

APPENDIX A: DETERMINATION OF EQUIVALENT PHOTON FIELDS THROUGH INTEGRATED 1D CONVOLUTION KERNELS

Figure A.1: Integration of a three dimensional energy deposition kernel over defined field bounds, after alignment with transverse plane calculation point (x, y). This results in the integrated 1D kernel valid for that calculation point and given field.	217
Figure A.2: Cylindrical scoring geometry for Monte Carlo simulation of energy deposition kernels. Square ring geometry was scored simultaneously.	221
Figure A.3: Isodose lines generated for the midplane of a 15×15 cm ² square incident field and 6 MV spectrum using the integrated 1D kernel convolution approach (solid lines), and Monte Carlo simulation (dotted lines). Shown are 1%, 5%, 10%, 30%, 50%, 70%, and 90% isodose curves.	227
Figure A.4: Total integrated energy of scatter kernel versus field size (related to kernel radius via reciprocity) for a 6 MV spectrum. The analytical fit to the circular field data is used to generate square field data and is compared to directly simulated results.	229
Table A.1: Fit statistics for the total integrated scatter kernel energy, using equation (A.3), and theoretical estimate of fit parameter A (see text for detail).	229
Figure A.5: Derived circular to square field relationships for cobalt-60, 6 MV, and 24 MV energy spectra compared with empirical BJR 25 data. Difference at 60 cm diameter is ~2%. Best fit line to BJR 25 data is: diameter/square side=0.891+0.00046·diameter. Best fit line of all energy spectra results shown is: diameter/square side=0.8915+0.000158·diameter.	230
Figure A.6: Magnitude difference (contours in cm) between equivalent square fields of various rectangular dimensions as calculated by the scatter kernel integration method (using a 6 MV spectrum) and those presented in BJR 25.	232
Figure A.7: Illustration of the difference between the accurately calculated kernel and the kernel associated with the equivalent square fields found by COE and BJR 25 look up table, for a 30×2 cm ² cobalt-60 beam. The inset magnifies the kernels	

around the point of forced interaction ($z=60$ cm), where the equivalent kernels overestimate the actual kernel. 235

Figure A.8: Result of different kernels on predicted central axis scatter for cobalt-60 beams. The actual kernel result represents the scatter dose predicted with the kernel generated with Clarkson radial integration over the 30×2 cm² field. Using the equivalent COE kernel provides a better match over all depth, while using the equivalent BJR 25 kernel provides a better match at shallower depth. The equivalent predicted scatter dose curves intersect the actual scatter dose at 16.4 cm for the COE equivalent kernel and 10.4 cm for the BJR equivalent kernel. Matching at a specific depth may be accomplished by choosing an equivalent field based on an energy relationship generated with truncated scatter kernels (the range of truncation has been chosen to result in a depth dose match at 10.0 cm). 236

Figure A.9: Calculation points chosen to illustrate the change in 1D kernel shape and hence scatter dose distribution as the point moves away from the central axis, for a 15×15 cm² field. See Figure A.10. 239

Figure A.10: Effect of moving off of the central axis, while trying to maintain an equivalent field relationship, using calculation points illustrated in Figure A.9. (a) The accurate 1D kernels calculated via Clarkson integration. (b) The resulting scatter dose using the accurate kernels in (a). (c) The kernels associated with the COE equivalent fields. (d) The resulting scatter dose using the equivalent kernels in (c). 240

APPENDIX B: CONVERTING DIVERGENT BEAM SCATTER FRACTION DATA INTO A PARALLEL GEOMETRY

No figures or tables.

APPENDIX C: ANALYTICAL PREDICTION OF FIRST SCATTER ENERGY FLUENCE INTO A PORTAL IMAGING DEVICE

Figure C.1: Scoring geometry. 248

Table C.1: Percentage agreement between analytical model and Monte Carlo simulation for various simple phantoms. 249

Figure C.2: Comparison of Monte Carlo simulated first scatter fluence with analytical results. 250

APPENDIX D: UNCERTAINTY ESTIMATES

Table D.1: Summary of percentage algorithm execution time as a function of calculation step.	256
Table D.2: Uncertainty estimates and associated calculation section of the algorithm in which they are involved.	256

CHAPTER ONE

RATIONALE

1.1 Description of treatment process

The main modalities for cancer treatment are surgery, chemotherapy, and radiotherapy, often delivered in combination. Radiotherapy may be administered via external radiation beams, or less often via application of radioactive sources inserted in the diseased tissue (brachytherapy). The success of a radiotherapy treatment is critically dependent on delivering the prescribed dose to the tumor while simultaneously minimizing damage to healthy tissue. This is a difficult undertaking, and requires a large number of steps involving many different types of professional staff including radiation oncologists, radiation therapists, and medical physicists.

Initially, the cancer needs to be diagnosed. Once location is identified (through palpation, exploratory surgery, endoscopy, or various imaging techniques), pathological assessment of a tissue biopsy assigns the tumor a grade and stage, which will help define the course of treatment and prescribed doses of chemotherapy and radiotherapy.

The patient is imaged using computed tomography (CT), and the 3D image set is used quantitatively for treatment planning and dose computations based on tissue densities. Treatment planning involves choosing the modality, energy, number, shape, and direction of radiation beams in order to deliver the prescribed dose to the tumor while minimizing dose to surrounding tissue. CT data are preferred since they are geometrically accurate and may be converted to electron density information using simple relationships for subsequent accurate calculation of the delivered dose distribution within the patient.

Once the beam configurations are decided upon, the treatment is simulated. This may be done by setting up the patient on a couch and recreating the planned beams using a 'conventional simulator', which closely mimics the motions and beam delivery of a real treatment unit, or it may be done by virtual simulation. The conventional simulator is equipped with a diagnostic x-ray tube, and therefore is much less costly (in money and patient dose) than a real treatment unit which has a linear accelerator. The simulation allows the treatment to be checked for any potential problems before treatment actually begins, making for a more efficient use of resources. Instead of delivering megavoltage radiation, the simulator 'delivers' a diagnostic x-ray beam. This ability allows diagnostic quality x-rays of the patient anatomy to be acquired when in simulated treatment position, which may be used to assess beam coverage of the tumor and to compare to megavoltage images acquired during real treatment. If the CT data set is available, a computer calculation of this x-ray image (digitally reconstructed radiograph) may also be available and used in virtual simulation.

When the treatment plan is successfully simulated, the patient may then be treated. The patient is set up in a manner as close as possible to the simulation set up. Additional customised beam shaping and/or intensity modifying devices (e.g. compensators, wedges, multileaf collimator) may be physically incorporated into one or more beams at this point. The prescribed dose is delivered in many fractions (for radiobiological advantage), typically 25-30 over a period of 5-6 weeks. Each fraction will involve the delivery of all fields of radiation in the treatment plan.

The entire process is complex and involves many professionals and machines. Each step adds to the overall uncertainty, and there is always a risk of human error.

1.2 Tissue response to radiation

The relationship between the delivered dose and the biological consequence in a particular tissue is described by a dose-response curve. These curves are sigmoidal in shape (see Figure 1.1) with steep slopes and variable relative positions, and are unique to a particular tissue type. A quantitative description of the slope is the normalised dose gradient (γ), and may be expressed as [Br84]: $\gamma = D \cdot (dR/dD)$, where D is the dose and R is the response of the tissue (percentage of cells unable to reproduce). This parameter describes the change in tumor response for a given relative increase in absorbed dose. Values of γ for tumor tissues are commonly above 3.0 and occasionally above 5.0 [Br84], whereas slopes for healthy tissue are usually even steeper [Mi87].

The higher a dose delivered to the tumor, the greater the ability to control the tumor. However, if increasing dose is delivered to the healthy tissue, the complication rate increases. The interplay between the dose-response curves of all tissues within the patient determines the outcome of a treatment. Ideally, normal and tumor dose-response curves would be separated to such an extent that the dose to the tumor for 100% response would lie at 0% response of the healthy tissue. Unfortunately this is not realistic. However, by delivering a treatment which maximizes the dose to the tumor and minimizes dose to healthy tissue, the resulting response points for a treatment will be pushed as far apart as possible (see Figure 1.1).

Due to the steepness of the dose-response curves, a small variation in delivered dose can result in a large change in tissue response, and therefore a large uncertainty in treatment outcome. Based on clinically available data, accuracy requirements for dose delivery have been recommended as 3% [Br84], 3.5% [Mi87], and an absolute maximum

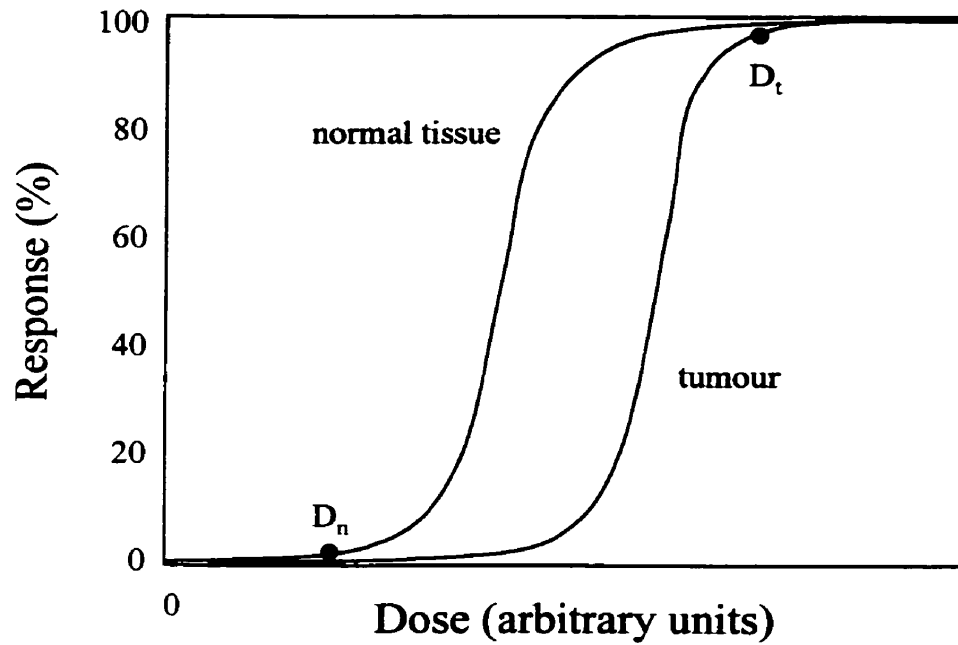


Figure 1.1: Example of a dose response curve for tumour control and normal tissue complication. D_n represents normal tissue dose and D_t tumour dose, for a given treatment. The treatment is designed to minimize D_n while maximizing D_t , taking advantage of the dose response gradients.

tolerance of 5% [IC76]. Since errors from each treatment step are considered to be independent of one another, they may be added together in quadrature to estimate the total error. This implies that every step in the treatment process may contribute only an uncertainty significantly less than the tolerated overall uncertainty.

Employing conventional radiobiological models for the healthy tissue and tumor responses, it has been estimated that a 2% increase in cure rate for early stage patients is achieved for every 1% gain in the accuracy of dose delivered [Bo88]. Considering that the number of new cases of cancer in Canada alone in the year 2000 is estimated to be 132,100 Canadians [Na00], this represents a substantial number of human lives potentially saved.

1.3 Uncertainties in radiotherapy treatment

Uncertainties in the radiotherapy treatment process may be subdivided into random and systematic categories. Random uncertainty results from a limited precision on a treatment parameter, while systematic uncertainty results from mistakes made at any point in the treatment process [Du84]. Theoretically, if they can be identified the systematic errors may be eliminated (e.g. incorrect laser alignment). Several investigators have attempted to estimate the uncertainty in the final dose delivered to the tumor by a methodical analysis of individual steps involved in treatment. An overall uncertainty of ~8% was estimated by Svensson [Sv84] accounting for contributions from the ionisation chamber calibration, dose rate calibration of the treatment machine, treatment planning, and patient setup. Using a similar approach, but with lower uncertainty estimates for individual steps, Mijnheer *et al* [Mi87] arrived at an overall uncertainty estimate of ~4% for a two-beam treatment. These values will vary between treatment institutes due to differing approaches to quality assurance of equipment, staff training, and treatment protocol for a given site.

So far, the discussion has ignored the possibility of human errors. These cannot be estimated theoretically, but can be studied through some form of retrospective analysis. One such study, involving 464 patients, introduced a separate human check performed after the first patient treatment [Le92b]. The study was performed to assess data transfer errors, which can include transcription errors, round-off errors, forgotten data, or interchange of data. Errors in the data transfer process were detected in 139/24128 parameters (<1%), but these were spread over 119/464 patients (~26%). Of these, 25 would have led to an error in dose delivery exceeding 5%. These major errors affected

25/464 patients (5%). Another study examining human errors was presented by Calandrino *et al* [Ca93]. This study specifically investigated errors in calculating the monitor units (ie. dose delivered). Even for computerized calculation systems, human errors are possible in the transcription or insertion of data into the system. The study involved 890 dose calculations on 750 patients, made by two physicists (to allow the check). Errors over 5% were encountered in 17/890 cases (1.9%). It was also found that the incidence of errors decreased over time since principal causes of mistakes were identified and given more attention as the study proceeded.

Another method of estimating overall treatment uncertainty is by experimentally measuring the dose delivered to various points and comparing to the predicted dose at those points. This approach is difficult since operators need to select and reproduce (i.e. fraction to fraction) appropriate point locations. Noel *et al* [No95] measured entrance and exit point doses using silicon diodes on the beam axis at the patient's skin. From these measurements, a dose estimate to the tumor was derived. During this five year study, 79 errors (defined as deviations between measured and expected readings greater than 5%) were detected out of 7519 patients. Of these errors, 45 would have caused an error of over 10% of the delivered dose. Human error accounted for 78 of the 79 errors.

Leunens *et al* [Le92a] made similar entrance/exit dose measurements using silicon diodes, on 11 head and neck treatments. Seven of these treatments were found to be in error by more than 5% of the expected dose.

Mitine *et al* [Mi91] made 261 entrance dose measurements using silicon diodes, on 34 fields for 10 head and neck patients. Twelve of these measurements were found to be in error by more than 5% of the expected dose. Examining only the first treatment, eight of the 34 fields were found to be in error by more than 5% of the expected dose.

1.4 Rationale for treatment verification in radiotherapy

It is demonstrated in the foregoing discussion that there is an array of potential errors associated with the radiotherapy treatment process. Errors in delivered dose of over 5% (and in some cases over 3%) may dramatically affect the treatment outcome of a patient. The use of *in vivo* methods of treatment verification have been determined to be very powerful for detecting and correcting errors during treatment.

Treatment techniques are becoming more complex (for example: more accurate dose calculation algorithms in three dimensions, greater availability of three dimensional image data, conformal field edges formed by multi-leaf collimators, step and shoot approaches, and intensity modulated radiotherapy). These developments allow the delivery of a three dimensional high dose volume, shaped to conform to the tumor edges while sparing surrounding healthy tissue. For these complex treatments, there is an increased chance of error in treatment delivery [Mi87], and therefore an even greater need for effective treatment verification. As will be emphasized in this thesis, the evolution is towards using imaging techniques to verify the 'exit' dose pattern, replacing point sampling measurements with planar measurements.

CHAPTER TWO

INTRODUCTION

2.1 Current Methods of Treatment Verification

As described in chapter one, the delivery of radiotherapy treatment to a patient is complex, involving many individuals and processes (such as diagnosis, imaging, delineation of disease, treatment planning, treatment simulation, manufacturing of beam modulation devices, and treatment delivery). Error in any step will contribute to uncertainty in the final delivered dose distribution. Therefore it is absolutely necessary to verify that a treatment has been properly performed. Many forms of treatment verification exist, as discussed below.

2.1.1 Record and verify systems

With the advent of microcomputers came the most straightforward approach to treatment verification, the 'record and verify' concept. In this technique, the treatment setup for all patients is stored on a central, computerised data base. This data base is interfaced with the treatment machine software and has the ability to check the current setting of treatment machine parameters (gantry angle, collimator angle, jaw settings, etc.) against the prescribed settings. If these do not match within a tolerance, delivery of the treatment beam is not allowed. This approach has been shown to significantly reduce treatment errors. For example, Podmaniczky *et al* [Po85] found mistakes in 1.0% of all radiation fields delivered per treatment machine per year. By analysing the situations

where errors occur, these systems may also identify problems in treatment procedures [Po85, Mu91]. Mohan *et al* [Mo85b] found significant errors in 1.2% of all fields treated, which would have affected ~60% of patients treated due to random occurrences. In particular, the systems are efficient at detecting major human errors such as wedge orientation and monitor unit settings (dose to be delivered) [Mu91]. A bar code scanner may extend this approach to the coding of customized beam modifying devices or patient positioning devices, which are not normally recognized by record and verify systems [Mi88]. However, this extended approach has not been widely adopted, probably due to increased manpower needed to implement it, and an increased potential for human error (ie. mislabeling).

In general, the record and verify approach is limited to checking of physical parameter settings of the treatment machine. The approach cannot detect the actual presence or location of shielding blocks, orientation of compensators, settings of treatment couch, or the patient setup. This can only be done by using small ‘test exposures’ of the patient with the radiation beam.

2.1.2 Geometric treatment verification

The patient anatomy, including the tumor region(s) as delineated by the physician, is required for a radiotherapy treatment. This information may be obtained through one or more of computed tomographic imaging (CT), magnetic resonance imaging, ultrasound imaging, nuclear medicine imaging, or x-ray imaging during treatment simulation. Most commonly, CT data are used to design the treatment plan, due to the good geometric characteristics, soft tissue discrimination, and the simple conversion of CT attenuation

coefficients to electron density information which is generally required by dose calculation algorithms. A computerised treatment planning system allows individual beams to be customised for a particular patient, and allows calculation of the resulting dose distribution. The shape and size of the treatment fields must geometrically coincide with the target volume, and need to be verified during the course of a patient treatment. This may be accomplished by imaging prior to or during treatment, commonly termed megavoltage imaging with the use of high energy x-rays. The congruence of the position of field edges with respect to patient anatomy between the megavoltage image and a pretreatment image (provided through either a simulator x-ray or a digitally reconstructed radiograph calculated from the CT data) constitutes a geometric verification.

Classically, radiographic 'portal' films have been widely used to gather the verification image. The term portal is used here since the treatment field is also known as the treatment portal (ie. opening), and hence the obtained image will be in the shape of this portal. Placed on the exit side of the patient and perpendicular to the incident beam, a portal film will record a projection of the patient anatomy within the treatment field. Note that a portal image is formed by a primary fluence component added to a scatter fluence component, and modulated by the detector response (in this case, a film cassette). A portal film may be acquired at the beginning of a treatment using only a small dose, and then processed and examined before the treatment is finished (called a localisation film). To reduce total patient treatment time, a portal film may be exposed over the entire treatment (called a verification film). In this approach, the setup can be corrected only on subsequent treatments, and furthermore the image quality will degrade with patient movement. In order to visualise anatomy outside the field, a double exposure approach

may be taken, where a short exposure of a large area, open field is taken followed by a 'test' exposure of the actual treatment. The disadvantages of using portal film include: time required for processing, poor image quality, sensitivity to filming technique, material and human resources needed for storage and retrieval, and cost of both film and processing. These factors have limited the number of portal films taken per patient treatment course.

Development of electronic methods of acquiring digital portal images has alleviated many of the problems associated with film. Technical details of the wide variety of such systems available experimentally and commercially are described in section 2.2.1. Electronic systems offer such benefits as real-time imaging (or close to real-time imaging), digital storage, and digital image processing techniques to allow extraction of more information from a gathered image.

While providing useful geometric information regarding the alignment of field and tumor, these methods do not provide any quantitative information relating to the dose deposited within the patient.

2.1.3 Dosimetric treatment verification

The accuracy of the delivered dose can be verified only by measurement during a course of radiotherapy treatment. The dose may be measured either at the beam entrance or exit points, relative to the patient. Film, ionisation chambers, thermoluminescent dosimeters (TLDs), and semiconductor detectors may be used. Film may provide dose information over an area, but results are sensitive to the film processor and film digitization method. The other methods provide only a single or a few point

measurements which cannot be used to identify the causes of any discrepancies between measured and prescribed dose [Wo90a]. TLDs for dosimetry were developed in the 1960s and 1970s. These dosimeters require calibration, pre- and post-irradiation annealing, regular cleaning, and regular sensitivity sorting. The use of TLDs and semiconductor detectors allow an investigation of all treatment parameters when a dose delivery error is detected. The main advantage of semiconductor detectors over TLDs is that the measurement results are available instantly. However, semiconductor devices have many other drawbacks. They require many correction factors to convert readings into dose. Due to the variability of response and some energy dependence, the characteristics of semiconductor detectors must be determined individually. If located at the entrance surface, these devices may cause significant attenuation of the primary fluence. Dose reductions of 4% at 10 cm depth [Mi91], and 5% at 5 cm depth [Ni88] have been found. Semiconductors are temperature dependent, thus when placed on the surface of the patient they must be allowed to reach a steady state to reduce variability. If placed at the entrance surface, both semiconductors and TLDs will increase the patient skin dose since they provide additional buildup material. For both semiconductors and TLDs, increased treatment setup time is required in order to properly position the detectors on the patient.

For dosimetry applications, electronic portal imaging devices offer many advantages over all of the above methods:

- 1) Dosimetric information may be provided over a large two dimensional area encompassing the treatment field. In principle, any setup errors may be detected from this information [Le86, Wo90].

- 2) Simultaneous verification of geometry and absolute dose delivered is possible, thus treatment times are not increased.
- 3) There is no physical contact needed between the patient, detector, and staff who must currently place dosimeters at the skin.
- 4) Images may be obtained in real-time (or close to real-time).
- 5) Since there is no increase in treatment times, an image for every treatment fraction may be taken and stored, providing a permanent dosimetric record.

The literature contains a variety of proposed dosimetric applications involving electronic portal imaging systems. This extends their application well beyond purely geometric verification. These proposed applications are summarised in section 2.2.2.

2.2 Potential of Portal Imaging Systems for Dosimetric Treatment Verification

2.2.1 Portal Imaging Systems

Before examining current portal imaging dosimetric application proposals or available methods of portal dose image prediction, an overview of portal imaging technology would be useful. Several different types of portal image detectors are currently available commercially, with more designs being researched. Excellent reviews of portal imaging system technology have been provided by Boyer *et al* [Bo92], Munro [Mu95], Webb [We93], and Antonuk [An98].

2.2.1.1 Camera/screen systems

The most prevalent commercially available systems are composed of a thin metal/phosphor screen which phosphoresces when energy is deposited, with the resulting optical image viewed by a video camera. The metal/phosphor screen is located behind the patient, perpendicularly oriented to the incident beam. The metal layer is beneficial to the imaging process for several reasons. The metal causes an increase in deposited energy in the phosphor due to the buildup effect created by charged particle cascade. The metal also serves to remove contaminant electrons, which may otherwise reach the detector material and increase image noise due to in-air scatter. Another 'side' benefit of the metal screen is the preferential attenuation of low energy scattered photons which reduces the scatter signal, thus increasing image quality. The role of the phosphor is to convert the energy deposited into optical photons which are captured by the camera. The camera is

mounted in the gantry of the radiotherapy treatment unit and views the phosphor through the use of one or two 45 degree mirrors. Susceptibility to radiation damage and noise due to primary photon interactions prevents the placement of the camera directly behind the screen. The camera may be the older tube style, or modern CCD (charge coupled device) variety. Investigators have found the newer CCD cameras to be superior for dosimetry applications due to improved signal linearity and reduced geometric distortion properties [Mu95]. Due to the low light intensity generated in the phosphor, the entire detection apparatus is mounted in a light-tight enclosure. These systems offer the possibility of real-time imaging, but the improvement in detection efficiency due to the conversion phosphor (one interacting electron may generate thousands of optical photons) is offset by the inefficient collection of these optical photons by the camera. The camera collection efficiency is typically $<0.1\%$ [Mu95]. Unfortunately, the need to maintain a clear optical path between camera and phosphor screen within a light tight enclosure results in an apparatus which is bulky and cumbersome. This is countered by engineering the devices to be retractable or removable when not in use. Commercially available versions of this type of detector include the Beamview^{PLUS} (Siemens Oncology Systems, Concorde, CA, USA), the SRI-100 now known as *iView* (formerly Philips Medical Systems, Crawley, UK, now Elekta Oncology Systems Ltd., Crawley, UK), TheraView (Cablon Medical BV, Leusden, The Netherlands), and PORTpro (Eliav Medical Imaging Systems, Haifa, Israel).

2.2.1.2 Liquid ionisation matrix

Another style of commercially available portal imager is the liquid ionisation matrix, originally developed by Van Herk and Meertens [Va88]. This design consists of a layer of ionisable liquid sandwiched between two circuit boards, each etched with 256 electrodes and oriented perpendicularly to one another. The ionisation in the liquid medium caused by interacting primary photons may be measured by sequentially applying a polarizing voltage on each row of the top circuit board, while reading the signal from the 256 electrodes on the bottom circuit board. A slow readout time of about 5-6 seconds makes this detector unsuitable for real-time imaging. Due to spurious signals generated in the electrodes and varying sensitivity across the matrix, the device must be routinely calibrated. However, it is less bulky than the camera/screen style. This detector is available as the PortalVision Mark 1 or Mark 2, from Varian Medical Systems Inc. (Palo Alto, CA, USA).

2.2.1.3 Solid state detectors – linear arrays

The main disadvantage of all linear arrays is the small angle of radiation which they subtend (compared to area detectors). To build up a 2D image, they must be scanned across the intended imaging plane, and therefore do not offer real time imaging capability.

A scanning linear array of silicon diodes was implemented by Lam *et al* [La86]. The design consisted of a line of 255 diodes at 2 mm spacing, with 1.1 mm lead buildup. The array was stepped in 2 mm increments across the field, with readings digitised into a computer.

Another linear detector incorporates a double row of scintillation crystals [Mo91]. The design consists of two rows of 64 scintillating crystals (ZnWO_4), coupled to photo diodes to detect the x-ray induced scintillation events. The dense scintillating crystal with its inherent signal amplification (conversion to optical photons), results in a high quantum efficiency for this detector, despite being a linear array.

2.2.1.4 Solid state detector arrays – area arrays

Solid-state area detectors in the form of active matrix flat panel imagers (AMFPIs) are the most likely candidates to succeed the prevalent camera/screen style. This technology has experienced rapid growth in recent years, in part due to the flat panel display industry. These detectors offer superior detection efficiency, reduced bulkiness, real-time imaging capability, and are resistant to radiation damage. Generally, they consist of a two dimensional pixelated array residing on a substrate (usually glass), an overlying x-ray converter, an electrode acquisition system (which controls the operation of the array and processes analog pixel signals), and a computer to control data acquisition and processing [An98]. Two different methods of detecting deposited radiation exist, and impact on the detector configuration. If indirect detection is employed, an overlying scintillator (ie. a phosphor screen, or an array of CsI crystals) is optically coupled to photosensitive elements on the array. The array of diode detectors may be placed in direct contact with the phosphor layer, greatly increasing optical signal capture compared to camera systems (detection efficiency of optical photons is ~30% versus <0.1% for camera systems [Mu95]) . Direct detection AMFPIs require a thick, overlying photoconductor which is electrically coupled to capacitive elements on the array. Each discrete pixel is

typically a photodiode for indirect detection designs, or a storage capacitor for direct detection designs. Several investigators have demonstrated successful application of this technology to portal imaging applications, and commercial products are just entering the market. Indirect, solid state detector systems are recently available from Varian Medical Systems Inc. (Palo Alto, CA, USA) and soon to be available from Elekta (Crawley, UK).

2.2.2 Proposed applications/implementations for portal image dosimetry

There exist many proposals throughout the literature on how to produce and use portal dose images. The following section describes the major applications.

2.2.2.1 Comparison of predicted image to measured image

Leong [Le86] implies a comparison with a precalculated portal dose image when he suggested that errors (such as the incorrect amount of dose delivered or an incorrect placement of a beam modifying device) may be instantly detected, if a portal dose image is available. Wong *et al* [Wo90a] found that detection of dosimetric discrepancies could be made when predicted and measured portal dose images are compared, and further proposed that ideally these images should compare pixel data to within 3%. Wong *et al* [Wo90a] used the Delta Volume dose calculation algorithm to predict portal dose images at planes very close to the exit surface of the patient, using a cobalt-60 beam. Kroonwijk *et al* [Kr98] compared measured and predicted portal dose images to demonstrate internal organ movement (primarily due to gas pockets in the rectum) for ten prostate cancer patients.

2.2.2.2 Adjustment of patient CT data

Ying *et al* [Yi90] described the possibility of using the measured and calculated portal dose images to improve the estimate of patient dose. Ying argued that if large setup errors are detected and corrected, then the differences in measured and calculated portal dose images are due to patient differences (ie. differences in the actual patient anatomy between the time of CT data acquisition and the time of treatment delivery). Ying proposed an iterative method to modify the original CT data until the calculated portal dose image matches the measured dose image. A more accurate patient dose distribution may then be calculated using the new CT data set. However, Ying does imply that a unique solution (independent of treatment site) to the modification of the CT data may be virtually impossible.

2.2.2.3 Exit dosimetry

In developing an early prototype electronic portal imaging system, Leong [Le86] suggested that an estimate of exit dose for the treatment may be made. Kirby *et al* [Ki93, Ki95] has demonstrated that a Philips SRI-100 portal imaging system may be calibrated to provide central axis exit dose estimates for patient treatments. The set of calibration data includes portal imager response with many field sizes (5×5, 10×10, 15×15, 20×20 cm²), thicknesses of homogeneous phantom of unit density (10, 20, 40 cm), and air gap distances (20, 30, 40, 50, 60 cm). The image of a steel ring of known diameter placed at the exit surface of the patient or phantom determines the air gap distance accurately, allowing an estimate of exit dose. This method agreed to within 3-9% of diode

measurements, with the accuracy depending on field size and treatment site. Additionally, comparison was made to exit dose calculations generated by a commercial treatment planning system (Target 2 GE Medical Systems, a Bentley-Milan algorithm), with these predictions agreeing to within 5-21% of diode measurements.

The approach taken by Boellaard *et al* [Bo97a] allows prediction of an entire plane of exit dose. A set of exit dose spread functions are derived from an extensive set of measured data. When convolved with the primary exit dose, these exit dose spread functions calculate the scatter exit dose, and may be summed to the primary exit dose estimate to yield total exit dose. On inhomogeneous phantoms, predictions compared to within 2.5% (1 standard deviation) of measured data. However, the method is only applicable at large air gaps (50 cm or more). A slightly modified version of this algorithm [Bo97b] includes an empirical geometry factor, which improves the results for inhomogeneous phantoms and patients to 1.7% (1 standard deviation).

2.2.2.4 Transit dosimetry

Transit dosimetry is related to exit dosimetry, but compares estimated and prescribed doses at some depth on the central axis of a treatment beam within the patient instead of at the exit surface. Transit dosimetry historically developed as a direct measurement of transmitted primary radiation, which then allows an estimate of the TAR (tissue air ratio) for the treatment field at some depth [Fe57; Ba76]. More recently, Pasma [Pa99b] derived an estimate of patient dose at 5 cm depth from a Philips SRI-100 portal imager using the predicted beam transmission (ratio of portal image dose with and without the patient), and an empirical relationship between portal dose and patient dose at 5 cm

depth. However, to understand differences between predicted and prescribed doses at 5 cm depth, a comparison between measured and predicted portal dose images was required.

The earlier exit dosimetry work of Boellaard [Bo97a, Bo97b] was modified to scale the calculated total exit dose to yield an estimated dose at the midplane of the phantom or patient [Bo98a, Bo98b]. Generally, the midplane dose estimates derived from measured portal images agreed to within 2.5% (1 standard deviation) of calculations performed with a treatment planning system.

2.2.2.5 Recalculating patient dose distribution

Another approach to utilizing portal dose image information is to recalculate the dose deposition within the patient [Ha96, Mc96a] without modifying the CT data but instead modifying the incident beam fluence. McNutt *et al* [Mc96a] used an iterative approach where the predicted portal dose image is used as an initial guess of the primary energy fluence exiting the patient. This distribution is backprojected through the patient (ie. CT data set) and the convolved with the dose kernels to determine a new predicted portal image. The ratio of the predicted primary energy fluence to the predicted portal dose image is then multiplied by the measured portal dose image with the result used as the new guess of primary energy fluence. The process is repeated until convergence is obtained, and an accompanying predicted three dimensional 'delivered' dose distribution is obtained. Using a liquid matrix portal imager and three phantoms, dose volume histograms calculated using the three dimensional matrix and resulting from the iterative technique and the forward dose calculation, compared to within ~3%. The method

proposed by Hansen *et al* [Ha96] is not iterative. The predicted scatter fluence is subtracted from the measured total fluence. The resulting primary fluence is backprojected through the patient CT data to yield a distribution of primary fluence in the patient. This distribution is convolved with appropriate dose deposition kernels to generate a patient dose distribution. Using an experimental scintillation crystal-photodiode linear array detector [Mo91] and treating the pelvis region of a humanoid phantom, the predicted central axis depth dose agreed to within 2% of measurement at selected points.

An underlying assumption of these approaches is that there are no changes in the patient anatomy between the times of CT data collection and treatment. This may lead to an incorrectly estimated distribution of patient dose.

2.2.2.6 Verifying dynamic treatment beams

Treatment techniques are becoming more complex and may involve the use of a multi-leaf collimator with dynamic leaf control, or a 'step and shoot' approach where the collimation is changed for each of several static treatment fields delivered. These complex techniques present challenges for their dosimetric quality assurance. Several groups have proposed the use of an electronic portal imager for pre-treatment verification [Ma97, Cu99, Pa99a], which only checks the incident beam fluence. This involves delivering the intended dose with appropriate beam shaping but *without* the patient present. By employing an electronic portal imager during this delivery, the integrated treatment may be measured and then compared with prediction. In principle, this process

may be employed over the course of an actual treatment delivery. This has not yet been done, but would be critically dependent on an accurate portal dose prediction algorithm.

2.3 Current Methods of Predicting Portal Dose Images

2.3.1 Problems to be addressed

There are several difficult radiation physics issues encountered in the prediction of dose deposition in a portal imaging system. These include:

- 1) transporting both primary and scattered photon fluence across an air gap which may widely vary in size (~10-100 cm)
- 2) predicting dose deposition in a multi-layered detector, which may exhibit regions of electronic disequilibrium (buildup at entrance surfaces or builddown at exit surfaces)
- 3) predicting dose deposition in high atomic number materials (such as phosphor)
- 4) the need for a fast implementation of any prediction algorithm, in order to be clinically useful for multi-field and/or dynamic treatments

The first issue involves accurately transporting both primary and scattered photon fluence across an air gap which may vary between approximately 10 cm and 100 cm. Generally, the image is formed by causing primary photon interactions to occur in an imaging detector material, and detecting the subsequent energy deposition by the electrons. The energy deposited in the detector medium may be maximized by placing a 'buildup' layer of material directly before the detector, in order to generate a charged particle cascade. This buildup material also serves to remove contaminant electrons, which may otherwise reach the detector material and increase noise due to in-air scatter, as well as degrade spatial and contrast resolution. The buildup material may be nearly

tissue equivalent (ie. *polymethylmethacrylate* or PMMA), or a thin sheet of metal (ie. brass, copper, lead, or steel). However, this results in a detector system of multiple materials and interfaces, which complicates the calculations since many dose algorithms do not perform optimally in these interface regions. Regions of charged particle disequilibrium may arise around the interfaces, which is of concern since most prevalent portal imagers (i.e. camera/screen) exhibit thin layers of detector material, usually <1 mm. Another complicating factor is the detector material itself, which may or may not be tissue equivalent. The liquid ionisation matrix detector is nearly tissue equivalent, but most other detectors involve the use of a high atomic number scintillating material (i.e. phosphor or crystals). The next-generation solid state detectors also use high atomic number phosphor to convert energy deposition into optical photons. The dose deposition process in high atomic number materials may be significantly different from tissue equivalent materials, due to differences in the weighting of photon interaction mechanisms. This is an important issue since, in general, dose calculation algorithms are designed to calculate dose to a water equivalent medium.

Any general method for predicting portal dose images will need to address all of these issues. Furthermore, with the increasing use of more dynamic radiotherapy treatments (eg. step and shoot, arc therapy, and intensity modulated radiation therapy), the speed of the prediction algorithm becomes an increasingly important factor affecting the ease of clinical implementation.

2.3.2 Use of treatment planning algorithms

The simplest approach to predicting portal dose images is to apply existing treatment planning algorithms to an 'extended' patient which includes the portal detector (ie. the portal detector becomes part of the dose calculation matrix which generally includes the patient only). If successful, this approach is attractive since most cancer treatment centres possess treatment planning systems, and therefore possess the resources to implement the approach.

The use of the Delta Volume dose calculation algorithm [Wo83] has been investigated for portal image dose prediction [Wo90a]. The algorithm was successfully utilized at the exit plane and very short air gaps using TLD and film dosimeters, which are nearly tissue equivalent detector materials. However, this approach is not suitable when a large air gap exists between the patient and the imager [Mc96b], since the Delta Volume dose calculation technique involves the density scaling method and straightline rays to account for inhomogeneities. The density scaling method scales the thickness of an inhomogeneity in proportion to its relative density. In three dimensions, the path between a small volume of scattering material and the calculation point of interest is scaled by an effective density. An overestimate of dose occurs in regions following an air gap, due to the incorrect assumption of straight line travel of primary electrons and multiply scattered photons [Mo86; Wo90b]. Instead, these particles take complex paths between the small scattering volume and the point of calculation. For a given pathlength through an equivalent thickness of water, the electrons and photons will spread out more in the presence of an air gap than without one. This effect has been demonstrated by Woo [Wo90b], where the error was shown to increase with increasing air gap and smaller field

sizes. Several of the patient dose calculation algorithms in clinical use [Cu85; Wo92] employ some form of this approach, as do many advanced convolution/superposition techniques [Ah89; Ma85; Mo86] which are beginning to be implemented clinically.

2.3.3 Three-dimensional superposition

The superposition method of dose calculation is based on physical principles and the use of precalculated, point interaction dose kernels. This technique divides the dose calculation volume into a three-dimensional grid of density voxels in which the total energy released per unit mass is first calculated with the knowledge of the incident energy fluence spectrum. This distribution is then ‘convolved’ with the dose point kernels to yield dose deposited in the medium, but since the kernels are spatially variant the process is more aptly described as a three-dimensional superposition. Mathematically, the process may be described as [Mc96b]:

$$D(\mathbf{r}) = \int \int \frac{\mu(\mathbf{r}-\mathbf{r}')}{\rho} \cdot \Psi(\mathbf{r}-\mathbf{r}') \cdot A[\rho \cdot l(\mathbf{r}'), \boldsymbol{\omega}] |\mathbf{r}'|^2 d|\mathbf{r}'| d\Omega \quad (2.1)$$

$\frac{\mu(\mathbf{r})}{\rho} \cdot \Psi(\mathbf{r})$ = total energy released per unit mass at point \mathbf{r} ,

$A[\rho \cdot l(\mathbf{r}'), \boldsymbol{\omega}]$ = dose deposition point kernel

$\rho \cdot l(\mathbf{r}')$ = radiological distance

$\boldsymbol{\omega}$ = angular direction

The point interaction dose kernels are usually precalculated by Monte Carlo simulation and represent the dose spread around a primary photon interaction in an infinite water phantom. Inhomogeneities are accounted for by scaling the kernel by the radiological

pathlength separating the interaction voxel and the scoring voxel. This scaling is handled slightly differently depending on the history of the particle depositing the dose [Ma85]. For this reason, separate dose kernels are created to reflect the history of the dose depositing particle (eg. dose due to electrons/positrons generated by initial primary photon interaction, dose due to interactions of photons which have already been scattered once, dose due to interactions of multiply scattered photons, and dose due to bremsstrahlung and positron annihilation photons). The primary and singly scattered kernels are density scaled along rays as described above, but the multiply scattered and bremsstrahlung kernels are scaled by the average 'bulk' phantom density, since they are a result of interactions spread throughout the medium. This dose calculation approach has been successfully demonstrated for patient dosimetry, and has recently been implemented in commercial treatment planning systems.

The 3D superposition method has been applied by McNutt *et al* [Mc96b] to the calculation of portal dose. In that work, the portal imaging device used was the liquid ionisation matrix type, which is a low atomic number material. A 6 MV photon beam³ was used, and air gaps ranged from ~10-25 cm. Results were promising, with the calculated portal dose images lying within 4% of the measured images for most pixels in the central low dose gradient region of the treatment field. However, this approach has not yet been applied to portal imagers involving high atomic number materials, nor in

³ For typical linear accelerators used in radiotherapy, photon spectra are polyenergetic. The term '6 MV' represents a photon beam containing photons with energies ranging from 0 to 6 MeV. Photons produced by linear accelerators are not monoenergetic since they are created through bremsstrahlung processes experienced by the interaction of a high-energy, nearly-monoenergetic electron beam and a high atomic number material 'target' [p. 216 of At86].

situations where the air gap is larger than 25 cm. Previous work [Wo90, Wo94] indicates that large errors may be encountered when density scaling primary dose kernels at both the front and back surfaces of the interfaces of inhomogeneities. Sauer [Sa95] demonstrated that dose kernels generated in water are not suitable to be applied to higher atomic number materials through density scaling and argued that this is due to the Z-dependence of the angular scattering power of electrons. Sauer [Sa95] suggests that use of primary dose deposition kernels generated specifically in the material of interest would be more appropriate. To date, this approach has not been investigated.

2.3.4 Two-dimensional superposition

Two-dimensional superposition approaches have arisen specifically to address the prediction of fluence or dose in portal imaging systems. The idea is to calculate either fluence or dose response in the portal image detector by transporting a 2D grid of 'pencil beams' of photons through the patient. A pencil beam is an infinitesimally narrow beam. The scatter component at the detector is calculated by a superposition of scatter kernels with the incident beam fluence. The scatter kernels in this approach are not the same as the point interaction dose kernels discussed above, but rather represent the scatter response at a certain distance behind a homogeneous slab of material due to an incident, infinitely narrow 'pencil beam' of photons. The incident beam may be modeled as being composed of a regular grid of these pencil beams, with the overall scatter contribution being the cumulative sum of individual pencil beams. The advantage of this approach is that the calculation speed for scatter contributed to a single scoring voxel in the portal detector system is then proportional to N^2 (if the incident beam is broken into $N \times N$

points), instead of at least N^3 valid for the 3D superposition approach (if the patient is broken into $N \times N \times N$ voxels). The extra N in the 3D approach comes from breaking the patient into N calculation voxels in depth, which is not necessary for the 2D approach.

2.3.4.1 Experimental scatter kernels

There have been two implementations of the 2D superposition approach proposed in the literature to date. The first is experimentally based [Pa98a], using a large quantity of measured data to derive scatter dose kernels valid for a particular portal imaging configuration. Unfortunately, the scatter kernels presented in that work are unphysical, since they demonstrate an extremely sharp rise in scatter response (factor of two) with increasing radius up to ~ 5 cm. This is inconsistent with Klein-Nishina cross section predictions (to first order), as well as with Monte Carlo simulations of scatter response behind homogeneous slabs due to incident photon pencil beams. It is expected that the scatter fluence response behind a homogeneous slab due to an incident pencil beam exhibits a maximum positioned 'in-line' with the incident pencil beam, and decreases smoothly with radial distance off-axis. The errors introduced by these kernels did not significantly affect the results, since the portal imager used in that work was at a fixed source-detector distance (SDD) of 160 cm. At that distance, the scatter fluence is only a small fraction ($<3\%$) of total signal for most clinical situations, and exhibits very little spatial variation (ie. a flat response). However, many other portal imaging systems do not possess this large SDD, and the errors in the kernels may become apparent for predictions at shorter SDDs.

2.3.4.2 Monte Carlo simulation of scatter kernels

The second implementation of the 2D superposition approach has involved generating the scatter kernels using Monte Carlo radiation transport techniques [Ha97]. This work generated scattered photon fluence kernels using an energy spectrum representing a 6 MV photon beam, and in-house Monte Carlo radiation transport software. The scatter kernels were used to remove the scatter signal in the portal image through an iterative deconvolution. The method defines the scatter signal by the superposition of the scatter fluence kernels with an open field measurement. This approach assumes that the response of the detector will be independent of the incident photon energy (ie. the fluence is proportional to signal for all incident photon energies). This assumption is only true when the detector is an ideal photon counter.

This work [Ha97] has been recently extended in an attempt to account for scatter dose response in a uniform detector medium [Sp00a, Sp00b]. This conversion involves analytical approximations to estimate the dose response to multiply scattered photons, while accurately modeling singly scattered photons through analytical techniques. However, the observed errors between measured and predicted image signals are up to 8% of the central axis signal [Sp00a].

2.4 The Need for a General Approach to Portal Dose Image Prediction

2.4.1 Summary of limitations of current approaches

A summary of the limitations of the currently available methods is presented here. For simpler treatment planning algorithms, the air gap separating the patient and the portal imager presents problems for the scatter component prediction.

The 3D superposition method may be suitable, but research needs to be done on increasing the accuracy in high Z materials, and around interface regions. Several groups have shown problems implementing this approach over air gaps [Wo90b, Wo94], and in high Z materials [Sa95]. The speed of the 3D approach may also become a limitation if faster, reliable, 2D methods are available.

The 2D methods do not account for patient inhomogeneities as accurately as full 3D approaches. However, this may not be important since the scatter fluence varies relatively slowly with spatial location in the portal image (ie. the effects of inhomogeneities are smeared out). Furthermore, both 2D approaches found in the literature [Pa98a, and Ha97 extended in Sp00b] are restricted to the types of portal imaging devices they were applied to, and do not represent a general approach for all detector systems.

2.4.2 Required features of a general approach

A general approach will successfully account for the problems described in section 2.3.1. The approach needs to work at small and large air gaps. The approach will predict dose in thin, multilayered detector systems involving high atomic number materials. Fast

execution will be a distinct advantage, increasing applicability to more complex treatments. The general approach should be easily extensible to any portal imaging system available commercially or experimentally now and in the future.

2.5 A Brief Overview of Monte Carlo Techniques used for Radiation Transport

Radiation transport software incorporating Monte Carlo simulation is a powerful research tool used throughout this thesis. It is therefore essential to understand this process and its limitations.

2.5.1 Monte Carlo technique

A random trajectory for a particle may be calculated given a knowledge of the probability distributions governing the individual interactions of the particle in the materials involved. The physical quantities of interest are tracked for a large number of particles, and this provides solutions pertaining to average quantities and any associated distributions. To reduce systematic errors, the probability distributions must be sampled in a random fashion, thus leading to the use of the term ‘Monte Carlo’ (ie. international gambling capital) to describe this approach to solving radiation transport problems.

This technique has been used increasingly over the last several years in the area of medical physics (including radiotherapy, diagnostic imaging, and nuclear medicine). This is due to the increase in cost effective computing power combined with the widespread availability of large scale, well-developed computer software packages. Furthermore, the Monte Carlo approach allows one to investigate parameters which may not be physically measurable.

The Monte Carlo technique is applied throughout this thesis as a tool. Various applications involve generating point-interaction dose kernels, scatter fluence kernels, pencil beam dose kernels, as well as patterns of photon fluence, mean energy, and mean

angle. Each of these will be described in turn. Although several software packages are available, EGS4 [Ne85] was utilized due to its widespread and proven application in the energy range involved in radiotherapy [Ro90].

2.5.2 The EGS4 radiation transport code

The EGS4 (electron gamma shower, version 4) code was developed originally at the Stanford Linear Accelerator Center [Ne85]. The code simulates photon and electron/positron interactions. Photon interactions include the photoelectric effect, Compton scattering, pair production, and elastic or 'Rayleigh' scattering. Electron/positron interactions include bremsstrahlung creation, positron annihilation, as well as multiple-scattering effects, and the creation of knock-on electrons. Knock-on electrons are those electrons that have been ejected from an atom due to an inelastic collision with an incident electron or positron.

Electron transport algorithms have been divided into two categories depending on how the energy of the primary electron is lost [Ro90]. In class I algorithms, the effects of all interactions of each type are grouped together for each simulation step. In class II algorithms, the effects of only a subset of the interactions of each type are grouped together, while the remaining interactions are simulated individually. Generally, class II algorithms are more accurate due to the inclusion of correlations between primary and secondary particles. In practice, the class II algorithm requires a cut-off energy (usually user-defined), above which an individual secondary particle is simulated. EGS4 is a class II algorithm, and as such, requires the user to specify the energy thresholds above which the secondary particles are simulated. These are the production threshold variables AE

and AP, for electron (knock-on electrons, bremsstrahlung) and photon production, respectively.

All Monte Carlo simulations performed in this work employ the *parameter reduced electron step transport algorithm (PRESTA)* [Bi87]. It has been shown that EGS simulation results may exhibit artifacts dependent upon energy step size [Ro84]. The PRESTA algorithm was developed to substantially reduce this artifact possibility by shrinking electron steps in the vicinity of an interface (ie. plane separating two materials or scoring regions). In this manner, the electron may cross the interface without ambiguity. To maintain simulation efficiency, PRESTA lengthens the electron steps as the electron recedes from an interface.

Any inelastic interaction will cause an energy decrease of the primary particle. Particle interactions are simulated until the energy of the primary particle falls below some threshold, in which case the remaining energy is deposited locally. In EGS4 this threshold is user defined, with the variables labeled as ECUT and PCUT for electron transport and photon transport, respectively.

Another important aspect of the EGS4 code package is that it contains cross section data (or the ability to generate this data) for all simulated interactions. The cross section data for elements are derived theoretically, while cross section data for compounds and mixtures of elements are generated through weighted combinations of element cross sections.

2.5.3 Selection of random numbers

The sampling of the particle interaction cross sections is required to be completely random, otherwise systematic errors will occur in the scored results. To obtain a truly random sequence of numbers, one would need to employ some natural phenomenon such as electrical noise or radioactive decay. The difficulty with this approach is in getting the data into a digital format useable by a computer.

However, mathematical approaches which may be implemented on computers can achieve pseudorandom sequences. While not truly random, these sequences are generally acceptable for Monte Carlo applications. The random number generator used in all simulations in this thesis is a well studied and widely implemented pseudorandom number generator known as RANMAR [Ma90], which uses a combination of a lagged Fibonacci sequence and an arithmetic sequence. This pseudorandom number generator satisfies very stringent tests [Ja90], and has a period of approximately $2^{144} \cong 2 \times 10^{43}$ which is more than adequate to avoid recycling of the same sequence for the simulations performed here.

2.5.4 Accuracy of EGS4

Since the physical processes are simulated by randomly sampling particle interaction cross sections, the results are subject to statistical uncertainty. This uncertainty is estimated by dividing the simulation into ten independent batches, each processing the same number of initial particles. For each scored quantity of interest, the final answer will be the average of the results of the ten batches. The uncertainty estimate on this answer is given by the variance of the mean.

There are also systematic errors present in the EGS4 code package. These may include programming errors, modeling inaccuracies, truncation (rounding) effects. As stated earlier, EGS4 is a popular radiation transport package, and has been used in literally hundreds of applications [NRa] thereby minimizing the probability of significant programming errors. Modeling inaccuracies are documented, and it is up to the user to ensure that the intended application does not function beyond modeling limits. Truncation errors will be minimized by good coding technique, which avoids using very small accumulation variables. A major advantage of using a widely employed code is that it has been tested in a variety of applications, and there is a development group providing support for its use [NRb].

The most significant limiting systematic error is that of the particle interaction cross section data (the probability of a photon experiencing a certain interaction). Any error in the cross section data will be directly transferred to the final results *via* the random sampling process. Estimates of uncertainty for the photon cross sections are broken down by interaction. Where the photoelectric effect dominates, uncertainty is 3-5%. However, this region is usually only dominant at very low energies relative to the therapeutic regime. In the region dominated by Compton scattering, the uncertainty is estimated at under 1% for low atomic number elements (Z), and 2-3% for higher Z elements. For pair production, the uncertainty is estimated to be 5%. For low Z materials, this is not of concern, since pair production does not dominate within the therapeutic energy regime. However, for high Z materials, pair production may dominate at the energies of interest (for example, this occurs at 12 MeV for calcium, 9 MeV for brass, and only 5 MeV for lead).

2.6 Equivalent Fields

The equivalent field method allows depth dose data for rectangular fields to be derived from depth doses of square or circular fields. The method is attractive since it is conceptually simple and well established in the radiotherapy community [Da96]. The standard definition of an equivalent field is the standard shape field size (either square or circular) which possesses the same central axis depth dose characteristics as the given non-standard field [Da96]. This relationship generally holds over the radiotherapeutic energy range (cobalt-60 to 24 MV photon beams).

Yeboah [Ye97, Ye00] applied the equivalent field concept to portal dosimetry. In that work, a field radius r_{eq} in a reference geometry (e.g. slab phantom with no air gap) was defined to be equivalent to a field r in the clinical geometry if both field sizes resulted in the same exit dose. An empirical relationship between the equivalent field radius, clinical field radius, and air gap was proposed. This empirical relation contained two fit parameters, one of which was dependent on phantom thickness. The fit parameters were obtained through modeling of Monte Carlo-generated data, and verified through experimental measurement.

The approach of Yeboah [Ye97; Ye00] is limited in several ways. It relates only single, central axis points to the reference geometry (and does not provide a framework for relating off-axis points). The fit parameters were shown to depend upon the portal image detector. Furthermore, the approach is not a physical model, but rather an empirical one, thus making generalization difficult.

2.7 Thesis Overview

The use of portal images during radiotherapy treatment is known to provide verification and allow correction of the geometric coincidence of treatment beam and treatment volume, as described in section 2.1.2. These images may be acquired on a wide variety of equipment, electronic or otherwise. An exciting new use of electronic portal imagers involves their application as an area dosimetric device with the potential of real-time dosimetry. Many potential dosimetric applications require the calculation of a map of dose deposited in the detector system. To be useful, the predicted portal dose images need to be accurate. This requires that the calculation algorithm be able to model a wide variety of detector designs, including both low and high atomic number, thin, and multiple layered materials. The calculation algorithm must be able to function accurately, independent of the detector position (e.g. at short or large air gap). Finally, with the movement towards dynamic therapies, the need for the calculation algorithm to be fast becomes increasingly important. The work presented in this thesis describes the development of a portal dose calculation algorithm that fulfills all of these needs, and therefore provides a useful tool for many portal dosimetry applications.

Appendix A presents the initial attempt at developing the algorithm. A one-dimensional approach based on equivalent fields theory was investigated. As briefly described in section 2.6, equivalent fields theory was developed to relate the dose deposition of different shapes of treatment fields. The motivation for this approach was derived from its simplicity and potential speed of implementation. However, it was found to be inadequate for accurate dose calculations off the central axis within the patient, let alone in complex detector systems outside the patient. The approach is also limited to

uniformly thick and homogeneous slab-like 'patients', and was not pursued further.

While not directly relevant to the final algorithm design, the work evolved into a novel application of the modern three-dimensional convolution dose calculation algorithm in redeveloping equivalent field relationships.

In chapter three, scattered photon kernels are generated using the EGS4 code. These kernels represent distributions of basic radiation field parameters of the scattered photon fluence at various planes behind homogeneous, uniform slabs of water due to an incident pencil beam of photons. The scored quantities include fluence, mean energy, and mean angle, and the resulting distributions are radially symmetric about the incident pencil beam. These kernels are further separated, depending on the history of the scattered photon: singly scattered photons, multiply scattered photons, and bremsstrahlung and positron annihilation photons. The energies of the incident photon pencil beams investigated include 2.0 and 10.0 MeV monoenergetic spectra, and 6 MV and 24 MV polyenergetic spectra. The scatter distributions are examined in detail, and analysed using a variety of approaches (scatter fraction, full width at half maximum, and modulation transfer functions).

In chapter four, the scatter kernels are implemented in a two dimensional algorithm which predicts radiation field parameters of scatter fluence reaching a portal imaging detector plane located behind a patient. The algorithm is described in detail, and tested on a variety of simple phantoms, at two photon beam energies (6 and 24 MV). Analytic calculations are compared to full Monte Carlo simulation. The accuracy of the algorithm is studied as a function of air gap, field size, phantom geometry, incident beam resolution, and photon history. It is found that by maintaining a small air gap of 10 cm,

errors in the predicted scatter fluence may be kept under 3%. This level of accuracy over a wide range of air gap and an assortment of phantom geometries is sufficiently low to warrant investigation into a method of converting the predicted fluence parameters into a dose estimate.

The method of converting the predicted fluence map into dose deposited in any arbitrary detector system is described in chapter five. Given a knowledge of the detector geometry and materials, a set of dose kernels may be calculated using the EGS4 code. A pencil beam of photons incident on the detector generates a dose kernel scored in the detector material layer (this is the material which actually measures dose). These are radially symmetric kernels, and are required over a range of incident monoenergetic photon energies (0.1-24 MeV) for the detector of interest, which is a water equivalent detector material in this chapter. The incident fluence is converted to dose *via* a convolution/superposition process of the dose kernels with the predicted fluence map. The algorithm dose predictions are compared to measured data for two different detector configurations, 6 and 23 MV beam energies, a wide range of air gap (10-80 cm) and several phantoms (including lung and pelvis treatment sites on an anthropomorphic phantom). Analysis was performed according to recommendations of Van Dyk *et al* [Va93] for assessing the accuracy of dose calculation algorithms of treatment planning systems. Approximately 96.5% of data points lying within low dose gradient regions (<30%/cm) agreed to within 3%, while 98.5% of data points lying in high dose gradient regions agreed within 4 mm spatial separation.

Chapter six describes the validation of the algorithm on a high atomic number detector system. The amorphous silicon detector used here incorporates a gadolinium

oxysulfide phosphor scintillating screen to convert deposited radiation energy to optical photons which form the portal image. A water equivalent solid slab phantom and an anthropomorphic phantom were examined at beam energies of 6 and 18 MV and over a range of air gaps (~20-50 cm). In the many examples presented in this chapter, portal dose images in the phosphor were predicted to within 5% in low dose gradient regions, and to within 5 mm (isodose line shift) in high dose gradient regions. Other basic dosimetric characteristics of the amorphous silicon detector were investigated, such as linearity with dose rate ($\pm 0.5\%$), repeatability ($\pm 2\%$), and response with variations in gantry rotation and source to detector distance. The latter investigation revealed a significant contribution to the image from optical photon spread in the phosphor layer of the detector. This phenomenon is generally known as 'glare', and has been characterised and modeled as a radially symmetric blurring kernel. This kernel is applied to the calculated dose images as a convolution, and is successfully demonstrated to account for the optical photon spread.

Chapter seven summarises the work, and makes recommendations on future areas of research which may build on this thesis.

CHAPTER THREE[‡]

PHOTON SCATTER IN PORTAL IMAGES: PHYSICAL CHARACTERISTICS OF PENCIL BEAM KERNELS GENERATED USING THE EGS MONTE CARLO CODE

3.1 Introduction

When a radiotherapeutic photon beam passes through the patient, some photons will undergo scattering events. These scattered photons may undergo further multiple scatterings within the patient. The image formed in the portal imager consists of signal contributions caused by both primary (unscattered) photons and scattered photons. While the primary photon contribution is relatively straightforward to estimate, one of the challenges in calculating portal dose images is to accurately account for the scatter photon contribution. Therefore this chapter presents a study of the physical nature and behavior of scattered photons in the context of portal imaging.

Several authors have investigated photon scatter in portal imaging. Jaffray *et al.* [Ja94] examined energy spectrum changes with air gap, and central axis scatter variation with air gap, phantom thickness, and circular field size. Hansen *et al.* [Ha97] used pencil beam photon scatter kernels generated by in-house Monte Carlo simulation software for deconvolution of scatter from portal images. Swindell *et al.* [Sw91; Sw96] examined scatter primary ratios (generated via in-house Monte Carlo simulation software) at various air gaps and the impact on portal imaging system design. Pasma *et al.* [Pa98a] estimated pencil beam scatter kernels from measured portal image data.

[‡] Based on [Mc00a].

This chapter presents pencil beam photon scatter kernels generated by the EGS4 (Electron Gamma Shower version 4 [Ne85]) Monte Carlo code. Photon scatter kernels for several incident photon energies (including 2.0 and 10.0 MeV monoenergetic and nominal 6 MV and 24 MV polyenergetic spectra), many phantom thicknesses (1-50 cm) and air gaps (0-100 cm) were produced. This information provides a comprehensive data base of pencil beam photon scatter kernels for use in predicting the amount and quality of photon scatter to portal imaging planes *via* a superposition method [Ha97; Pa98a]. This provides a reliable set of pencil beam fluence kernels calculated by a widely accepted and freely available radiation transport simulation system. For incident spectra containing higher energy photons, the importance of simulating charged particle transport and subsequent production of bremsstrahlung and positron annihilation photons, is clearly demonstrated in this chapter. Pencil beam scatter kernel data has been generated for many air gap values, instead of just one or two as previously reported. This enhanced resolution combined with the inclusion of charged particle and combined photon-electron transport allows for improved accuracy of portal fluence image calculations over previous efforts. Some analysis in the current chapter provides an extension of the previously published data, as well as independent confirmation of portions of those results. Further analysis includes an estimate of the variation of full width at half maximum of the scatter kernels, and central axis scatter fraction as a function of photon history, air gap, phantom thickness, and incident energy. In addition, modulation transfer functions were calculated [Ba81], providing a theoretical limit to the spatial resolution of any portal imaging system.

3.2 Materials and Methods

3.2.1 Simulation geometry for ideal pencil beams

An infinitely thin pencil beam of photons was made perpendicularly incident upon (i.e. parallel to the central axis of) a semi-infinite homogeneous slab of water. Any non-primary photon passing out of the slab on the exit side may contribute to the pencil beam scatter kernels. The scatter kernels are scored in a plane perpendicular to the incident pencil beam, as a function of radius from the incident pencil beam (i.e. cylindrical geometry). All pencil beams were generated using at least 4×10^7 incident photons. This resulted in a maximum variance in the scored total scatter fluence of less than 3% of the maximum total scatter fluence within a scoring plane. Radial scoring bin size was set at 0.25 cm increments over a range of 0-60 cm. The planar fluence of scattered particles was tallied in each bin, as well as the mean energy, and mean angle with respect to the incident pencil beam. The mean energies and mean angles were averaged over all scored photons for a particular bin. The medium behind the water slab phantoms was air, as depicted in Figure 3.1. Pencil beam data were generated with four incident photon energy spectra (2.0 and 10.0 MeV monoenergetic and 6 and 24 MV polyenergetic), 21 slab thicknesses (1-10 cm in 1 cm increments, 12-20 cm in 2 cm increments, 25-50 cm in 5 cm increments), and 21 air gap distances (0-100 cm at every 5 cm). The code was also modified to track the particle history, by employing the LATCH parameter. Photons were tracked and scored in four categories according to scattering history: i) primary (unscattered) photons that are not part of the scatter kernel by definition, (ii) singly-scattered photons, (iii) multiply-scattered photons, and (iv) photons arising from bremsstrahlung or positron annihilation events.

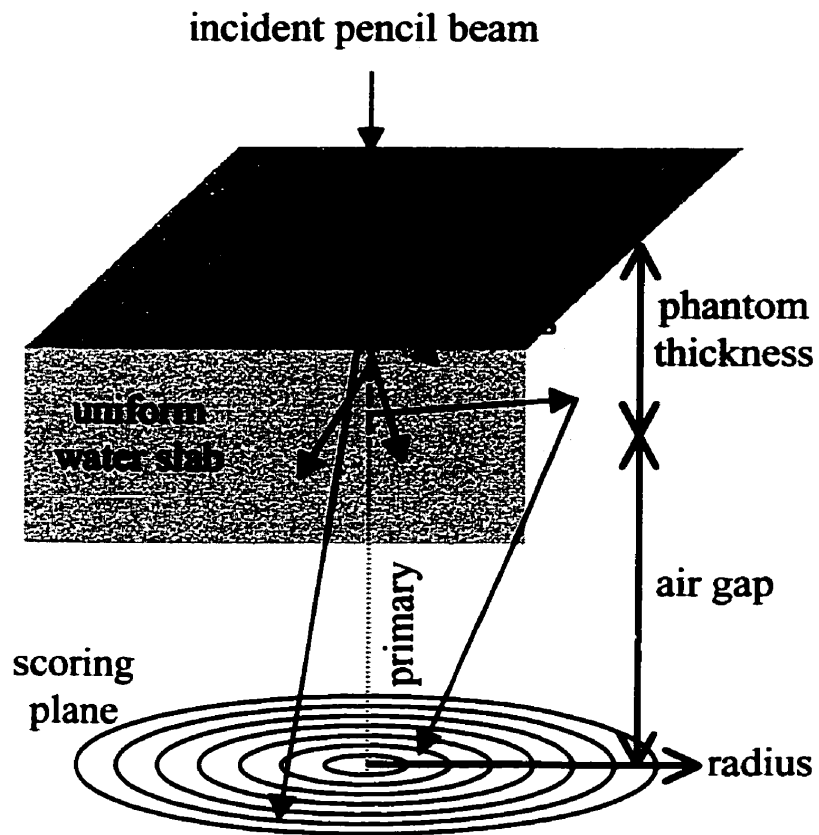


Figure 3.1: Geometry of pencil beam simulation. Scattered photon fluence, mean energy, and mean angle were scored within the radial bins as a function of air gap, phantom thickness, and photon history.

The result of these simulations is a library of data describing the scattered photon distribution at various portal imaging planes (air gaps) and over a wide range of phantom thicknesses, for an impulse input of photons.

3.2.2 Monte Carlo simulation

Parameters ECUT and PCUT, which represent the total energy of electrons and photons below which no radiation transport takes place (as described in section 2.5.2), were set to 0.80 MeV and 0.01 MeV respectively. ECUT was set low enough to ensure that there was no impact on bremsstrahlung production, yet high enough to significantly decrease simulation times. The two incident polyenergetic energy spectra reported here represent nominal 6 MV and 24 MV photon beams from typical linear accelerators [Mo85a].

The singly-scattered photon fluence component may be calculated from first principles using Compton kinematics, Klein-Nishina cross sections, and an inverse square effect. A computer program was written to perform this calculation for pencil beam rays for all phantom thicknesses, air gaps, and incident energy spectra examined here. Singly-scattered photon fluence contributions are summed from along the ray line, and summed over the incident energy spectra (if polyenergetic) for scoring bins identical to those used in the Monte Carlo simulations. However, in-air scatter behind the phantom slabs was ignored in the calculation. Furthermore, the singly-scattered photon energy was calculated for each scoring bin, and then fluence averaged to find the mean energy. The results of these analytical calculations are used to verify the accuracy of the singly-scattered component (fluence and mean energy) of the Monte Carlo simulations.

3.2.3 Scatter fraction, full width at half maximum, and modulation transfer function

Some additional parameters were calculated to further characterize the pencil beam photon scatter kernels. Scatter contribution as a fraction of total fluence (scatter plus primary) was examined on the central axis for 21 air gaps and 21 phantom thicknesses. The reciprocity theorem was used to relate the circular scoring area with an incident pencil beam to incident field size with an infinitesimally small scoring area on the central axis. Due to the use of reciprocity, the calculated scatter fractions are valid for incident parallel, circular field sizes, which are converted to square field sizes by area equivalence. The use of reciprocity also implies that the incident energy spectra and photon fluence are assumed to be constant across the incident field, which is not fully representative of the clinical situation. Before calculation of the scatter fraction, the planar fluence data were converted to spherical fluence data by dividing each scoring bins' fluence by the cosine of the mean angle for that bin. Where possible, scatter fractions are compared to results obtained by Jaffray *et al.* [Ja94]. That work presented only a very small fraction of the data presented in this chapter, so only a few comparisons are possible.

The full width at half maximum of the photon fluence scatter kernels was calculated for varying air gaps and phantom thickness, and for each scattered fluence component.

The modulation transfer function (MTF) is a quantitative measure of system performance, defined as the ratio of output modulation to input modulation [Ba81]. Modulation transfer functions were calculated by taking the modulus of the Fourier transform of the pencil beam photon scatter kernels added to the primary. This is

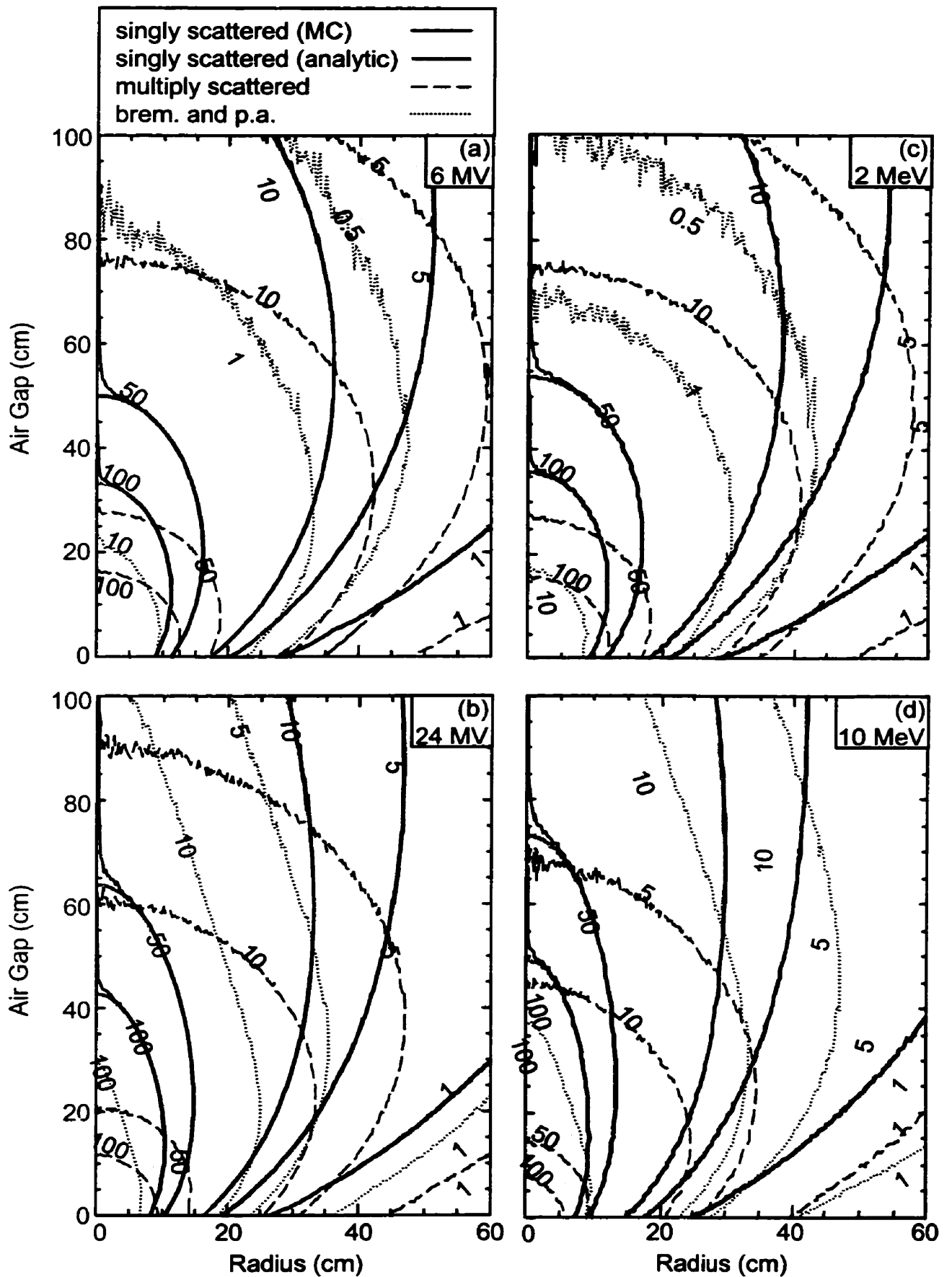
performed with total scatter fluence kernels and behavior is examined as a function of air gap and phantom thickness. The calculated MTFs are an approximation since the incident pencil beam is in a parallel geometry, and the scatter generated is assumed to be similar to that of a diverging geometry.

3.3 Results and Discussion

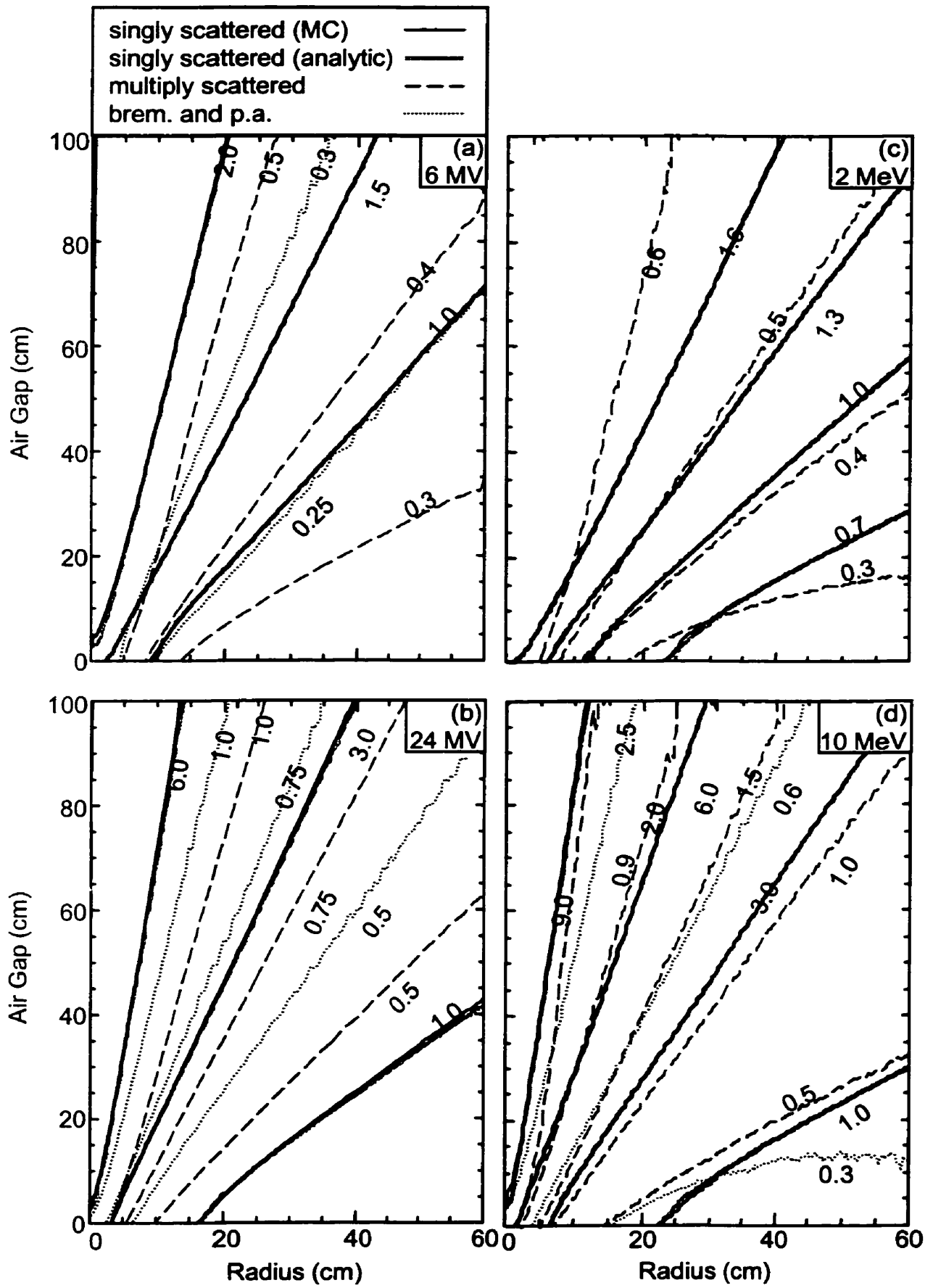
3.3.1 Comparison of singly-scattered fluence with analytical calculation

The singly-scattered fluence and mean energy distributions matched the Monte Carlo simulation results. Figures 3.2 and 3.4 include an overlay of the analytical results for predicting fluence with air gap and phantom thickness, demonstrating nearly identical distributions to the Monte Carlo results. The slight differences at small scoring radius are due to the analytical calculation not accounting for in-air photon scatter. The analytical prediction of mean energies of the singly-scattered fluence as a function of air gap and phantom thickness are overlaid in Figures 3.3 and 3.5. The results are nearly identical to those of the Monte Carlo simulation, for the monoenergetic spectra. Small differences are observed in the polyenergetic spectra results due to the effect of energy binning in the analytical calculation.

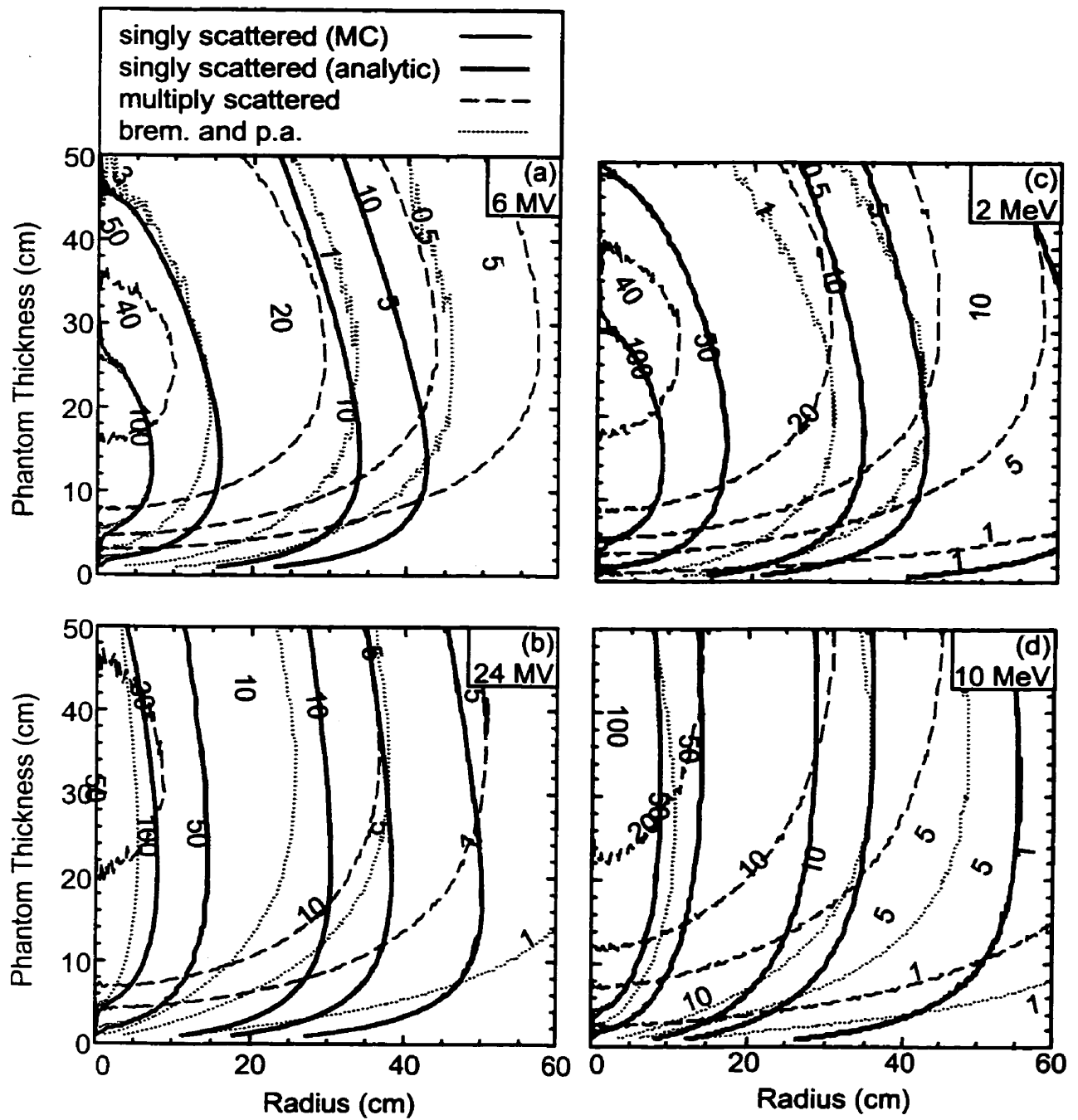
(OVERLEAF) Figure 3.2: Monte Carlo prediction of iso-scattered lines. The scattered photon fluence is normalized to the incident fluence (units are $\times 10^{-6} \text{ cm}^{-2}$) and due to an incident (a) 6 MV, (b) 24 MV, (c) 2 MeV, and (d) 10 MeV pencil beam behind a 20 cm thick water slab, at various air gaps. Solid lines represent singly-scattered photon fluence, dashed lines represent multiply-scattered photon fluence, and dotted lines represent bremsstrahlung and positron annihilation photons. Gray lines represent results of an analytical singly-scattered fluence calculation for comparison. Background shading indicates dominance of the singly-scattered photon fluence whereas no shading indicates dominance of the multiply-scattered fluence component *except* in (d), where no shading indicates dominance of the bremsstrahlung and positron annihilation photons.



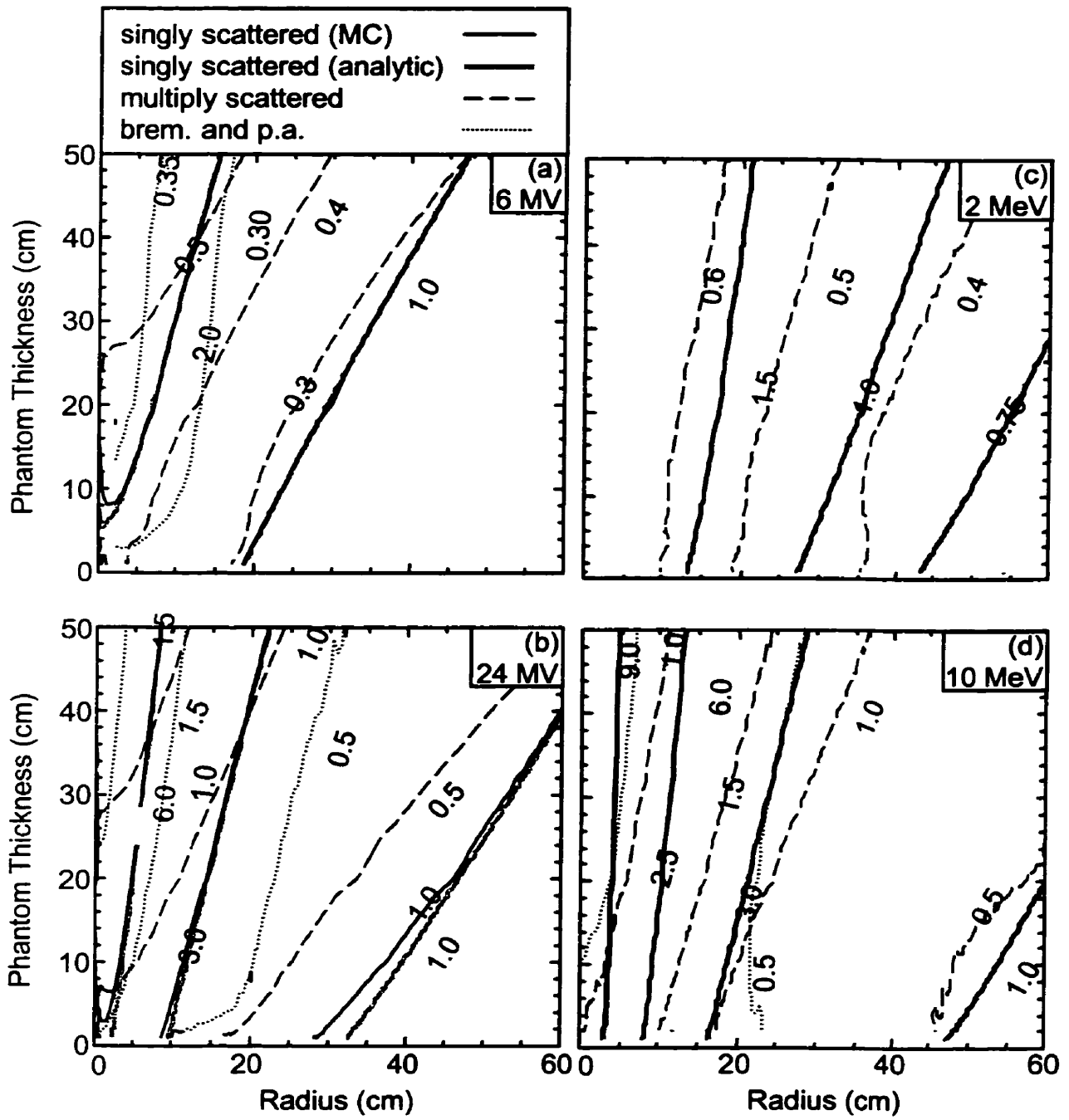
(OVERLEAF) Figure 3.3: Monte Carlo prediction of iso-mean energy lines. Mean energy (MeV) of scattered photon fluence due to an incident (a) 6 MV, (b) 24 MV, (c) 2 MeV, and (d) 10 MeV pencil beam behind a 20 cm thick water slab, at various air gaps. Solid lines represent mean energy of singly-scattered photons, dashed lines represent mean energy of multiply-scattered photon fluence, and dotted lines represent mean energy of bremsstrahlung and positron annihilation photons. Gray lines represent results of an analytical singly-scattered fluence calculation, for comparison.



(OVERLEAF) Figure 3.4: Monte Carlo prediction of iso-scattered fluence lines. The scattered photon fluence is normalized to the incident fluence (units are $\times 10^{-6} \text{ cm}^{-2}$) and due to an incident (a) 6 MV, (b) 24 MV, (c) 2 MeV, and (d) 10 MeV pencil beam at a 30 cm air gap, behind various thickness' of water phantom. Solid lines represent singly-scattered photon fluence, dashed lines represent multiply-scattered photon fluence, and dotted lines represent bremsstrahlung and positron annihilation photons. Gray lines represent results of an analytical singly-scattered fluence calculation for comparison. Background shading indicates dominance of the singly-scattered photon fluence whereas no shading indicates dominance of the multiply-scattered fluence component *except* in (d), where no shading indicates dominance of the bremsstrahlung and positron annihilation photons.



(OVERLEAF) Figure 3.5: Monte Carlo prediction of iso-mean energy lines. Mean energy (MeV) of scattered photon fluence due to an incident (a) 6 MV, (b) 24 MV, (c) 2 MeV, and (d) 10 MeV pencil beam at a 30 cm air gap, behind various thicknesses of water phantom. Solid lines represent mean energy of singly-scattered photons, dashed lines represent mean energy of multiply-scattered photon fluence, and dotted lines represent mean energy of bremsstrahlung and positron annihilation photons. Gray lines represent results of an analytical singly-scattered fluence calculation for comparison.



3.3.2 Influence of air gap on pencil beam scatter kernels

Introduction of an air gap allows divergent scatter generated within the patient to physically miss the portal imaging detector. The larger the air gap, the smaller the solid angle defined by a portal imaging detector of given dimension, and therefore the less likely scatter will impinge upon the detector. Figures 3.2 (a) and (c) present the variation of the scattered photon fluence kernel as a function of air gap, for a 6 MV and 2 MeV spectra incident upon a 20 cm thick water slab. The singly-scattered fluence is more forward directed than the multiply-scattered fluence, and of greater magnitude as expected from the Klein-Nishina cross section governing Compton scatter.

Bremsstrahlung and positron annihilation comprise the smallest contribution to total scatter fluence. In contrast, for the higher energy spectra (24 MV and 10 MeV, in Figures 3.2 (b) and (d)), using the same geometry, the bremsstrahlung and positron annihilation component is on the same order of magnitude as the multiply-scattered photons, throughout the majority of kernel radii and air gaps examined. Singly-scattered photons are more forward directed than the lower energy spectra examples. Again, this is predicted by the Klein-Nishina cross section at higher energies.

The dominant scatter component is calculated for each plot in Figure 3.2. Singly-scattered (represented by shading) or multiply-scattered fluence (represented by no shading) is dominant for the 6 MV, 24 MV, and 2 MeV spectra. Only singly-scattered or bremsstrahlung and positron annihilation fluence is dominant for the 10 MeV spectrum. However, for the 24 MV spectra the bremsstrahlung component may exceed the multiply-scattered fluence at smaller radius and moderate to large air gaps, but these regions are dominated by singly-scattered fluence. For all spectra, the singly-scattered fluence dominates at smaller radii and larger air gap. The edge of the dominant singly-scattered

shading shows a geometric divergence. Furthermore, the region of singly-scattered fluence dominance expands towards larger radius and smaller air gap, as the pencil beam energy increases. This is explained by the reduction in the magnitude of the multiply-scattered and bremsstrahlung and positron annihilation fluence more than compensating for the narrowing of the singly-scattered fluence, as incident energy increases. It is evident that singly-scattered photon fluence comprises the largest portion of scattered photon fluence for all energy spectra examined here, over a radius range that increases linearly with air gap.

The behavior of the corresponding mean energies of the scattered photon pencil beam kernels is a direct consequence of the preferential loss of large angle scattered photons (and therefore lower energy photons). This effect becomes more noticeable as the air gap is increased, since the solid angle of a given scoring plane dimension decreases. This implies that the mean energies of all scattered photons should increase with increasing air gap, which is observed. For the 6 MV and 2 MeV incident spectra (Figures 3.3 (a) and (c)), the multiply-scattered photons demonstrate a flatter distribution of mean energies and lower magnitude, when compared to the singly-scattered photons. The bremsstrahlung and positron annihilation photons show the flattest mean energies, and are of very low magnitude. This also applies to the 24 MV and 10 MeV incident spectra (Figures 3.3 (b) and (d)).

3.3.3 Influence of phantom thickness on pencil beam scatter kernels

As the phantom thickness is increased, total scatter fluence at any given air gap increases, reaching a maximum at some thickness dependent on incident energy, and then slowly begins to decrease. Similar results have been reported by Jaffray *et al.* [Ja94] and

Pasma *et al.* [Pa98a]. This effect is analogous to the buildup of photon scatter within a phantom, which eventually reaches equilibrium with the primary, whereupon photon scatter begins to decrease as the primary attenuates further. This relationship is evident in Figures 3.4 (a) and (c), which describe the scattered photon pencil beam kernel behavior with increasing phantom thickness for a 6 MV and 2 MeV energy spectra incident on slabs of water of varying thickness, at an air gap of 30 cm. For the 6 MV spectrum, there is a buildup which peaks at approximately 12 cm, 25 cm, and 16 cm for singly-scattered, multiply-scattered, and bremsstrahlung and positron annihilation photons respectively. Figure 3.4 (b) and (d) illustrates the slower buildup of scattered photons for the 24 MV and 10 MeV energy spectra. For the 24 MV spectrum the scattered photon buildup peaks at approximately 18 cm, 30 cm, and 20 cm, for singly-scattered, multiply-scattered, and bremsstrahlung and positron annihilation photons respectively. All scattered photons demonstrate more forward-peaked distributions at higher energy (although the multiply-scattered photons are only slightly more forward-peaked).

Again, the dominant scatter fluence is overlaid in Figure 3.4, with shading and no shading representing the dominance of singly-scattered fluence and multiply-scattered fluence respectively for the 6 MV, 24 MV, and 2 MeV spectra. Only singly-scattered and bremsstrahlung and positron annihilation fluence dominate the scatter for the 10 MeV spectrum. The singly-scattered fluence dominates multiply-scattered fluence at smaller radii and thinner phantoms, since the multiply-scattered fluence is a broader distribution and demonstrates a slower buildup to a maximum. For similar reasons, singly-scattered fluence dominates the bremsstrahlung and positron annihilation fluence of the 10 MeV spectrum, at smaller radii and very thin phantoms, except that the bremsstrahlung component builds up nearly as quickly as the singly-scattered fluence.

It is evident from Figures 3.4 (a) and (c), in addition to Figures 3.2 (a) and (c), that the resulting scatter fluence maps for the 6 MV and 2 MeV spectra demonstrate a high degree of similarity. This resemblance indicates that the scatter fluence distributions are not strongly dependent upon the incident energy spectrum. Although the polyenergetic spectra used here were generated by modeling specific linear accelerators [Mo85a], the results should not vary significantly for different brands of accelerators.

The behavior of mean energies with increasing phantom thickness is similar to their dependence on air gap. The beam hardening of the primary fluence will contribute to this effect for polyenergetic spectra, leaving higher energy photons in the beam to be scattered, as the phantom thickness increases. Furthermore, geometric arguments may be applied to explain this. As the phantom thickness is increased, the mean source location of scatter is removed further 'upstream' from a given detector position. The increased 'scatter source' to detector distance results in behavior similar to the dependence on air gap, in that the mean energy of all scattered photons increases with increasing phantom thickness for a given detector location. This permits preferential scatter and absorption of lower energy photons over greater distances. The effect is observed with all incident energy spectra (Figure 3.5). Backprojecting the mean angular data (angles with respect to incident pencil beam) at the 30 cm air gap results in the mean total scatter (fluence weighted) source location changing from 0.2 cm to 12.4 cm (measured upstream from the exit surface) for a 1 cm thick and 50 cm thick phantom using the 6 MV spectrum. Repeating this analysis using the 24 MV spectrum demonstrates similar behavior, where the mean total scatter source location moves from 0.2 cm to 11.6 cm for 1 cm and 50 cm thick phantoms.

The variation of mean energy with phantom thickness and radius for both the multiply-scattered and the bremsstrahlung and positron annihilation photons is flatter (in the absolute sense) than that of the singly-scattered fluence. At lower incident energies, the bremsstrahlung and positron annihilation photon mean energies are flatter than the multiply-scattered photon pattern, but this is no longer true for the 24 MV spectrum.

3.3.4 Scatter fraction

This quantity is an estimate of the amount of scatter present in relation to the total photon fluence (scatter plus primary) present at a given point on a detector surface. The scatter fraction on the central axis as a function of air gap and phantom thickness for a 27×27 cm² equivalent field size is presented in Figure 3.6. The behavior of scatter fraction with incident field size and phantom thickness at an air gap of 30 cm is illustrated in Figure 3.7. The dependence of scatter fraction on incident field size and air gap is demonstrated in Figure 3.8, for a phantom thickness of 20 cm.

Several observations regarding the behavior of the scatter fraction on the central axis are evident. A general increase in the scatter fraction with increasing phantom thickness is observed using both energy spectra. This is due to an increase in contributing scatter material combined with increased attenuation of the primary over larger thicknesses. The behavior of these two factors results in similar scatter fraction maps for both energy spectra, except at larger fields and thicker phantoms, as illustrated in Figure 3.7(a). A decrease in scatter fraction with increasing air gap is observed in Figures 3.6(a) for fixed phantom thickness and in Figure 3.8(a) for fixed field size, as expected due to the decreasing solid angle with increasing air gap. The scatter fraction increases with incident field size due to increased volume of scattering material encompassed by the

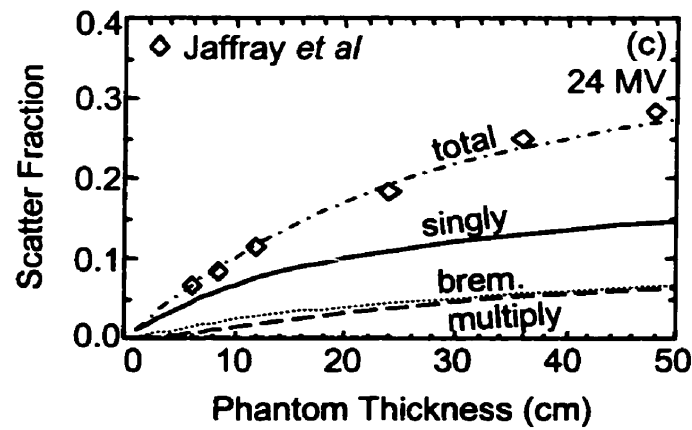
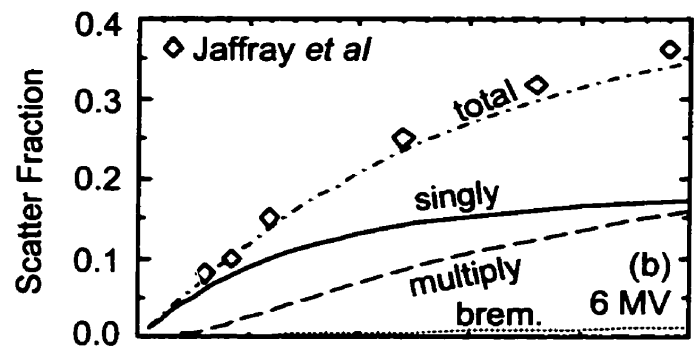
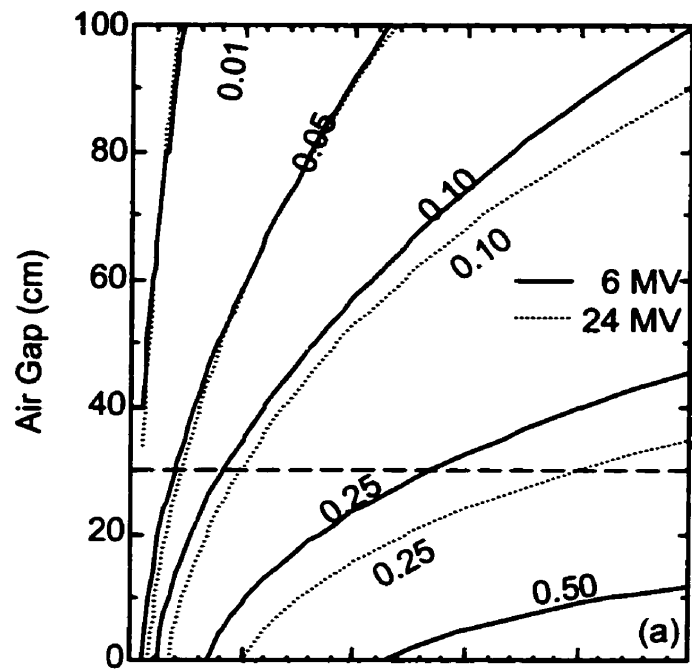
larger field size. Interestingly, the tradeoff between the geometrical parameters of field size and air gap results in straight contours for both energy spectra, not only for a phantom thickness of 20 cm as shown in Figure 3.8 (a), but for all phantom thicknesses simulated. After accounting for the difference between parallel and diverging geometry as described in Appendix B, the data presented in Figures 3.6-3.8 correspond well with the corresponding scatter fraction data calculated by Jaffray *et al.* [Ja94].

It is clear that singly-scattered photons are the most important contributors to scatter fluence at the portal imaging plane for both low and high energy spectra, accounting for more than 50% of the total scatter on the central axis (except at smaller air gaps and thicker phantoms). For the 6 MV spectrum, the multiply-scattered photons comprise the majority of the remaining scatter fluence, approaching the magnitude of singly-scattered photons only at smaller air gaps and thicker phantoms, whereas the contribution of bremsstrahlung and positron annihilation photons are minor. For the 24 MV spectrum, the significance of bremsstrahlung and positron annihilation significance is increased to approximately coincide with or exceed that of multiply-scattered photons.

(OVERLEAF) Figure 3.6(a): Total scatter fraction as a function of air gap and phantom thickness, for a $27 \times 27 \text{ cm}^2$ field. Solid lines represent results using a 6 MV spectrum, dotted lines represent results using a 24 MV spectrum. The straight, dashed line locates the cross section plotted in Figures 3.6 (b) and 3.6 (c).

(OVERLEAF) Figure 3.6(b): Cross section of the 6 MV results corresponding to dashed line in Figure 3.6(a). The solid line represents scatter fraction due to singly-scattered photons, the short dashed line represents scatter fraction due to multiply-scattered photons, the dotted line represents scatter fraction due to bremsstrahlung and positron annihilation photons, and the long dashed line represents the total scatter fraction. Comparison of total scatter fraction is made to data (\diamond) of Jaffray *et al* [Ja94].

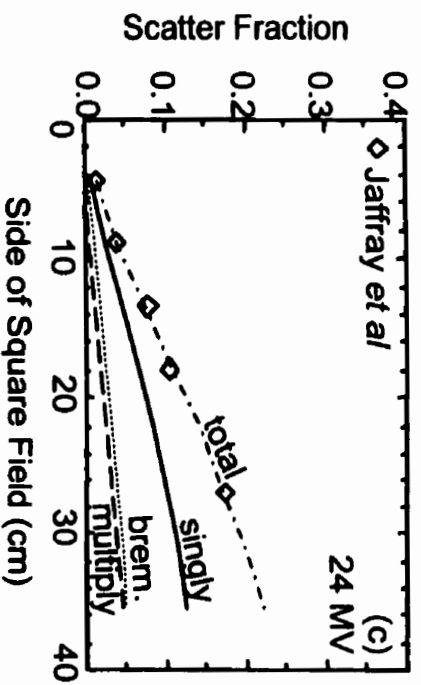
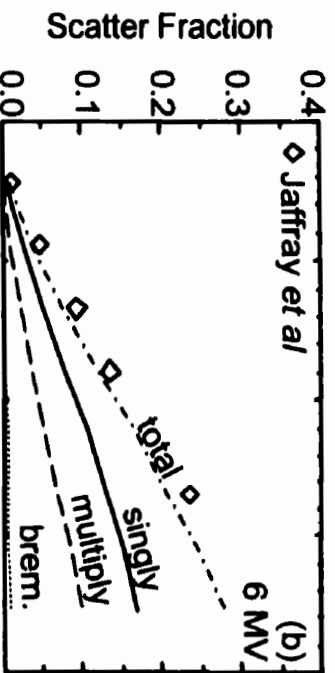
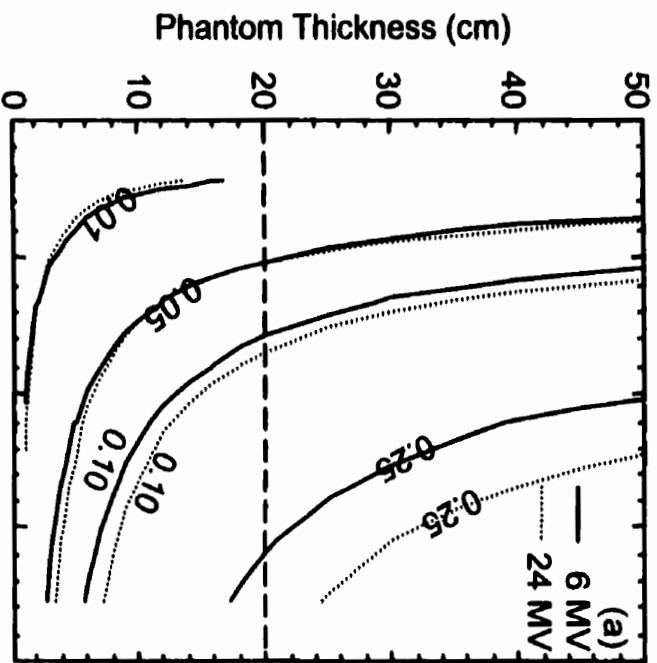
(OVERLEAF) Figure 3.6(c): Cross section of the 24 MV results corresponding to dashed line in Figure 3.6(a). Line legend as in 3.6(b) description.



(OVERLEAF) Figure 3.7(a): Total scatter fraction as a function of phantom thickness and field size, for a 30 cm air gap. Solid lines represent results using a 6 MV spectrum, dotted lines represent results using a 24 MV spectrum. The dashed line locates the cross section plotted in Figures 3.7(b) and 3.7(c).

(OVERLEAF) Figure 3.7(b): Cross section of the 6 MV results corresponding to dashed line in Figure 3.7(a). The solid line represents scatter fraction due to singly-scattered photons, the short dashed line represents scatter fraction due to multiply-scattered photons, the dotted line represents scatter fraction due to bremsstrahlung and positron annihilation photons, and the long dashed line represents the total scatter fraction. Comparison of total scatter fraction is made to data (\diamond) of Jaffray *et al* [Ja94].

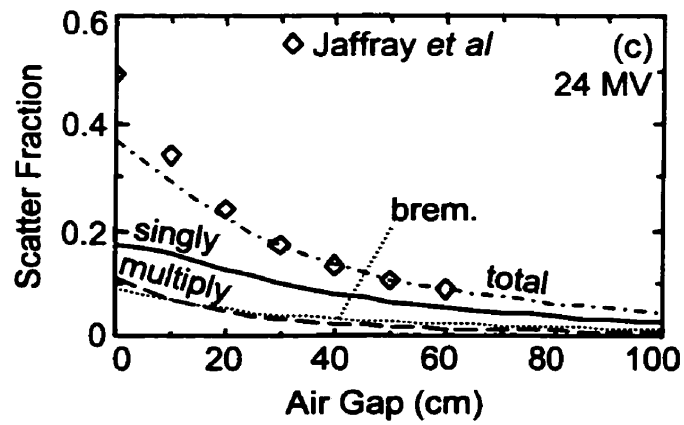
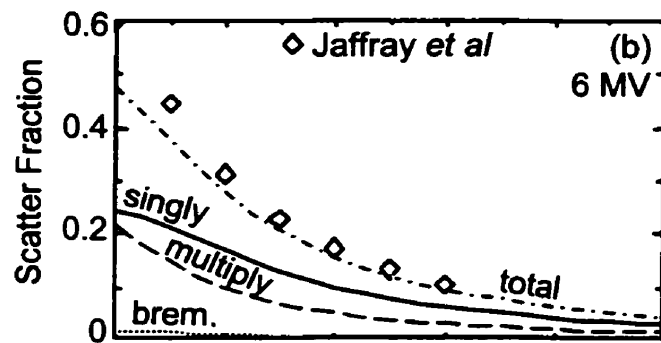
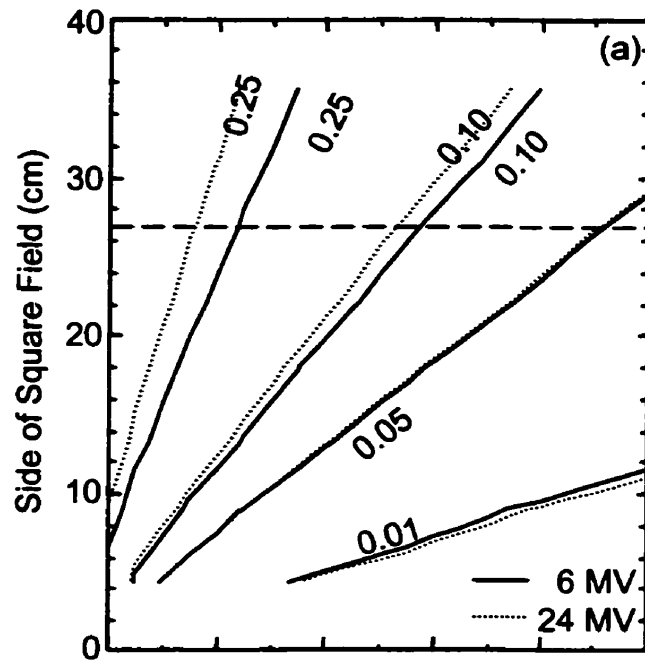
(OVERLEAF) Figure 3.7(c): Cross section of the 24 MV results corresponding to dashed line in Figure 3.7(a). Line legend as in 3.7(b) description.



(OVERLEAF) Figure 3.8(a): Total scatter fraction as a function of field size and air gap, for a 20 cm thick water phantom. Solid lines represent results using a 6 MV spectrum, dotted lines represent results using a 24 MV spectrum. The dashed line locates the cross section plotted in Figures 3.8(b) and 3.8(c).

(OVERLEAF) Figure 3.8(b): Cross section of the 6 MV results corresponding to dashed line in Figure 3.8(a). The solid line represents scatter fraction due to singly-scattered photons, the short dashed line represents scatter fraction due to multiply-scattered photons, the dotted line represents scatter fraction due to bremsstrahlung and positron annihilation photons, and the long dashed line represents the total scatter fraction. Comparison of total scatter fraction is made to data (\diamond) of Jaffray *et al* [Ja94].

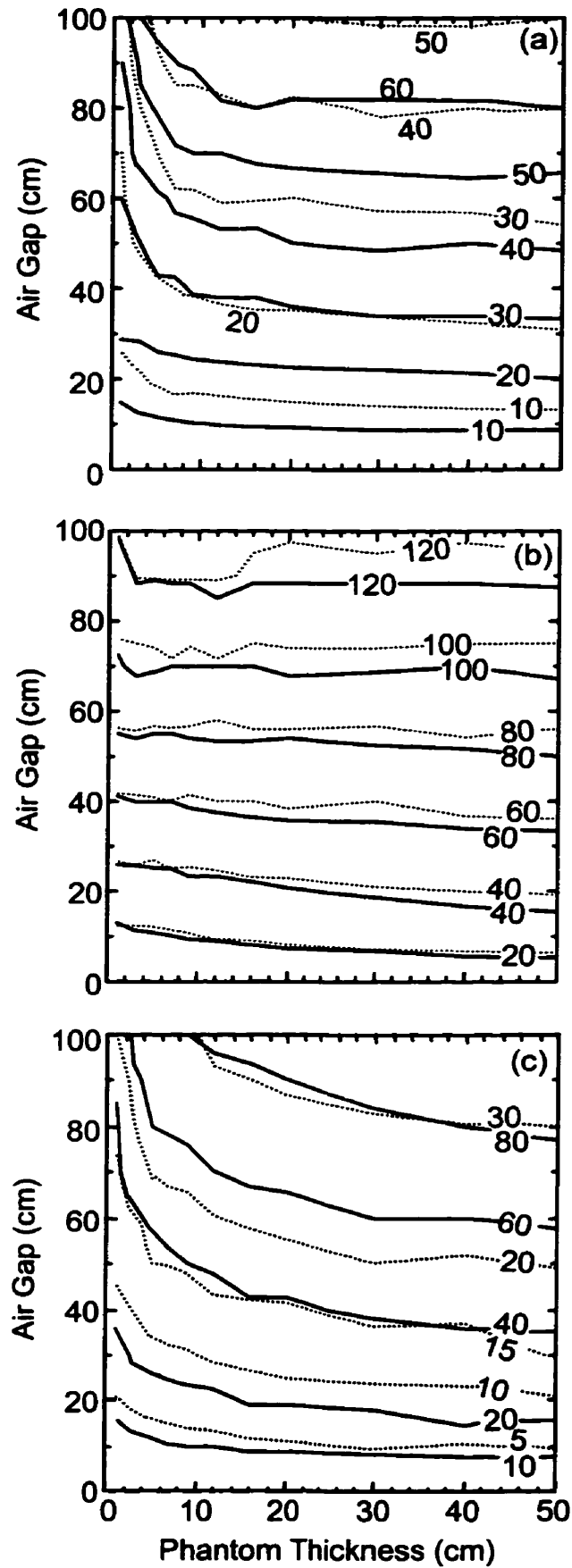
(OVERLEAF) Figure 3.8(c): Cross section of the 24 MV results corresponding to dashed line in Figure 3.8(a). Line legend as in 3.8(b) description.



3.3.5 Full width at half maximum of scatter fluence

To further characterize the scattered photon fluence distributions, the full width at half maximum (FWHM) illustrated in Figure 3.9, is examined. As expected, the higher energy spectrum results in narrower distributions of singly-scattered, as well as bremsstrahlung and positron annihilation photons. The FWHM is approximately linear with air gap and is another indicator of the geometrical divergence of fluence throughout the air gap. For larger phantom thickness, the width of the scatter fluence kernels broadens slowly with increasing phantom thickness. The increase in FWHM occurs more quickly for smaller phantom thicknesses for singly-scattered, and bremsstrahlung and positron annihilation photons. These observations may be explained with simple physical arguments, recalling that the scattered fluence is the result of interactions along the entire primary pencil beam. As the source of scattering is moved from the exit plane towards the entrance plane, the attenuation and divergence effects, as well as the anisotropic nature of the scatter, will broaden the scattered fluence distribution. The distribution of scattered photons from material close to the exit will therefore be the narrowest and thus the observed increase in FWHM with increasing phantom thickness is to be expected. For scatter components with diffuse scattering sources, such as the multiply-scattered fluence, the effects of attenuation and divergence will be less apparent, and the scatter will be more isotropic. This explains the smaller dependence of FWHM with phantom thickness for this component. At small phantom thicknesses, the FWHM of singly-scattered and bremsstrahlung/positron annihilation fluence demonstrates a stronger dependence on phantom thickness, because of the quicker buildup of scatter into a transient equilibrium condition (forward scatter being generated while primary decreases).

(OVERLEAF) Figure 3.9: Full width at half maximum data (in cm) as a function of air gap and phantom thickness for scattered photon fluence pencil beams representing (a) singly-scattered photons, (b) multiply-scattered photons, and (c) bremsstrahlung and positron annihilation photons. Solid lines represent 6 MV spectrum and dotted lines represent 24 MV spectrum.



3.3.6 Modulation transfer function

For a constant phantom thickness, the MTF improves with increasing air gap, since fewer scattered photons reach the scoring plane as it moves away from the phantom. The significance of even a small air gap is shown in Figure 3.10, where the MTF is shown to approach unity at all spatial frequencies as the air gap increases. For a constant air gap, an increasing phantom thickness results in a decrease in MTF (Figure 3.11). This is due to the increasing scatter fluence generated in thicker phantoms as well as the greater attenuation of the primary signal. Once beyond a small air gap of ~5cm, the air gap will only affect high spatial frequency MTF by at most ~10%, whereas the phantom thickness variation between 1-40 cm will affect MTF by at most ~7%. The MTF calculated here presents the contribution of photon scatter within the patient to the total MTF of the portal imaging system.

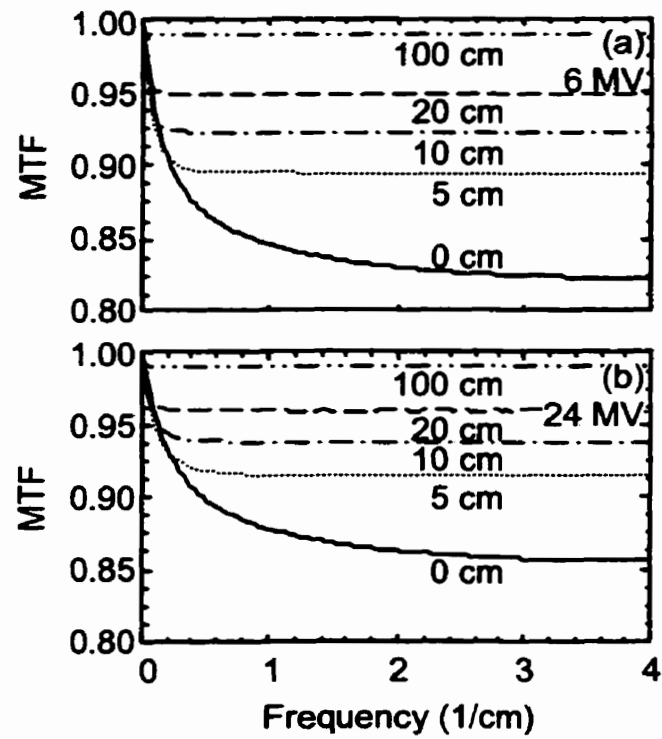


Figure 3.10: Modulation transfer function of point spread functions using (a) 6 MV, and (b) 24 MV pencil beam through a 20 cm thick water phantom, for various air gaps.

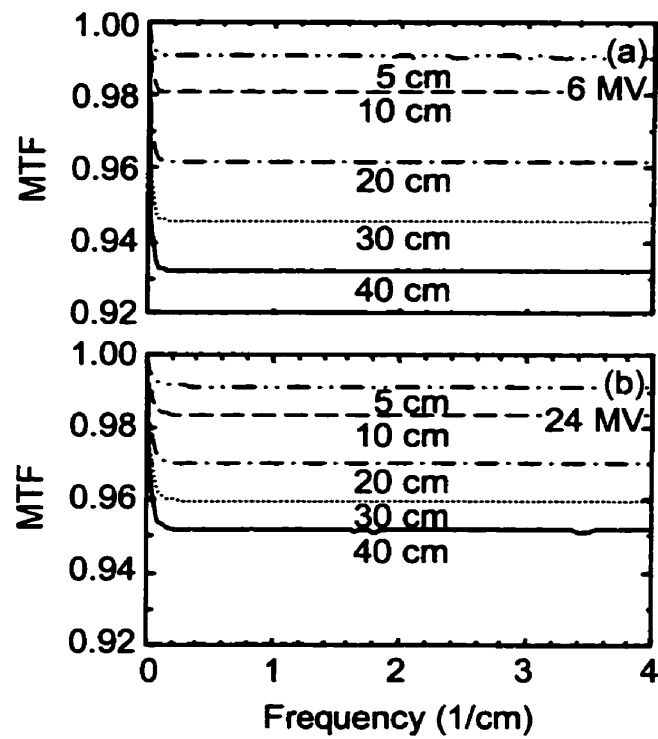


Figure 3.11: Modulation transfer function of point spread functions using (a) 6 MV, and (b) 24 MV pencil beam, at an air gap of 30 cm for various phantom thickness'.

3.5 Summary and Conclusion

The nature of photon scatter behind homogeneous slabs of water at various air gap distances has been studied for incident photon pencil beams, using the EGS4 Monte Carlo based radiation transport code. Incident energies examined include monoenergetic spectra of 2.0 MeV and 10.0 MeV and polyenergetic spectra representing nominal 6 MV and 24 MV photon beams. The magnitude and mean energy of scattered photon fluence kernels as a function of air gap, phantom thickness, and photon history (singly-scattered, multiply-scattered, or bremsstrahlung and positron annihilation events) was examined. For high incident energies, the significance of bremsstrahlung and positron annihilation photon fluence approaches that of multiply-scattered photon fluence. This implies that accurate scatter fluence kernels for high energy photon beams must be generated using methods which incorporate electron interactions (for example, EGS4 which simulates coupled photon-electron interactions). The similarity of the 6 MV and 2 MeV scatter fluence distributions (Figure 3.2 (a) and (c) and Figure 3.4 (a) and (c)) indicate that the distributions are only weakly dependent on the exact details of the incident energy distribution. Therefore, the distributions due to the polyenergetic spectra presented here (6 and 24 MV) should be valid for linear accelerators of different manufacturers, but similar nominal energies. The mean energies of singly-scattered photons show a significant variation across phantom thickness and air gap, whereas the mean energies of multiply-scattered and bremsstrahlung and positron annihilation photons are much flatter. This indicates that the energy spectra of the scattered photons is complex, implying that analytical approaches to predicting scatter fluence energy spectra may have some difficulty (excluding the singly-scattered fluence). The straightness of the mean energy

contours (Figure 3.3 and Figure 3.5) indicate that a geometric divergence of scatter fluence is occurring.

Using reciprocity allows the scatter fraction on the central axis behind the water slabs for various incident circular field sizes, phantom thickness', and air gaps to be examined from the viewpoint of a detector. First order scattering is shown to be the major component of the scatter fraction over the range of air gaps, phantom thicknesses, and energy spectra examined here, generally accounting for 50% or more of the total scatter except for small air gaps and thick phantoms. This finding indicates that a portal dose image prediction algorithm may only need to accurately model singly-scattered photon fluence, for certain clinical situations. The magnitude of bremsstrahlung and positron annihilation photons increases significantly as the incident photon energy increases, exceeding that of multiply-scattered photons for all field sizes and phantom thicknesses examined here (valid for the 10.0 MeV and 24 MV spectra). Again, this emphasises the need to accurately model bremsstrahlung interactions for higher energy beams.

The full width at half maximum parameter was used to characterize the spread of the pencil beam kernels with air gap, phantom thickness, and photon history. The width of all scattered photon kernels changed very little with phantom thickness, and steadily increased with increasing air gap. This again indicates primarily a geometrical dependency of the shape of the scattered photon kernels, for both energy spectra studied here.

Modulation transfer functions were calculated representing the degradation due to photon scatter in the patient, the theoretical limiting MTF of any portal imaging system. Introduction of a small air gap was demonstrated to provide a ~6% improvement in MTF

at high spatial frequencies. This implies that as large an air gap as possible should be used to improve portal image quality, if the field of view is not compromised. Variation in phantom thickness between 1-40 cm, and variation in air gap between 5-100 cm were shown to have less than a 10% impact on the MTF at most spatial frequencies.

CHAPTER FOUR[†]

PHOTON SCATTER IN PORTAL IMAGES: ACCURACY OF A FLUENCE BASED PENCIL BEAM SUPERPOSITION ALGORITHM

4.1 Introduction

In the previous chapter, the physical characteristics of scattered photon radiation at a portal imaging detector were studied through the analysis of radially symmetric scatter distributions (or ‘kernels’) behind slab phantoms generated by an incident pencil beam of photons. These planar scatter kernels may be utilized in a two dimensional, superposition approach to calculate the scattered photon fluence due to a patient, incident on a portal imaging detector. The accuracy and behavior of this fluence estimation method over a wide range of clinical circumstances is investigated in this chapter.

While film and electronic portal imaging systems were originally designed for geometric verification, recent efforts [Es96; Fi93; Ha96; Ha97; He95; Ki93; Ki95; Le86; Pa98a; Pa98b; Pa99d; Va92; Wo90a; Yi90; Zh95] have demonstrated their effectiveness for a variety of dosimetric applications. A portal image is formed by a primary fluence component added to a scatter fluence component, and modulated by detector response. The calculation of the primary fluence component using ray tracing methods is trivial, and therefore if the contribution of scatter to the portal image can be determined with sufficient accuracy and a knowledge of detector response is possessed, the final predicted

[†] Based on [Mc00b].

portal image may be compared quantitatively to an acquired image [Es96; He95; Ki93; Ki95; Le86; Pa98a; Pa98b; Wo90a; Yi90; Zh95]. Due to the wide variety of portal imaging systems available (e.g. screen/film [Fi93; Va92], screen/camera [Bo92; Mu95], scintillation detector [Bo92; Mu95], liquid ionization chambers [Bo92; Mu95], linear diode arrays [Bo92; Fi96], and amorphous silicon arrays [Bo92; Mu95]), it is beneficial to separate the portal image calculation process into two steps: (a) predict the fluence and energy incident into a detection plane and (b) calculate the portal dose image using the predicted energy fluence map and the specific detector response. The separation of fluence transport from detector response allows detailed modeling of each detector to be performed independently, without affecting performance of the fluence transport algorithm. The current chapter explores step (a) by examining a pencil beam algorithm used to predict basic radiation field parameters (such as scatter fluence, mean scattered photon energies, and mean scattered photon angles) at an arbitrary imaging plane distal to the patient. The modeling of specific detector response, referred to in step (b) above, will be presented elsewhere.

The prediction of portal dose images using various calculation techniques has been studied by a small number of groups. Portal dose images for a cobalt-60 beam were predicted using the delta-volume technique and compared to measured images [Wo90a; Yi90], but a recent publication by McNutt *et al.* [Mc96b] shows that this technique is unsuitable for prediction at larger air gaps. Portal dose image prediction has also been investigated using a convolution/superposition of Monte Carlo generated point-interaction dose kernels [Mc96a; Mc96b]. In these works, a 6 MV beam was examined over small air gaps (11-22 cm), predicting dose deposition in a low atomic number, water equivalent detector. Pencil beam style algorithms, which are inherently faster than 3D superposition

algorithms, have been implemented by Hansen *et. al* [Ha97] and Pasma *et. al* [Pa98b]. Hansen *et. al* [Ha97] employed in-house Monte Carlo simulation software to generate pencil beam scatter fluence kernels for 6 MV beams which were used to deconvolve the scatter from EPID (electronic portal image detector) images through an iterative approach. This allowed an estimate of the primary signal from which radiological thickness was calculated. The inhomogeneous phantoms examined in that work generated small amounts of scatter (scatter to primary ratio of <6%) at the air gaps examined. Pasma *et. al* [Pa98b] derived pencil beam scatter kernels specific to a Philips SRI-100 electronic portal imaging system, from measured data for 6, 23, and 25 MV photon beams. These kernels were used to predict the scatter dose component of an EPID, which when added to a primary dose estimate yields a portal dose image. These experimentally derived scatter kernels were applied at larger air gaps (~40-100 cm), where the air gap serves to remove a considerable portion of the scattered photons [Ja94; Mc00a]. although these large air gaps are typical for Elekta (formerly Philips) treatment machines, several commercial electronic portal imagers provide air gaps of less than 40 cm [Mu95; Sh96a], while portal film cassettes may be placed to achieve almost any air gap. Varian and Eliav offer variable source detector distances (SDDs). Theraview/Cablom offer SDDs of 135-165 cm, whereas Siemens offers a fixed SDD of 140 cm resulting in air gaps of 10-35 cm. Although the work of Hansen *et. al* [Ha97] indicated that their version of the pencil beam fluence algorithm was promising at low energies, there has been no formal study of the factors influencing the predictive accuracy of pencil beam methods applied to transmission radiography, nor in predicting other interesting radiation field parameters such as scattered photon energies and scattering angles.

This chapter investigates the accuracy of a pencil beam algorithm for predicting scatter photon fluence, as well as associated mean energies and mean angles with respect to the incident beam axis (θ_z) at arbitrary portal imaging planes, for nine phantom geometries and several field sizes (10x10, 8x14, 20x20, and 30x30 cm²).

4.2 Materials and Methods

4.2.1 Monte Carlo simulation of radiation transport

The EGS4 (Electron Gamma Shower version 4 [Ne85]) radiation transport computer code was used to perform all simulations in this chapter. As in chapter three, parameters ECUT and PCUT were set to 0.80 MeV and 0.01 MeV respectively. ECUT was set low enough to ensure that there was no impact on bremsstrahlung production, and high enough to significantly decrease simulation times. Two polyenergetic incident energy spectra were used, representative of nominal 6 MV and 24 MV linear accelerators [Mo85a].

4.2.2 Generating ideal pencil beams using Monte Carlo simulation

Details of the creation of the data base of pencil beams used here have been presented previously (chapter three and [Mc00a]), so only a brief summary is provided.

An infinitely thin pencil beam of photons was made perpendicularly incident upon a semi-infinite slab of water. Concentric ring scoring bins (radial dimension 0.25 cm) were created in several planes lying behind and parallel to the water slab. The planar fluence of scattered photons was tallied in the radial bins, as were the mean energy, and mean θ_z . Pencil beam data were generated for a range of slab thicknesses (between 1-50 cm), and air gap distances (0-100 cm). Photons were tracked and scored according to scattering history: (i) primary (unscattered) photons, (ii) singly-scattered photons, (iii) multiply-scattered photons, and (iv) photons arising from bremsstrahlung or positron annihilation events. The result of these simulations is a library of data describing the scattered photon distribution at various imaging planes and over a wide range of phantom

thicknesses, for an impulse input of photons. As an example, scatter kernels resulting from pencil beams representing 6 MV and 24 MV polyenergetic energy spectra [Mo85a] incident on a 20 cm thick phantom and 30 cm air gap are presented in Figure 4.1. Scatter fractions for broad beam situations may be estimated from these kernels as described in section 3.2.3 and 3.3.4.

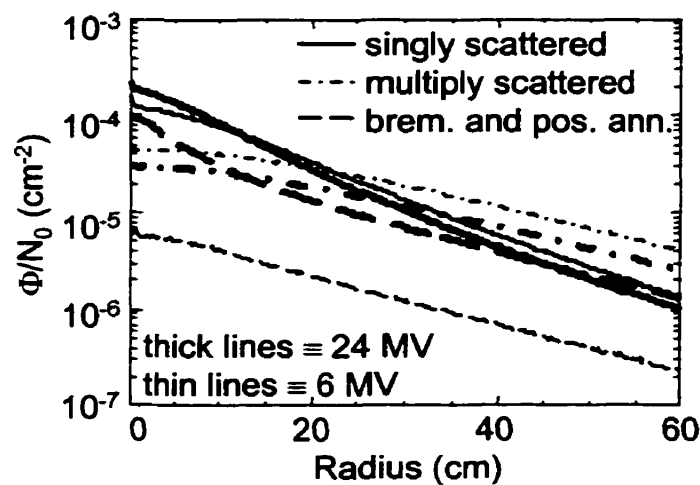


Figure 4.1: Scatter fluence kernels per incident particle, scored at an air gap of 30 cm behind a 20 cm thick water slab due to incident polyenergetic pencil beam representing 6 MV (thin lines) and 24 MV (thick lines) spectra.

4.2.3 Pencil beam algorithm to predict scatter fluence

The algorithm implemented here involves a fast, 2D superposition of scatter fluence kernels. *A priori* information regarding the treatment setup is required, including the energy spectrum and relative fluence distribution of the incident beam(s), and density information describing the patient (e.g. CT data). A superposition of the Monte Carlo-generated scatter fluence kernels with the incident beam fluence allows the pattern of scattered photon fluence, mean energy, and mean θ_z at an arbitrary portal imaging plane to be predicted. However, before this process occurs, the patient density data are analyzed to form an equivalent homogeneous phantom (EHP). The EHP concept was introduced by Pasma *et al.* [Pa98a]. The calculation of the EHP consists of finding the equivalent thickness of water for each column of voxels in the patient data set, along the incident beam direction. A corresponding new air gap value is obtained by reorienting the equivalent thickness of water to maintain the centre of mass position, and finding the new exit surface to imaging plane distance. Generating the EHP data set in a parallel geometry requires processing times of less than 0.5 seconds (on a Silicon Graphics O2 R10000 platform) for a phantom data set of $256 \times 256 \times 40$ voxels.

A grid of pencil beams is then transported through the water equivalent patient, where the EHP thickness and air gap determine the scatter kernel chosen for a particular point, and the resulting fluence contribution is weighted by the appropriate relative fluence of the incident beam, which in this chapter is assumed to be an ideal step function. The scatter fluence, mean of mean energies ($\bar{\bar{E}}$), and mean of mean θ_z ($\bar{\bar{\theta}}_z$) of scattered photons may be tallied for a regular 2D array of scoring voxels in the imaging plane, where the distance separating the scoring voxel center and the incident grid point

for that pencil beam defines the radius at which to sample the scatter kernel. Predicted mean of mean energy and mean of mean θ_z values are fluence weighted. For a scoring location in the portal imaging plane at $\bar{r}' = (x', y')$, the calculations may be expressed as:

$$\phi_s(\bar{r}') = \iint \phi_0(\bar{r}) \cdot K_\phi(t(\bar{r}), g(\bar{r}), |\bar{r} - \bar{r}'|) d^2\bar{r} \quad (4.1)$$

$$\bar{\bar{E}}(\bar{r}') = \frac{\iint \phi_0(\bar{r}) \cdot K_\phi(t(\bar{r}), g(\bar{r}), |\bar{r} - \bar{r}'|) \cdot K_E(t(\bar{r}), g(\bar{r}), |\bar{r} - \bar{r}'|) d^2\bar{r}}{\iint \phi_0(\bar{r}) \cdot K_\phi(t(\bar{r}), g(\bar{r}), |\bar{r} - \bar{r}'|) d^2\bar{r}} \quad (4.2)$$

$$\bar{\bar{\theta}}_z(\bar{r}') = \frac{\iint \phi_0(\bar{r}) \cdot K_\phi(t(\bar{r}), g(\bar{r}), |\bar{r} - \bar{r}'|) \cdot K_{\theta_z}(t(\bar{r}), g(\bar{r}), |\bar{r} - \bar{r}'|) d^2\bar{r}}{\iint \phi_0(\bar{r}) \cdot K_\phi(t(\bar{r}), g(\bar{r}), |\bar{r} - \bar{r}'|) d^2\bar{r}} \quad (4.3)$$

where $x, y =$ x and y coordinates of incident photon beam

$x', y' =$ x and y coordinate of scoring voxel in scoring plane

$\bar{r} =$ vector coplanar to scoring plane, representing (x, y) as projected into scoring plane

$\bar{r}' =$ vector coplanar to scoring plane, representing (x', y') in the scoring plane (note that \bar{r} and \bar{r}' share the same origin)

$\phi_s =$ scattered photon fluence into scoring voxel at \bar{r}

$\bar{\bar{E}} =$ mean of mean energies of scattered photon fluence at \bar{r}

$\bar{\bar{\theta}}_z =$ mean of mean angles (with respect to z -axis) of scattered photon fluence at \bar{r}

- K_{ϕ} = scattered photon fluence kernel
- $K_{\bar{E}}$ = mean energy of scattered photon fluence kernel
- $K_{\bar{\theta}_z}$ = mean angle (with respect to z-axis) of scattered photon fluence kernel
- ϕ_0 = incident relative fluence distribution (incident photon beam fluence normalised to central axis value)
- t = radiological thickness (i.e. equivalent thickness of homogeneous water) of patient through (x, y)
- g = air gap (distance separating patient exit surface and scoring plane) through (x, y)

The resolution of the incident grid of pencil beams (i.e. the number of pencil beams per unit beam area) into a phantom will have a direct impact on the accuracy of predicted parameters. However, if the choice of incident grid resolution is made to ensure oversampling of the scatter kernels, then the prediction accuracy will not be affected. Since the scatter kernels were scored using radial bins of 0.25 cm width, a choice of 0.1 cm for the incident grid resolution guarantees an oversampling situation. This resolution was used for the incident grid in all studies performed in this chapter, except in one series, where the effect of changing this incident grid resolution was examined.

4.2.4 Monte Carlo simulation using phantoms

The predictions of the pencil beam algorithms are compared with results of direct EGS4 simulation of homogeneous and inhomogeneous phantoms. User code DOSXYZ

[Ma95] provides independent simulation results, which are used here as the ‘gold standard’ for evaluating radiation field parameters which cannot be measured, such as fluence from specific photon histories (e.g. singly or multiply-scattered, bremsstrahlung and positron annihilation), mean energies, and mean angles. Incident fields were simulated in a parallel geometry. Staying in a parallel framework and using the same radiation transport code ensures that differences (beyond statistical uncertainty) between the pencil beam algorithm calculation and the DOSXYZ simulations will occur due to only deficiencies in the implemented pencil beam algorithm.

The user code DOSXYZ was modified to score photon fluence through several planes perpendicular to the incident beam direction. The user specifies the z-coordinate (dimension parallel to the incident beam direction) locations as well as finite dimension of the scoring grid and scoring voxel size (2D) in these planes. Planar photon fluence, mean energy, and mean θ_z are scored for each rectangular, planar voxel. For the simulations performed in this chapter, the scoring grid size was set at $40 \times 40 \text{ cm}^2$ with the centre coinciding with the central axis of the incident beam, while the dimensions of the 2D scoring voxels were set at $1.0 \times 1.0 \text{ cm}^2$. The code was also modified to track particle history, in the same manner as was done for the pencil beam scoring in section 4.2.2 above. In all DOSXYZ simulations, the incident fluence was set at $4 \times 10^5 \text{ photons/cm}^2$.

The nine phantom geometries tested here (illustrated in Figure 4.2) were chosen based on variations of simple configurations used for testing inhomogeneity corrections of dose deposition algorithms [Va93]. Phantom 1 is a homogeneous slab of water, 20 cm thick. Phantoms 2, 3, and 4 are simple lung slab inhomogeneities while phantoms 5 and 6 are simple thin bone slab inhomogeneities. Phantom 7 simulates a lateral neck treatment

(long thin column of air in a column of water) whereas phantom 8 models a mediastinum treatment (with rectangular lungs). Phantom 9 is a homogeneous half slab of water, with the incident beam centred on the slab edge. In all cases, the incident fields were applied as ideal step functions, with no account taken for off-axis energy spectra changes.

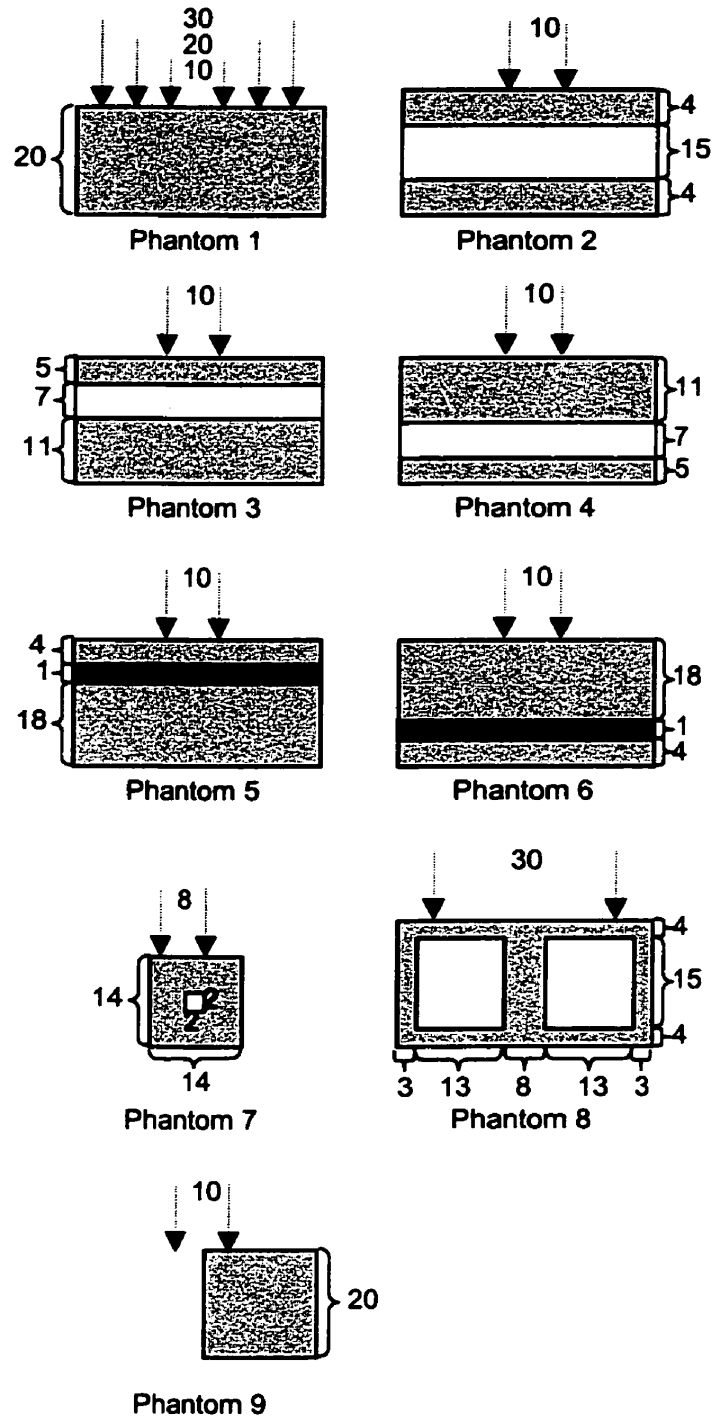


Figure 4.2: Phantom cross sections, with all dimensions in centimeters. Incident beam edges are indicated by dotted arrows. Density is gray-scale coded as $\blacksquare \rho=1.9 \text{ g/cm}^3$, $\blacksquare \rho=1.0 \text{ g/cm}^3$, $\square \rho=0.2 \text{ g/cm}^3$, $\square \rho=0.0012 \text{ g/cm}^3$.

4.2.5 Experimental validation of Monte Carlo simulations

A comparison of Monte Carlo results was made with the measured central axis data of Jaffray *et al.* [Ja94] to establish the validity of the simulations. This is important, since the accuracy of the pencil beam algorithm predictions is evaluated by direct comparison to the Monte Carlo simulation output. The user code DOSXYZ was modified to account for detector response in a 2×2 cm² area around the central axis. The modeled detector was that used by Jaffray *et al.* [Ja94], an ionization chamber (PTW N23323-2359) with a 4 cm diameter PMMA buildup cap. As described by Jaffray *et al.* [Ja94], the response of the ion chamber was estimated to be:

$$q(E) = \left(\frac{\mu_{en}}{\rho} \right) \Big|_E S_{wall}^{air} m_{detector} A_w \Big|_E E \quad (4.4)$$

where $(\mu_{en}/\rho)|_E$ is the mass energy absorption coefficient for the buildup cap, S_{wall}^{air} is the ratio of mass stopping powers (air to wall), $m_{detector}$ is the mass of the detector, $A_w|_E$ is the wall correction factor, and E is the energy of an incident photon. Since the mass stopping power ratio varies slowly over the energy range of interest [IC76], and the mass of the detector is constant, these parameters are not significant for a calculation of scatter fraction. The wall correction (A_w) was calculated according to Attix [p. 353 of At86]. By taking advantage of the scattered and primary photon fluence tracking, the Monte Carlo simulation was able to separately score the detector response for the scatter signal and the primary signal. These data were used to calculate the scatter fraction estimates. The Monte Carlo simulation used 20 cm thick water slabs, which are almost radiologically pathlength-equivalent to the 17 cm thick PMMA slabs used in the measurements [Ja94].

Several square field sizes were simulated (5×5 , 10×10 , 20×20 , 30×30 cm²) as the incident parallel beams.

4.2.6 Assessment of accuracy

Pencil beam algorithm predictions are compared directly to the modified DOSXYZ output of planar scatter fluence, mean energy, and mean θ . To summarize comparisons of data sets succinctly, the maximum difference as a percentage of total signal on the central axis at the imaging plane was used for fluence predictions, whereas absolute maximum differences were used for mean energy and mean angle predictions. Since a parallel beam geometry is used here, the estimated errors, as a percentage of total signal, will not fall off as rapidly with increasing air gap as for a diverging geometry. However, if the differences between a parallel and a divergent beam are accounted for in a renormalization of the primary (see Appendix B), an approximate conversion of the percentage error to values more closely reflecting a divergent geometry may be performed. If this is done, trends in the error estimates are preserved, with a maximum increase of 2.5% in the percentage errors, and in fact <1.0% for most of the phantoms and air gaps examined here. Therefore, while the percentage error estimates presented in this chapter are made using data generated with a parallel beam, the discussion and conclusions will be valid for diverging beams.

Furthermore, it should be noted that a conversion of the raw predicted fluence data to dose in a given detector would result in a reduction in the magnitude of estimated percentage errors. This is due to most detectors responding less to lower energy incident

photons compared to higher energy photons [Ja94], thereby reducing the importance of detector signal arising from scattered photons.

The main factors affecting the pencil beam algorithm accuracy include (a) field size effects, (b) the deviation of the EHP from the semi-infinite slab geometry in which the scatter kernels were generated, (c) the use of the EHP to represent a complex patient density distribution, (d) the resolution of the incident pencil beam grid, and (e) the air gap.

Field size effects were determined by comparing results of 10×10 , 20×20 , and 30×30 cm² fields on the homogeneous water slab, phantom 1. It is expected that the errors in the predictions of the pencil beam algorithm will increase in proportion to the field area, due to the presence of systematic errors. The effect of the deviation of the EHP from the ideal semi-infinite slab geometry was examined in a physically extreme situation, that of the half slab (phantom 9), whereas the impact of the creation of the EHP was studied through several phantom configurations, including both lower and higher density inhomogeneities at a variety of locations.

The impact of air gap on the pencil beam algorithm accuracy is examined for all phantoms. As the air gap increases, the scatter drops off quickly [Ja94; Mc00a] (even with a diverging beam, the scatter decreases more rapidly than the primary), and therefore it is expected that the error as a percentage of total signal will decrease with air gap.

The resolution of the incident pencil beam grid was varied over 0.1 to 5.0 cm, to determine the effect on pencil beam algorithm accuracy. By keeping the field size constant (10×10 cm²), some resolution choices do not line up with the field edges (sub-optimal), and some do line up and provide equal coverage along the field edges (optimal).

Results will be dependent on exact details of field shape and size, but by estimating the worst case performance based on the sub-optimal choices of resolution, a general estimate of algorithm accuracy is obtained that should be independent of field shape. This study was carried out using the half slab, phantom 9, since the exiting scatter fluence distribution contains a broader frequency content than would result from most phantom geometries. A higher frequency content in the scatter distribution requires a higher incident pencil beam resolution in order to reproduce it. Thus, this phantom is a good choice for estimating an upper limit on the required input grid resolution. The study was performed using scatter fluence data generated at a 5 cm air gap, since larger air gaps result in a loss of frequency content (e.g. the scatter fluence distribution becomes broader) and thus do not require as high an incident pencil beam resolution.

4.3 Results and Discussion

4.3.1 Experimental validation of Monte Carlo simulations

The scatter fractions estimated by employing a model of the detector response in the Monte Carlo simulation code were compared to measured data found in the literature [Ja94]. A simple correction [Appendix B and Mc00a] was applied to the Monte Carlo estimates to account for differences between the parallel and diverging primary fluence components (inverse square effect and normalization). The comparison is presented in Figure 4.3. The overestimate by the Monte Carlo simulations at larger field sizes is a result of the conversion to a diverging geometry not accounting for the increased divergence of scatter fluence occurring in a diverging geometry. Overall, the comparison is good, giving confidence in the Monte Carlo simulation results.

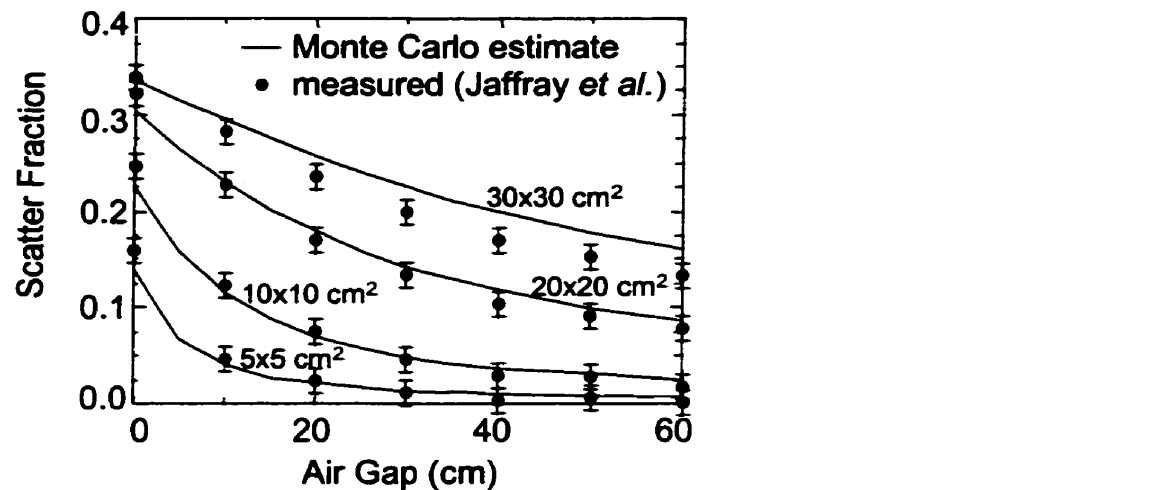


Figure 4.3: A comparison of scatter fractions measured by Jaffray *et al* [Ja94] using an ionization chamber (6 MV, 17 cm PMMA slab), and estimated with Monte Carlo techniques including a model of detector response (6 MV, 20 cm water slab). Monte Carlo estimates were converted [Appendix B and Mc00a] from a parallel geometry to a diverging geometry. Four field sizes are shown. Deviations at large field sizes are due to assumptions in the conversion from parallel to diverging geometry, as explained in Appendix B.

4.3.2 Accuracy of pencil beam algorithm in predicting fluence

4.3.2.1 Effect of field size

Phantom 1 serves as an ideal case, for which the pencil beam algorithm should operate the most accurately, since the geometry most closely resembles that under which the pencil beam scatter kernels were generated (homogeneous and uniformly thick). For a $10 \times 10 \text{ cm}^2$ field and a 6 MV spectrum, maximum errors in predicted scatter fluence did not exceed 0.3%. However, any systematic errors involved in implementing the pencil beam algorithm will be proportional to incident field size, since this parameter determines the number of scatter kernels to be summed for scatter prediction. Field sizes of $20 \times 20 \text{ cm}^2$ and $30 \times 30 \text{ cm}^2$ were studied to establish the magnitude of systematic errors (see Figure 4.4). In Table 4.1, it is observed that the percentage error is roughly linearly proportional to field size, over a selection of air gap values. The phantoms simulated in DOSXYZ are not semi-infinite in extent (nor can they be in clinical situations), thus it is expected that the pencil beam algorithm will systematically overestimate the multiple-scatter fluence. This is due to the presence of multiple-scatter contributions from extremely distant points in the semi-infinite phantom, during the scatter kernel calculation. Since treatments with field sizes larger than $20 \times 20 \text{ cm}^2$ occur infrequently (even mantle treatments involve effective areas of $\sim 20 \times 20 \text{ cm}^2$, due to blocking), it is expected that the field size will not contribute errors of greater than $\sim 0.8\%$.

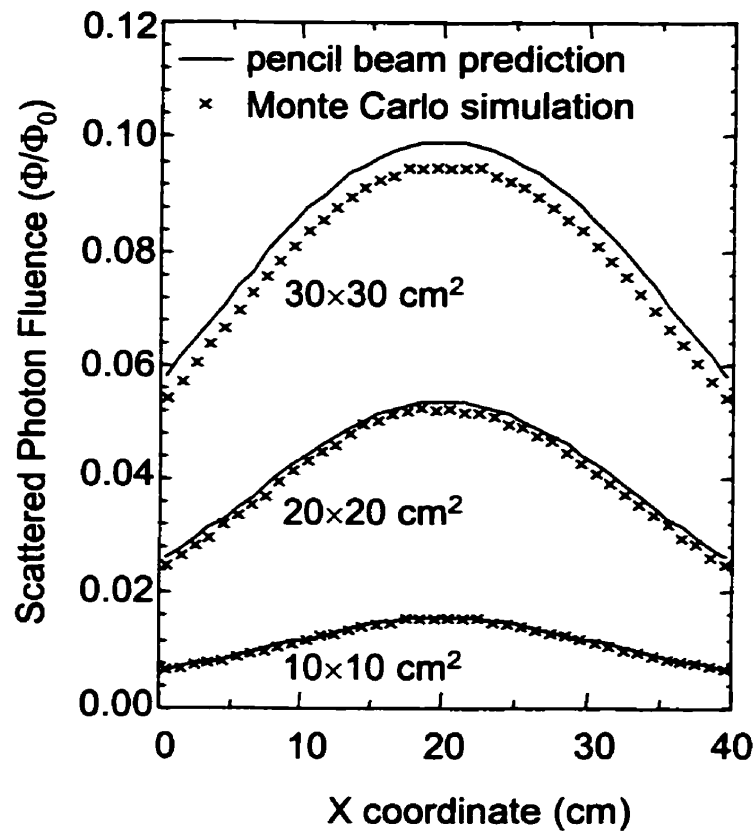


Figure 4.4: Cross section through centre of scoring plane showing predicted total scatter fluence per incident beam fluence for phantom 1 at 30 cm air gap for $10 \times 10 \text{ cm}^2$, $20 \times 20 \text{ cm}^2$, $30 \times 30 \text{ cm}^2$ incident fields with a 6 MV energy spectrum.

Air Gap (cm)	$10 \times 10 \text{ cm}^2$	$20 \times 20 \text{ cm}^2$	$30 \times 30 \text{ cm}^2$
0	0.3	0.8	1.8
10	0.2	0.6	1.4
20	0.2	0.6	1.2
40	0.1	0.5	0.9

Table 4.1: Maximum difference between predicted and simulated scatter fluence as a percentage of total fluence on central axis at scoring plane, for phantom 1 and a 6 MV energy spectrum, as a function of air gap and incident field size.

4.3.2.2 Effect of air gap

Table 4.2 summarizes the maximum errors in predicted scatter fluence as a percentage of the total fluence on the central axis in the imaging plane, for all phantom configurations examined here. As air gap is increased, the errors due to replacing the true phantom with an EHP are reduced, since the scatter fluence rapidly decreases [Ja94; Mc00a].

For the phantoms studied here, the error in the pencil beam algorithm prediction for 6 MV photon beams is greater than that for 24 MV photon beams, at any given air gap. This is a consequence of the increased primary to scatter ratio of the higher energies, with the increase in the magnitude of primary fluence being more significant than the changes in the scatter fluence. Since Table 4.2 presents percentage errors with respect to total fluence on the central axis, the increasing primary fluence of the 24 MV beam results in a decrease in percentage error estimates as compared to the 6 MV beam.

Singly-scattered photons comprise the majority of error in scatter fluence prediction over short air gaps for all phantoms examined here (demonstrated in Figure 4.5), with the exception of phantom 7, where the error in multiple-scatter fluence prediction dominates due to the much smaller lateral dimensions of this phantom. Note that the error estimates shown in Figure 4.5 are not additive over the scattered photon components, since these are maximum percentage errors within an entire scoring plane, and are therefore not necessarily resulting from the same physical position.

For all phantoms examined, the maximum percentage error in the predicted scatter fluence falls below 3% with an air gap of only 10 cm, and below 1.5% for an air gap of 20 cm (refer to Table 4.2). The 5% tolerance for absorbed dose delivery as recommended by the ICRU 24 [IC76] is used here as a guideline for estimating the accuracy required by

this algorithm as approximately 3%. The errors introduced by this fluence prediction algorithm will be added in quadrature to errors introduced by subsequent dose prediction (step (b) in section 4.1). Therefore, introducing an air gap of at least 10 cm for portal image acquisition will generally ensure that the pencil beam algorithm presented here will predict portal fluence in the forward direction with reasonable accuracy ($<3\%$ of total fluence). This implies that the pencil beam algorithm presented will be applicable to the vast majority of clinical portal imaging system configurations. With the increasing trend towards dynamic treatments, the necessary patient clearance of the portal imager should ensure that air gaps of less than 10 cm are encountered infrequently. In the rare situation where an air gap greater than 10 cm cannot be attained, then an alternate analytical technique exists [Appendix C and Mc98a] that accurately predicts the singly-scattered photon fluence component. Since this is the major scatter component at small air gap for most phantom configurations, the overall error would be significantly reduced.

Energy (MV)	Air Gap (cm)	P1	P2	P3	P4	P5	P6	P7	P8	P9
6	0	0.3	-4.1	3.0	-5.8	2.9	1.5	1.1	6.9	0.7
6	10	0.2	-0.9	1.4	-1.9	1.3	0.9	0.8	2.7	0.3
6	20	0.2	0.2	0.6	-0.5	0.6	0.5	0.5	1.4	0.2
6	40	0.1	0.1	0.2	-0.08	0.2	0.2	0.3	0.8	0.07
24	0	0.2	-3.1	1.6	-4.4	0.7	-0.5	0.7	4.2	0.6
24	10	0.1	-0.8	0.8	-1.6	0.4	-0.2	0.6	1.6	0.3
24	20	0.1	-0.2	0.4	-0.7	0.1	-0.1	0.4	0.9	0.1
24	40	0.1	-0.05	0.1	-0.2	0.06	-0.07	0.2	0.4	0.07

Table 4.2: Maximum difference between predicted and simulated scatter fluence as a percentage of total fluence (scatter plus primary) on central axis at scoring plane, for phantoms 1-9 (P1-P9), as a function of air gap and incident energy spectra. A negative value indicates an underestimate relative to the Monte Carlo simulation results. All field sizes are $10 \times 10 \text{ cm}^2$, except for phantom 7 ($8 \times 14 \text{ cm}^2$) and phantom 8 ($30 \times 30 \text{ cm}^2$).

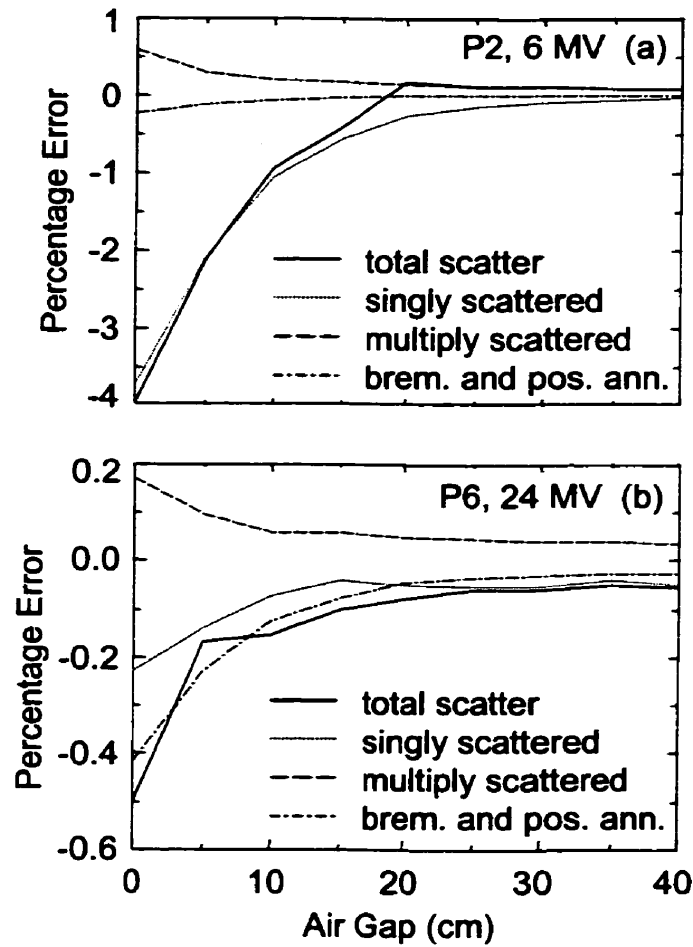


Figure 4.5: Maximum error between predicted scatter fluence and DOSXYZ output as a percentage of total fluence on the central axis, as a function of air gap, 10x10 cm² field. Results shown are for (a) phantom 2 with a 6 MV beam, and (b) phantom 6 with a 24 MV beam.

4.3.2.3 Effect of generating scatter kernels in a semi-infinite slab geometry

The deviation of the EHP from a semi-infinite slab geometry will have different effects depending on photon history. As mentioned in section 4.3.2.1, the pencil beam algorithm will overestimate the multiply-scattered fluence component, for all finite phantom situations. Although this error increases when the phantom dimensions are very small (i.e. as far as possible from the semi-infinite slab geometry), the proportion of multiply-scattered photons decreases quickly with air gap, thus reducing the importance of accurate prediction of this component. This error is also more apparent for the 6 MV spectrum than for the 24 MV spectrum, due to the increased significance of multiply-scattered photon fluence at lower incident energies.

The effect upon the singly-scattered and bremsstrahlung components is somewhat different. Since these two components are more forward-directed than the multiply-scattered fluence, the accuracy of the predicted fluence is affected only near phantom edges. This is illustrated in Figure 4.6, using the half slab geometry (phantom 9). The multiply-scattered fluence is overestimated, as expected. The predicted singly-scattered fluence drops off too quickly under the air side of the half slab as compared to the Monte Carlo data. This occurs due to the difference in geometry between the ideal semi-infinite slab, which the pencil beam scatter kernel was generated in, and the geometry of the half slab phantom. When created, the singly-scattered fluence kernels experienced attenuation uniformly around the incident pencil beam (ie. in a semi-infinite slab), whereas in the half slab geometry, singly-scattered photons exiting the face of the half slab do not experience significant attenuation and therefore generate a higher fluence under the air-side of the half slab in the full Monte Carlo simulation. Since the bremsstrahlung component is not

quite as forward-directed as the singly-scattered fluence, the effect is moderated but still noticeable.

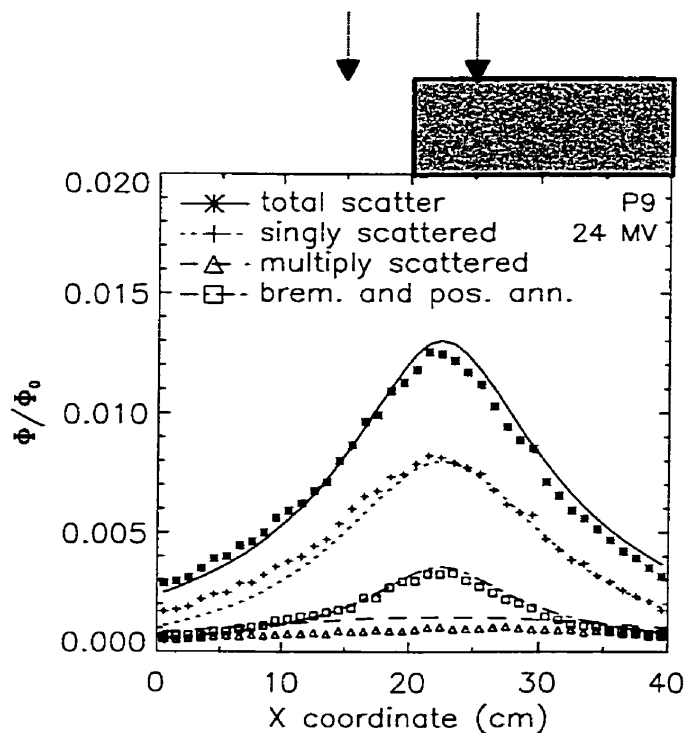


Figure 4.6: Cross section through centre of scoring plane ($y = 20$ cm), showing predicted scatter fluence per incident beam fluence by photon history component. Symbols represent DOSXYZ output, lines signify pencil beam algorithm prediction. Results are for phantom 9 (half-slab phantom) at a 30 cm air gap using a 24 MV energy spectrum. The orientation of the phantom and incident field are depicted at the top of the figure.

4.3.2.4 Errors due to use of the EHP concept

When the true phantom column is replaced by the EHP column, the distribution of scattered photon fluence production is changed. The significance of this change depends upon the size, density, and position of the inhomogeneity with respect to the size of the phantom. While the scattered photons originate from a three dimensional volume, their mean source position may be estimated by performing a fluence-weighted backprojection of the angular information from a given scoring plane. This information may be used to make some generalizations regarding the behavior of the algorithm. The movement of the mean scatter source is important, since the divergence of scatter will be incorrectly accounted for by the scatter kernel, and thus will cause an underprediction of scatter fluence for an 'upstream' shift and an overprediction for a 'downstream' shift. If the true phantom column contains a small, higher density inhomogeneity (e.g. phantoms 5 and 6), then the creation of the EHP column will move the mean scatter source downstream, towards the exit surface, resulting in the pencil beam algorithm overpredicting the scattered fluence as observed in Table 4.2. However, a very small underprediction occurs when using the 24 MV spectrum with phantom 6, which may be attributed to increased bremsstrahlung production inside the deep bone slab occurring in the Monte Carlo simulation and not accounted for by the pencil beam algorithm. This is due to differences in atomic number of the defined bone used in the phantom, where the Monte Carlo simulation uses a higher atomic number compacted bone composition [IC84], the pencil beam algorithm uses density-scaled water. Generally, the effects of bone inhomogeneities will be small due to their small physical dimension.

If the true phantom column contains a low density inhomogeneity (e.g. phantoms 2-4), then the mean scatter source location within the created EHP column becomes a

complex issue. Generally, low density inhomogeneities (e.g. lung) within the human body are larger than high density (e.g. bone) inhomogeneities, thus possessing a greater potential for creating perturbing effects in the photon fluence. When the low density inhomogeneity is near the exit surface of the phantom, the mean scatter source of the EHP column is moved upstream, away from the exit surface, resulting in the pencil beam algorithm underpredicting the scattered fluence. This effect is partially compensated by the systematic overprediction of the multiply-scattered component as discussed in section 4.3.2.1 and 4.3.2.3. However, if the low density inhomogeneity is near the entrance surface of the phantom, the mean scatter source of the EHP column is moved downstream, towards the exit surface. This effect is due to the movement of the centre of mass in the original phantom, which directly influences the mean scatter source position in the EHP column. For example, the centre of mass moves upstream a total of 2.0 cm between phantoms 3 and 4 (from a location of 12.5 cm below the entrance surface for phantom 3 to 10.5 cm below the entrance surface for phantom 4). Of course, the exact position of the centre of mass is dependent upon the size, position, and density of the inhomogeneity. The resulting pencil beam algorithm overprediction for phantom 3 and underprediction for phantom 4 are observed in Table 4.2. Of interest is the cross-over point, that is, the position of the inhomogeneity where the pencil beam algorithm neither overpredicts nor underpredicts the scattered photon fluence. For the 7 cm lung inhomogeneity of phantoms 3 and 4, the estimated point where this occurs is when the centre of the inhomogeneity is ~1-2 cm above geometric centre of the phantom.

Figure 4.7(a) demonstrates the over-prediction of multiple-scatter fluence and under prediction of the other scatter components, for phantom 2 at a 30 cm air gap using a 6 MV beam and $10 \times 10 \text{ cm}^2$ field. Figure 4.7(b) shows a similar pattern, explained in the

previous paragraph, for phantom 6 at a 30 cm air gap using a 24 MV beam and $10 \times 10 \text{ cm}^2$ field.

For the inhomogeneous phantoms, the largest absolute errors occur at the exit surface (see Table 4.2), ranging from 1.1% to 6.9% for the 6 MV spectra and 0.5% to 4.4% for the 24 MV spectra. The worst performance is for the mediastinum geometry, where the maximum errors in predicted scatter fluence are 6.9% and 4.2% for 6 MV and 24 MV energy spectra respectively, occurring at the exit surface. It is important to realize that there exists a variation of error within any scoring plane, and in fact a large portion of the scatter fluence error is significantly less than the maximum value, as illustrated in Figure 4.8 for the mediastinum phantom.

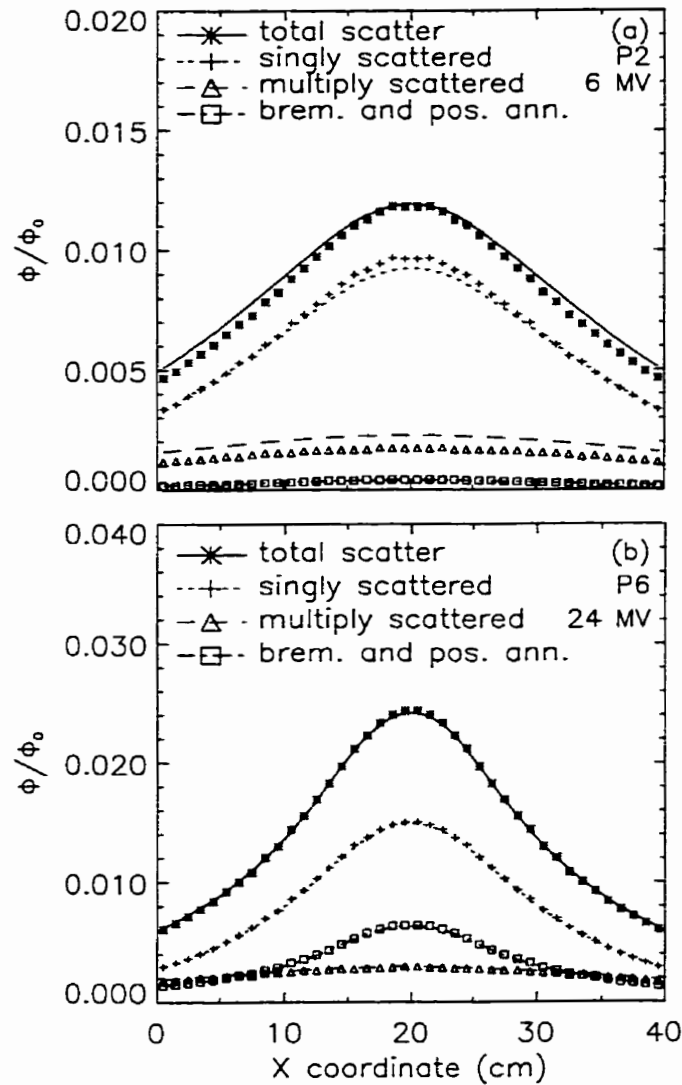
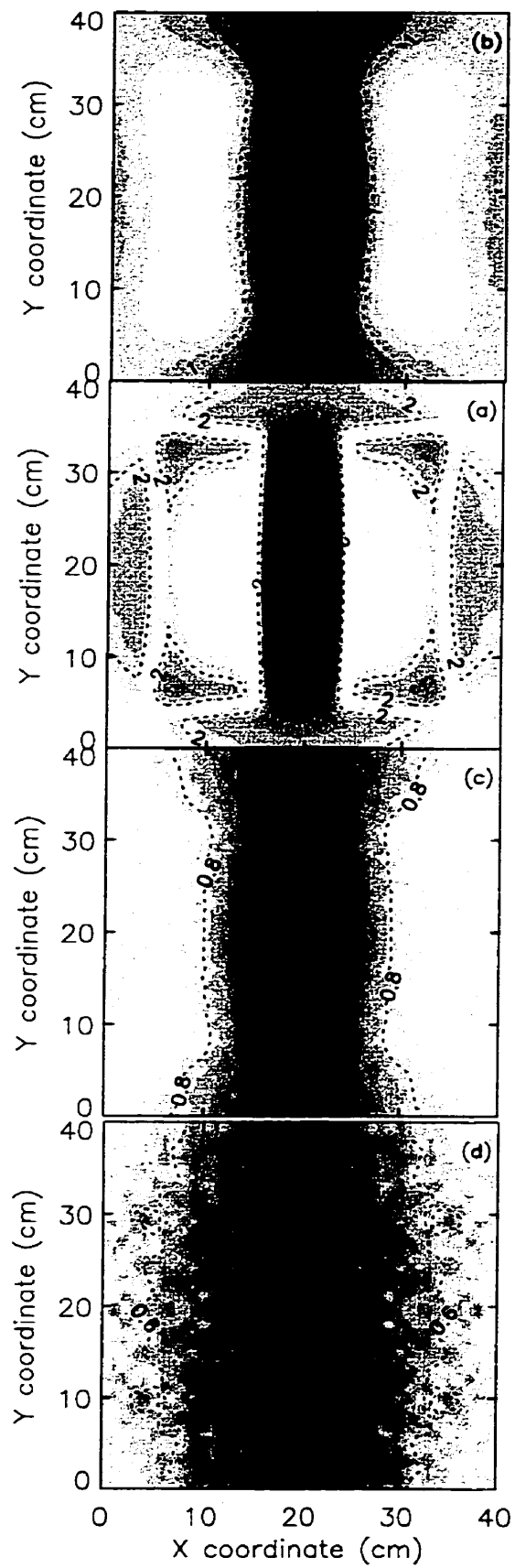


Figure 4.7: Cross section through centre of scoring plane ($y = 20$ cm) showing predicted scatter fluence per incident beam fluence by photon history component. Total scatter fluence is represented by *, singly-scattered fluence by +, multiply-scattered fluence by Δ , and bremsstrahlung and positron annihilation fluence by \square . Symbols represent DOSXYZ output, lines signify pencil beam algorithm prediction. Results are for phantom 2 at a 30 cm air gap using a 6 MV beam (a), and phantom 6 at 30 cm air gap using a 24 MV beam (b).

(OVERLEAF) Figure 4.8: Error in scatter fluence (per incident beam fluence) predicted by the pencil beam, as a percentage of total fluence on the central axis, for phantom 8 using a 6 MV beam and $30 \times 30 \text{ cm}^2$ field, for air gaps of (a) 0 cm, (b) 10 cm, (c) 20 cm, and (d) 40 cm.



4.3.2.5 Sampling resolution of incident beam

The impact of the resolution of the incident pencil beam grid on the pencil beam algorithms' accuracy was studied by varying this parameter between 0.1 and 5.0 cm, using phantom 9 with a 6 MV spectra and $10 \times 10 \text{ cm}^2$ field, at a 5 cm air gap. In this section, maximum percentage error is defined by the largest difference between the predicted scatter fluence using a given resolution and that predicted by the highest resolution (0.1 cm), to isolate the effects of incident grid resolution. This maximum difference was normalized to the maximum total fluence signal under the water portion of the half slab phantom, in order to avoid normalization to an open beam fluence, which would artificially reduce the error estimates.

The maximum percentage error in predicted total scatter fluence was found to be dependent on the grid points providing coverage extending to the field edges. For example, an incident resolution of 5 cm performed as well as 1.5 cm, since the sample grid points at 5 cm resolution cover both the phantom edge and field edge, whereas the choice of 1.5 cm does not properly represent either the field or phantom edges. This effect makes it difficult to choose a minimum resolution that will be generally applicable to arbitrary field shapes. However, by examining the variation of maximum percentage error with incident pencil beam grid resolution, an estimate of worst case performance for any field shape can be made by fitting a line to the poorest-performing incident resolutions. This is done in Figure 4.9, where it is evident that choosing an incident pencil beam grid resolution of 0.5 cm will limit the impact upon predicted scatter fluence to $\sim 1\%$ of total fluence. It should be noted that as the air gap increases, this requirement falls off rapidly due to the broadening of the scatter fluence distribution (for instance, at a 20 cm air gap, a choice of ~ 1.5 cm will have a similar effect on accuracy), and therefore a

resolution choice of 0.5 cm is conservative. The choice of resolution will also have a direct impact on the execution speed of the algorithm. This pencil beam algorithm predicts all three components of the scattered fluence, the mean energies, and the mean angles, in 1.5 seconds per 100 cm² field size using an incident grid resolution of 0.5 cm, on an SGI O2 R10000 platform using Fortran 77. In contrast, the Monte Carlo simulations consume at least 10 hours per 100 cm² field size using the 6 MV spectrum and at least 20 hours per 100 cm² field size using the 24 MV spectrum.

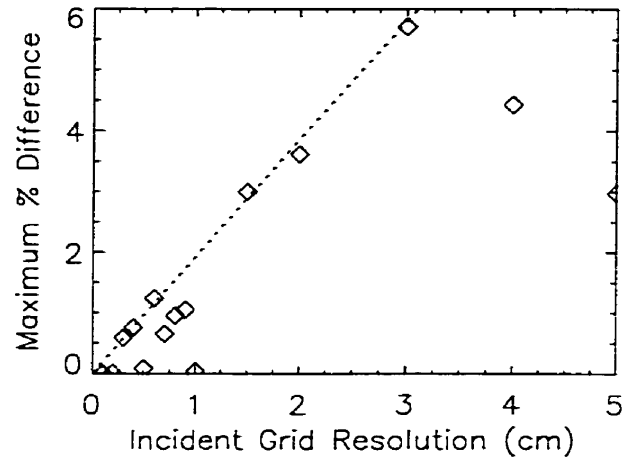


Figure 4.9: Dependence of maximum percentage error of pencil beam algorithm scatter fluence estimate on spatial resolution of incident pencil beam grid. The dotted line represents the estimate of worst performance.

4.3.3 Accuracy of pencil beam algorithm in predicting mean energy and mean angle

The pencil beam algorithm predicted mean of mean energies (using equation 4.2) associated with the fluence for each photon history to within 0.25 MeV and 0.65 MeV for the 6 MV and 24 MV simulation results respectively, over all air gaps. The mean energy prediction for the multiple-scatter fluence component is systematically low, due to the generation of the scatter kernel in a semi-infinite phantom (thereby allowing more lower energy, higher orders of scatter contributing from distant points). An example of this is given in Figure 4.10. For the majority of air gaps (usually greater than 15 or 20 cm) and phantom configurations, the absolute error in predicting the mean energy of the multiple-scatter component exceeded that of any other component. Mean of mean angles were predicted (using equation 4.3) to within 15° at the exit surface, and to within 5° at air gaps of 10 cm or more (for examples, see Figure 4.10).

The importance of the associated errors may be estimated in the context of applying these predicted radiation field quantities to estimate portal dose. Most portal image detector systems demonstrate a lower relative response to low energy photon fluence [Ja94], so errors in the mean energies will have a reduced impact. Angular corrections for pathlength through a portal detector would be implemented as the cosine of the predicted angle, which will also reduce the effect of any errors. The important demonstration is that these radiation field quantities can be predicted accurately using a simple and fast technique, and any associated errors will have a reduced effect when converting fluence to dose.

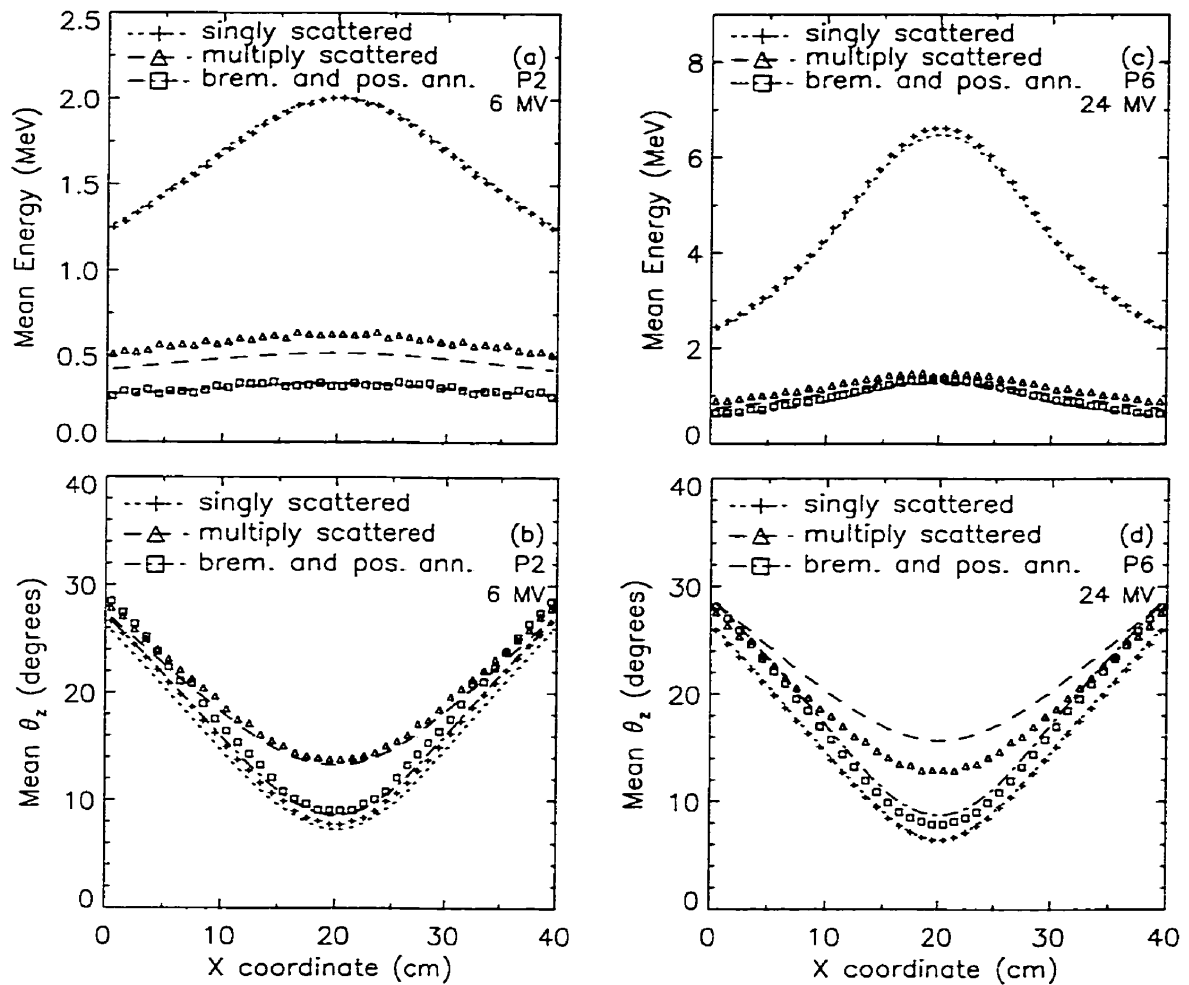


Figure 4.10: Cross section through scoring plane ($y = 20$ cm), showing predicted mean energy (a and c), and mean angle with respect to the incident pencil beam (b and d), by photon history component. Results for single scatter are represented by +, multiple-scatter by Δ , and bremsstrahlung and positron annihilation fluence by \square . Symbols represent DOSXYZ output, while lines signify pencil beam algorithm prediction. Results in (a) and (b) are for phantom 2 at a 30 cm air gap using a 6 MV, 10×10 cm² field, while those for (c) and (d) are for phantom 6 at a 30 cm air gap using a 24 MV, 10×10 cm² field

4.4 Conclusion

By combining the EHP concept [Pa98a] with the use of pencil beam scatter kernels [Mc00a] generated by the widely accepted EGS4 radiation transport code [Ne85], a fast, superposition pencil beam algorithm for predicting scatter photon fluence has been implemented. The predictive accuracy of this algorithm has been assessed for several inhomogeneous phantom configurations, and was found to be dependent on air gap, inhomogeneity, beam energy, incident beam resolution, and photon history. Error in the predicted total scatter fluence never exceeded 6.9% of the total signal on the central axis of the detector plane, and in all cases studied fell to under 2.8% by introducing an air gap of 10 cm (within the ICRU 24 recommendation [IC76] of 5% for absorbed dose delivery). Error in predicted mean energy was below 0.25 MeV and 0.65 MeV for the 6 MV and 24 MV energy spectra respectively, whereas error in predicted mean θ_z was under 5° for air gaps ≥ 10 cm. It is concluded that this algorithm is reasonably accurate for use in forward-projecting scattered photon fluence, mean energy, and mean θ_z , at air gaps of 10 cm or more. Furthermore, this algorithm's performance, in both speed and accuracy, is suitable for coupling with a detector-specific, dose prediction algorithm to be developed in the following two chapters.

CHAPTER FIVE[†]

A TWO-STEP ALGORITHM FOR PREDICTING PORTAL DOSE IMAGES IN ARBITRARY DETECTORS

5.1 Introduction

In chapter four, the accuracy and behavior of a two-dimensional, superposition algorithm for predicting scattered photon fluence into a portal imaging detector was investigated. It was established that this approach was accurate enough to warrant further study, specifically to find a method of converting predicted fluence to dose in the imaging detector. A method for taking the incident predicted photon fluence (both primary and scatter components) and using it to calculate the resulting dose deposited in a portal image detector system is presented in this chapter.

Film and electronic portal imaging systems have traditionally been used for geometric treatment verification. However, recent efforts [Es96; Fi93; Fi96; Ha96; Ha97; He95; Ki93; Ki95; Le86; Mc96a; Mc96b; Pa98a; Pa98b; Pa99d; Va92; Wo90a; Yi90; Zh95] have demonstrated their potential in a variety of dosimetric treatment verification applications. One important application involves the comparison of a theoretically predicted portal dose image with a portal dose image acquired during treatment [Wo90a], preferably in real time. Any discrepancy between the two images may indicate a treatment delivery error (e.g. incorrect patient positioning, beam modifier setup, dose

[†] Based on [Mc00c]

delivery, etc.). Once the error is identified, it may be corrected by interrupting the treatment (intratreatment approach), or correction of subsequent treatment fractions (intertreatment approach) [Sh96b]. A second related application is the subtraction of the calculated scatter dose component from a measured image, with a subsequent backprojection of fluence through the patient [Yi90; Ha96; Mc96a], which assumes the patient geometry has not changed since the initial CT simulation. The successful implementation of such applications hinges on the ability to accurately predict portal dose images.

Portal dose image prediction has been studied previously by several research groups, using a variety of approaches. The delta-volume algorithm was used [Wo90a] to predict portal dose images for a cobalt-60 beam, which were compared to measured images. Comparison was made at small air gaps, and it has subsequently been demonstrated that the delta-volume technique is not suitable for prediction at larger air gaps [Mc96b]. The superposition of Monte Carlo-generated, point-interaction dose kernels has been used for portal dose image prediction for a 6 MV beam over small air gaps (11-22 cm) using a water-equivalent detector [Mc96b]. Concerns involving scaling of the primary dose kernel for high atomic number materials and across larger air gaps [Wo90b] were not addressed, although some work on the former has been presented by Sauer [Sa95]. These issues are important, since many commercial portal imagers incorporate a high atomic number material as the dose detector. Meanwhile, other groups [Ha97; Pa98a] have examined pencil beam style algorithms (two-dimensional), which are attractive since they are inherently faster than three-dimensional superposition approaches. In-house Monte Carlo simulation software was used by Hansen *et al* [Ha97] to generate pencil beam scatter fluence kernels for a 6 MV photon beam, which allows

the removal of scatter from the portal dose images through an iterative deconvolution process, and an estimate of radiological thickness of the patient. Air gaps ranging from ~32-90 cm were examined in that work, but no attempt was made at converting the fluence into detector dose. This has been rectified recently, where an analytical approach was employed to convert to dose in a Compton recoil electron detector, and successful predictions at small air gaps were made [Sp00b]. In contrast, an experimental approach was taken by Pasma *et al* [Pa98a], which involved the derivation of scatter dose kernels from an extensive series of measurements for 6, 23, and 25 MV beams. These kernels are applicable only to a Philips SRI-100 electronic portal imaging system. The predicted images in that work were taken over a range of air gaps of ~40-60 cm.

When applied at larger air gaps or to small phantoms, the portal dose image contains very little scatter [Ja94; Mc00a], and consequently the accurate prediction of this component is not stringently necessary, nor challenging to the prediction algorithm. Although larger air gaps are typical for Elekta (formerly Philips) treatment machines, several commercial electronic portal imagers provide air gaps of less than 40 cm [Mu95; Sh96a], while portal film cassettes may be placed to achieve almost any air gap. Varian and Eliav offer variable source detector distances (SDDs). Theraview/Cablon offer SDDs of 135-165 cm, Siemens offers a fixed SDD of 140 cm resulting in air gaps of 10-35 cm. Due to these concerns, a prediction algorithm which can perform accurately over a wide range of air gaps is required. However, with the increased use of dynamic treatments and controlling of gantry motion from outside the treatment room, this concern may diminish in the future.

To circumvent these problems, an algorithm has been developed here, which is flexible enough to predict the dose deposition in virtually any portal imaging detector

(including high Z detectors), over a wide range of air gap, and using a wide range of beam energies. The algorithm is implemented in two steps: (i) primary and scattered photon fluence into the detector is predicted, and (ii) this fluence map is then converted to deposited dose. The first step is independent of the detector, whereas the second step is completely governed by the detector configuration. The separation of the dose calculation in this manner allows detailed Monte Carlo modeling of specific detectors to be performed, without affecting the fluence prediction. This gives the algorithm great adaptability, which is important due to the wide variety of portal imaging systems available (e.g. screen/film [Fi93; Va92], screen/camera [Mu95; Bo92], scintillation detector [Bo92], liquid ionization chambers [Mu95; Bo92], linear diode arrays [Bo92; Fi96], and amorphous silicon arrays [Mu95; Bo92]). The algorithm requires knowledge of the patient density (CT data), SDD, and incident beam fluence and energy spectrum. Pre-calculated, Monte Carlo-generated scatter fluence kernels (independent of the detector) and dose deposition kernels (characterizing the materials and geometry of a specific detector) are employed. The scatter fluence kernels are valid for polyenergetic incident beams, and need only be calculated once per incident energy spectrum. They have been shown to be highly independent of the exact details of the energy spectrum [Mc00a] and should therefore be independent of linear accelerator manufacturer. The dose deposition kernels need only be calculated once for any detector. As the algorithm predicts dose, it may be calibrated to treatment machine output, allowing quantitative comparisons of absolute measured and predicted dose images, not just qualitative comparisons of relative images.

The presented algorithm offers a fast (2D) approach, and is demonstrated to be accurate over small and large air gaps. This work extends previous studies which

examined the fluence prediction step [Mc00b] in detail. In this chapter, the dose conversion step of the algorithm is developed in detail, and the performance for a variety of phantoms, beam energies, and air gaps is compared with measurements using a linear array ionization chamber detector incorporating both low and high atomic number buildup materials.

5.2 Materials and Methods

5.2.1 Predicting fluence reaching the portal imager

The portal dose prediction algorithm is implemented in two steps. The first step involves calculating a map of photon fluence incident upon the portal image detector. Assuming an ideal point source, diverging rays are traced through a 3D computed tomography data set to the surface of the detector, along which the radiological pathlength is calculated using a fast technique [Si85]. The radiological pathlength is defined as the exact distance a rayline traverses through a 3D voxel multiplied by the electron density of the voxel, summed over all voxels encountered throughout the length of the rayline. Combined with a knowledge of the incident energy spectrum and a 2D map of relative incident fluence, this allows the primary fluence at the detector to be calculated per energy bin. The primary photon fluence spectrum at a point in the scoring plane is found as:

$$\frac{d\phi_p(\bar{r}, E)}{dE} = \frac{d\phi_0(\bar{r})}{dE} \cdot \exp(-\mu(E) \cdot t(\bar{r})) \cdot \left(\frac{f_0}{SDD}\right)^2 \cdot \cos(\theta) \quad (5.1)$$

where $x =$ x coordinate of incident photon beam

$y =$ y coordinate of incident photon beam

$x' =$ x coordinate in scoring plane

$y' =$ y coordinate in scoring plane

$\bar{r} =$ vector coplanar to scoring plane, representing (x, y) as projected into scoring plane

$\bar{r}' =$ vector coplanar to scoring plane, representing (x', y')

$E =$ photon energy

$\frac{d\phi_0(\bar{r})}{dE} =$ incident relative beam fluence spectrum

$t =$ radiological thickness (ie. equivalent thickness of homogeneous water) of patient along diverging ray line through (x, y)

$\mu =$ linear attenuation coefficient for water

$f_0 =$ distance between source of primary photons and measurement surface where incident beam fluence distribution was acquired

SDD = source to detector distance

$\theta =$ angle between central axis ray line and line joining source and (x', y')

The four terms in equation 5.1 signify the incident beam fluence spectrum, exponential attenuation, inverse square fall off (due to divergence from a point source), and a term to convert to planar fluence, respectively. Recall that by definition, the total primary fluence at a scoring voxel, $\phi_p(\bar{r})$, may be found by summing contributions over all energy:

$$\phi_p(\bar{r}) = \int \frac{d\phi_p(\bar{r}, E)}{dE} dE \quad (5.2)$$

The incident energy spectra used here are obtained from Monte Carlo simulation [Mo85a] (with the 24 MV spectrum of that work being truncated to 23 MV) and rebinned into eight energy divisions. The 2D maps of relative incident fluence are measured using a scanning ionization chamber with appropriate brass buildup cap, to remove contaminant electrons.

The fluence and associated mean energies of scattered photons entering the detector are calculated using 2D scatter fluence kernels. These radially symmetric

kernels are generated using the EGS4 Monte Carlo radiation transport code [Ne85]. Each kernel represents the scatter fluence response at a given distance (air gap) behind a homogeneous slab of water, due to an incident pencil beam of photons. These kernels have been generated for a range of slab thicknesses (1-50 cm) and air gaps (0-100 cm). The associated mean energies of the scattered photon fluence were also scored. A description of the creation and analysis of these scattered photon fluence kernels is presented elsewhere [Mc00a] as well as in chapter three of this work. A superposition of appropriate scatter kernels with the incident beam fluence map allows the prediction of fluence and mean of mean energies of the scattered photons entering the detector, as described below.

Before the scatter calculation occurs, the patient density data are converted to an equivalent homogeneous phantom (EHP) as introduced by Pasma *et al* [Pa98a]. The conversion consists of replacing the original CT voxel data with the radiological pathlength data, along diverging raylines. The radiological pathlength data (which may be interpreted as the water-equivalent thickness along a ray line) is shifted along the rayline to maintain the position of the original centre of mass. A new air gap distance is calculated, representing the exit surface to detector surface along the diverging ray line. A grid of pencil beams is then transported through the patient, where the EHP thickness and air gap determine the scatter kernel chosen for a particular point, and the resulting fluence contribution is weighted by the appropriate relative fluence of the incident beam. The scatter fluence and the mean of mean energies calculations are described in section 4.2.3. Note that a single scattered fluence value and mean of mean energies value is obtained for each scoring voxel, and therefore this scattered fluence calculation approach will be termed the 'monoenergetic' approach. However, the calculation may be modified

to provide a distribution of scattered fluence and mean energies, by tracking individual scatter fluence and mean energy contributions to a scoring voxel from all transported pencil beams. For *each* transported pencil beam, the fluence and mean energy contributions of scattered photons to a scoring voxel at \bar{r}' are given by

$\phi_0(\bar{r}) \cdot K_\phi(t(\bar{r}), g(\bar{r}), |\bar{r} - \bar{r}'|)$ and $K_{\bar{E}}(t(\bar{r}), g(\bar{r}), |\bar{r} - \bar{r}'|)$, where the variables are the same as in section 4.2.3. This tracking results in a set of $\{\phi_s, \bar{E}\}$, which afterwards may be binned into n discrete energy bins of width 2α via the summation

$\sum_{i=0}^n \sum_{\bar{E}_i - \alpha}^{\bar{E}_i + \alpha} \phi_s$, which yields the discrete distribution representing $\frac{d\phi_s(\bar{r}')}{d\bar{E}}$. For this

distribution, the sum over mean energies results in $\phi_s(\bar{r}') = \int \frac{d\phi_s(\bar{r}')}{d\bar{E}} d\bar{E}$. Since this

technique produces a distribution of scattered fluence and associated mean energies, it is called the pseudo-polyenergetic approach.

The resolution of the grid for all calculations in this chapter is chosen to be 0.5 cm. A study of the factors affecting the accuracy of predicting the magnitude and quality of scattered photon fluence using this technique has been performed [chapter four; Mc00b] and 0.5 cm was found to be a good choice to ensure accuracy and maintain speed. Currently, the algorithm does *not* account for electron fluence into the portal image detector, which may originate at the exit side of the patient. This electron fluence will be exiting with an angular spread due to scattering interactions within the patient as well as beam divergence, and will therefore decrease rapidly with air gap. Electrons which reach the detector will in most cases be absorbed in a buildup layer of the image detector, which is thicker than the range of the most energetic electron. Therefore, for a properly designed detector, patient-generated electrons will not produce image signal.

5.2.2 Converting fluence to dose in the detector

The predicted fluence entering the detector is used to generate a dose map. This step requires pre-calculated dose deposition kernels unique to a specific detector configuration (see Figure 5.1). These are generated using EGS4 [Ne85] and user code DOSRZ. For a given detector, a radially symmetric dose pattern is scored due to a perpendicularly incident, monoenergetic photon pencil beam. The dose kernel is scored in the material layer which generates the portal image signal (ie. not the buildup or other surrounding material), and kernels are calculated for a range of incident energies (0.1-0.6 in steps of 0.1, 0.8, 1.0, 1.25, 1.5, 2.0-6.0 in steps of 1.0, 8.0, 10.0-24.0 in steps of 2.0; units of MeV). The simulation parameters ECUT and PCUT are set to 0.516 MeV and 0.005 MeV for all simulations in this chapter. Resulting statistical errors in the scored dose kernels are $\pm 1.2\%$, averaged over all incident energies and radial bins, and do not exceed $\pm 5\%$ for any individual bin. To find the primary dose image, dose kernels are convolved with the primary fluence for each scored energy bin, then summed together for the total dose deposited due to primary photons. This process may be written as:

$$D_p(\bar{r}') = \iiint \frac{d\phi_p(\bar{r}', E)}{dE} \cdot K_D(|\bar{r} - \bar{r}'|, E) d^2\bar{r} dE \quad (5.3)$$

where: $x =$ x coordinate of incident photon beam

$y =$ y coordinate of incident photon beam

$x' =$ x coordinate in scoring plane

$y' =$ y coordinate in scoring plane

$\bar{r} =$ vector coplanar to scoring plane, representing (x, y) as projected into scoring plane

$\bar{r}' =$ vector coplanar to scoring plane, representing (x', y')

$E =$ photon energy

$\frac{d\phi_p(\bar{r}')}{dE} =$ primary fluence spectrum

$K_D =$ radially symmetric dose kernel for a specific detector, for an incident pencil beam of photons of energy E , per incident photon

$D_p =$ dose deposited in the detector layer due to primary photons

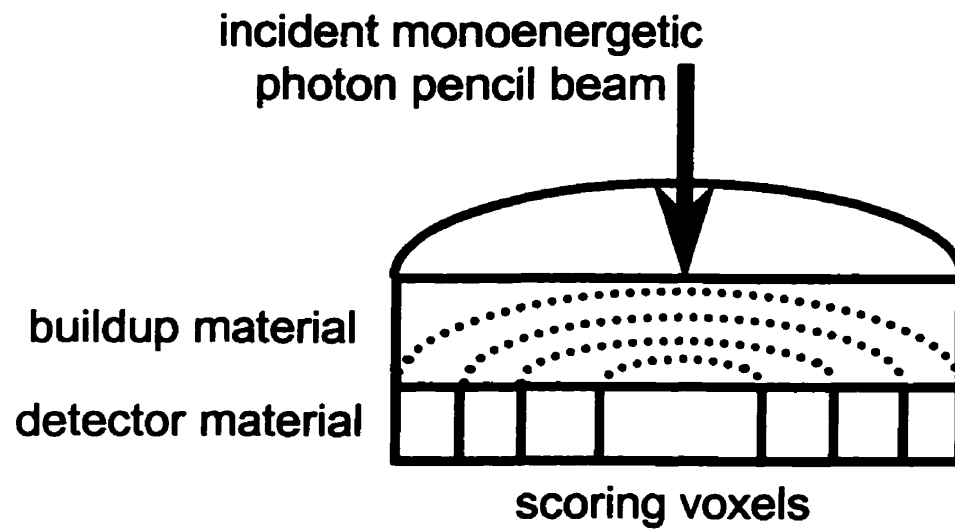


Figure 5.1: Cross section illustrating geometry of dose kernels for a portal imaging detector consisting of two layers of material.

Since the energy spectrum of the scatter fluence is not known exactly, the method for converting the primary fluence to dose cannot be applied to the scatter fluence. The dose image for the scattered fluence is found by employing the reciprocity theorem. The reciprocity theorem is used here to relate the scored dose kernels to incident scatter fluence. The dose deposited at a point in the detector due to an incident small photon beam (of area $1 \times 1 \text{ cm}^2$) is approximately the same as that contained in the dose kernel integrated over the dimensions of the scatter scoring voxel ($1 \times 1 \text{ cm}^2$). Performed for all incident photon energies, the result is a function converting incident fluence to dose (C_s), as:

$$C_s(E) = 8 \int_{\theta=0}^{\frac{\pi}{4}} \int_{r=0}^{\frac{s}{2 \cos \theta}} K_D(|\vec{r}'|, E) \cdot r \cdot dr d\theta \quad (5.4)$$

where the integration is performed in cylindrical coordinates over the square bounds of the scoring voxel of side s ($=1 \text{ cm}$ in this work). The factor of eight comes from the 8-fold symmetry of the square, and therefore integration over only one-quarter of a quadrant is required. This function may be employed using either the monoenergetic or pseudo-polyenergetic scatter fluences described in section 5.2.1. In the monoenergetic approach, the dose due to scattered photons (D_s) is calculated as

$$D_s(\vec{r}') = C_s(\bar{E}(\vec{r}')) \cdot \phi_s(\vec{r}') \quad (5.5)$$

whereas the pseudo-polyenergetic method calculates scattered photon dose as

$$D_s(\vec{r}') = \int C_s(\bar{E}(\vec{r}')) \cdot \frac{d\phi_s(\vec{r}', \vec{E})}{d\bar{E}} d\bar{E} \quad (5.6)$$

In this chapter, the pseudo-polyenergetic approach is used, since it offers increased accuracy due to sampling over more energies than the monoenergetic method.

When converting fluence to dose, the primary and scatter fluence are assumed to be perpendicularly incident upon the detector. The primary will not be highly oblique (ie. ~8 degrees at the corner of a 20×20 cm² field at isocentre) and while the scatter fluence may demonstrate significantly oblique angles at very short air gaps, the magnitude of contribution to total dose will be dominated by the primary. Establishing electronic equilibrium in the detector layer of the imaging device will reduce the effect of this error by moving the rapidly changing buildup region above the detector layer, which will then lie within the slowly decreasing region of the depth dose curve. In the comparisons presented in this chapter, no significant error (>3%) has been observed due to the assumption of perpendicular incidence.

5.2.3 Off-axis spectrum softening

The portal dose prediction algorithm is flexible, allowing complex models representing the fluence distributions exiting the radiotherapy treatment unit head to be incorporated (for example, those resulting from BEAM [Ro95] simulations). A simple approach is demonstrated here by including the influence of the flattening filter on the primary energy fluence spectrum. Position (relative to the target), dimensions, and material of the flattening filters for the 6 MV and 23 MV beams were required. The raytracing algorithm was used to generate files containing data representing the pathlength through the flattening filters between an ideal point source and isocentre, and only need to be generated once. The pathlength information is used to modify the weighting of each energy bin of the original (on-axis) primary fluence spectrum. No

significant increase in algorithm execution time was observed when incorporating this feature.

5.2.4 Experimental validation

The algorithm output was compared to measured data behind a 29 cm thick simple polymethylmethacrylate (PMMA) slab phantom, a simple square cork inhomogeneity ($10 \times 10 \times 10 \text{ cm}^3$) in a 19 cm thick PMMA slab, and an anthropomorphic phantom (PIXY Alderson Phantom, Radiology Support Devices Inc., Long Beach, CA) Photon beams with nominal energies of 6 MV and 23 MV were used, for two treatment sites on the anthropomorphic phantom (lung and pelvis, respectively). A range of air gaps (10-80 cm) was examined. CT data for the anthropomorphic phantom were collected on a Siemens Somatom 4 Plus, and converted from original attenuation units (known as Hounsfield units or HU) to electron density information using $\rho_e = 0.001 * \text{HU}$ for $\text{HU} \leq 100$ and $\rho_e = 0.0005695 * \text{HU} + 0.44501$ for $\text{HU} > 100$, based on linear fits to measured data and work by Battista [Ba80]. Incident field fluence data were measured using a scanning ionization chamber (PTW corp.) with a brass buildup cap. A linear array of 47 fluid filled ionization chambers (LA48 from PTW Corporation, Freiburg, Germany) was utilized as the portal image detection device, allowing a profile to be collected in ~ 1.5 seconds. Profiles were taken in the cross-plane axis, aligned with isocentre, and are normalized to the maximum dose point within the profile. For the simple cork inhomogeneity phantom, additional profiles were taken parallel to these, at 5 cm off-axis (backprojected to isocentre) to lie underneath the cork. For the anthropomorphic phantom measurements,

two different configurations were used, one with PMMA buildup (3.5 cm), and the other with brass buildup (0.2 cm), while only the PMMA buildup detector was used in the simpler phantoms. The use of two different detectors allows the investigation of the accuracy of the dose deposition kernels when a high atomic number material is used in the detector configuration.

Although the LA48 has a manufacturer-specified error of $\pm 1\%$, an independent error estimate was obtained by setting up, acquiring a profile, then taking down the detector five times at a single SSD (130 cm). This was performed for both treatment sites, using both detector configurations, and allows the variation of the measured profiles to be estimated (see results in section 5.3.3).

5.3 Results and Discussion

5.3.1 Dose kernels

The dose kernels generated for a specific detector configuration allow an estimate of detector response to be made. By integrating the energy deposited in the detector layer over all radii, an estimate of total energy deposited is obtained for a specific incident photon energy. The results of this integration are presented in Figure 5.2 for eight detectors. Three of the detectors were chosen for comparison to previously published results, including a high resolution storage phosphor, a standard storage phosphor with 0.8 mm lead buildup, and a Kodak X-omat film sandwiched between two 0.8 mm lead plates. The response functions for these detectors have been estimated with Monte Carlo simulation and verified with experiment [Ba87; Ba91], and compare well with those estimated here using EGS4. The other detectors presented represent an LA48 array with 3.5 cm of PMMA buildup, an LA48 array with 0.2 cm brass buildup, the Philips SRI-100 metal/phosphor detector with an extra 0.1 cm steel buildup plate [Pa98a], and the Siemens Beamview^{Plus} metal/phosphor detector. These four response functions compare well with similar systems presented by Jaffray [Ja94], where the LA48 configurations used here approximate Compton detectors (ie. where signal is generated due only to Compton recoil electrons). Compared to the Compton detector approximations, the relative increase in the metal/phosphor detector response at low energies demonstrates greater sensitivity to low energy scattered photon fluence. The pseudo-polyenergetic approach of taking several samples from across the scatter energy fluence spectrum has a significant effect for high Z detectors (see Figure 5.3) due to their complex response at

low energies, and should provide increased accuracy over an approach based on selection of a single monoenergetic kernel.

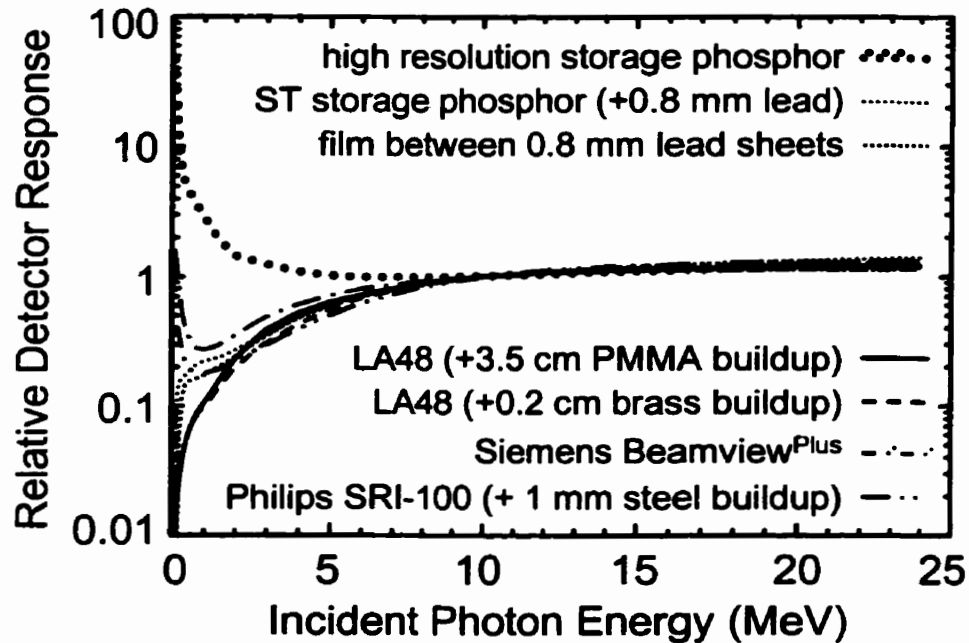


Figure 5.2: Detector response (normalized at 10 MeV) for eight portal imaging detectors obtained by integrating energy deposited over entire detection layer. Detectors include a high resolution storage phosphor [Ba91], ST storage phosphor with 0.8 mm lead buildup [Ba91], film sandwiched between two 0.8 mm lead sheets [Ba87], linear array (LA48) with 3.5 cm PMMA buildup, LA48 with 0.2 cm brass buildup, Siemens Beamview^{Plus} detector, and a Philips SRI-100 with an additional 0.1 cm of steel buildup [Pa98a].

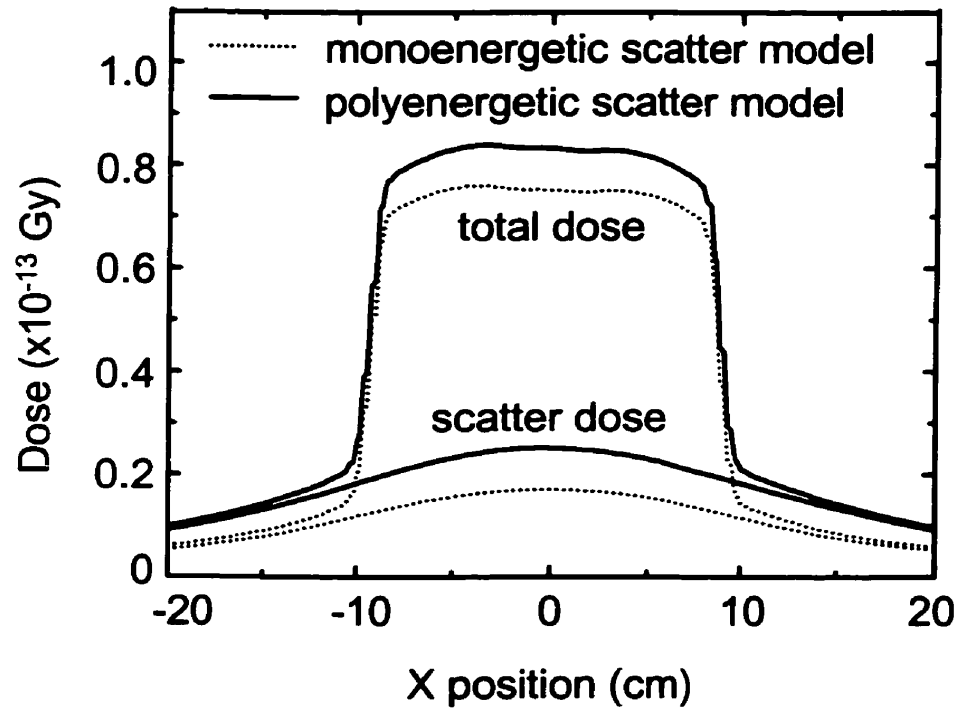


Figure 5.3: Difference between monoenergetic and pseudo-polyenergetic approach for modeling scatter dose kernels illustrated with the metal/phosphor Beamview^{Plus} detector, for a slab of PMMA, 15×15 cm², 6 MV field, at 20 cm air gap.

5.3.2 Effects of the flattening filter

Including the effects of the flattening filter on the primary energy fluence results in a significant improvement in the agreement between measured and predicted dose profiles, as demonstrated in Figure 5.4. The off-axis softening of the primary spectrum due to a decreasing pathlength through the flattening filter results in a lower predicted dose profile with increasing off-axis radius when compared to predicted profiles without the flattening filter modeled. Profiles in Figure 5.4 are for a large air gap in order to reduce the scatter dose to a small, flat contribution. Modeling of the treatment head may be easily incorporated into the flexible portal dose prediction algorithm, and this comparison demonstrates its potential importance.

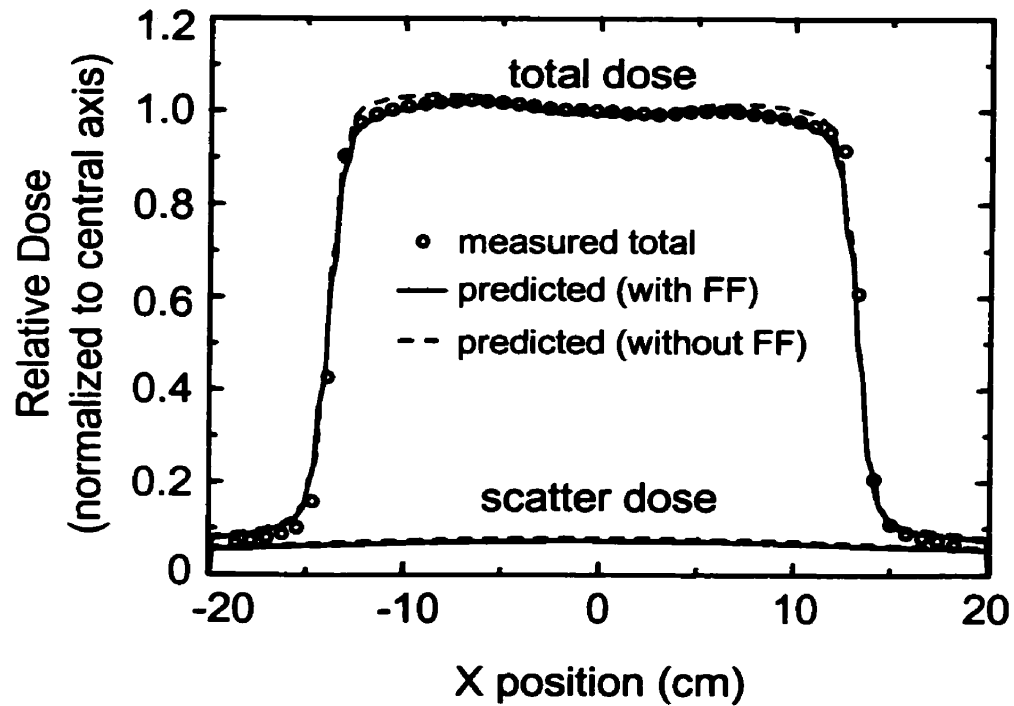


Figure 5.4: Demonstration of improvement in comparison with measured data obtained by modeling primary energy fluence hardening through the flattening filter (FF). Data is acquired using an incident 6 MV, $15 \times 15 \text{ cm}^2$ field, with the LA48 detector with PMMA buildup, 29 cm thick PMMA slab phantom, at an air gap of 80 cm. Comparison is done at large air gap to reduce the scatter dose contribution to a small uniform value.

5.3.3 Experimental validation of portal dose prediction algorithm

Predicted portal dose images for each phantom at a 10 cm air gap are illustrated in Figure 5.5. Predicted and measured profiles in the cross plane (or x direction) are presented for the simple slab phantom, the simple lung phantom, and for the anthropomorphic phantom (both 6 MV lung and 23 MV pelvis sites) in Figure 5.6. The data presented for small air gaps of 10 cm demonstrates the algorithms' ability to accurately handle scatter fluence and scatter dose prediction, even when this component is a significant fraction of total dose. The error estimated (as described in section 5.2.4) for the measured values is $\pm 1.3\%$, which is within the symbol size. Analysis of comparisons for each individual phantom has been performed in accordance with recommendations of Van Dyk *et al* [Va93]. Data points are separated into three categories: relative dose $< 7\%$ and dose gradient $< 30\%/cm$, relative dose $> 7\%$ and dose gradient $< 30\%/cm$, and dose gradient $> 30\%/cm$. For the first two categories, histograms of the percent differences are presented, whereas for the third category, histograms of the isodose line separation are presented. Dose gradients were calculated as the maximum gradient around a dose point, whereas the isodose line separations were estimated as the deviation between measured and predicted relative dose values divided by the gradient [Mc96b]. This analysis is presented in Figure 5.7. In situations of large scatter fraction (simple slab phantom), a systematic overestimate of scatter dose may be observed. This is at least partially attributable to the systematic overestimation of the multiply-scattered photon fluence component by the fluence prediction portion of the algorithm [Chapter Four and Mc00b]. In future versions of the algorithm, this effect may be reduced by

regenerating the scatter fluence kernels in phantoms with finite lateral dimension, or by an empirical correction based on the lateral extent of the phantom.

Combining all data points for all phantoms, detectors, and air gaps, approximately 96.5% of the data points in low dose gradient regions (N=1682) compare to within 3% of maximum relative dose, and 98.5% of the data points in high dose gradient regions (N=198) are within 4 mm. This quality of performance is within the current recommendations governing treatment planning algorithms [AA98]. With the movement towards clinical implementation of 'step and shoot' and dynamic treatments, algorithm speed becomes an increasingly important issue, due to the increased number of beam deliveries. The total time to calculate a portal dose image at a $1 \times 1 \text{ mm}^2$ resolution over a $40 \times 40 \text{ cm}^2$ scoring plane takes <3 minutes on a Pentium PIII-450 MHz computer when coded in the Interactive Data Language programming environment (Research Systems Inc., Boulder, CO).

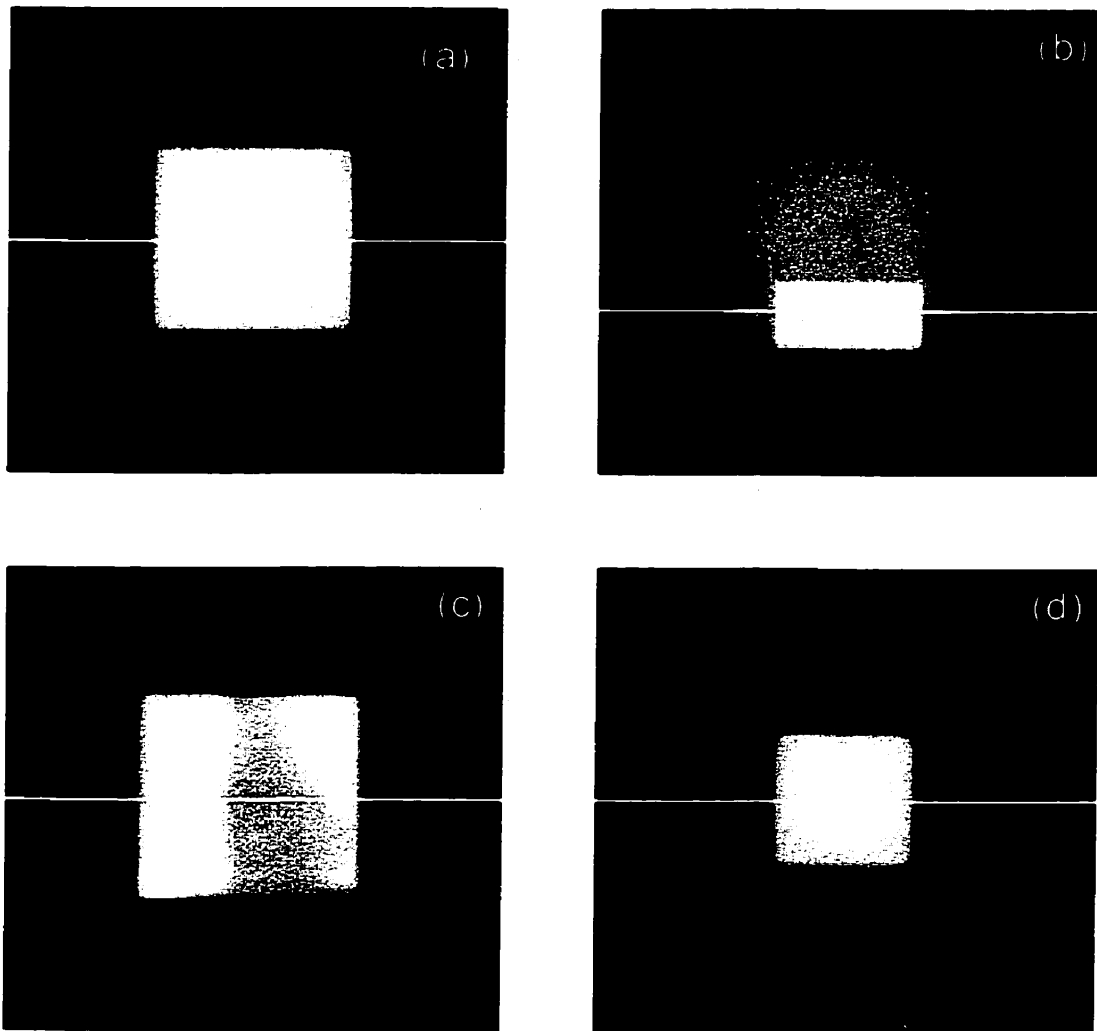


Figure 5.5: Predicted total portal dose images at 10 cm air gap behind a slab phantom (a), a simple lung phantom (b), thorax of anthropomorphic phantom (c), pelvis of anthropomorphic phantom (d). Beam energy and field size are 6 MV, $15 \times 15 \text{ cm}^2$ for (a), (b), and (c), and 23 MV, $10 \times 10 \text{ cm}^2$ for (d). Position of measured profiles presented in Figure 5.6 corresponds to horizontal white lines.

(OVERLEAF) Figure 5.6: Sample predicted and measured profiles behind all phantoms tested here. Beam energy and field size are 6 MV, 15×15 cm² for (a), (b), and (c), and 23 MV, 10×10 cm² for (d). Both small and large air gaps are demonstrated (with normalization performed to maximum point of total dose at small air gap, to keep relative magnitudes at different air gaps preserved). Calculated scatter dose is also illustrated. Detector configurations are LA48 with PMMA buildup in (a) and (b), and LA48 with brass buildup in (c) and (d). Error in the measured data points is estimated at ±1.3% (see section 5.2.4 for explanation).

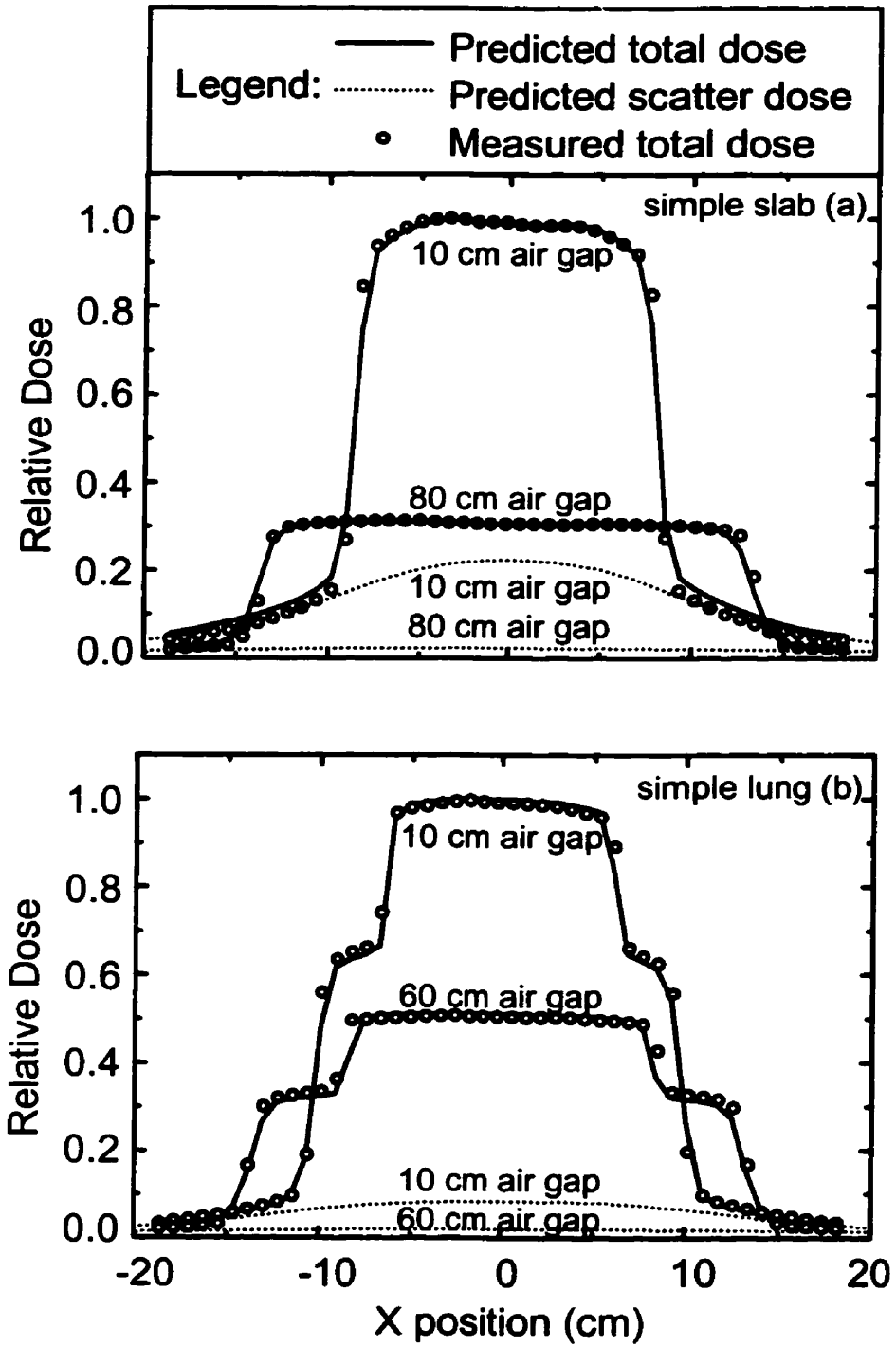
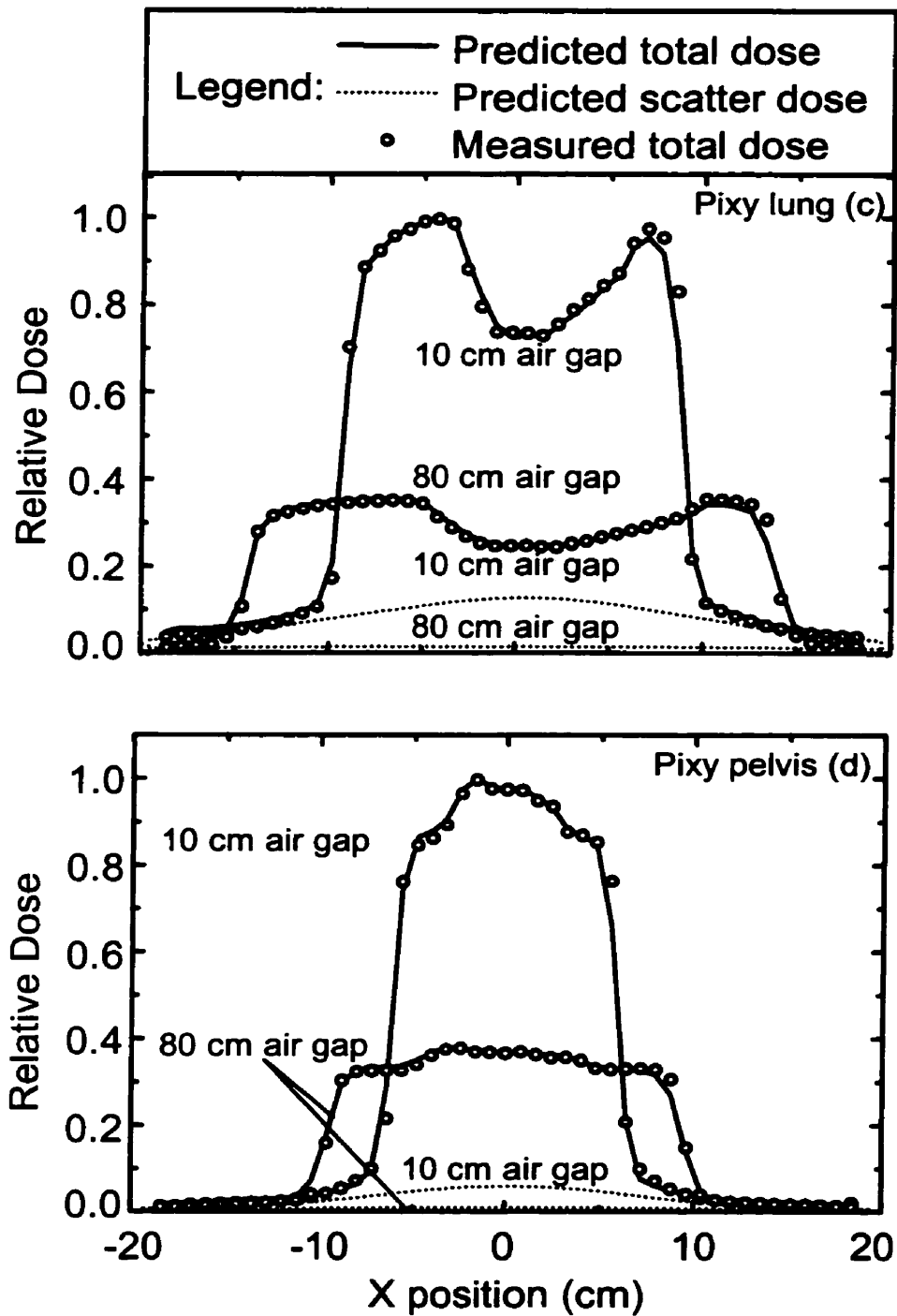


Figure 5.6 continued on next page...

Figure 5.6 continued...



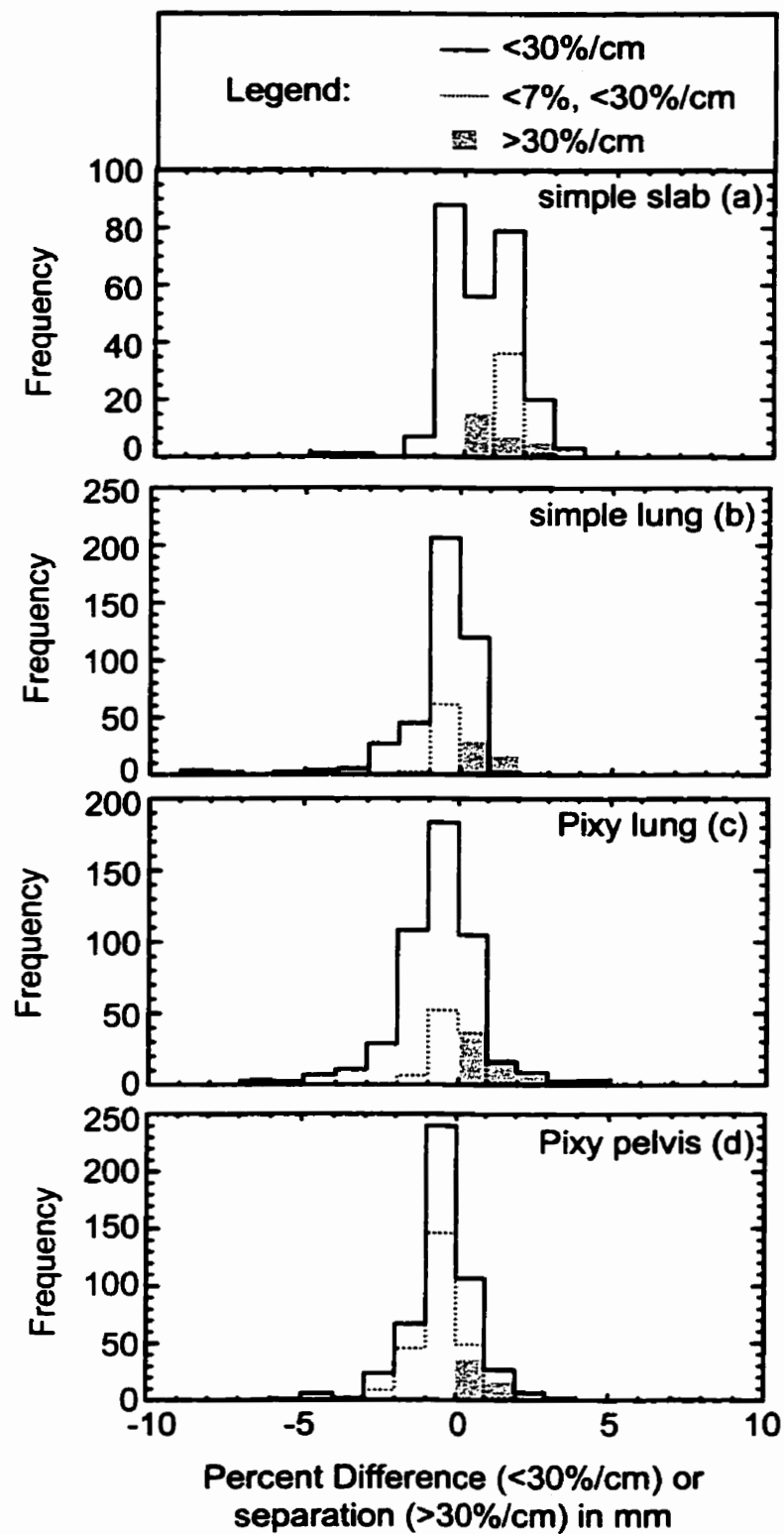


Figure 5.7: Analysis of measured and predicted total dose comparison, using categories proposed by Van Dyk *et al* [Va93].

5.4 Discussion and Conclusions

An algorithm has been presented which predicts portal dose images.

Implementation involves first predicting the primary and scattered photon fluence into a detector, then predicting the dose response of the detector. The algorithm utilizes pre-calculated libraries of scatter fluence kernels and dose deposition kernels, which are obtained through Monte Carlo radiation transport techniques. The algorithm is fast, allows a separation of primary and scatter, and can model arbitrary detector materials. The algorithm may take advantage of energy fluence modeling of the radiotherapy treatment heads. The ability to incorporate easily the effect of the flattening filters on the primary energy fluence spectrum was demonstrated. The pencil beam dose kernels for several detector configurations were analysed to produce detector response curves. The accuracy of the algorithm was investigated for 6 MV and 23 MV beams over air gaps of 10-80 cm for a PMMA slab phantom, a PMMA slab with a cork inhomogeneity, and an anthropomorphic phantom. Two different detector configurations were used, involving low and high atomic number buildup material. For dose gradients $<30\%/cm$, the difference between 96.5% of predicted and measured dose points is within 3%. For higher dose gradient regions, penumbras are within 4 mm. This level of accuracy is within the guidelines set out for treatment planning dose calculation algorithms [AA98]. It is concluded that this approach represents a fast, accurate, and flexible solution to portal dose image prediction.

The presented method compares favourably with existing portal dose image prediction techniques [Pa98a; Mc00b] in terms of accuracy ($<3\%$). Being a two-dimensional approach, it is also simple to implement and quick to execute (inherently

faster than any full three-dimensional technique). The separation of the fluence calculation from the dose calculation provides the algorithm with a great deal of flexibility, allowing the dose response of arbitrary portal image detectors to be modeled accurately via Monte Carlo techniques. In chapter three [Mc00a], the scatter fluence kernels have been shown to be nearly independent of the details of the energy spectrum of the incident beam, and therefore should be widely applicable for most commercial linear accelerator units. The dose kernels for any portal image detector may be easily generated with a basic understanding of EGS4 and detector specifications of materials, thicknesses, and densities. Once generated, both the fluence and dose kernel libraries do not need to be calculated again. The next chapter presents a validation of the algorithm on a high atomic number portal imaging device.

CHAPTER SIX

DOSIMETRIC INVESTIGATION AND PORTAL DOSE IMAGE PREDICTION USING AN AMORPHOUS SILICON ELECTRONIC PORTAL IMAGING DEVICE

6.1 Introduction

The previous chapter presented a two-step algorithm for predicting portal dose images, and verified the performance using a low atomic number detector. To establish the validity of the algorithm on a detector system more representative of those available clinically, including multiple thin layers and a high atomic number dose detection layer, the algorithm was tested using a state-of-the-art amorphous silicon imaging device. Chapter six not only presents this validation, but also examines some of the basic dosimetric properties of the detector system.

Geometric treatment verification of external beam radiation therapy portals is crucial to ensure proper target coverage and normal tissue avoidance. Most often verification is performed through the use of radiographic film or electronic portal imaging devices (EPIDs). Over the last several years, much effort has been devoted to expand the use of megavoltage imaging to include dosimetric applications [Le86, Wo90a, Yi90, Ha96, Ha97, Ki95, Ki93, He95, Pa98a, Pa98b, Es96, Zh95, Fi93, Va92, Fi96, Mc96a, Mc96b, Kr98, Mc00c, Bo97a, Bo97b, Bo98a, Bo98b], with the ultimate purpose of dosimetric treatment verification. A simple, yet effective application discussed by

Leong *et al.* [Le86], Wong *et al.* [Wo90a], and more recently demonstrated by Kroonwijk *et al.* [Kr98], consists of a direct and real-time comparison of a measured portal dose image with a theoretically predicted portal dose image. Discrepancies between the measured and predicted image indicate treatment delivery errors, which may be corrected once identified. This is such a powerful application that Leong [Le86] suggests the potential for 'total elimination of procedural errors in the delivery of radiation'. Ideally the comparison step would be fully computerized using artificial intelligence software and performed within the first few monitor units delivered in a treatment fraction.

Another dosimetric treatment verification application of EPIDs involves the removal of scatter from the measured portal image, then backprojecting the remaining primary component through the patient CT data set which allows a calculation of deposited dose in the patient [Ha96, Mc96a]. Others have used simpler approaches to relate measured portal images with patient mid-plane and/or exit dose estimates [Ki95, Ki93, Es96, Fi93, Fi96, Va92, Bo97a, Bo97b, Bo98a, Bo98b], but still require separate primary and scatter estimates in the portal image. Megavoltage CT imaging is also a related application since it greatly benefits from the removal of the predicted scatter component from the measured image [Sp00a].

In chapter five, a two-step algorithm for predicting portal dose images in arbitrary detector systems was proposed and verified using a low atomic number detector system [Mc00c]. This flexible algorithm separately models the photon fluence through the patient and the dose deposited within the detector system. The fluence calculation involves geometric ray tracing to calculate the primary fluence entering the detector and a 2D convolution between the incident treatment beam fluence and pencil beam fluence

kernels representing the behavior of the scattered photons. The scattered fluence kernels are calculated using Monte Carlo techniques and take a large amount of computational effort to generate, but need only be calculated once. It has been demonstrated that these scattered fluence kernels are not strongly dependent upon the details of the incident photon spectrum used to generate them [Mc00a]. The predicted fluence is then convolved with dose kernels that are specific to a particular detector system. Each detector system has a unique set of dose kernels, which may be generated with an elementary knowledge of the freely available EGS4 package [Ne85] and user code DOSRZ [Ma95]. The dose kernels are generated for a range of monoenergetic photon energies using Monte Carlo methods, providing the algorithm with many exciting features. For example, variations in energy response are accurately accounted for, dose deposition in any type of material (low or high atomic number) is modelled, electronic disequilibrium in thin, multi-layered detector systems is modelled, and self scatter contributions from the detector system itself are included.

The algorithm was shown to predict measured data within $\pm 3\%$ for a variety of phantoms, air gaps, beam energies, and two different detector configurations [Mc00c]. However, the algorithm was not directly verified on a high atomic number detector system. Due to the widespread use of metal screen/phosphor based detectors, and the recent commercial availability of next-generation flat panel, amorphous silicon detectors (which may also incorporate metal screen/phosphor detector layers), a rigorous validation of the algorithm on this type of detector is of great interest. In this chapter, the portal dose image algorithm is refined and validated against measurements made with the indirect detection PortalVision aS500 amorphous silicon flat panel imager (Varian

Medical Systems, Palo Alto, CA). The term ‘indirect’ implies that the photodiodes have an overlying metal/phosphor layer, which converts the incident radiation to optical photons that are subsequently detected by the amorphous silicon array producing the image signal [El99]. Some basic dosimetric characteristics of the aS500 imager are also investigated here, including linearity of response with dose rate and frame acquisition, and response with varying source to detector distance (SDD). The collected data reveal that a significant amount of optical photon spread occurs within the phosphor layer of the detector. This phenomenon is known as ‘glare’ and has been previously identified as a major effect in camera-based metal screen/phosphor detectors, which also allow additional optical photon scattering from components such as mirrors and camera lenses [He95, Mu95]. The presence of glare in amorphous silicon EPIDs implies some difficulty for dosimetric applications using these systems. It is demonstrated that the effect may be accounted for by using a radially symmetric glare kernel to model the optical photon spread. The invariant kernel is derived from collected data and, when applied to predicted dose images, substantially improves comparison with measurement. The finding of a substantial contribution of glare to the amorphous silicon EPID images here is in contrast with previous work [Mu98a] which indicate that this effect is insignificant for indirect detection flat panel detectors. This apparent contradiction is explained in section 6.3.1.3.

6.2 Materials and Methods

6.2.1 Flat panel detector characteristics

6.2.1.1 Detector description

The aS500 detector consists of a metal plate (1 mm copper) overlying a scintillating layer of phosphor (~0.5 mm) which converts incident radiation into optical photons. The generated light image is sensed by an array of photodiodes directly adhered to an amorphous silicon panel. Each pixel on the amorphous silicon panel consists of a light sensitive photodiode and a thin film transistor. The photodiodes are semiconductor light sensors that generate a current or voltage when the P-N junction in the semiconductor is illuminated by light [Ha95]. These behave like capacitors, since incident light is integrated and captured as an electric charge. The thin film transistor acts as a switch to control the signal readout, which is digitized through a 14 bit analog to digital converter. The sensitive area of the aS500 detector is $\sim 40 \times 30 \text{ cm}^2$, with a pixel size of $0.784 \times 0.784 \text{ cm}^2$ resulting in an image size of 512×384 pixels. The detector used in this work is mounted on a Varian 2100EX dual energy (6 and 18 MV) linear accelerator and has a thickness of 4 cm, a mass of 7 kg, and is mounted on a retractable arm which allows variable SDDs.

Flat panel detectors have been divided into two classifications [El99] called “direct” and “indirect” configurations. The indirect configuration employs a scintillator screen to convert deposited radiation energy to optical photons for readout. This is in contrast to the “direct” configuration, where no scintillator is used and the photodiode

array directly senses the radiation energy. While direct flat panel detectors have been shown to possess a radiation response similar to that of an ionization chamber, their sensitivity to incident radiation is lower by at least a factor of 10 when compared to indirect detectors [El99]. El-Mohri *et al* [El99] argue that the difference in sensitivity is due to the reduced gain offered by the photodiodes in the direct detection compared to that offered by the phosphor layer of the indirect detection. Therefore, a great sensitivity advantage is gained if indirect detection configurations are used for dosimetric applications.

6.2.1.2 Energy response

The portal dose calculation algorithm requires a set of dose kernels which score the dose deposited in the detector layer (phosphor) due to an incident pencil beam of monoenergetic photons. As described in section 6.2.2, EGS4 with usercode DOSRZ was employed to generate this set of dose kernels. This approach has previously been shown to yield accurate results, and has been verified [Chapter Five and Mc00c] against published data available on several detector configurations by calculating detector response functions. A detector response function is computed by integrating the deposited energy of the scored dose kernel over all radii, for each incident photon energy.

In the clinical configuration of the detector, the thickness of the overlying metal plate is insufficient to provide electronic equilibrium in the phosphor layer. This is of concern, since the image will be more susceptible to secondary electrons generated within the patient, which may increase image noise and reduce subject contrast. Furthermore, the overlying layer of metal serves to attenuate preferentially lower energy

photons (ie. a disproportionate amount of scatter) and therefore improve image quality by increasing the primary to scatter ratio. With the water equivalent thickness of the metal plate and other overlying materials being approximately 1 cm, the concern is significant when using the higher energy 18 MV photon beam. To investigate the consequence of this lack of buildup, images were gathered with the aS500 EPID in two different configurations. The first configuration (configuration 'A') was the standard clinical situation with no additional buildup, whereas the second configuration (configuration 'B') added a 3.0 cm slab of solid water equivalent material directly on the top surface of the EPID. Note that the collision touch detection guard was removed to make this possible. The response of a water-equivalent detector was also calculated for comparison. The water-equivalent detector was defined as a 20 cm diameter cylinder of water with a thickness of 40 cm and with a detector layer defined between 3.3 and 3.6 cm below the surface.

The user code DOSRZ separately scores dose from scattered photons, thus allowing an investigation into the importance of this portion of the total detector signal. Self-generated scatter contributions as a percentage of total signal were examined for the aS500 in both A and B configurations, and for the water-equivalent detector.

Kausch *et al.* [Ka99] used Monte Carlo modeling of both radiation and optical photon transport within metal/phosphor detectors. An interesting result was the strong dependence of the escape probability on depth of an optical photon generated in the phosphor (and therefore on where the radiation dose is deposited). Due to this result, the phosphor layer in the aS500 detector was split into three equal phosphor thicknesses for the Monte Carlo simulations in this work. This allows an investigation into the

dependence of the detector response on the relative depth in the phosphor. However, since the findings of Kausch *et al.* [Ka99] indicated that optical photons created in the deepest layer (closest to the exit side) of the phosphor had the highest escape probability, the dose kernels generated in the exit layer of the phosphor are used for portal dose image prediction in this chapter.

6.2.1.3 Linearity

The linearity of the detector response to incident radiation was investigated with two experiments. Linearity with respect to the number of acquired frames (which are then averaged into a single image) was examined using images acquired with 1-10 and 100 frames. The linear accelerator (linac) was configured for a fixed $15 \times 15 \text{ cm}^2$ open field with gantry at 0° , and the detector was positioned at 150 cm SDD. The pixel average and standard deviation over a $\sim 1 \text{ cm}^2$ (13×13 pixels) region of interest (ROI) at field centre were recorded and used as the signal and error estimate, respectively.

Linearity with respect to dose rate was explored by acquiring constant frame averaged images (10 frames) and varying the dose rate of the linear accelerator from 100 to 600 MU/min in steps of 100 MU/min. The linac was configured for a fixed $15 \times 15 \text{ cm}^2$ open field with gantry at 0° , and the detector was positioned at 150 cm SDD. Two 13×13 pixel regions of interest were examined, one inside and one outside the field. One region was aligned to the field centre, the other was placed $\sim 4.3 \text{ cm}$ outside the field edge (as measured at the detector).

6.2.1.4 Glare

The problem of optical photon scatter (or ‘glare’) in camera-based metal/phosphor EPIDs is a well known phenomenon [He95; Mu95; Mu98b; Pa99a]. The effect is primarily attributed to multiple reflections between the screen and mirror [Mu98b; Pa99a], but may also arise due to optical diffusion within the translucent phosphor layer. The multiple optical reflection events have been modelled by Munro *et al* [Mu98b] and Partridge *et al* [Pa99a] and shown to be highly asymmetrical in the gun-target axis for screen mirror systems. Furthermore, Partridge *et al* [Pa99a] demonstrated that these multiple reflections may contribute as much as 20% of the primary signal in the field centre, and dominate other potential sources of glare. Heijman *et al*. [He95] modeled the glare phenomenon for a camera based SRI-100 EPID (metal/phosphor detector viewed by a CCD camera through two front surface mirrors, made by Elekta Oncology Systems, Crawley, UK), through a convolution of the dose image with a radially symmetric glare kernel representing the spread of optical photons, combined with a measured sensitivity matrix which helps account for the asymmetric portion of the glare phenomenon. The aS500 detector does not possess any mirrors or lenses, however it does incorporate a translucent phosphor layer, hence a symmetrical glare effect (which would be much smaller than that due to multiple reflections) may be present. If this glare effect is due to optical dispersion within the phosphor layer itself, the use of a louvre grid which was shown [Pa99a] to significantly reduce multiple reflections in screen/camera systems would likely be ineffective.

A series of measurements was performed, demonstrating the presence of the glare effect in the aS500 detector. Images were acquired at a gantry angle of 0° for an open

15×15 cm² field at SDDs of 120 cm, 150 cm, and 180 cm for both the 6 and 18 MV beam energies. These measurements were repeated with the gantry at 270° to remove the possible influence of backscattered photons that may be present when the gantry was set to 0° and the detector was in close proximity to the floor. This was a concern since metal/phosphor detectors demonstrate increased response to 180° backscattered photons which have an energy of 0.25 MeV independent of incident beam energy. An increased response due to backscattered photons should become evident as an increase in background signal in situations where backscattering material (such as floors and walls) are closer to the detector.

The glare effect was modeled using an iterative approach. The glare kernel of Heijman *et al.* [He95] was fitted using two exponential functions added to a delta function (strictly speaking, the delta function is actually a rect() function when applied, due to the discrete coordinate system of the image). This was used as the first estimate of the glare kernel. The predicted dose image was convolved with the kernel and the result compared to the measured EPID image. The delta portion of the glare kernel was increased or decreased until no further improvement in image comparison was measured. It is well known that the convolution of any image with a delta function simply returns the image (scaled by the area under the delta function). Therefore, although the approach outlined above assumes a specific functionality, it allows a convergence to the correct magnitude of glare contribution. The appropriateness of the non-delta component is clear when comparing the measured and predicted images at points outside the field.

6.2.2 Portal dose prediction algorithm

The portal dose image prediction algorithm used in this chapter has been described in detail in chapter five [Mc00c], so only a brief overview is presented here.

The algorithm is implemented in two steps. The first step involves calculating a map of photon fluence incident onto the portal image detector. A 2D data set of radiological pathlength is found by applying a fast ray tracing [Si85] technique from an ideal point source through the patient's 3D computed tomography data set to the EPID surface. With a knowledge of the incident energy spectrum and a 2D map of relative incident beam fluence, the primary fluence per energy bin entering the detector may be calculated. The incident energy spectra used were generated via Monte Carlo techniques [De00, Mo85] (6 MV, and 18 MV by interpolating 15 and 24 MV). The 2D maps of relative incident fluence are measured using a scanning ionization chamber with appropriate polymethyl methacrylate (PMMA) buildup cap, to remove contaminant electrons. Currently this is not an efficient method for collecting these data, and future work will explore the feasibility of using incident fluence matrix export options available in some commercial treatment planning systems. Alternative methods to estimate the incident beam fluence include Monte Carlo simulation [Ro95] and head scatter models.

The fluence spectrum of scattered photons entering the detector are calculated using 2D scatter fluence spectra kernels generated by Monte Carlo techniques. A description of the creation and analysis of these scattered photon fluence kernels was discussed in chapter three and presents scattered fluence kernels generated in semi-infinite water slabs, and tracks fluence and mean energies. A superposition of appropriate scatter kernels with the incident beam fluence map allows the prediction of

fluence and energies of the scattered photons entering the detector. The incident fluence is sampled over a regular grid of points, with each point uniquely determining a scatter kernel based on radiological thickness and air gap valid at that point. The sampling resolution of the incident fluence for all calculations in this chapter is chosen to be 0.5 cm. This choice introduces less than a 1% error in predicted scatter fluence, as found in a study of the factors affecting the accuracy of predicting the magnitude and quality of scattered photon fluence using this technique [Mc00b].

The libraries of scattered fluence kernels were recalculated for this chapter with EGS4 and user code DOSRZ using water slabs of finite radius (17.5 cm) to reduce the small overestimation of the multiply-scattered photon fluence component, as described previously in chapter four [Mc00b]. Furthermore, the fluence was scored in 0.1 MeV wide energy bins, allowing access to the full scatter fluence energy spectrum data for these scattered fluence kernels, not just mean energies. The fluence kernels were compared to the previously generated data set for consistency, whereas the fluence kernels and the scattered fluence spectra for the singly-scattered photon component were compared to results of a computer program, which calculated this using an analytical approach involving Klein-Nishina cross sections, Compton kinematics, and inverse square fall-off. Using the new kernel libraries containing the scatter fluence spectra data, fluence energy spectra of the scattered photons are contributed by every pencil beam transported through the patient and are tallied in each scoring voxel in the detector plane, resulting in an estimate of the energy spectrum of the scatter fluence. The calculation evolves from section 5.2.1 to estimate the scattered photon fluence spectrum as

$$\frac{d\phi_s(\bar{r}', E)}{dE} = \iint \phi_0(\bar{r}) \cdot K_{\neq(E)}(t(\bar{r}), g(\bar{r}), |\bar{r} - \bar{r}'|) d^2\bar{r} \quad (6.1)$$

where $x, y =$ x and y coordinate of incident photon beam

$x', y' =$ x coordinate in scoring plane

$\bar{r} =$ vector coplanar to scoring plane, representing (x, y) as projected into scoring plane

$\bar{r}' =$ vector coplanar to scoring plane, representing (x', y')

$E =$ photon energy

$\phi_0 =$ incident relative fluence distribution (incident photon beam fluence normalised to central axis value)

$K_{\phi E} =$ scattered photon fluence spectrum kernel

$t =$ radiological thickness (ie. equivalent thickness of homogeneous water) of patient along diverging ray line through (x, y)

$g =$ air gap (distance separating exit surface and scoring plane) along diverging ray line intersecting (x, y)

Note that $\phi_s(\bar{r}') = \int \frac{d\phi_s(\bar{r}')}{dE} dE$ describes the total scatter fluence at the scoring voxel.

The predicted fluence entering the detector is converted to a dose map. This step requires pre-calculated dose deposition kernels unique to a specific detector configuration. These are also generated using EGS4 and user code DOSRZ. For a given detector, the radially symmetric dose pattern due to a perpendicularly incident, monoenergetic photon pencil beam is scored. In the case of the aS500 detector, dose kernels are scored in the phosphor layer which generates the portal image signal, for a range of incident energies (0.1-0.6 in steps of 0.1, 0.8, 1.0, 1.25, 1.5, 2.0-6.0 in steps of 1.0, 8.0, 10.0-24.0 in steps of 2.0; units of MeV). ECUT and PCUT represent the lower

energy limit for electron transport and photon transport respectively, and are set to 0.516 MeV and 0.005 MeV. Resulting statistical errors in the scored dose kernels are $\pm 3.6\%$ (for the aS500 configuration A), $\pm 2.6\%$ (for the aS500 configuration B), and $\pm 1.5\%$ (for the water detector), averaged over all incident energies and radial bins. For any individual scoring bin, the statistical uncertainty does not exceed $\pm 0.8\%$ of the dose scored in the smallest radial bin for all incident energies and detectors described here. The primary dose image is calculated by convolving the dose kernel with the primary fluence for each scored energy bin, then summing the dose maps from all energy bins (see equation 5.3).

The scattered fluence spectrum is converted to dose (D_s) via the method introduced in section 5.2.2, and modified to make use of equation 6.1:

$$D_s(\vec{r}') = \int C_s(E(\vec{r}')) \cdot \frac{d\phi_s(\vec{r}', E)}{dE} dE \quad (6.2)$$

6.2.3 Experimental validation

The algorithm output was compared to measured data acquired with the aS500 EPID for several phantom configurations. These included a 26 cm thick homogeneous, solid water, slab phantom and an anthropomorphic phantom (Rando, Alderson Corp.). Three treatment sites on the anthropomorphic phantom were studied: lung, pelvis, and head at nominal photon beam energies of 6, 18, and 6 MV respectively. A range of air gaps (~20-50 cm) was examined. CT data for the anthropomorphic phantom was collected on a Picker PQ5000 CT scanner, and the attenuation data (in Hounsfield units) were converted to electron density information using $\rho_e = 0.001 * HU$ for $HU \leq 100$ and $\rho_e = 0.000525 * HU + 1.04746$ for $HU > 100$, based on linear fits to measured data and work

by Battista *et al.* [Ba80]. Incident field fluence data was measured using a scanning ionization chamber (PTW corp.) with a PMMA buildup cap. The aS500 EPID was used to measure image data in both configurations (A and B), without and with and extra buildup layer, as described in section 6.2.1.2.

6.3 Results and Discussion

6.3.1 Flat panel detector characteristics

6.3.1.1 Energy response

Scored dose kernels for the aS500 EPID (configurations A and B) are presented in Figure 6.1. The dose kernels for an incident photon energy of 1 and 10 MeV in Figure 6.1(a) demonstrate peaked kernels with exponential tails. The width of the dose kernels increases at higher energies due to the greater energy (and therefore range) of electrons generated. The width of the dose kernels is generally greater for the detector in configuration B, since the greater buildup thickness allows more electron scattering before the phosphor layer is reached, and also because more scattered photons are generated in the thicker buildup layer.

The dose kernels as a function of radius and incident photon energy are presented in Figure 6.1(b), with configuration A using solid lines and configuration B using dotted lines. The regions where photoelectric effect, Compton scatter, and pair production interactions dominate (as calculated by the XCOM package [Be]) are labelled. Configuration B exhibits wider kernels (especially in the high Compton and pair production regimes for radii > 0.2 cm) due to the reasons mentioned above.

When the dose kernels are converted into deposited energy and integrated over all scoring bins, a detector response function is generated. This assumes that the measured optical signal in the amorphous silicon detector will be proportional to the deposited

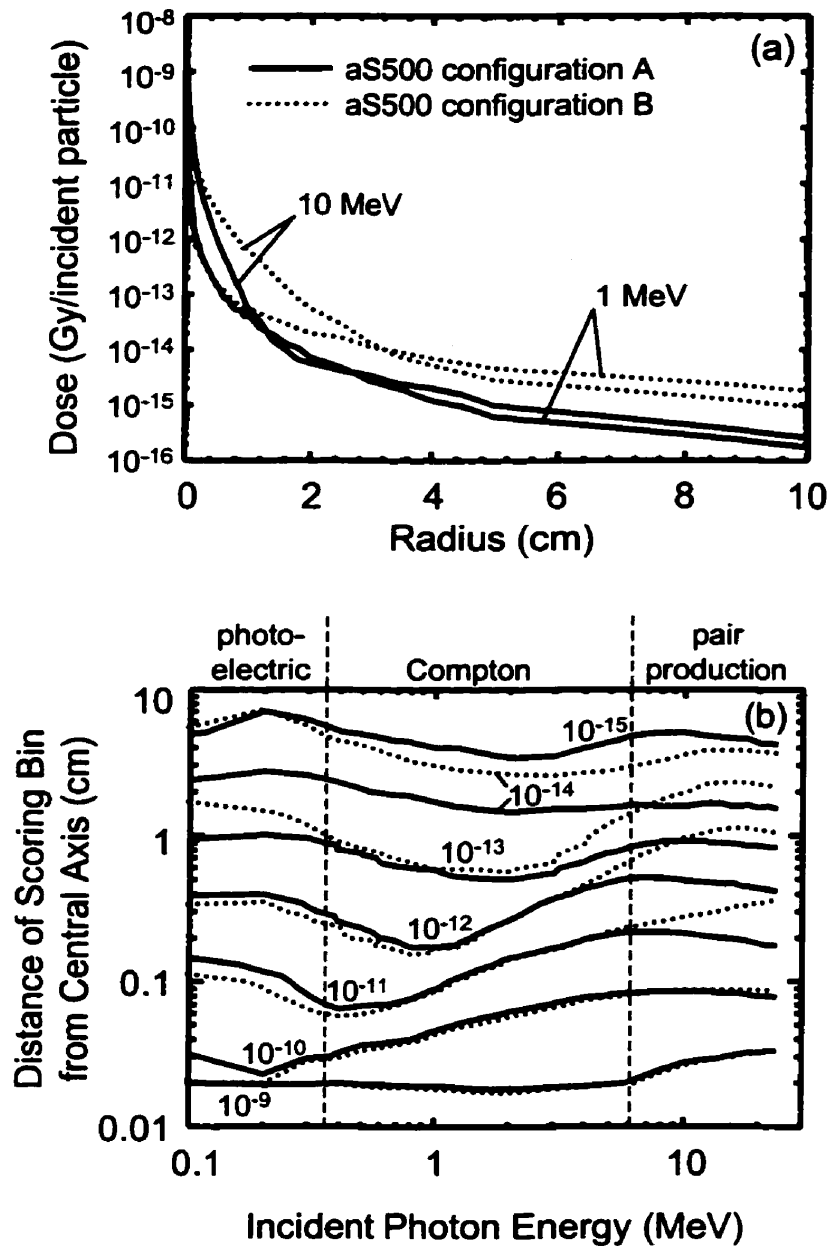
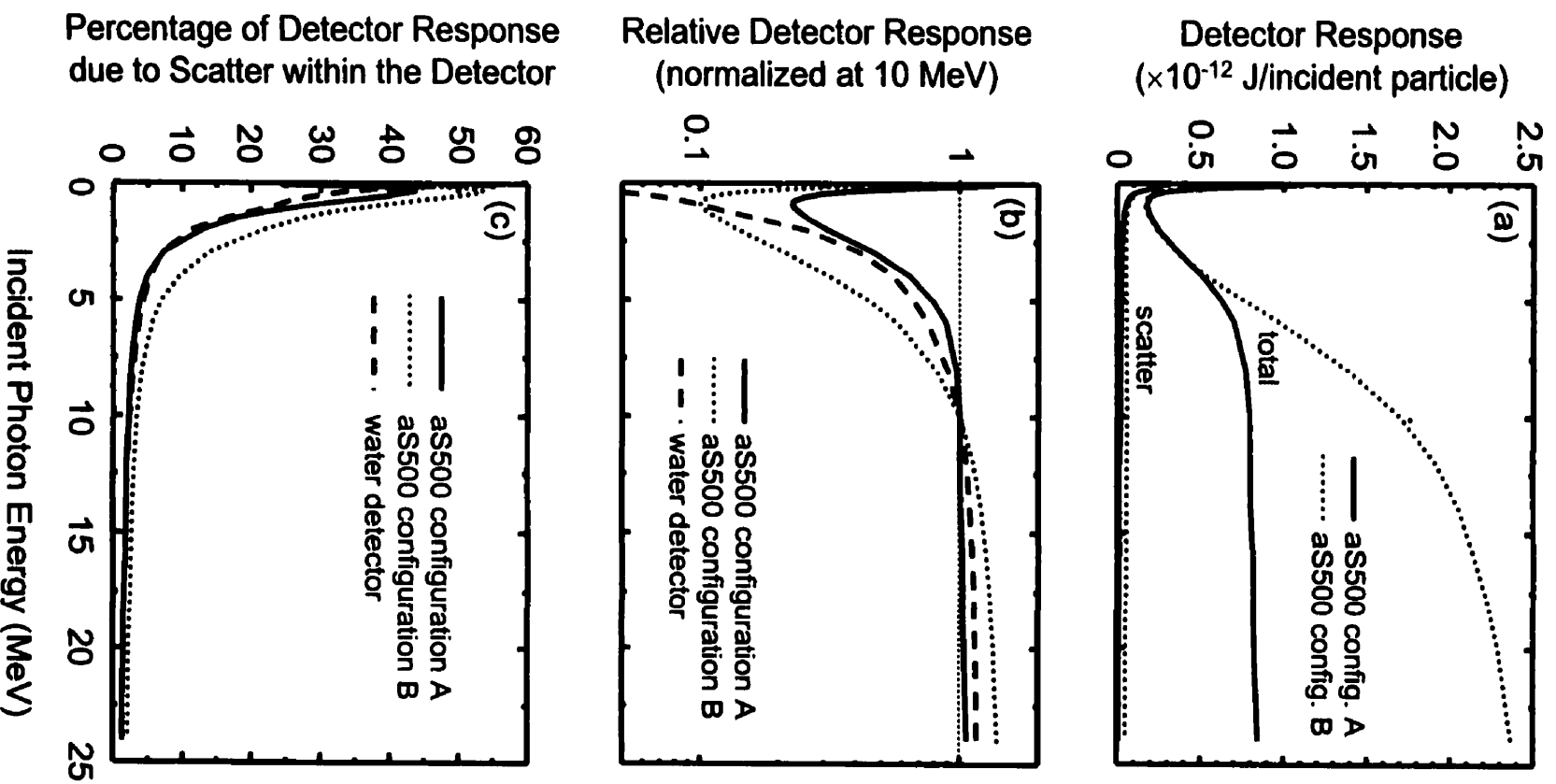


Figure 6.1: (a) Dose kernels for the aS500 detector in configuration A (solid line) and B (dotted line), for 1 MeV and 10 MeV incident photon energy. (b) All dose kernels for the aS500 detector in configuration A (without extra buildup, solid lines) and B (with extra buildup, dotted lines), as a function of radius and incident photon energy. Dose contours are labeled in units of Gy/incident particle.

(OVERLEAF) Figure 6.2: (a) Detector response for the aS500 detector in configuration A (solid lines) and B (dotted lines). (b) Relative detector response normalized to 10 MeV for the aS500 detector in configuration A (without extra buildup, solid line) and B (with extra buildup, dotted line), and a water detector (dashed line). (c) Percentage of total deposited energy which is attributable to scattered photons arising in the detector itself, for the aS500 detector in configuration A (solid line) and B (dotted line), and a water-equivalent detector (dashed line).



dose, which is generally assumed to be true [Ra93; Ka99]. These results are presented in Figure 6.2. The response due to scatter within the detector itself is available, since the user code DOSRZ separates scatter dose from the total dose, and becomes important only at lower incident photon energies. It is apparent from Figure 6.2(a) that the standard configuration (A) of the aS500 detector does not have enough buildup to achieve electronic equilibrium in the phosphor layer at higher photon beam energies. For this detector, the response levels off at ~ 7 MeV, in contrast to configuration B where the response begins to level off around 24 MeV. The curves begin to separate at ~ 4 MeV. Therefore, a thicker buildup layer than currently exists will serve to increase the detector response to incident photons of energy greater than ~ 4 MeV. This will increase image quality for all incident beam energies greater than 4 MV, since scatter will be preferentially attenuated and the higher energy primary photons will generate a greater relative response in the detector. This is an important finding for potentially improving detector design for improved image quality (since the effects on spatial resolution and noise would need to be investigated). Furthermore, this implies that researchers using the detector for megavoltage CT will need to have the optimal buildup for the beam energy used in order to maximize image signal while minimizing noise and dose to the patient.

The relative detector responses are presented in Figure 6.2(b), with a water-equivalent detector added for comparison. The response curves are normalized to 10 MeV. The aS500 detector exhibits the characteristic increase in response at lower photon energies known to occur for metal/phosphor detectors (due to the importance of the photoelectric effect in the high atomic number phosphor layer), as may be observed in previous work [Ja94, Mc00c]. Note that the aS500 in configuration B exhibits better low

energy filtration ($\sim 1-10$ MeV) than the water detector, and also a greater relative response at energies over 10 MeV.

The percentage of energy deposited due to scattered radiation within the detector itself is important for energies below $\sim 2-4$ MeV, as illustrated in Figure 6.2(c). The aS500 EPID in configuration B demonstrates an overall higher self-scatter contribution than configuration A, due to the larger layer of buildup (and thus larger amount of scattering material). This figure demonstrates the significance of the scatter signal, and the importance of being able to accurately model it. Note that the Monte Carlo generated dose kernels of the approach presented in this chapter inherently incorporate this effect.

The variation in detector response with depth in the phosphor layer was examined. Figure 6.3 presents the detector response curves for the aS500 EPID in configurations A and B. Again the lack of electronic equilibrium above ~ 7 MeV for the aS500 in configuration A is observed, since the exit layer has a greater response than the entrance layer above this energy. In configuration B, the adequate choice of buildup over all incident energies examined results in the exit layer yielding a smaller response function than the entrance layer. The difference in detector response with phosphor layer is small, but these differences will likely increase if the phosphor thickness is increased.

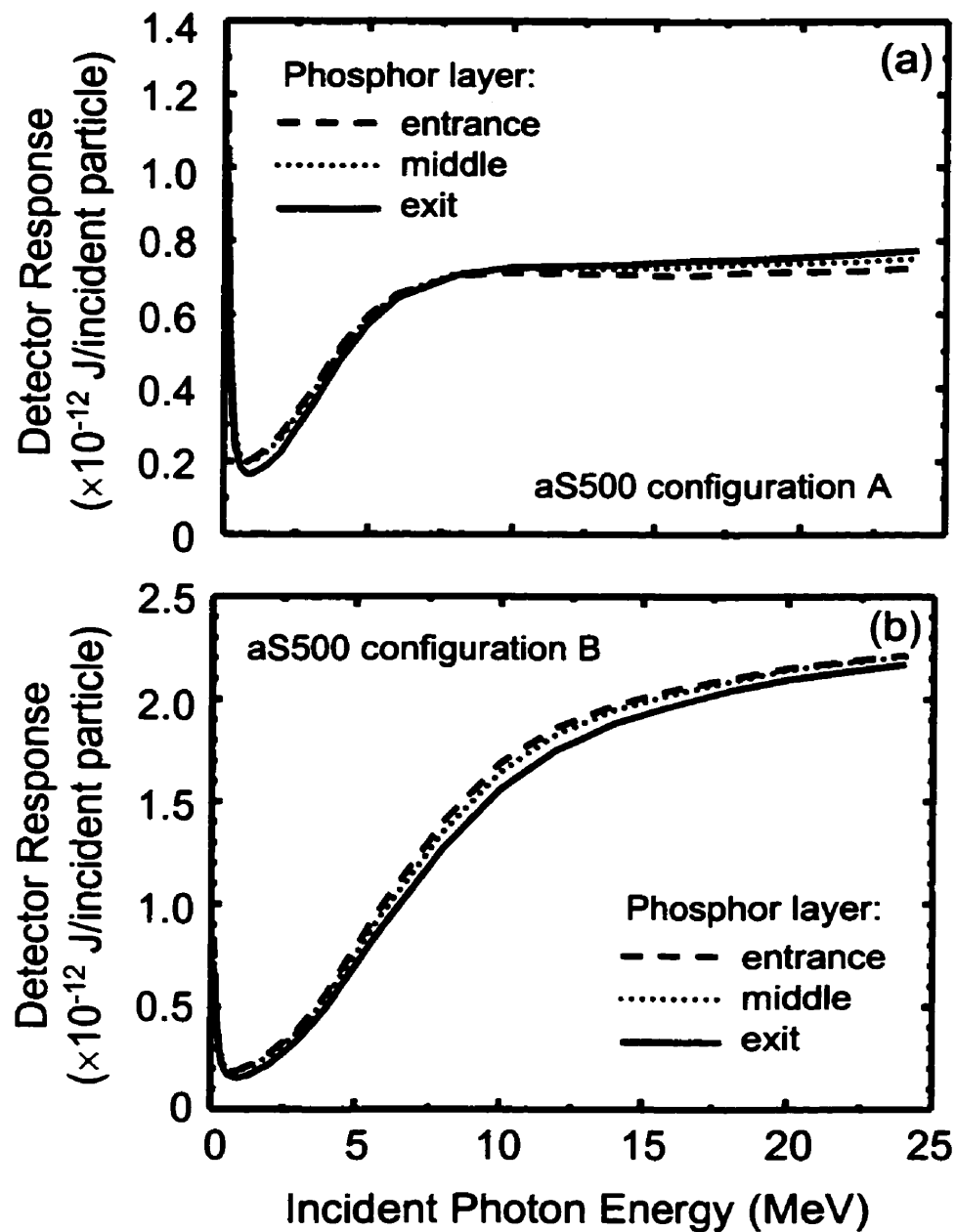


Figure 6.3: (a) Detector response of various layers of phosphor in the aS500, configuration A. Entrance layer (dashed line), middle layer (dotted line), and exit layer (solid line) are presented. (b) Detector response of various layers of phosphor in the aS500, configuration B. Entrance layer (dashed line), middle layer (dotted line), and exit layer (solid line) are presented.

6.3.1.2 Linearity

The linearity of detector response with an increasing number of frames being integrated into the image is presented for both 6 and 18 MV beam energies in Figure 6.4(a). The detector responds within $\pm 0.5\%$, except for one outlier.

The dose rate dependence of detector response for a 6 MV beam is presented in Figure 6.4(b). A central axis ROI is examined, as well as an ROI outside the field edge. The requested dose rate (valid for the calibration geometry) was varied between 100 and 600 MU/min. A constant 10-frame average acquisition time of 2 seconds was used, resulting in smaller error bars with increasing dose rate. The detector responds within $\pm 2\%$ (with one outlier) of ideal linearity. This is higher than earlier investigations [E199], which have found $\pm 1\%$ linearity, but is based on only one measurement series. Linear accelerator stability will also contribute to this result.

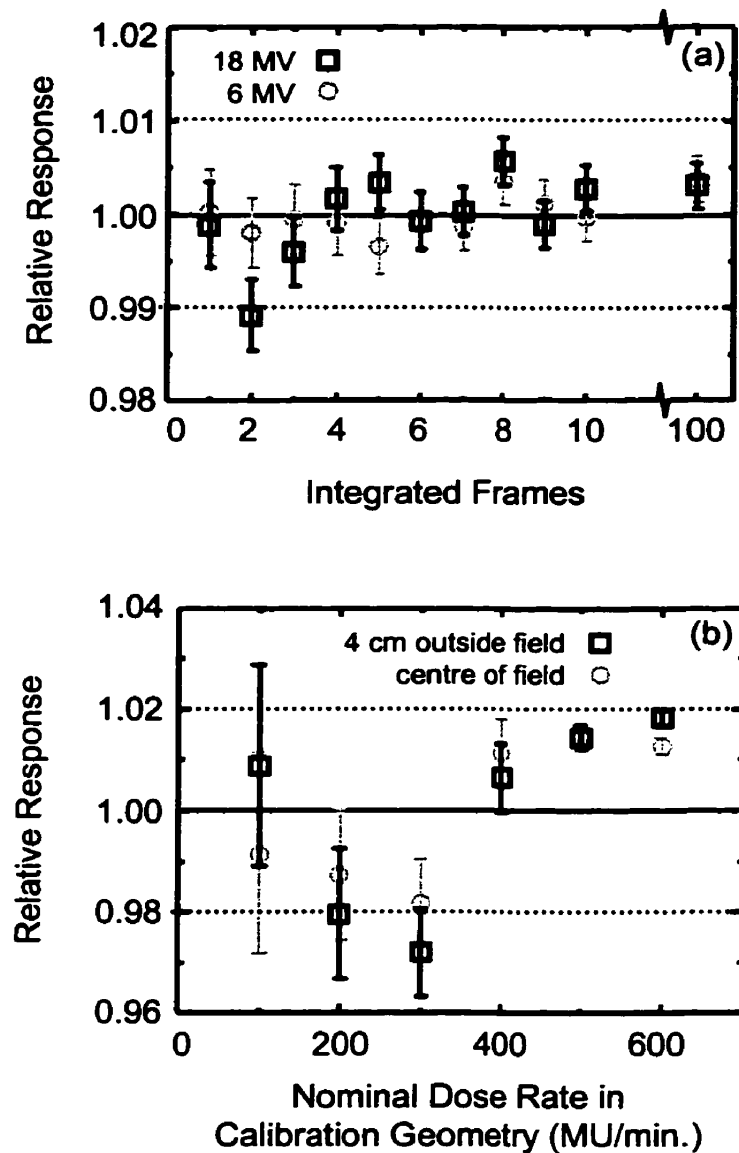


Figure 6.4: (a) Linearity of aS500 detector in configuration A with frame integration, using images of an open, $15 \times 15 \text{ cm}^2$ field for 6 MV (circles) and 18 MV (squares) beams. (b) Dose rate dependence of aS500 in configuration A, using images of an open, $15 \times 15 \text{ cm}^2$, 6 MV field. Two ROI's are examined in the images, one on the central axis (circles) and one $\sim 4 \text{ cm}$ outside the field edge (squares).

6.3.1.3 Glare

Profiles of aS500 images (configuration A) of an open field ($15 \times 15 \text{ cm}^2$) taken at various SDDs are presented in Figure 6.5. The central axis greyscale decreases in a manner very closely reproducing the inverse square law. By taking the average greyscale in a 1 cm^2 ROI at the image centre and normalising to the 120 cm SDD image, the inverse square law was obeyed within 1.7% for the 6 MV data and within 0.6% for the 18 MV data. However, if a region outside the field is examined, no appreciable decrease in greyscale is observed (in fact, there appears to be a very slight increase). Since there was no absorber in the beam path, the effects of scattered radiation should be negligible. In addition, the spatial dependence of the energy spectra incident on the detector should simply move along linear dimensions with increasing SDD. For example, the energy spectra incident at point $P=r$ cm off central axis for SDD = 100 cm should be the same as at point $Q=1.5 \cdot r$ cm off central axis for SDD = 150 cm. This will not be strictly true since an ideal point source is assumed, but should be relatively accurate since the contribution of flattening filter and collimator effects is only ~9-13% of the total fluence for an open field [De00]. Thus, the compensation of the inverse square law in regions outside of the field may *not* be explained through energy spectrum arguments. However, an optical photon effect (glare) does explain this behavior, as follows. The glare effect has been previously modelled as a convolution of some blurring kernel (a point spread function describing the glare effect) with the incident dose image, which produces the optical photon image [He95]. The invariant glare kernel in that work was depicted essentially as a delta function added to a slowly decreasing tail component. When the SDD is increased, field dimensions scale linearly, and therefore the incident field area (as

measured at the detector) increases by the square. Therefore, for a point outside the main field, a glare effect (if present) would be proportional to the area of the incident field through the convolution relationship. This would explain an exact compensation of the decrease expected by the inverse square fall off. It is observed in Figure 6.5 that this accurately describes the acquired data. Furthermore, if the effect is an optical one, then it should be present in a magnitude independent of incident beam energy. This is observed in Figures 6.5 and 6.6. Figure 6.6 presents relative profiles, which are normalized to the greyscale value on the central axis. Notice that the magnitude of the effect outside the field is similar when comparing images acquired at 6 and 18 MV beam energies.

One small effect which may be of concern here, is the presence of backscattered photons from the floor. Compton kinematics indicates that 180° backscattered photons possess an energy ~ 0.25 MeV, independent of incident photon energy. It is known that metal/phosphor detectors exhibit an increase in response at lower energies, and thus this effect is a concern here. A second set of open field (15×15 cm²) images was taken at various SDDs, but with the gantry at 270° , to greatly increase the distance between the detector and backscatter (in this instance, the wall), and therefore allow the inverse square effect to remove most of the backscatter fluence. The data indicate that this orientation does not change the profiles significantly ($<1\%$), and thus backscattered photons are not responsible for the observed effect. Therefore, the glare effect is present in the aS500 detector, and is likely to be present in all flat panel detectors incorporating scintillation layers which allow optical photon spread.

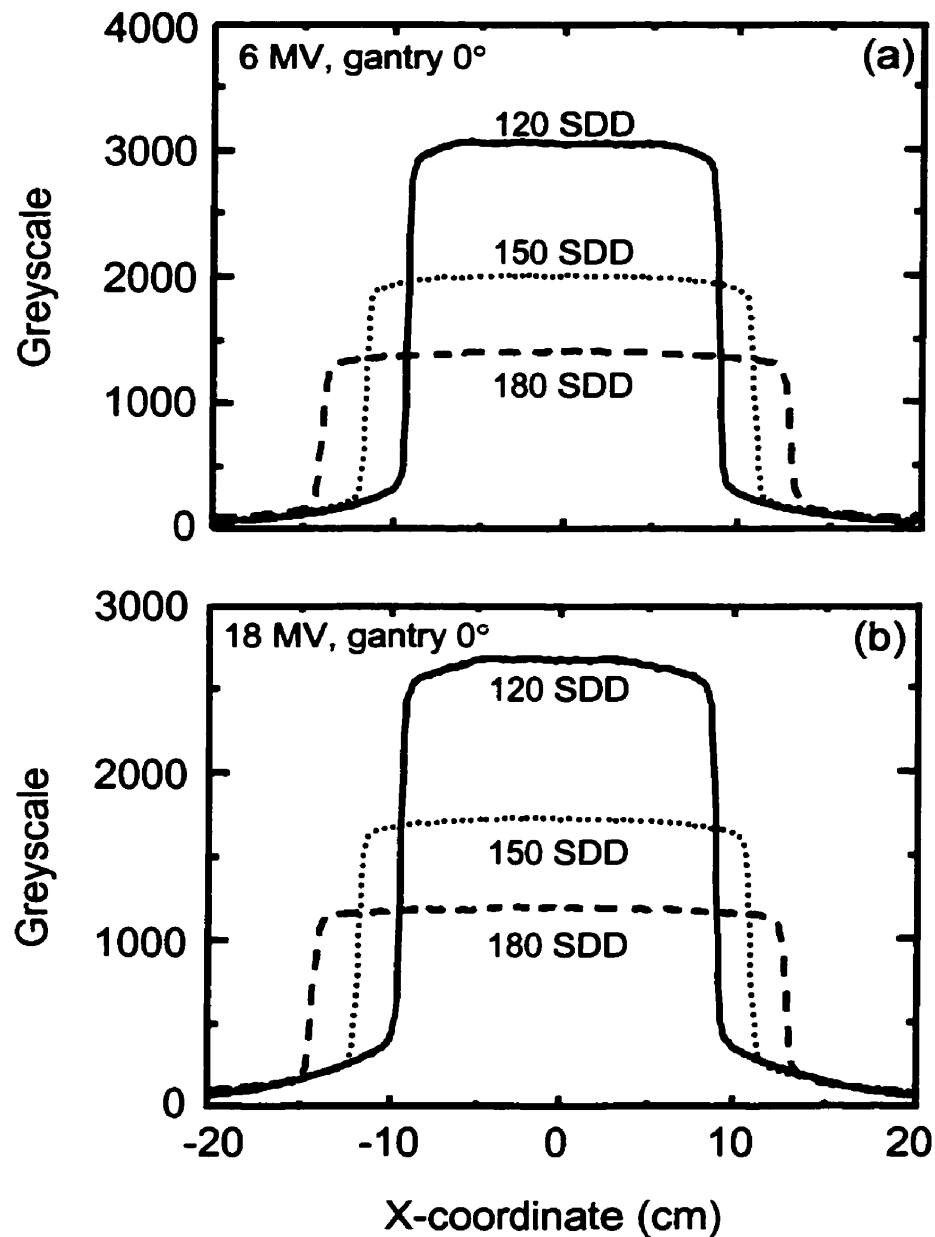


Figure 6.5: (a) Profiles of images acquired using the aS500 detector in configuration A, for an open, $15 \times 15 \text{ cm}^2$, 6 MV field. SDD's include 120 cm (solid line), 150 cm (dotted line), and 180 cm (dashed line). (b) Profiles of images acquired using the aS500 detector in configuration A, for an open, $15 \times 15 \text{ cm}^2$, 18 MV field. SDD's include 120 cm (solid line), 150 cm (dotted line), and 180 cm (dashed line).

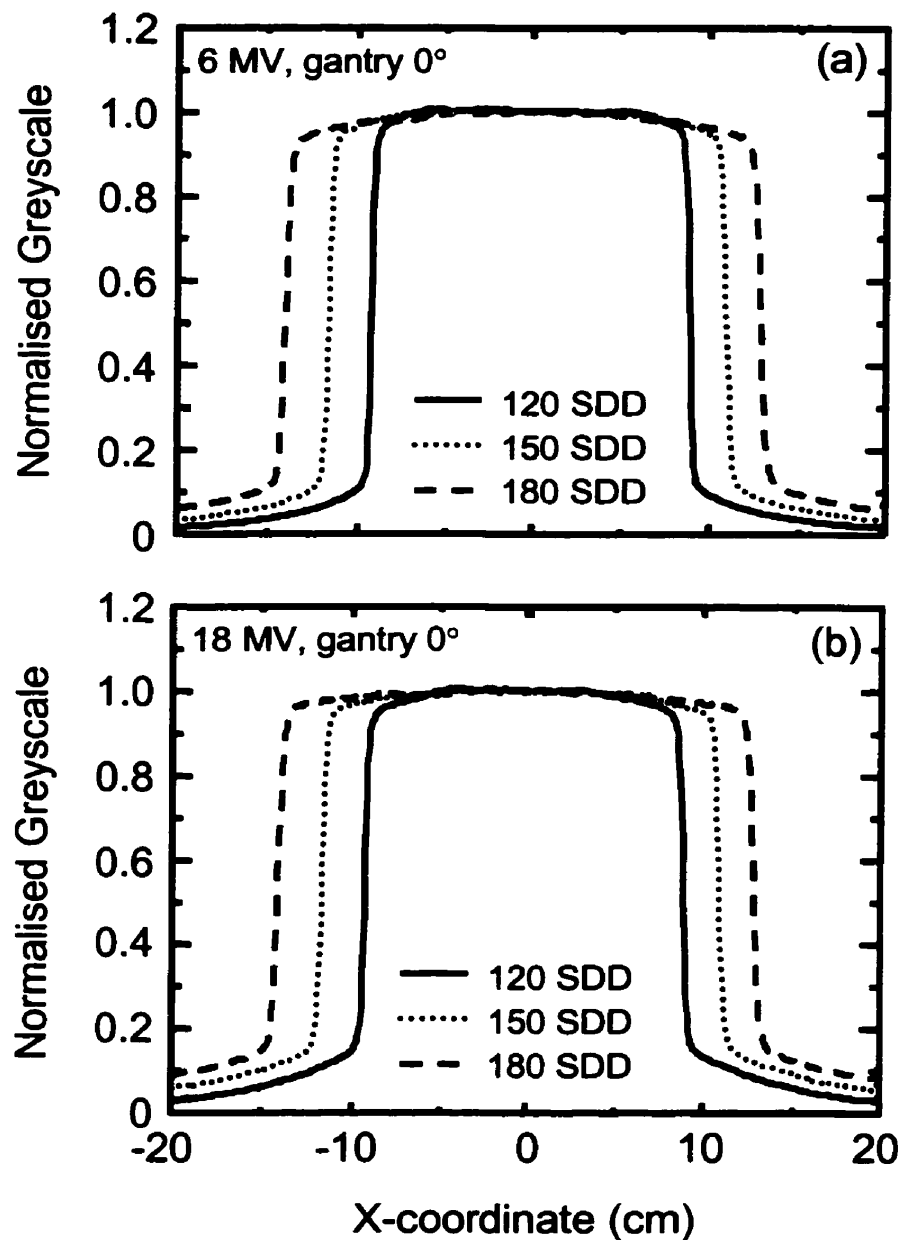


Figure 6.6: (a) Profiles of images acquired using the aS500 detector in configuration A, for an open, $15 \times 15 \text{ cm}^2$, 6 MV field. Profiles are normalized to central axis, and SDD's include 120 cm (solid line), 150 cm (dotted line), and 180 cm (dashed line). (b) Profiles of images acquired using the aS500 detector in configuration A, for an open, $15 \times 15 \text{ cm}^2$, 18 MV field. Profiles are normalized to central axis, and SDD's include 120 cm (solid line), 150 cm (dotted line), and 180 cm (dashed line).

The glare effect was specifically investigated by Munro and Bouius [Mu98a] for a similar flat panel detector and they concluded that the effect was negligible. This is probably due to the small range of illuminated areas studied in their work. The pertinent experiment involved a very small detector ($9.6 \times 9.6 \text{ cm}^2$) and a change in illuminated area on the detector surface from 67.2 to 91.9 cm^2 . Based on the current work, less than a 1% effect would be expected from this magnitude of illuminated area change.

The glare effect is modeled with a radially symmetric function which is convolved with the calculated portal dose image. This was performed iteratively, using the kernel first proposed by Heijman *et al.* [He95] as the initial estimate. This proposed kernel was fitted to the function $g(r) = a \cdot \exp(-b \cdot r) + c \cdot \exp(-d \cdot r)$ with $a = 0.02196 \pm 0.0007$, $b = 2.7 \pm 0.1$, $c = 0.0013 \pm 0.0001$, $d = 0.13 \pm 0.02$. This fitted function was then added to a delta function. A predicted open field ($15 \times 15 \text{ cm}^2$) dose image (P_d) was convolved with the glare kernel and the result compared to the corresponding measured aS500 image. The delta function portion of the glare kernel was adjusted until differences between the convolution product and measured image no longer decreased. The spatial resolution of the glare kernel used here is $1 \times 1 \text{ mm}^2$, and the delta function was defined as a single pixel at the centre of the glare function. The resulting glare function and raw data are plotted in Figure 6.7(a). This glare kernel is applied to predicted dose images throughout the rest of this chapter. Profiles through the predicted dose image, dose image after convolution with the glare kernel, and corresponding measured aS500 image are presented in Figure 6.7(b), for an SDD of 120 cm and 6 MV beam. Excellent agreement is obtained throughout the profile, with a significant gain in signal outside of the field ($\sim 3\text{-}4\%$ of central axis signal for this example). It is interesting to note that the measured

images exhibit profiles which have sharper penumbras than the predicted images. This is due to the use of an incident fluence matrix (in the prediction algorithm) that was measured with a scanning ionization chamber of inner diameter ~6 mm, serving to spread the penumbra of the predicted dose profile more than the measured profile (recall pixel widths of 0.784 mm). The glare function derived from the images taken at SDD's of 120, 150 and 180 cm demonstrated variations of <1.5% in the delta function height, indicating independence on SDD, as expected from the glare effect.

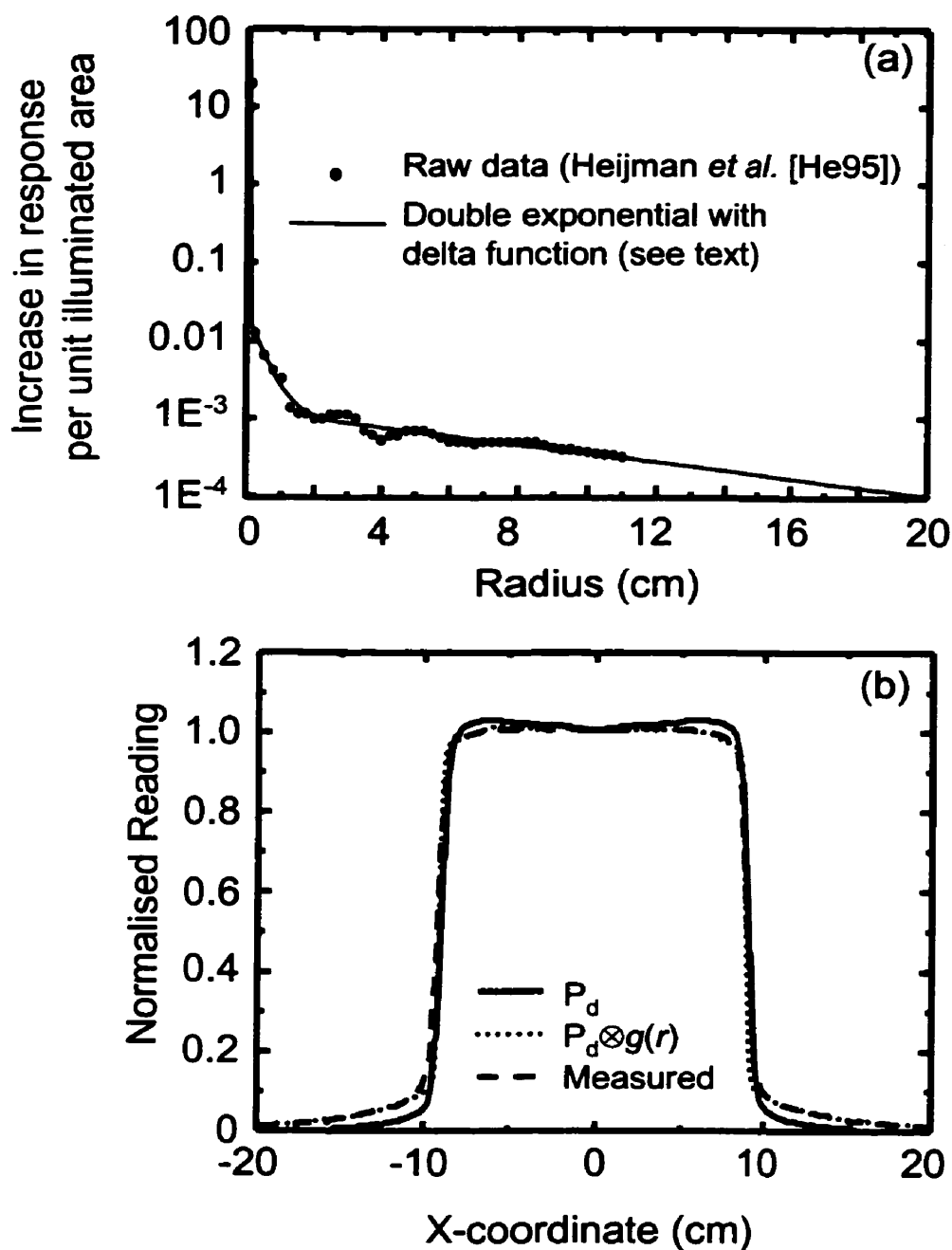


Figure 6.7: (a) Glare kernel used to model the glare effect. The initial kernel estimate is represented by solid circles, the dotted line represents the final glare kernel. (b)

Normalized profiles of a predicted portal dose image of an open, $15 \times 15 \text{ cm}^2$, 6 MV field (solid line), the result of convolving this image with the glare kernel (dotted line), and the measured data using the aS500 in configuration A (dashed line).

6.3.2 Experimental validation of dose algorithm

6.3.2.1 Scatter fluence kernels

To verify the accuracy of the scatter fluence kernels, comparison of the singly scattered photon fluence component to results of analytical calculations is made in Figures 6.8(a) and 6.9(a). Comparison is excellent throughout the data set, except for minor discrepancies at small radius, due to the analytical calculation not modeling in-air scatter. When compared to similar distributions presented in chapter three [Mc00a], small differences are observed due to the use of a finite radius phantom, including differences in singly scattered fluence at larger radii and small air gap, and a small decrease in multiple scatter fluence magnitude at any given air gap/radius. The spatial locations labelled α and β (marked by stars) representing radii 0-0.25 cm and 19.75-20.0 cm, both at air gap 30 cm, have been chosen for closer examination. Figures 6.8 (b) and (c) and 6.9 (b) and (c) illustrate the energy fluence of the scattered photons through those scoring bins. For both the 6 and 18 MV beam energies, several observations may be made. An overall decrease in fluence is observed in moving from location α to β , as expected from the Klein-Nishina cross section. The bulk of the singly-scattered photon fluence decreases in energy, also expected, since higher angle scatter results in lower energy scattered photons. The multiply-scattered energy fluence maintains its shape (heavily weighted to lower energies), while decreasing in magnitude. Singly- and multiply-scattered photon fluence is of greater magnitude at the 6 MV beam energy, whereas the bremsstrahlung and positron annihilation component becomes more important at the 18 MV beam energy. For the 18 MV beam (and somewhat less

noticeably in the 6 MV beam) a spike in the bremsstrahlung and positron annihilation component is observed in the 0.5-0.6 MeV energy bin. This is due to the two-photon positron annihilation process requiring a minimum of 1.022 MeV energy in the positron in order to yield two 0.511 MeV photons.

Another verification of the Monte Carlo-scored energy fluence spectra is presented in Figures 6.8(d) and 6.9(d). The analytical calculation results were tallied by energy bin (bin width 0.25 for 6 MV beam and 0.5 for 18 MV beam), and overlaid with the Monte Carlo results (bin width 0.1 MeV) for points α and β . Due to the different bin widths, the distributions were converted to counts/MeV and normalised to unit area, to allow comparison. It is evident that the analytical and the Monte Carlo results are similar. These comparisons establish confidence in the Monte Carlo simulations of the scatter fluence spectra kernels.

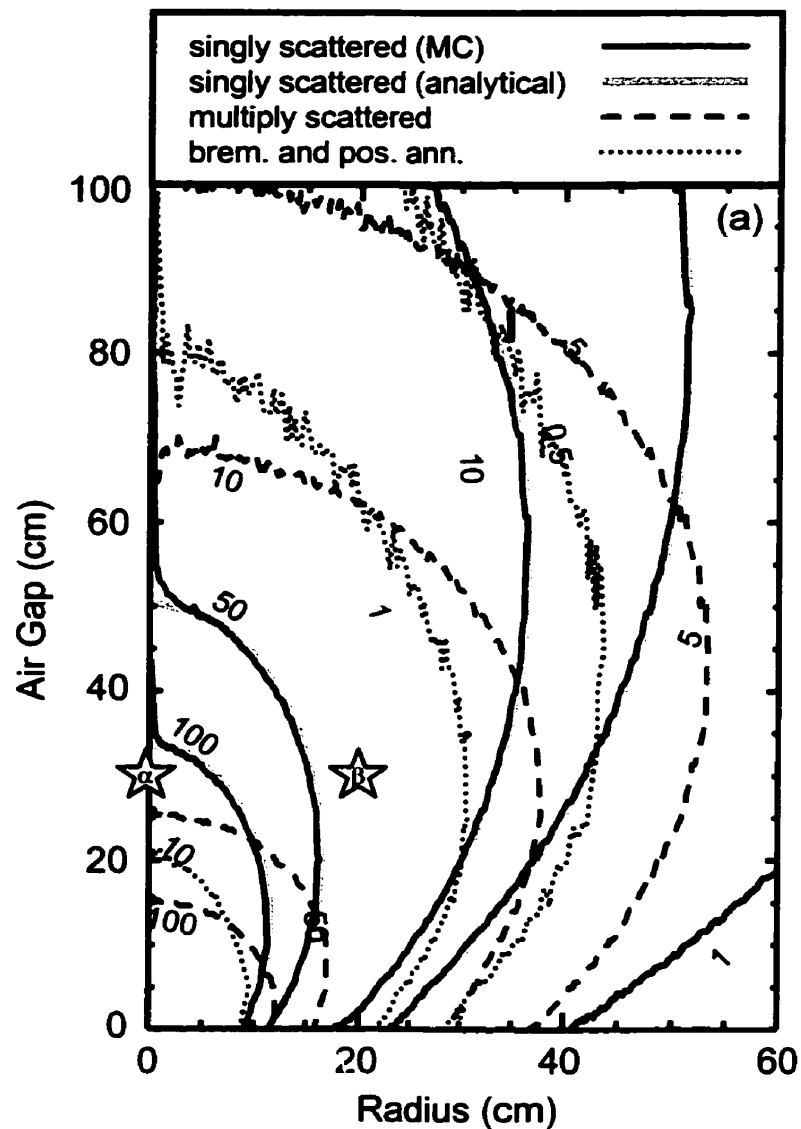
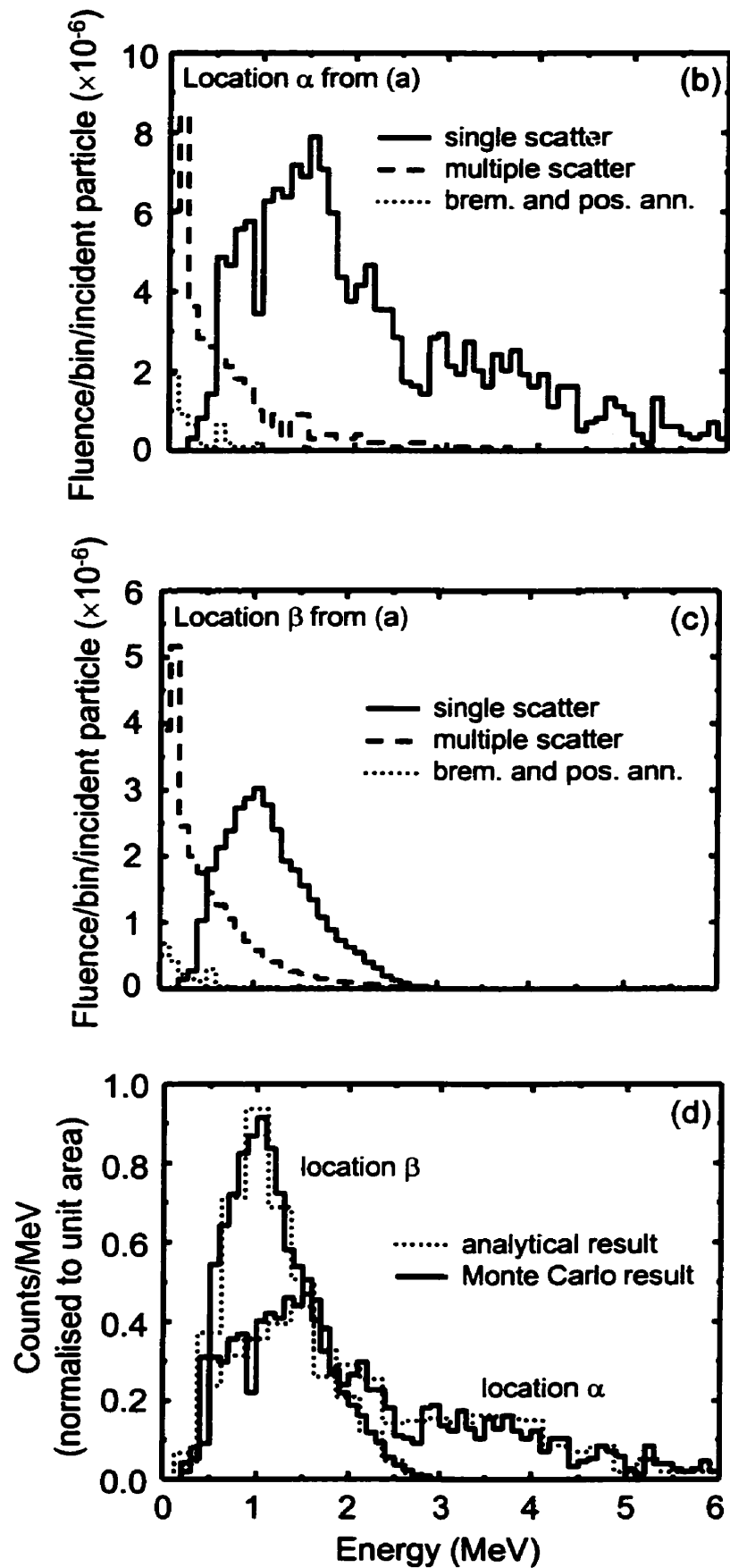


Figure 6.8: (a) Scattered photon fluence normalized to the number of incident particles ($\times 10^{-6} \text{ cm}^{-2}$) due to an incident 6 MV pencil beam of photons, behind a 20 cm thick water slab with radius 17.5 cm, at a range of air gaps. Solid lines represent singly-scattered photon fluence, dashed lines represent multiply-scattered photon fluence, and dotted lines represent bremsstrahlung and positron annihilation photons. Gray lines represent results of an analytical singly-scattered fluence calculation for comparison. Locations α and β are used in further analysis presented in (b, c, d) on next page.

(OVERLEAF) Figure 6.8: (b) Scattered fluence energy spectrum in location α . (c) Scattered fluence energy spectrum in location β . (d) Comparison of Monte Carlo scored (solid lines) and analytically calculated (dotted lines) singly-scattered photon energy fluence, at locations α and β .



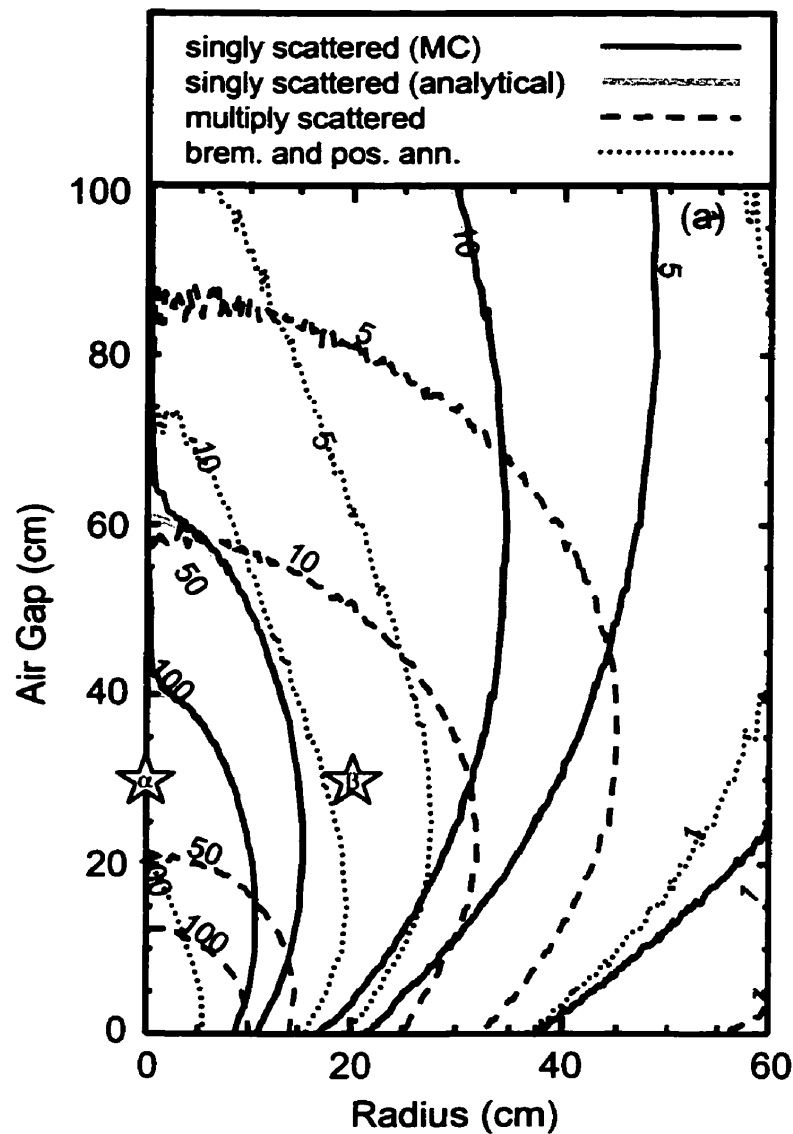
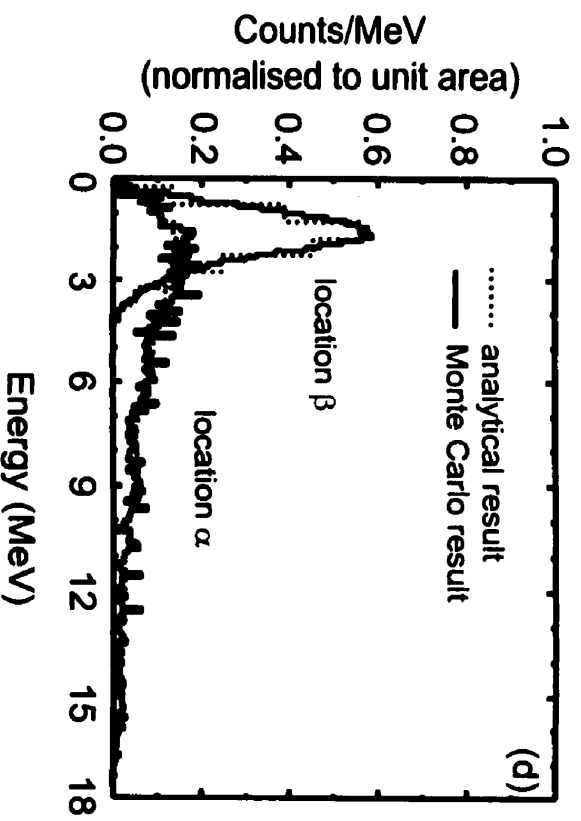
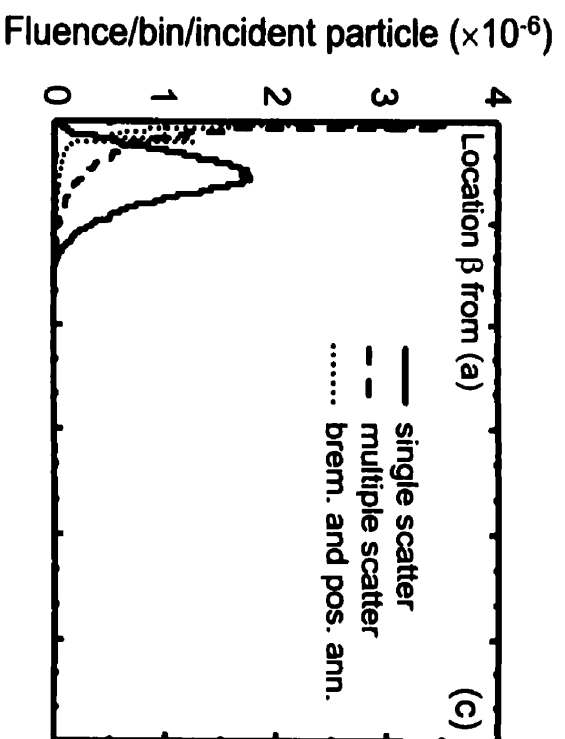
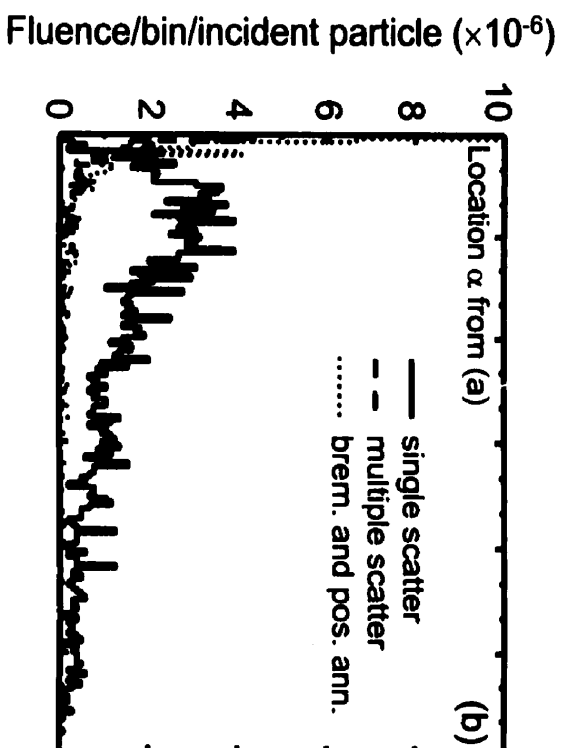


Figure 6.9: (a) Scattered photon fluence normalized to the number of incident particles ($\times 10^{-6} \text{ cm}^{-2}$) due to an incident 18 MV pencil beam of photons, behind a 20 cm thick water slab with radius 17.5 cm, at a range of air gaps. Solid lines represent singly-scattered photon fluence, dashed lines represent multiply-scattered photon fluence, and dotted lines represent bremsstrahlung and positron annihilation photons. Gray lines represent results of an analytical singly-scattered fluence calculation for comparison. Locations α and β are used in further analysis presented in (b, c, d) on next page.

(OVERLEAF) Figure 6.9: (b) Scattered fluence energy spectrum in location α . (c) Scattered fluence energy spectrum in location β . (d) Comparison of Monte Carlo scored (solid lines) and analytically calculated (dotted lines) singly-scattered photon energy fluence, at locations α and β .



6.3.2.2 Comparison of predicted and measured images

Predicted and measured profiles in the cross plane (x direction) through the central axis are presented for the simple slab phantom in Figure 6.10. The predicted dose data are presented in three parts: the predicted total dose (D_p), the scatter dose component, and the predicted dose convolved with the glare kernel ($D_p \otimes g(r)$). Data in Figure 6.10 (a) and (b) were generated with an incident $15 \times 15 \text{ cm}^2$, 6 MV field using the aS500 detector in configuration A at an SDD of 150 cm. Data in Figure 6.10 (c) and (d) were generated with an incident $15 \times 15 \text{ cm}^2$, 18 MV field using the aS500 detector in configuration B at an SDD of 120 cm. The inclusion of the glare effect is observed to improve the agreement in both cases (especially for the 18 MV example). Analysis of comparisons of the predicted and measured images has been performed in accordance with recommendations of Van Dyk *et al.* [Va93]. Although these recommendations are made for patient dose calculation, the categories of analysis applied to calculated and measured portal images, appears useful. Data points are broken into three categories: relative dose $<7\%$ and dose gradient $<30\%/cm$ (low dose gradient), relative dose $>7\%$ and dose gradient $<30\%/cm$, and dose gradient $>30\%/cm$ (high dose gradient). For the first two categories, histograms of the percent differences are presented, for the third category, histograms of the isodose line separation are presented. Dose gradients were calculated as the maximum gradient around a dose point, whereas the isodose line separations were estimated as the deviation between measured and predicted relative dose values divided by the gradient [Mc96b]. In the images presented here, none possess low dose gradient pixels under 7% relative magnitude. This is because situations where a large contribution of scattered dose to the portal imager were deliberately investigated to

ensure the portal dose prediction algorithm was adequately challenged. In Figure 6.10 (b), 91.5% of the predicted low dose gradient pixels $>7\%$ agreed within $\pm 5\%$ of the measured values, whereas 95.0% of the predicted high dose gradient pixels agreed within ± 5 mm of the measured values. In Figure 6.10 (d), 100% of predicted low dose gradient pixels $<7\%$ and 91.9% of the predicted low dose gradient pixels $>7\%$ agreed within $\pm 5\%$ of the measured values, whereas 97.8% of the predicted high dose gradient pixels agreed within ± 5 mm of the measured values.

Figure 6.11 presents data generated by a 15×15 cm², 6 MV field incident perpendicularly onto the chest of the Rando phantom, and using the aS500 detector in configuration A at an SDD of 130 cm. Notice that the heart and spinal column are located in the central image region. In Figure 6.11 (d), the glare modeling is demonstrated to have a significant improvement in the regions outside of the primary field. The histogram analysis reveals 86.1% of the predicted low dose gradient pixels $>7\%$ agreed within $\pm 5\%$ of the measured values, whereas 93.5% of the predicted high dose gradient pixels agreed within ± 5 mm of the measured values.

Figure 6.12 presents data generated using a 15×15 cm², 18 MV field and the aS500 detector in configuration A at an SDD of 130 cm. The field is perpendicularly incident on the pelvis region of the Rando phantom. Note that the images presented in Figure 6.12 (a) and (b) have been contrast enhanced (in equal amounts) for presentation purposes only. The glare modeling is demonstrated to significantly improve the predicted profile in the regions outside of the primary field. The histogram analysis reveals 91.1% of the predicted low dose gradient pixels $>7\%$ agreed within $\pm 5\%$ of the

measured values, whereas 98.2% of the predicted high dose gradient pixels compared to within ± 5 mm of the measured values.

Figure 6.13 presents data generated using a 15×15 cm², 6 MV field and the aS500 detector in configuration A at an SDD of 130 cm. The field is laterally incident on the head of the Rando phantom. In Figure 6.13 (d), the glare modeling is demonstrated to have a significant improvement in the regions outside of the primary field. Notice the misalignment between the measured and predicted images (the head appears to be slightly rotated in the counter-clockwise direction in the predicted image), which also shows up in a poor profile comparison in Figure 6.13 (d). This tilt was likely introduced by a poor alignment of phantom with lasers when the CT data set was acquired. This visual assessment of poor alignment is confirmed in the quantitative analysis. The histogram analysis reveals only 83.9% of the predicted low dose gradient pixels $>7\%$ agreed within $\pm 5\%$ of the measured values, whereas 93.5% of the predicted high dose gradient pixels compared to within ± 5 mm of the measured values.

In the simple phantom situation the quality of performance of the portal dose prediction algorithm is within the current recommendations for treatment planning algorithms [AA98]. In the more complex anthropomorphic phantom situations, the quality decreases due to the increased difficulty in reproducibility of setup, as well as inexact modeling of the scattered photons. The quality of performance found here is similar to the current recommendations for treatment planning algorithms [AA98].

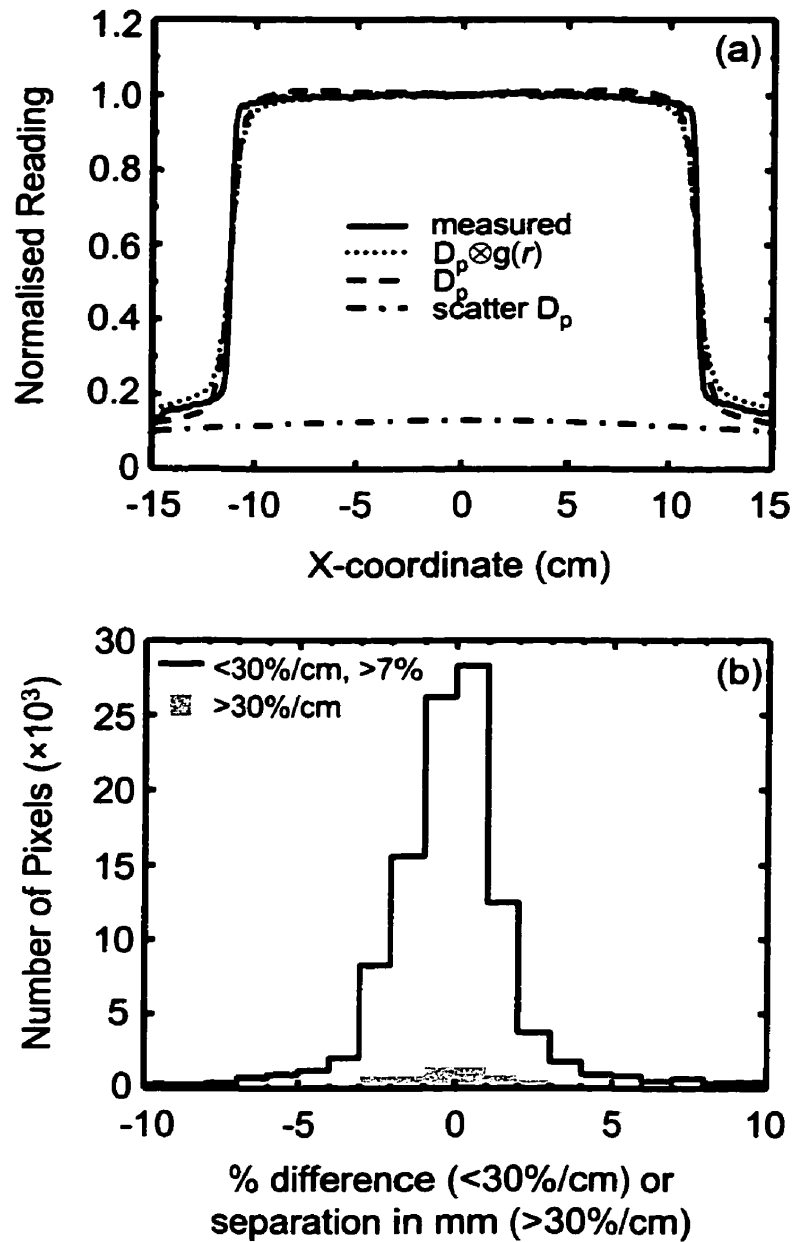


Figure 6.10: (a) Measured and predicted image profiles through isocentre at 150 cm SDD for a $15 \times 15 \text{ cm}^2$, 6 MV field incident on a 26 cm thick, homogeneous, water-equivalent slab using the aS500 in configuration A. Included are the measured data (solid line), predicted dose convolved with glare (dotted line), predicted dose without glare (dashed line), and scattered dose (dash-dot line). (b) Analysis of comparison of measured and predicted images in (a). Figure 6.10 continued on next page.

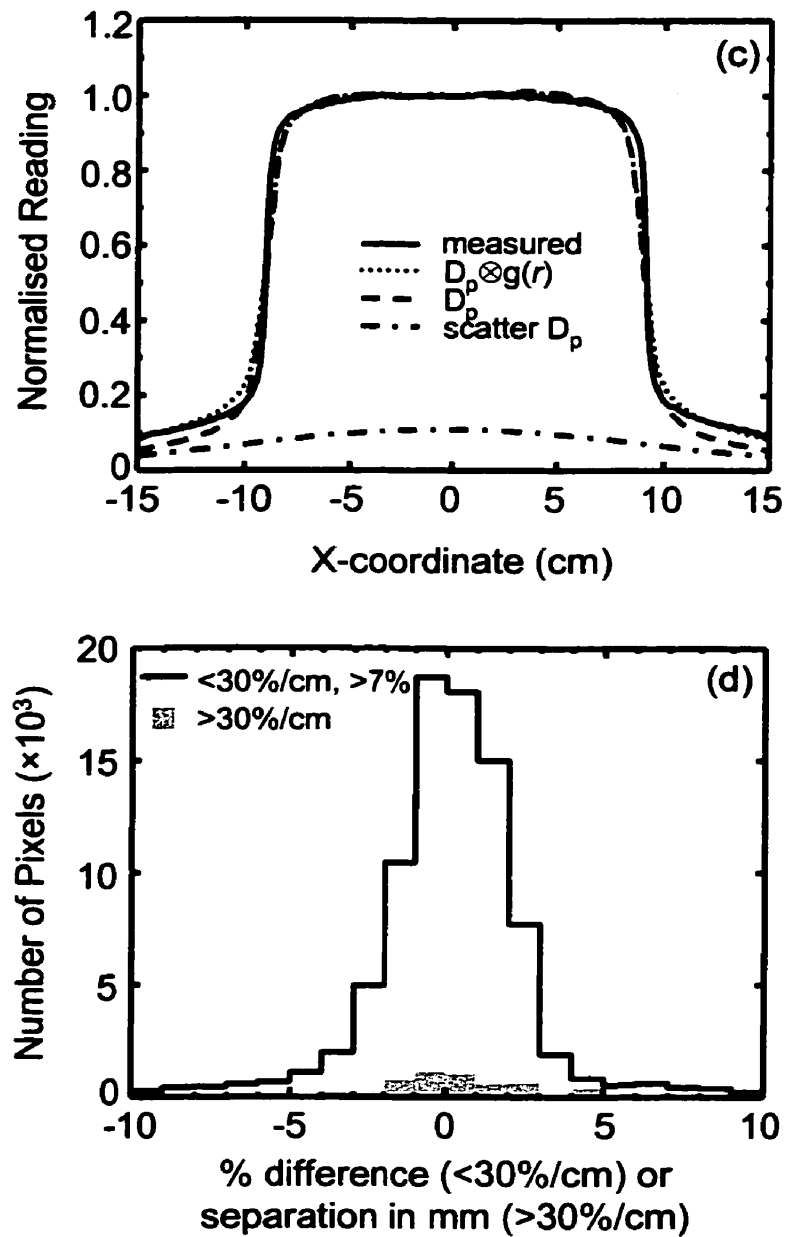


Figure 6.10 (continued): (c) Measured and predicted image profiles through isocentre at 120 cm SDD for a $15 \times 15 \text{ cm}^2$, 18 MV field incident on a 26 cm thick, homogeneous, water-equivalent slab using the aS500 in configuration B. Line labeling as in (a). (d) Analysis of comparison of measured and predicted images in (c).

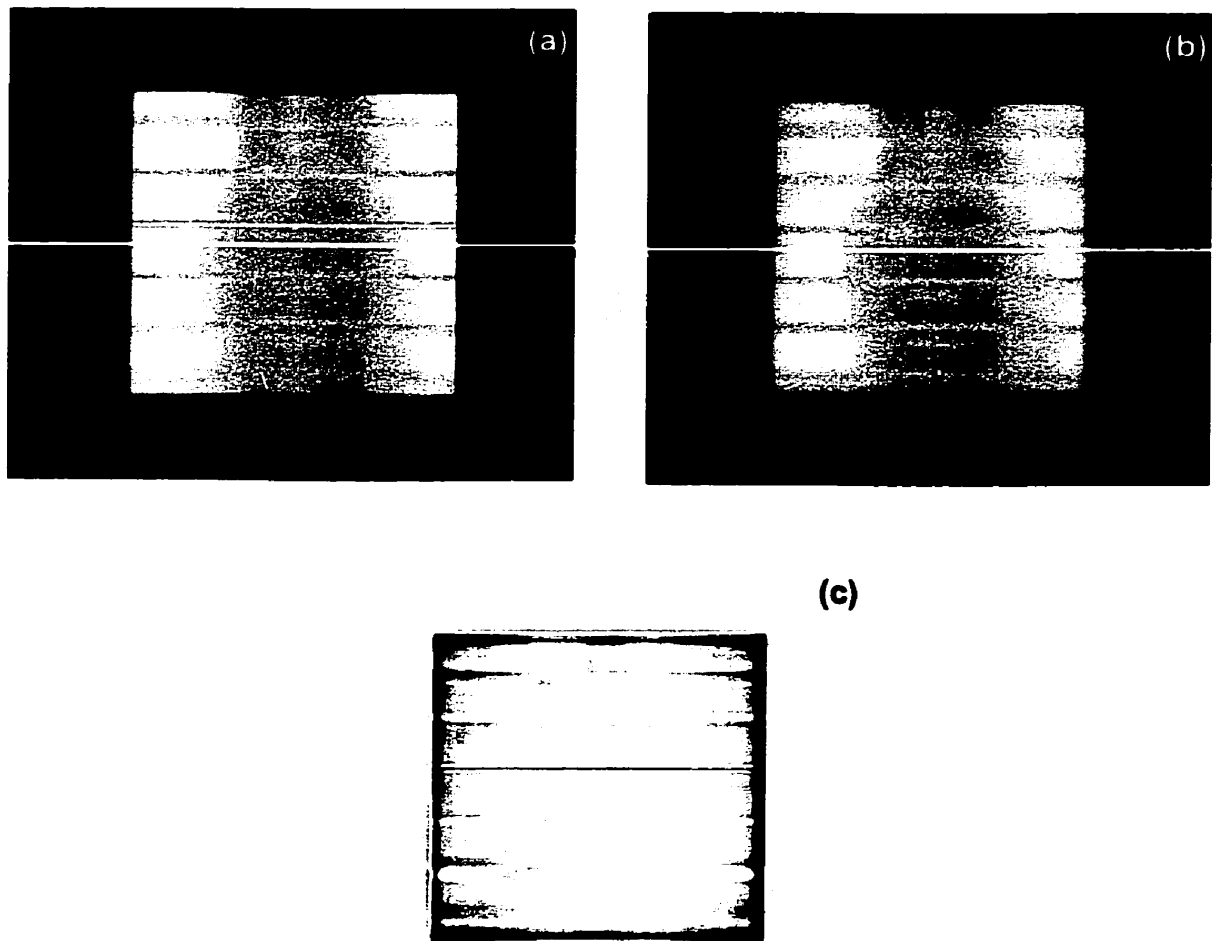


Figure 6.11: (a) Measured image at 130 cm SDD for a $15 \times 15 \text{ cm}^2$, 6 MV field incident on the chest of the Rando phantom. (b) Associated predicted image for configuration in (a). (c) Difference image using (a) and (b), 50% relative dose difference indicated by black, 0% relative dose difference indicated by white. Figure 6.11 continued on next page.

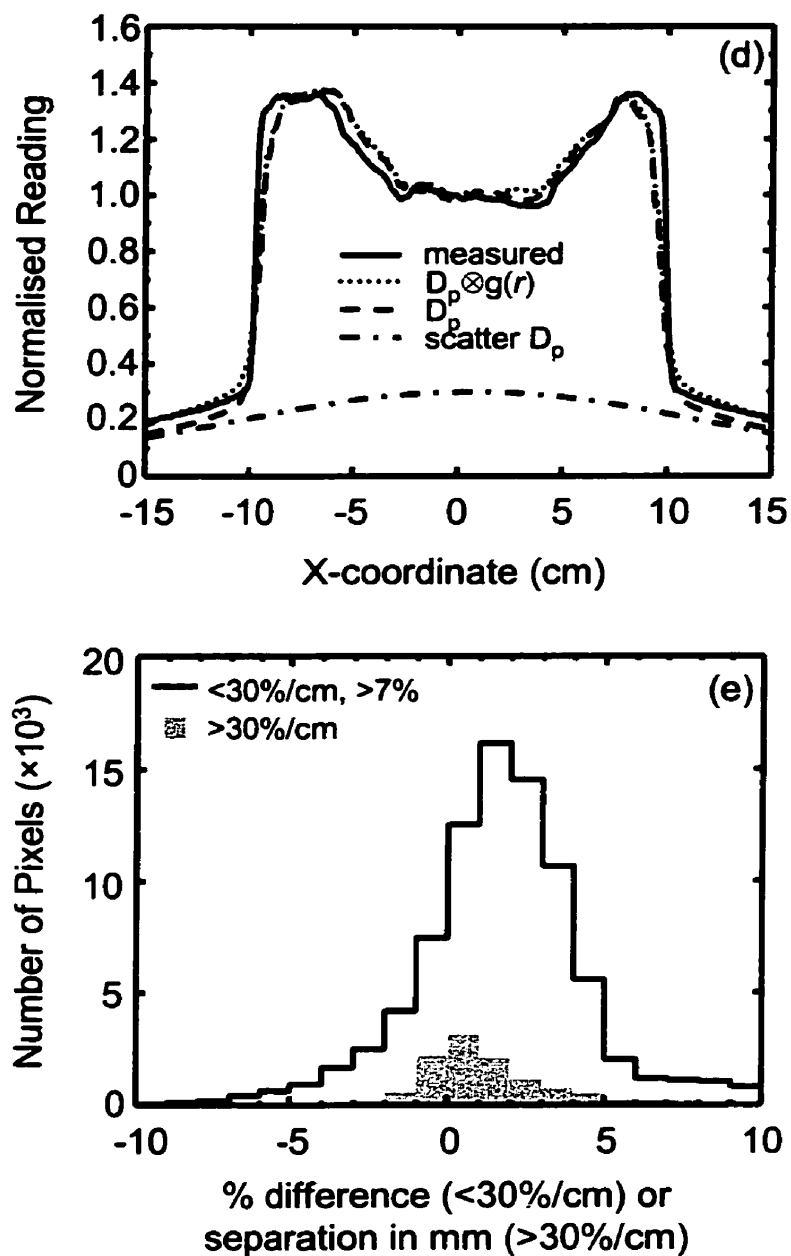


Figure 6.11 (continued): (d) Profiles taken transversely through the images in the location indicated by the white line in (a) and (b). Included are the measured data (solid line), predicted dose convolved with glare (dotted line), predicted dose without glare (dashed line), and scatter dose component (dash-dot line). (e) Analysis of comparison of measured and predicted images presented in (a) and (b).

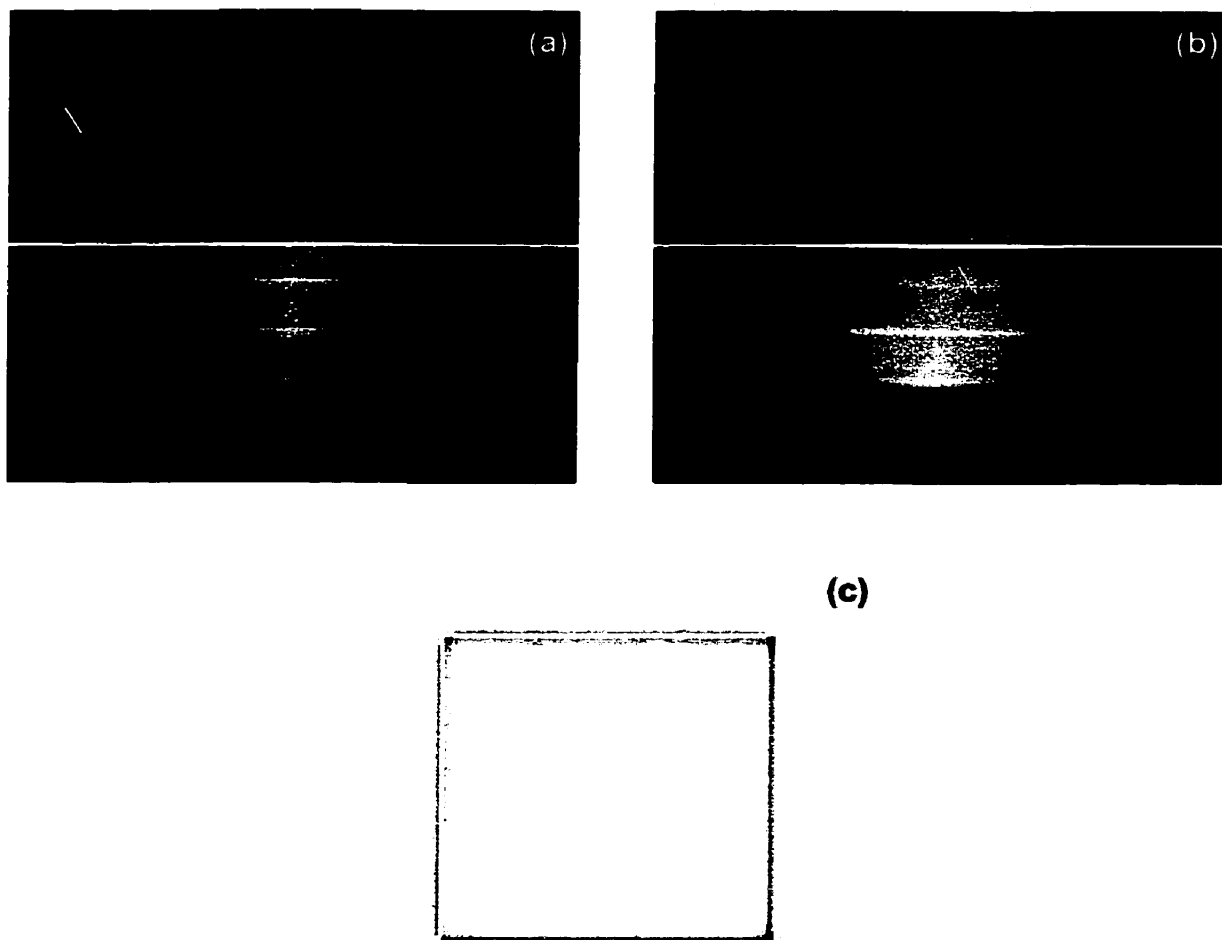


Figure 6.12: (a) Measured image at 130 cm SDD for a $15 \times 15 \text{ cm}^2$, 6 MV field incident on the pelvis of the Rando phantom. (b) Associated predicted image for configuration in (a). Note that a contrast enhancement function was applied equally to each image, strictly for improved visual clarity and not for analysis. (c) Difference image using (a) and (b), 50% relative dose difference indicated by black, 0% relative dose difference indicated by white. Figure 6.12 continued on next page.

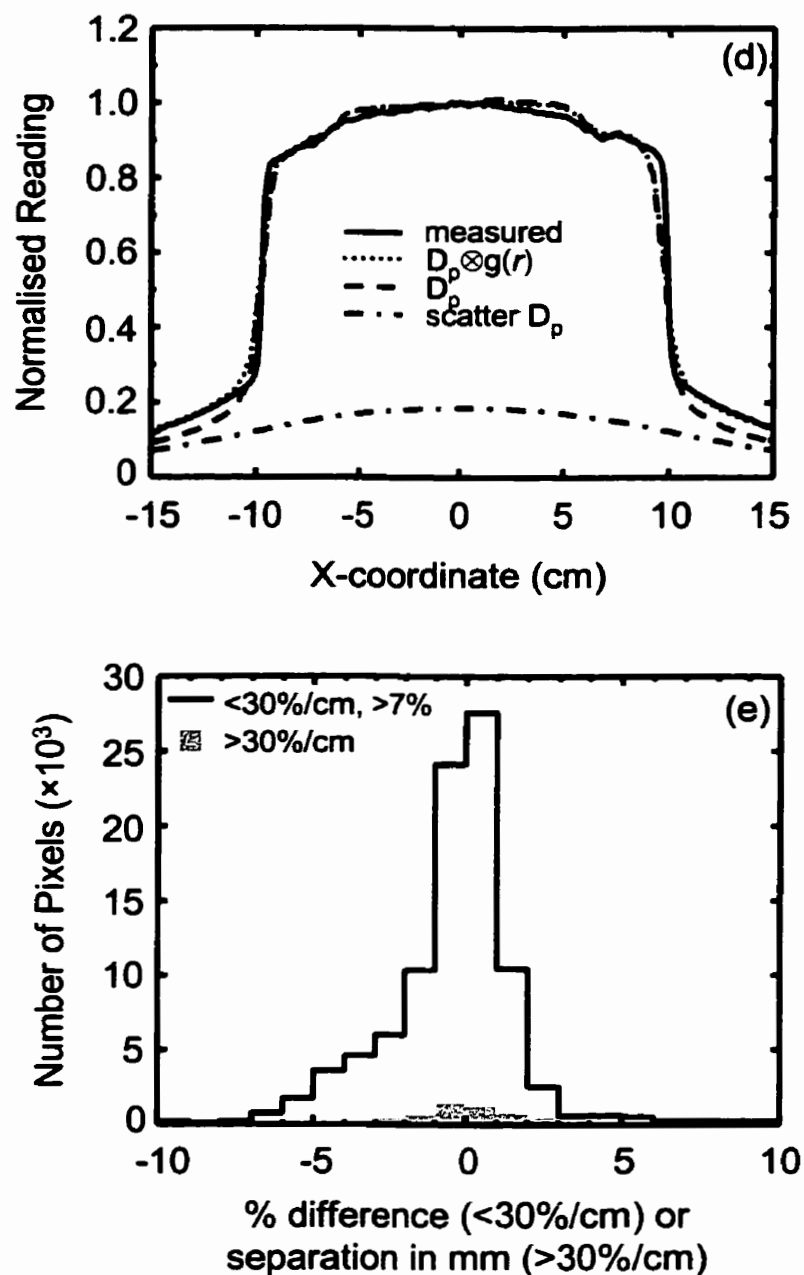


Figure 6.12 (continued): (d) Profiles taken transversely through the images in the location indicated by the white line in (a) and (b). Included are the measured data (solid line), predicted dose convolved with glare (dotted line), predicted dose without glare (dashed line), and scatter dose component (dash-dot line). (e) Analysis of comparison of measured and predicted images presented in (a) and (b).

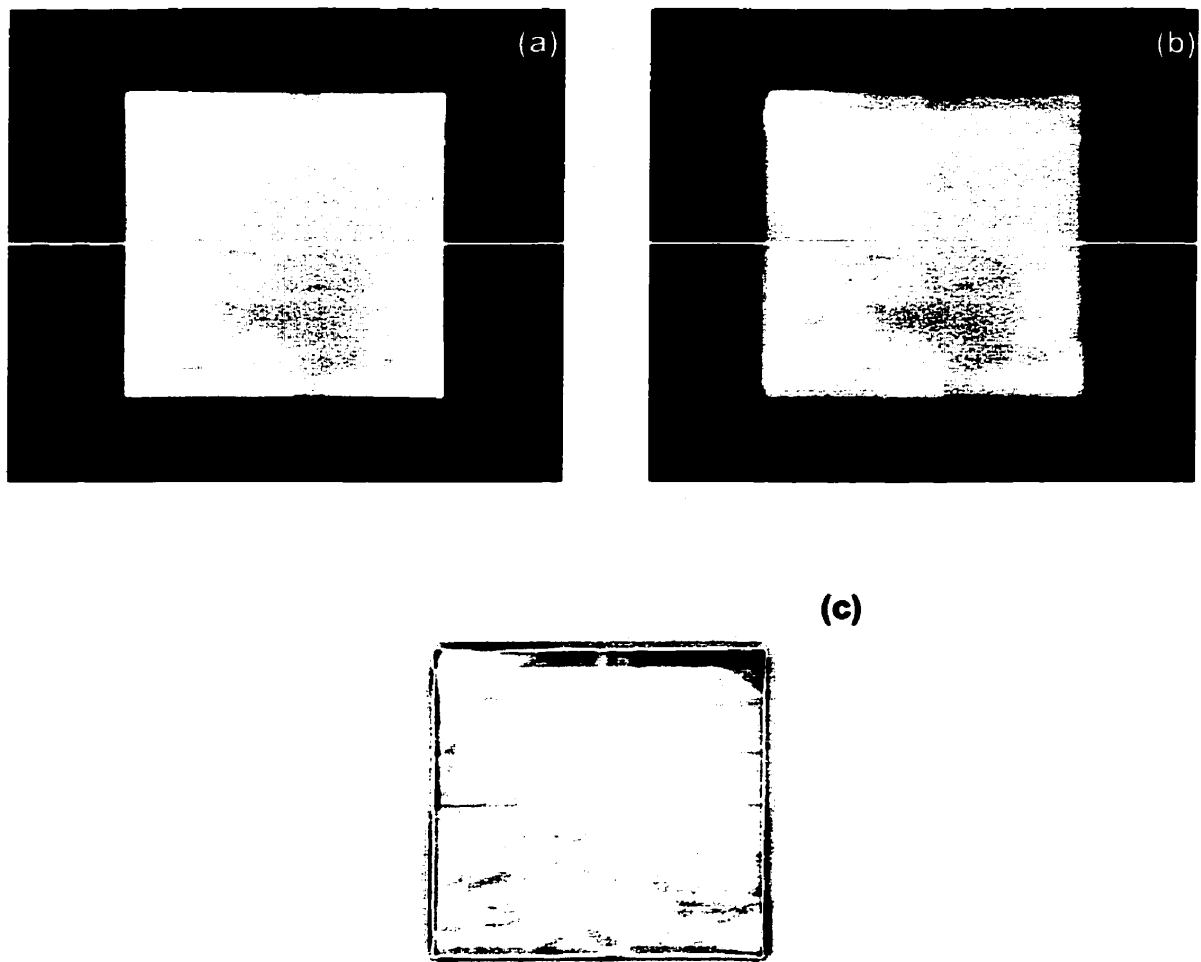


Figure 6.13: (a) Measured image at 130 cm SDD for a $15 \times 15 \text{ cm}^2$, 6 MV field laterally incident on the head of the Rando phantom. (b) Associated predicted image for configuration in (a). (c) Difference image using (a) and (b), 50% relative dose difference indicated by black, 0% relative dose difference indicated by white. Figure 6.13 continued on next page.

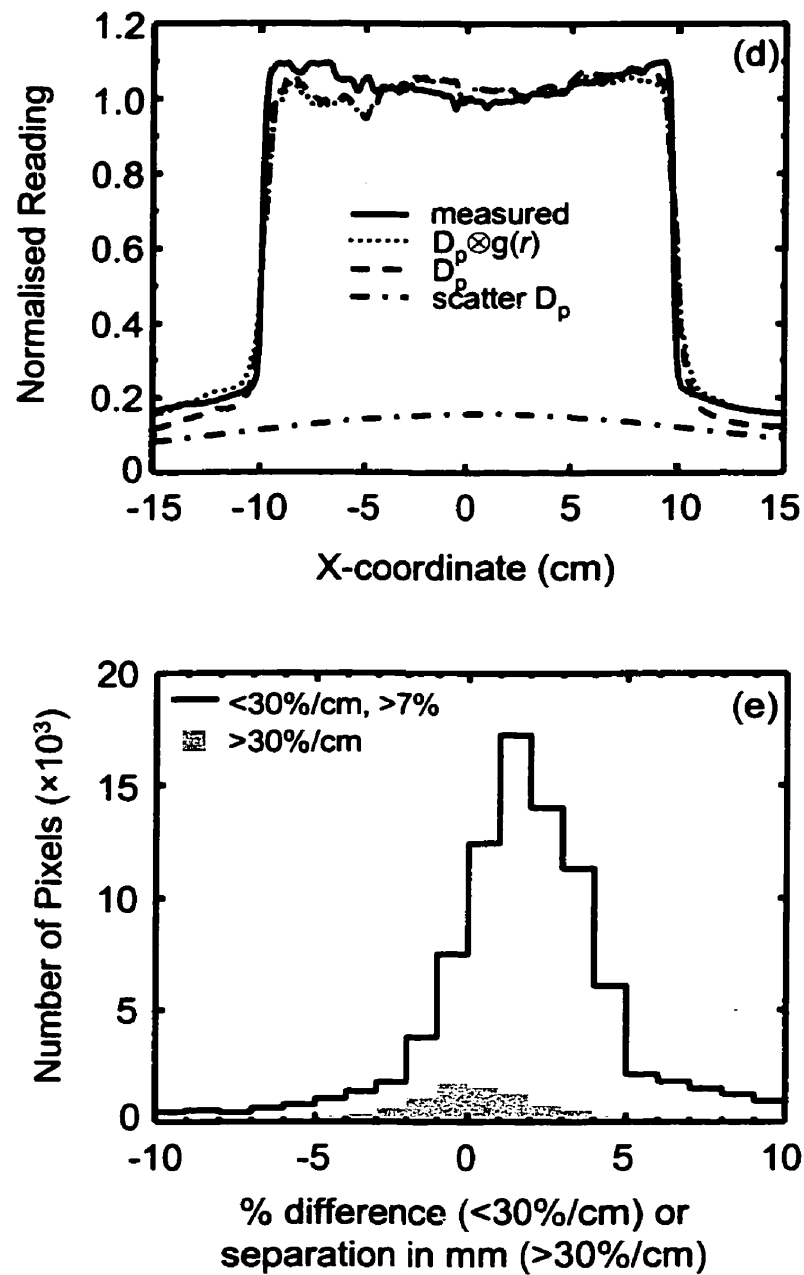


Figure 6.13 (continued): (d) Profiles taken transversely through the images in the location indicated by the white line in (a) and (b). Included are the measured data (solid line), predicted dose convolved with glare (dotted line), predicted dose without glare (dashed line), and scatter dose component (dash-dot line). (e) Analysis of comparison of measured and predicted images presented in (a) and (b).

In addition to accuracy, the algorithm speed is important. This is due to the trend towards more dynamic radiation treatments involving many or even moving beams. The total time to calculate a portal dose image at a $1 \times 1 \text{ mm}^2$ resolution over a $40 \times 40 \text{ cm}^2$ scoring plane is ~2 minutes on a Pentium PIII-550 MHz computer when coded in the Interactive Data Language (Research Systems Inc., Boulder, CO) programming environment. The majority of this time (approximately 75%) is spent on ray tracing through the CT data set to calculate the exact diverging radiological pathlength. Porting just this portion of the code into a lower level language is expected to bring the total calculation time to under thirty seconds per portal dose image on the current hardware platform.

6.4 Conclusions

The basic dosimetric characteristics of the aS500 amorphous silicon EPID have been investigated. The linearity with dose rate was found to be $\pm 2\%$ and the linearity with frame averaging was found to be $\pm 0.5\%$, sufficient for utilization in dosimetry. An examination of EPID images with increasing SDD indicated the presence of additional signal in the image which could not be accounted for through energy spectra and detector response arguments. However, this image data could be successfully explained through an optical glare effect occurring in the phosphor layer. The effect was modeled here by convolving a glare kernel with the predicted dose image to yield a result which may then be directly compared to the measured image. The glare kernel used was derived from the work of Heijman *et al.* [He95] on a video based metal/phosphor detector and modified to optimize the open field predictions in the aS500 EPID. The identification of a significant glare component in this type of detector is in contrast to previous work [Mu98a]. It was proposed here that the previous null finding was due to a small detector size (relative to the aS500) combined with a correspondingly small range of illuminated areas. The glare kernel in this chapter may be used in two ways. The convolution of the glare kernel with the predicted dose image provides a result that is comparable to the measured image. It is also possible to iteratively deconvolve the glare kernel from the measured image, to yield a dose image. However, only the former approach is investigated here.

Monte Carlo-generated dose kernels for the aS500 detector in two configurations (with and without additional buildup) were studied. Detector response analysis revealed that the inherent buildup is only adequate up to ~ 4 MeV photons, and that the photon

scatter occurring within the detector became significant at low energies (<2-3 MeV). Furthermore, the addition of buildup should improve image quality for photon beams >6MV, due to the increased detector response to primary photons.

A two-step algorithm for predicting portal dose images [Mc00c] was refined and validated on the aS500 amorphous silicon EPID, which served as a high atomic number detector. A water equivalent solid water slab phantom and three simulated treatment fields (mediastinum, pelvis, and lateral head) on an anthropomorphic phantom were studied. Beam energies of 6 and 18 MV and a range of air gaps (~20-50 cm) were used. Modeling of the glare effect was demonstrated to show improved comparison to measured data, especially in image areas outside of the primary field. Portal dose images in the phosphor and coupled to the glare model generally allowed prediction to within 5% in low dose gradient regions, and to within 5 mm (isodose line shift) in high dose gradient regions, of the measured image.

CHAPTER SEVEN

SUMMARY

7.1 Conclusion

When treating cancer patients using radiation therapy, outcome is dependent on destroying the cancerous tissue while simultaneously minimizing damage to healthy tissues. Verifying the geometric intersection of the treatment volume with the treatment beam leads to a reduced uncertainty in the dose delivery. Classically, geometric verification has been performed with radiographic film. This slow and labour-intensive approach has by and large been replaced with electronic portal imaging devices. Recently, researchers have begun exploring methods of extending electronic portal imaging devices to perform dosimetric measurements. This allows a two-dimensional dosimetric verification of each treatment in addition to the geometric verification, with no increase in time or labour costs.

The major proposed dosimetric applications of portal imaging devices include a comparison of measured and predicted images [Le86; Wo90a; Kr98], recalculating of patient dose distributions using measured dose images [Ha96; Mc96a; Yi90], and various estimates of exit dose or midplane dose [Bo97a; Bo97b; Bo98a; Bo98b; Ki93; Ki95]. The successful implementation of these applications requires the accurate calculation of dose deposited within the portal image detector.

To date, several methods have been proposed to predict portal dose images including the use of a patient dose calculation algorithm [Wo90a], the three-dimensional convolution/superposition algorithm [Mc96b], and two-dimensional pencil beam

algorithms [Ha97; Pa98a]. None of these methods has been shown to be applicable over the wide range of commercial and experimental portal imaging systems currently available. The patient dose calculation algorithm [Wo90a] is not accurate when scaling over the large air gaps involved [Mc96b]. The three-dimensional convolution/superposition algorithm has been shown to have problems with air gaps [Wo90b; Wo94] and when applied to high atomic number materials [Sa95]. The two-dimensional pencil beam approaches proposed to date are also limited. The approach taken by Pasma [Pa98a] requires an extensive series of measurements, requires a detector calibration to dose-to-water, and uses nonphysical scatter kernels which may not provide accurate results at shorter air gaps. The method proposed by Hansen [Ha97] is limited to a detector that approximates a photon counter, and has not been investigated over a wide range of air gap or beam energy. This group has recently moved away from fluence kernels generated with Monte Carlo simulation, towards an analytically-based approach. The recently proposed method [Sp00b] attempts to convert fluence to dose through an analytical approach assuming an ideal Compton recoil detector, which indicates 2-3% error for low atomic number detectors. A significant portion of the error is due to approximations in the dose conversion of multiply-scattered photon component [Sp00b]. The algorithm performs accurately for the singly-scattered photon component, but significant errors have been encountered in the multiply-scattered photon dose component when applying the method to high atomic number detectors (up to 8% of central axis signal [Sp00a]). According to Wong [Wo90a] this error is too high for dosimetric applications. In fact, Wong [Wo90a] recommended an accuracy of about 3% to elicit useful information from the comparison of predicted and measured portal dose images.

Therefore, portal dose calculations must be accurate to fully realise their potential applicability.

The main objective of this research was to devise an algorithm which will accurately predict portal dose images in arbitrary portal image detector systems, under a variety of clinically realistic conditions. The initial approach attempted to utilize equivalent-fields concepts, due to their simplicity and the extensive relevant experience of the supervisor in this particular area. This method was demonstrated to be too inaccurate for off-axis dose calculations within the patient, and was not pursued further for portal dose image prediction. However, the work effectively bridged two generations of dose calculation algorithms, allowing a unique redevelopment of the older equivalent-fields theory (one-dimensional) through the application of modern three-dimensional convolution dose calculation techniques. The equivalent-field investigation is presented in Appendix A of this thesis.

At that time, the available algorithms that had potential for portal dose image prediction were analysed and it was felt that a two-dimensional pencil beam approach was attractive due to the inherent speed advantages over three-dimensional convolution/superposition algorithms. The main objective of this thesis has been achieved with a two-dimensional, pencil beam style algorithm, which separates the fluence prediction and the conversion of fluence to dose into two stages. The development of this algorithm is detailed in chapters three through six.

Chapter three describes the calculation of the scattered photon fluence kernel libraries using Monte Carlo methods. These radially symmetric kernels have been generated for many thicknesses (1-50 cm) of homogeneous water slabs and at many air

gap values (0-100 cm). Incident photon energies used include monoenergetic 2.0 and 10.0 MeV spectra, and polyenergetic 6 and 24 MV spectra. The resulting kernels are examined for the behavior of fluence and mean energy with air gap, phantom thickness, and photon history. The kernels are further processed to yield scatter fractions, full width at half maxima, and modulation transfer functions, to augment the understanding of these kernels. The kernels are found not to have a strong dependence upon the exact nature of the incident energy spectra, and should therefore be widely applicable across linear accelerators made by different manufacturers.

A two-dimensional pencil beam style algorithm is described in chapter four. The algorithm implements the scattered photon fluence kernels generated in chapter three through a superposition of appropriate scatter kernels with the incident beam fluence. This yields a prediction of radiation field parameters of the scattered photon fluence entering a portal imaging detector plane. Factors such as air gap, field size, phantom geometry, incident beam resolution, and photon history affect the accuracy of this approach, and are therefore studied in detail. It was found that the algorithm is accurate to within 3% of maximum dose for a variety of phantom geometries and field sizes, when an air gap of 10 cm is introduced. This (or larger) size of air gap will allow enough scatter to diverge to ensure the accuracy of the predicted scatter fluence. This level of accuracy was considered sufficient, using ICRU24 recommendations [IC76], to justify further efforts into coupling the fluence prediction algorithm to a dose conversion algorithm.

Chapter five described the method by which the predicted primary and scattered photon fluence distributions are converted into dose images. The method permits

individual portal image detector systems to be modelled, given a knowledge of the geometry and material composition. Monte Carlo methods are used to calculate dose deposition kernels for a variety of incident photon pencil beams. These are then either convolved (for primary fluence) or superposed (for scatter fluence) with the predicted fluence distributions to yield separate estimates of primary and scatter dose images. The predicted dose images are compared to data measured with a linear array of 47 fluid-filled ionisation chambers. Simple slab and anthropomorphic phantoms (using lung and pelvis treatment sites) are examined, at 6 and 23 MV beam energies, and over a wide range of air gaps. The predicted dose images are compared to the measured dose profiles and are found to lie within 3% of maximum dose in regions of low dose gradient ($<30\%/cm$) and within 4 mm displacement in regions of high dose gradient ($>30\%/cm$).

Chapter six presents an investigation into some simple dosimetric properties of a high atomic number detector system, and also provides a validation of the algorithm against this type of detector. The amorphous silicon flat panel detector investigated in this chapter incorporates a metal/phosphor screen to generate an image composed of optical photons. Independence of response on dose rate ($\pm 0.5\%$), linearity with frames acquired ($\pm 2\%$), and response with variations in gantry rotation and source to detector distance were investigated. A 'glare' phenomenon (optical photon spread) was observed, and was characterised and modeled as a radially symmetric blurring kernel. This kernel was applied to the calculated dose images as a convolution and successfully accounted for the optical photon spread. The portal dose calculation algorithm was validated on a water-equivalent, solid slab phantom, and an anthropomorphic phantom were examined at beam energies of 6 and 18 MV and over a range of air gaps (~ 20 -50 cm). In the many

examples presented in this chapter, portal dose images in the phosphor were predicted to within 5% in low dose gradient regions, and to within 5 mm (isodose line shift) in high dose gradient regions.

The algorithm, as developed in chapters three through six, is able to overcome all of the major obstacles described in section 2.3.1. The algorithm has been demonstrated to accurately (using the guidelines of AAPM 62 [AA98]) predict portal dose images in thin and multi-layered detectors, as well as both low and high atomic number detectors. The algorithm has also been successfully demonstrated over a wide range of clinically relevant parameters, such as air gap, beam energy, and patient inhomogeneity. The algorithm execution time is fast and competitive with existing portal dose calculation techniques. It is expected that when ported to a computer language which provides better optimisation support, the execution time will be significantly better than that of any existing technique. Execution speed is becoming a more important factor as radiation treatments become more dynamic in nature, thus requiring more computational effort to generate enough dosimetric data for a treatment verification. Furthermore, the algorithm may easily incorporate any current or future detector system that may be modeled using Monte Carlo methods. To generate the necessary dose kernels for a detector system is straightforward and requires only elementary knowledge of the radiation transport code EGS4. This algorithm is a significant contribution to the field of radiotherapy, and enables the advancement and improvement of several proposed dosimetric applications of portal imaging systems. These will increase the overall accuracy and effectiveness of radiotherapy treatments, ultimately increasing cure rates of cancer.

7.2 Future Work

Two minor modifications of the algorithm may be made to enhance the overall applicability and clinical usefulness. These are: modeling of photon scatter and attenuation in compensators and physical wedges, and allowing input of incident beam fluence matrices from commercial treatment planning systems. Both of these could be easily accomplished if the algorithm was implemented into a commercial treatment planning system, which already implements these features for patient dose calculation. An added benefit of this would be the reduction of calculation time to well under 30 seconds per field, since the main time sink of the primary fluence calculation would already be done as part of the patient dose calculation.

Calculating the attenuation of primary photons in a compensator or physical wedge is straightforward if the thickness and material is known, whereas the photon scatter may be modeled using an analytical approach to calculate the singly-scattered photon fluence [Mc98a]. Multiply-scattered photon fluence due to compensators or physical wedges will be small compared to singly-scattered fluence, since the materials are generally thin (0.1-1.5 cm of metal), will be disproportionately attenuated by the patient since they are of lower energy, and will diverge more quickly, since they exhibit higher exit angles with respect to the incident beam direction. Often, the scatter from beam modifying devices is ignored in patient dose calculations, and this is likely be a better approximation for portal image detectors, due to the increased distance from the beam modifying device. Many of the state-of-the-art 3D superposition algorithms currently implemented on some of the commercial treatment planning systems, already

account for attenuation and beam hardening of primary photons through beam modifying devices.

The use of commercial treatment planning systems to provide an estimate of incident beam fluence would be a significant step towards clinical adaptation of the algorithm, by providing one of the necessary *a priori* data sets. With the increasing use of intensity-modulated radiotherapy techniques, some commercial treatment planning system vendors have implemented beam fluence export options. Unfortunately, the systems at this institute do not currently possess licensing for these fluence export features, although it is being considered for the future. When appropriate licensing is obtained, the impact of the additional uncertainty of the exported incident beam fluence data would have to be studied. Clearly, the accuracy would be directly dependent on the quality of the 'head scatter' model implemented. A more attractive method of accessing the incident beam fluence data would be implementation of the algorithm in a commercial treatment planning system. This would save having to export and import beam fluence data.

An important dosimetric application of predicted portal dose images is the comparison to measured images to reveal treatment setup errors, which may then be corrected through either intra- or inter-treatment intervention. The clinical feasibility of this application is greatly enhanced if the comparison is completely automated, and done quickly (within the first few seconds of treatment) to allow immediate intervention. Exploratory work in this area has begun, by examining the application of neural networks to identify simple setup errors, and much more work needs to be done. This will require research to obtain a better understanding of the differences between the measured and

predicted images. It is not yet known if the set of possible image differences will lead to a unique indication of the cause of the treatment error. Furthermore, tolerances will need to be set for the image differences. For example, what will constitute an ‘acceptable’ image difference that will not impact patient treatment by over 3%? These tolerances will probably need to be determined experimentally and may vary depending on treatment site.

The proposed back-projection method of dose verification [Ha96; Mc96b] will benefit from an accurate portal dose calculation algorithm. However, this approach assumes the patient CT data set acquired during simulation is the same during treatment (which is generally untrue). Backprojection of fluence and subsequent recalculation of dose within the patient will lead to higher uncertainties in this distribution due to the assumption of static CT data, as well as additional errors introduced by the backprojection. Although the portal dose image comparison approach discussed above also assumes static CT data, any treatment delivery error could be identified and corrected within the first few seconds of treatment (e.g. *without* requiring a backprojection calculation). However, if radiotherapy treatments begin incorporating megavoltage CT, or when tomotherapy [Ma99] becomes clinically available, the patient CT data may be collected at the time of treatment. This would allow a more accurate use of both the backprojection approach and the dose image comparison method, since the patient CT data would more exactly represent the patient at the time of treatment.

Intensity modulated radiation therapy (involving extremely complex beam deliveries with gantry and multileaf collimator movement during treatment) is a state-of-the-art application where this algorithm could have a direct impact. Currently, only

pretreatment verification of the radiation delivery is possible. This involves delivery of the treatment to a radiographic film phantom [Ch96] or gel dosimeter [OI98] to estimate patient doses. Alternatively, the treatment may be delivered to a portal imaging device, without any phantoms (or patient) present to attenuate the beams or generate scatter [Cu99; Ma97; Pa99b; Pa00]. This approach can be used to verify leaf movement or incident fluences. An extension of this method would be to accumulate portal images throughout the treatment with the patient present, and compare these to predicted portal images. This could provide a dosimetric treatment verification of the entire treatment delivery.

APPENDIX A¹

DETERMINATION OF EQUIVALENT PHOTON FIELDS THROUGH INTEGRATED 1D CONVOLUTION KERNELS

A.1 Introduction

Equivalent field relationships are based on the equality of central axis depth dose curves for variously shaped fields [Da96]. This is the most commonly accepted definition and will be used in this appendix. It is acknowledged that alternate definitions exist (e.g. Tatcher and Bjärngård [Ta93]). The equivalent field relationships developed in the British Journal of Radiology Supplement 25 [Da96] using measured data, may be examined with 3D scatter kernels used in convolution dose calculation techniques, and produced by Monte Carlo simulation. The use of Monte Carlo-generated data overcomes several difficulties associated with measured dose quantities, including: (a) inability to separately determine primary and scatter components, (b) lack of lateral electronic equilibrium at small field sizes [Ri90], (c) conversion of measured square field data to theoretical circular field data, and (d) extrapolations of measured dose to zero-field size, which are susceptible to uncertainties [Bj88].

The convolution method for the calculation of three dimensional dose distributions in homogeneous or heterogeneous media is an accepted, physically sound operation involving the convolution of a map of energy deposition with a function representing the primary fluence distribution [Ba92]. The map is generally termed the energy deposition kernel and often computed using Monte Carlo methods. The use of

¹Based on [Mc99]

one-dimensional kernels has been examined previously with empirical approaches [Jo49, Iw85, Iw90] and Monte Carlo generated data [Fi88, Ba97]. In this appendix, Monte Carlo generated scatter kernels and a one-dimensional convolution approach are used to investigate the properties of “equivalent fields” of radiation.

An equivalent field relationship associating circular to square fields will be derived and compared to the BJR 25 empirical data. The good comparison provides evidence that phantom scatter behavior is mainly responsible for the functionality of equivalent field relationships. The use of a single circular to square field relationship for high energy photon beams (cobalt-60, 6 MV, and 24 MV) will be validated through a demonstration. This energy independence of the equivalent field tables has been unclear to date [Ve97, Mc98b].

It will be shown that choosing an equivalent field implies an optimal matching of central axis depth dose curves at a single depth. Furthermore, the extent to which the equivalent field concept loses validity for highly elongated fields, highly irregular field shapes, and points away from the central axis will be demonstrated.

A.2 Theory

A.2.1. Integrated 1D kernels for dose calculation

The convolution approach to predicting dose deposition is well known [Ma85, Ah87, Ho94]. Only a review of the relevant portions will be presented here.

A point spread function describing the spatial energy deposition around a primary interaction site may be calculated through Monte Carlo simulation. This point spread function is generally termed the energy deposition kernel (EDK). When spatial invariance of the EDK is assumed, the dose deposition arising from scattered radiation transport through a medium may be modeled as a pure convolution process of the EDK and the primary fluence distribution. Scoring the energy deposited via charged particles arising from primary interactions separately from the energy deposited via charged particles arising from scattered photons allows the “primary dose” distribution and the “scattered dose” distribution to be calculated separately. Mathematically, one may express the dose as a superposition integral in 3D between the EDK and *terma* (the total energy released per unit *mass*, which is proportional to the primary fluence). For monoenergetic primary photons of energy E_p in a homogeneous medium and parallel geometry, the kernel is invariant, and thus the superposition reduces to a convolution yielding the dose as:

$$D_{3D} = \left(\frac{\mu}{\rho}\right)_p \cdot (E_p) \cdot (\Phi \otimes K_p + \Phi \otimes K_s) \quad (\text{A.1})$$

where D_{3D} is the dose deposited, K_p is the primary EDK, K_s is the scatter EDK, and Φ is the primary fluence. For a polyenergetic incident spectrum, this calculation is repeated for each energy bin in the incident spectrum [Pa93].

By pre-integrating the full three dimensional EDK in the transverse dimensions over limits of the defined field bounds, an integrated 1D kernel representation along the depth axis (z) is obtained for a particular calculation point of interest in the transverse plane (x, y). Pre-integrating the scatter kernel and then performing a 1D convolution with depth is mathematically equivalent to a full 3D convolution approach [Fi88, Ba97]. Thus, convolving the primary fluence with the integrated 1D kernel for a particular transverse plane calculation point and incident field definition will yield the same dose distribution along the depth axis as a full 3D convolution calculation. This approach is inadequate for use as a modern clinical dose calculation engine (due to the constraining assumptions of a homogeneous medium of uniform thickness, and parallel incident beam), but is extremely useful for studying equivalent fields relationships, due to the summary of information onto a common depth axis.

The 1D kernel approach relies on a Monte Carlo-generated 3D cylindrical kernel data set and Clarkson radial integration to generate an appropriate 1D kernel for an arbitrary transverse plane calculation point (x, y), as illustrated in Figure A.1. Since the kernels are scored in ring shaped voxels, the angular integration of the kernel around the interaction point is implicitly performed. The integrated 1D kernel (K_{1D}) at point (x, y) may be calculated using the scatter EDK (K_s) and the incident beam fluence profile (Φ_{2D}) as:

$$K_{1D}(x, y, z) = \int_0^{2\pi} \int_0^{\infty} K_s(r, \theta, z) \cdot \Phi_{2D}(r, \theta) r dr d\theta = \int_0^{\infty} K_s(r, z) \cdot \left(\int_0^{2\pi} \Phi_{2D}(r, \theta) d\theta \right) r dr \quad (\text{A.2})$$

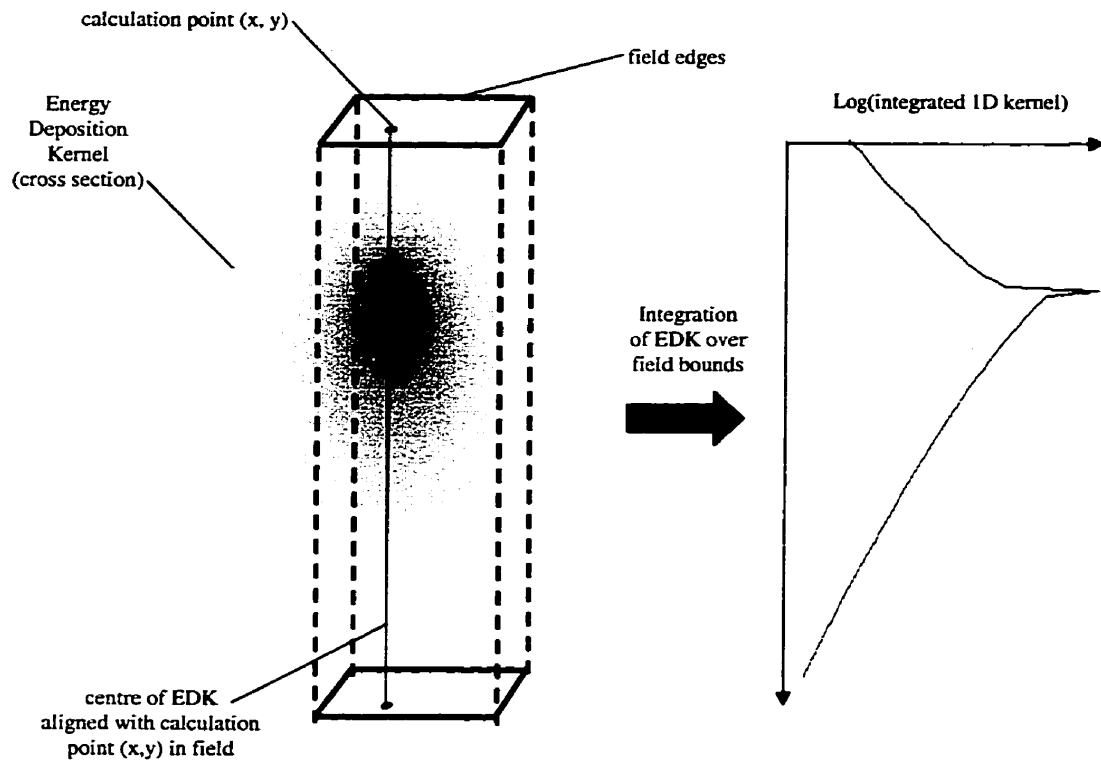


Figure A.1: Integration of a three-dimensional energy deposition kernel over defined field bounds, after alignment with transverse plane calculation point (x, y) . This results in the integrated 1D kernel valid for that calculation point and given field.

The scatter kernels are generated in homogeneous water and are therefore representative of phantom scatter contributions. Any derived equivalent field relationships are then characterizing phantom scatter behavior only, and do not include possible head scatter dependencies. Furthermore, the integrated 1D kernel method developed here does not account for divergent beam geometry, which would require a full superposition approach. However, equivalent field relationships generated in a parallel geometry produce good central axis agreement in diverging geometry. This important assumption was verified by comparing Monte Carlo simulated central axis depth dose curves for square and equivalent rectangular fields, as described in section A.3.3.

The integrated 1D kernel convolution method allows a direct and simple comparison of kernels and associated depth dose curves at arbitrary transverse calculation points and for arbitrary field shapes. This useful characteristic allows modern convolution dose calculation techniques to be used to study equivalent fields, since information is summarized onto the depth axis.

A.2.2. Equivalent Fields

The common definition of equivalent fields is “any set of fields which possess the same central-axis depth dose characteristics [Da96]”. For a given energy spectrum incident on a homogeneous medium and assuming lateral electronic equilibrium, the primary component of the central axis depth dose for any shaped field will be the same, and only differences in the scatter component will affect the final shape of the central axis depth dose. Therefore, convolution dose calculation theory implies that it is the difference in scatter contribution and hence the scatter kernel, that ultimately determines

the equivalency of various fields. In the convolution approach to scatter calculation, two factors affect the final scatter estimate: 1) the integrated energy of the scatter kernel, and 2) the shape of the scatter kernel. These factors are a direct consequence of convolution mathematics. If the kernel shape is similar (as for centred square and circular fields), then the differences in the total integrated kernel energy will dominate the differences in the resulting calculated scattered dose. Thus, equivalent field relationships may be derived by comparing the integrated energy of the kernels, when the kernels are of similar shape. In situations of lateral electronic disequilibrium, for which the depth dose will also be affected by the primary kernel, factors (1) and (2) above for both primary and scatter kernels must be used to determine field equivalency. In this appendix, only situations where lateral electronic equilibrium exists will be considered.

A.3 Methods

A.3.1 Generating scatter kernels using Monte Carlo simulation

Monte Carlo simulation using EGS4 [Ne85] is employed to determine the EDKs in a cylindrical coordinate system. A modified version of the user code INHOMP was used to generate the EDKs in a cylindrical geometry. This serves to remove sampling problems encountered if a discrete data set scored in a spherical coordinate system (e.g. as generated by Mackie *et al* [Ma88]) were to be used for integration over cylindrical bounds onto the depth axis. Scoring of deposited energy was separated into: (a) primary photon interactions (the primary kernel), and (b) scattered photon interactions, as well as bremsstrahlung and positron annihilation events (the scatter kernel). Incident photons were forced to interact at a point deep within the phantom geometry. This biasing was offset by weighting the photon and all its daughter particles by the photon's probability of interacting in the phantom. The scoring voxels were defined to ensure high resolution in areas of rapid energy deposition falloff (0.05 cm around the interaction point). Scoring regions consisted of disks of varying thickness centred on and perpendicular to the depth axis, and partitioned by radial bounds (see Figure A.2). The kernels were scored in a water slab 300 cm thick, with radial boundaries extending from 0.1 cm up to 1000 cm radius. The forced interaction point lies at a depth of 60.0 cm within the scoring geometry, allowing forward scatter to be tracked to 240 cm and back scatter to 60 cm. The EGS4 transport parameters ECUT and PCUT were set to 0.551 keV and 0.01 keV respectively, and all kernels were simulated using 5×10^6 incident photons.

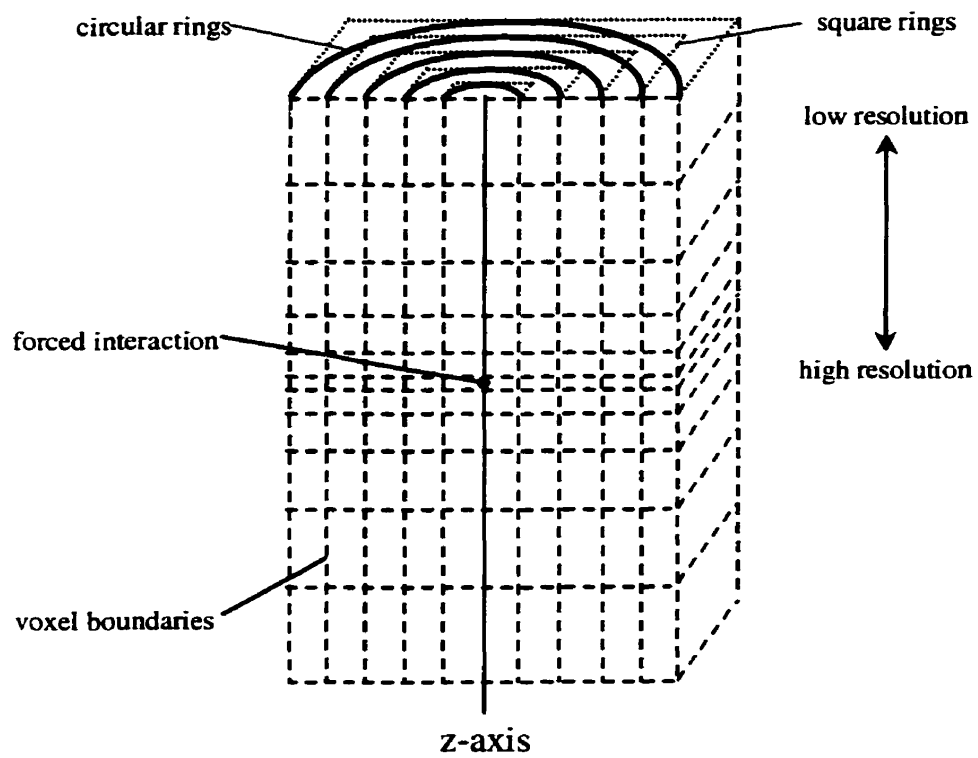


Figure A.2: Cylindrical scoring geometry for Monte Carlo simulation of energy deposition kernels. Square ring geometry was scored simultaneously.

Kernels were generated for monoenergetic energies ranging from 0.1 MeV to 22 MeV. The accuracy of the integrated 1D kernel calculation method was verified for polyenergetic spectra via comparison with such experimentally measured parameters as tissue maximum ratio (TMR) tables. Furthermore, an independent polyenergetic (6 MV beam) Monte Carlo simulation of a 15×15 cm² field was used to verify the accuracy of the integrated 1D kernel dose calculation approach applied at points off of the central axis.

A.3.2 Deriving equivalent fields through conservation of energy

The Monte Carlo code used to generate the cylindrical kernels was modified to simultaneously score energy deposition in square annular 'rings', as illustrated in Figure A.2. Integrating the kernel contributions from within square and circular shaped transverse bounds yields total energy deposited by scatter kernels for various field sizes (through reciprocity), thus creating ideal data sets that may be used to verify circular to square field equivalence relationships. This concept may be extended to fields of arbitrary shape, whereby an integration of energy over the field bounds yields the contained energy. A unique equivalent circular or square field may be obtained by equating the integrated energies. This method is hereafter referred to as COE (for conservation of energy approach).

Fitting an analytical function to the Monte Carlo-scored scatter kernel data reduces the effects of statistical noise. The directly scored square field data may be used to verify the accuracy of the analytic fit to the circular field data. Previous work has demonstrated that the derived equivalent fields are not critically sensitive to the exact

nature of the scatter radius function used [Ba56, As80, Da96]. Therefore, a function similar to the BJR 25 scatter radius function but providing a significantly better fit to the kernel data is chosen:

$$S_r = A[1 - \exp(-Br^c)] \quad (\text{A.3})$$

where A , B , and C are fitting parameters, and S_r describes the integrated kernel energy as a function of radius. Parameter A represents the total energy contained in the scatter kernel, B and C govern the increase of equation (A.3) with field size. A unique energy-radius relationship is generated for each polyenergetic beam energy spectra by summing the spectrally weighted result from each monoenergetic kernel.

These relationships may be used in a similar manner as the scatter radius function [Da96] to derive the equivalent square field for a particular circular field radius. However, these relationships: (1) have been derived using Monte Carlo simulation, (2) allow an equivalent field choice to be made based on conservation of energy of the integrated 1D scatter kernel, and (3) yield an associated equivalent field kernel which may be used to generate a depth dose curve using convolution techniques.

A.3.3 Application to equivalent fields concepts

The COE approach was used to generate equivalent field relationships for circular, square, and rectangular fields, using cobalt-60, 6 MV, and 24 MV energy spectra [Ha87, Mo85]. These were compared to BJR 25 data.

A comparison of Monte Carlo simulated central axis depth dose curves between parallel and diverging beams was made. EGS4 with user code DOSXYZ was employed to generate central axis depth dose data for two pairs of square and equivalent rectangular

fields, using a 6 MV energy spectra incident on a large cube of homogeneous water. The equivalent rectangular field choice was made using the COE approach, which assumes a parallel incident field. The field size pairs simulated were a 10x10 cm² and equivalent 17x7 cm², as well as a 27x27 cm² and equivalent 45x20 cm². For the diverging geometry the simulation assumed an ideal point source at 100 cm SSD, and field sizes were defined at the phantom surface. For the 10x10 cm² and 17x7 cm² fields, the average percentage differences over 0-30 cm of the central axis depth dose curve were 1.5% and 1.6% for the parallel and diverging geometries respectively, whereas the average statistical uncertainties (added in quadrature) were 2.0% and 2.3% respectively. For the 27x27 cm² and 45x20 cm² fields, the average percentage differences were 2.9% for each of the parallel and diverging geometries respectively, whereas the average statistical uncertainties were 2.5% and 2.8% respectively. The differences in the results of the parallel and diverging geometries are small, and this supports our contention that the equivalent field relationships generated within a parallel framework will be valid in a diverging geometry.

The validity of the equivalent field method for highly elongated rectangular treatment fields (specifically, 30x2 cm² field and cobalt-60 spectrum) was investigated. This was accomplished through comparison of the actual 1D kernel on the central axis (that is, the kernel resulting from integration over the given field bounds) with equivalent circular fields' 1D kernels and depth dose curves. Both COE equivalent and BJR 25 equivalent fields are examined. It is demonstrated that an equivalent field will only provide an exact depth dose match at a single depth.

Compared to the BJR 25 tables, the COE method predicts equivalent fields that provide a better depth dose curve match over all depths, since information from the entire kernel depth range is used. In contrast, the BJR 25 equivalent field tables are generated by dose matching at a depth of 10 cm, which is a clinically practical choice for a significant number of treatments. The COE method may be modified to ensure matching depth dose curves at a specific depth by generating the energy-field size relationship (equation A.3) using scatter kernels truncated along the z -axis. This approach generates equivalent fields with better depth dose matching over the range of kernel truncation (i.e. over shallower portions of depth dose curves). This modified approach is shown to provide an equivalent field with an exact depth dose match at 10.0 cm depth, for the same elongated field scenario as above ($30 \times 2 \text{ cm}^2$).

The equivalent fields technique applied to off-axis points has been previously examined by Tatcher and Bjärngard [Ta93], and hence the validity of the COE method as implemented in the present work was investigated for off axis calculation points (both inside and outside of the defined beam). This study consists of a direct comparison of both 1D kernel shape and resulting depth dose curves of actual kernels and COE equivalent kernels generated at various off-axis points, within and around an incident $15 \times 15 \text{ cm}^2$ field exhibiting an ideal step profile and cobalt-60 energy spectrum.

A.4 Results and Discussion

A.4.1 Validation of integrated 1D kernel dose calculation technique

The accuracy of the integrated 1D kernel dose calculation method was verified by comparison with a Monte Carlo simulation of a three-dimensional isodose distribution of a $15 \times 15 \text{ cm}^2$ uniform field, using a polyenergetic 6 MV spectrum. The voxel size in the full 3D simulation was $1.0 \times 1.0 \times 0.5 \text{ cm}^3$ from the surface to a depth of 7.0 cm, then 1.0 cm^3 for the remainder of the phantom. Good comparison was observed in the isodose distribution of a midplane, with the largest differences occurring in regions of high dose gradient (Figure A.3). Only 7.5% of the midplane voxels differ by more than 2% of the maximum dose. The method was also compared to central axis tissue-maximum ratios (for 6 MV and 24 MV spectra), and tissue-air ratios for a cobalt-60 beam spectrum using experimental data presented in the CRC Handbook [Ja93] and the BJR 25. For a $15 \times 15 \text{ cm}^2$ field, the 1D kernel convolution dose calculation results agree to within 1.5% of maximum TMR in regions of charged particle equilibrium for all energy spectra. Therefore, the integrated 1D kernel dose calculation yielded results in agreement with Monte Carlo simulation for a parallel, uniform square field incident on a homogeneous water slab.

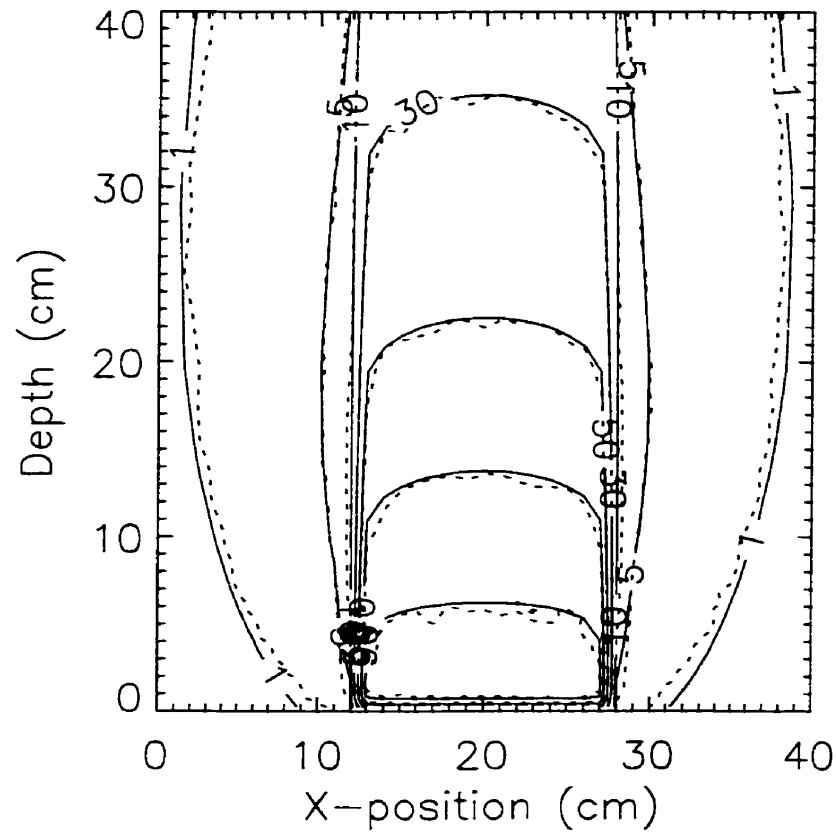


Figure A.3: Isodose lines generated for the midplane of a $15 \times 15 \text{ cm}^2$ square incident field and 6 MV spectrum using the integrated 1D kernel convolution approach (solid lines), and Monte Carlo simulation (dotted lines). Shown are 1%, 5%, 10%, 30%, 50%, 70%, and 90% isodose curves.

A.4.2 Deriving equivalent field relationships through conservation of energy

For circular fields, the total integrated scatter energy deposition as a function of radius was modeled with equation (A.3) as described in section A.3.2. The analytical fit and Monte Carlo-integrated data sets are compared in Figure A.4. The fit parameters were determined using a robust non-linear Pearson minimization (provided by commercial curve fitting software), and the relevant fit statistics are listed in Table A.1. A rough estimation of the total energy contained within the scatter kernel was performed to verify the validity of the value of parameter A . The calculation consisted of summing the difference between the incident photon energy and the average energy absorbed per photon [Jo83], per spectral energy bin, over all energy bins. This calculation yielded results which agreed with the fit parameters to within 3.5% (Table A.1).

The total scatter energy contained within a given square field was obtained by Clarkson radial integration of the analytical function describing the circular field data, over the square field limits. For any given circular field, an associated equivalent square field may be chosen based on conservation of energy (Figure A.5). The resulting equivalent field relationship compares well to the BJR 25 data at the zero field size limit, but diverges at larger field sizes. Differences are, however, only ~2% at 60 cm diameter field size. This circular to square field conversion relationship is found to be similar over widely varying incident energy spectra.

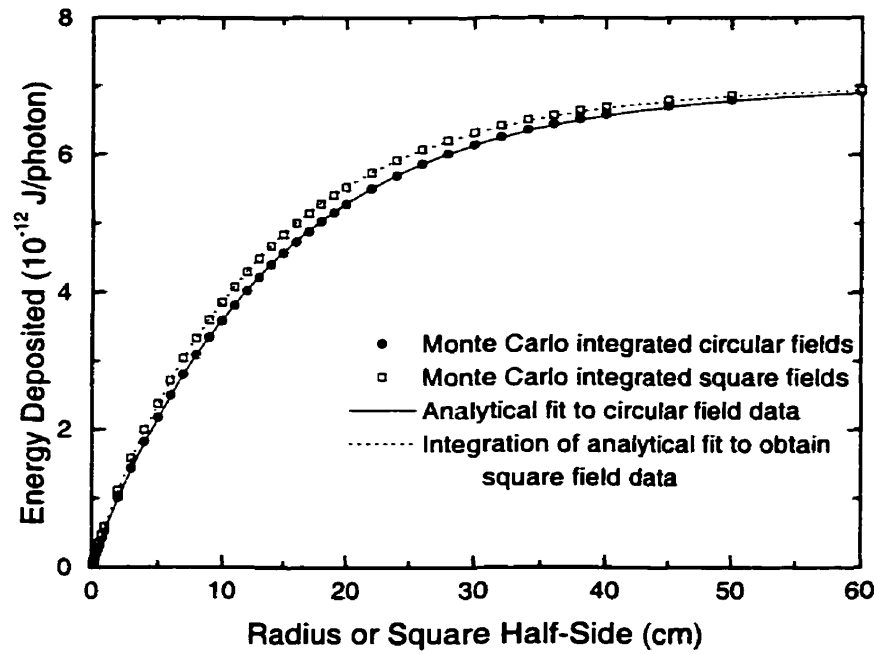


Figure A.4: Total integrated energy of scatter kernel versus field size (related to kernel radius via reciprocity) for a 6 MV spectrum. The analytical fit to the circular field data is used to generate square field data and is compared to directly simulated results.

	Cobalt-60 spectra	6 MV spectra	24 MV spectra
A (joules/photon)	6.333×10^{-12}	7.019×10^{-12}	8.66×10^{-12}
Standard Error in A	0.006×10^{-12}	0.006×10^{-12}	0.02×10^{-12}
B (cm^{-1})	0.0726	0.0773	0.087
Standard Error in B	0.0006	0.0005	0.001
C (unitless)	0.986	0.967	0.946
Standard Error in C	0.003	0.003	0.006
F-value	379562	526041	102395
A (theoretical estimate)	6.3×10^{-12}	7.1×10^{-12}	8.9×10^{-12}

Table A.1: Fit statistics for the total integrated scatter kernel energy, using equation (A.3), and theoretical estimate of fit parameter A (see text for detail).

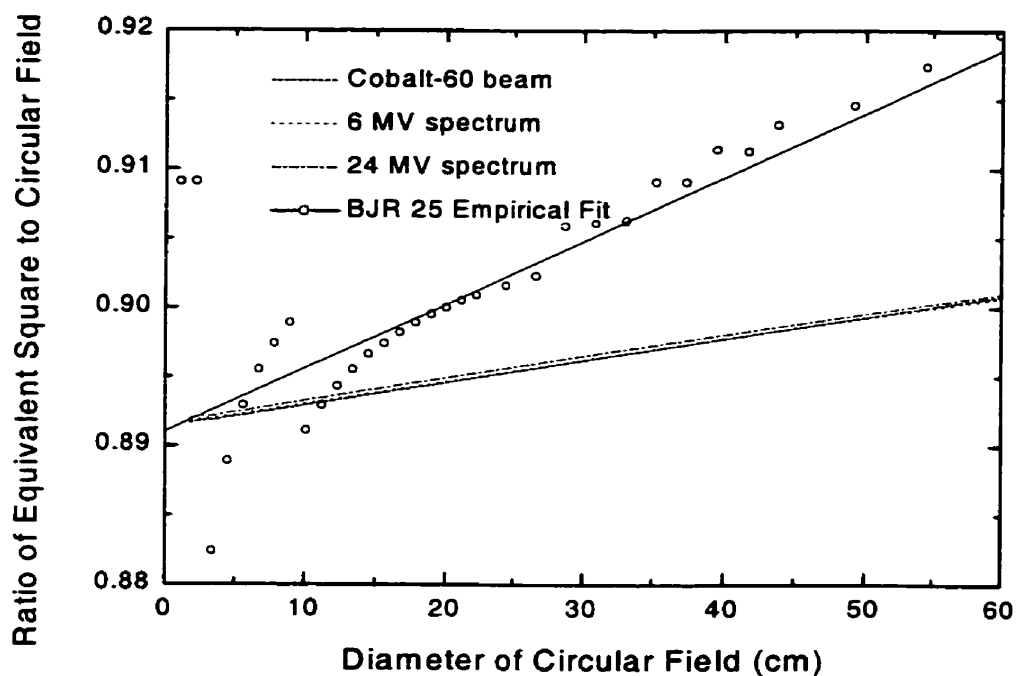


Figure A.5: Derived circular to square field relationships for cobalt-60, 6 MV, and 24 MV energy spectra compared with empirical BJR 25 data. Difference at 60 cm diameter is ~2%. Best fit line to BJR 25 data is: diameter/square side= $0.891+0.00046 \cdot \text{diameter}$. Best fit line of all energy spectra results shown is: diameter/square side= $0.8915+0.000158 \cdot \text{diameter}$.

A.4.3 Energy independence of equivalent fields

The results from section A.4.2 above suggest that the three-dimensional shape of the scatter kernels is responsible for the similarity of the equivalent field relationship for varying energy spectra. This provides support for the use of a single circular to square equivalent field table for all high energy beams. While the 3D shape of the scatter kernel does change significantly with energy, the relative difference in total energy content as integrated over square and circular limits centred on the central axis does not. Thus, the energy independence of equivalent field relationships is a direct consequence of the physical nature of the phantom scatter kernels.

A.4.4 Generating equivalent field relationships for rectangular fields

The conservation of energy method may be easily applied to rectangular and irregular shaped fields. Tables of equivalent circular and square fields for each incident energy spectra were generated via COE, for a series of rectangular fields. For most common field sizes, the equivalent square fields are within 0.5 cm of the BJR 25 tables, but differences of up to 2.5 cm occur at extremely large, moderately elongated field sizes (e.g. $60 \times 15 \text{ cm}^2$), as illustrated in Figure A.6. However, at these field sizes the difference in equivalent square field size only result in small errors in percentage depth dose. For example, the COE-based equivalent field predicted for a 6 MV, $30 \times 5 \text{ cm}^2$ field is $8.9 \times 8.9 \text{ cm}^2$, whereas the BJR 25 predicts $8.2 \times 8.2 \text{ cm}^2$ (a difference of 8.5% on a side). The experimental percentage depth doses [Ja93] for these curves differ by no more than 0.6% (of maximum dose) over all depth. Therefore, the differences in predicted equivalent field sizes between the COE approach and the BJR 25 tables translate into small

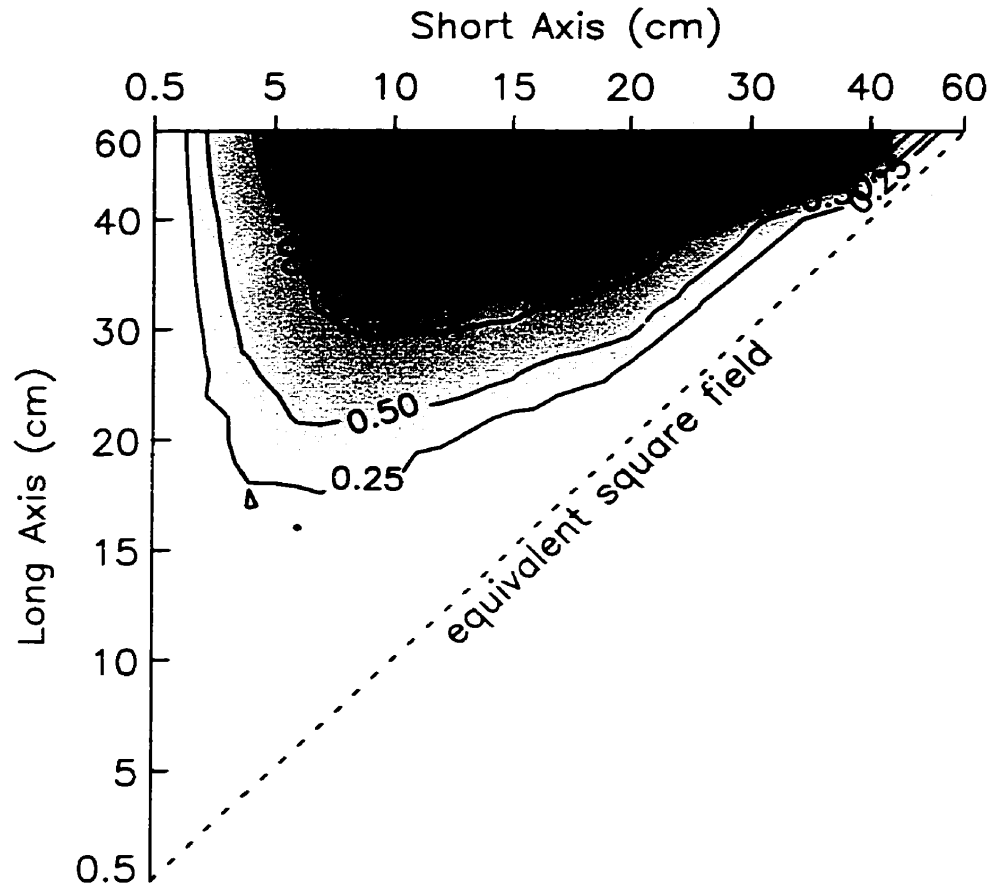


Figure A.6: Magnitude difference (contours in cm) between equivalent square fields of various rectangular dimensions as calculated by the scatter kernel integration method (using a 6 MV spectrum) and those presented in BJR 25.

differences in predicted dose. The calculated circular conversion tables demonstrate a similar comparison to the BJR 25 tables and are similar for all energies. These results show that a conservation of energy approach applied within a convolution calculation framework and only accounting for phantom scatter, will generate equivalent field relationships comparable to those experimentally derived for rectangular fields.

A.4.5 Validity of the equivalent fields concept

The validity of the equivalent fields concept for highly elongated fields is studied (for a $30 \times 2 \text{ cm}^2$ field and cobalt-60 spectra), by examining the two kernels associated with the predicted equivalent fields ($4.38 \times 4.38 \text{ cm}^2$ COE, $4.1 \times 4.1 \text{ cm}^2$ BJR 25) and their resulting scatter depth dose predictions. Figure A.7 shows the actual scatter kernel as generated with Clarkson radial integration, and the two kernels valid for the predicted equivalent fields. Note that polyenergetic kernels (energy bin weighted) are shown for illustration purposes, whereas the scatter dose calculations are actually performed using several monoenergetic kernels. The resulting predicted scatter dose distributions are included in Figure A.8. It is observed that both kernels associated with the equivalent fields (COE and BJR 25) result in an overprediction at shallow depths, and an underprediction deeper in the phantom, compared with using the actual kernel. Since the shapes of the equivalent field kernels are very similar, their predicted scatter doses parallel one another, with the dose difference arising mainly due to the difference in the total energy of the kernels (i.e. the area underneath). The difference in shape between the equivalent kernels and the actual kernel is more significant than the difference in shape

between the equivalent kernels. This manifests itself in the convolution dose result since all the equivalent dose curves are similar in shape to each other (merely shifted along the dose axis due to slightly different total energy content of the kernels), yet different in shape from the actual dose curve. This emphasizes that no two fields are truly equivalent in the strict sense of matching depth dose curves. Additionally, an equivalent field-approximated depth dose curve will generally overestimate the dose at shallow depths while underestimating at deeper points. The magnitude of this effect will depend on the irregularity of the field shape, specifically, on the amount of large radius kernel contribution versus small radius kernel contribution. This simple example demonstrates that an equivalent field choice based on a single parameter (total scatter energy content in COE or estimated scatter dose content in BJR 25) necessarily implies an optimal matching at a particular depth. The work of Tatcher and Bjärngard [Ta93] is supported by these results, which indicate that the inclusion of depth in any equivalency relationship should increase the accuracy of the match at a particular point.

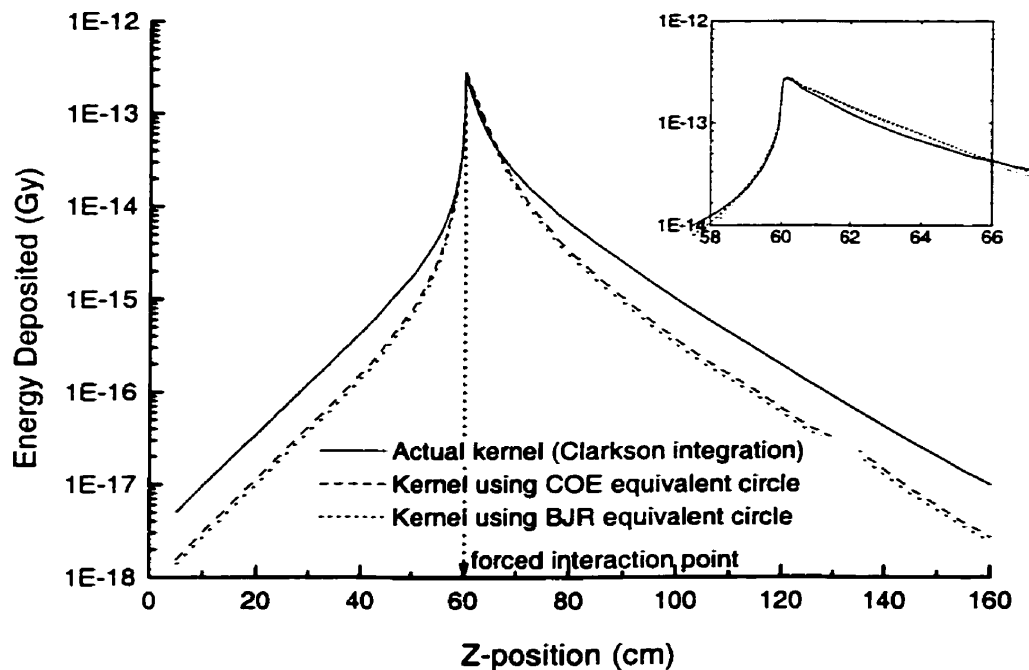


Figure A.7: Illustration of the difference between the accurately calculated kernel and the kernel associated with the equivalent square fields found by COE and BJR 25 look-up table, for a $30 \times 2 \text{ cm}^2$ cobalt-60 beam. The inset magnifies the kernels around the point of forced interaction ($z=60 \text{ cm}$), where the equivalent kernels overestimate the actual kernel.

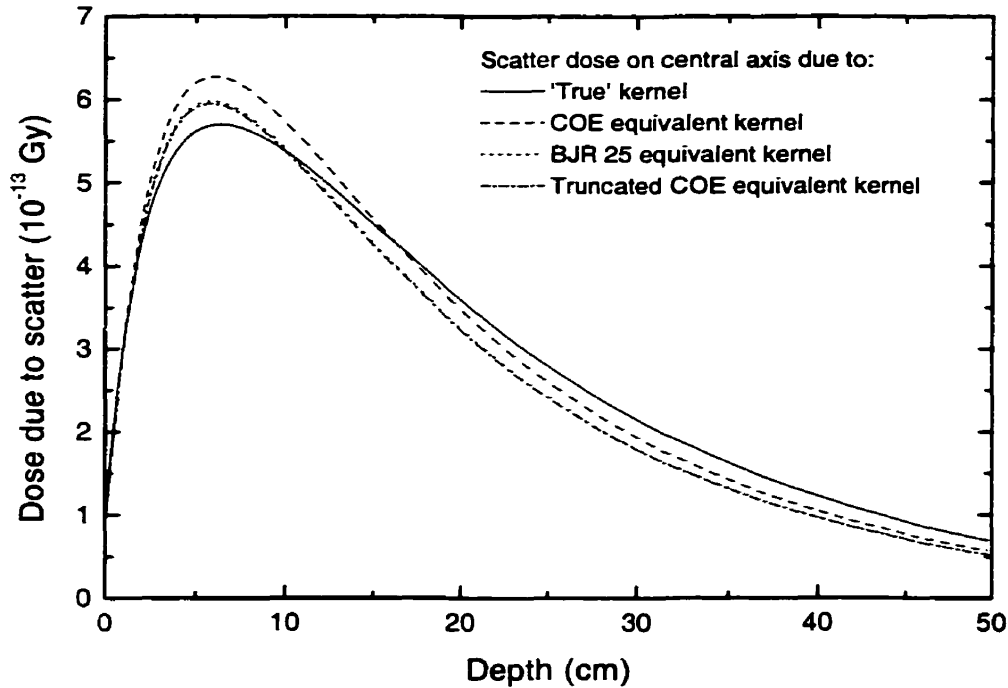


Figure A.8: Result of different kernels on predicted central axis scatter for cobalt-60 beams. The actual kernel result represents the scatter dose predicted with the kernel generated with Clarkson radial integration over the 30×2 cm² field. Using the equivalent COE kernel provides a better match over all depths, whereas using the equivalent BJR 25 kernel provides a better match at shallower depth. The equivalent predicted scatter dose curves intersect the actual scatter dose at 16.4 cm for the COE-equivalent kernel and 10.4 cm for the BJR-equivalent kernel. Matching at a specific depth may be accomplished by choosing an equivalent field based on an energy relationship generated with truncated scatter kernels (the range of truncation has been chosen to result in a depth dose match at 10.0 cm).

A.4.6 Modifying depth dose matching by using truncated kernels

Generating an energy-fieldsize relationship equation (A.3) using scatter kernels truncated in the forward direction at +15 cm with respect to the forced interaction point (chosen empirically) results in an exact matching at 10.0 cm depth of predicted central axis depth dose curves. This indicates that the COE method may be modified to achieve depth dose matching at specific depths. This exact depth dose matching at 10.0 cm depth for a $30 \times 2 \text{ cm}^2$ field of cobalt-60 and its 'truncated' COE-equivalent $4.09 \times 4.09 \text{ cm}^2$ field is illustrated in Figure A.8. Since the kernel shapes associated with all of the equivalent fields in Figure A.8 remain sufficiently similar to one another, no significant shape differences in the resulting scatter depth dose curve appear. The main difference between these equivalent kernels is the total scatter energy content, which results in a shifting of the scatter depth dose curve downwards with decreasing energy content. Using a 'truncated' COE approach results in an improved dose match over shallower depths at the expense of greater depths, and also demonstrates how the total energy content of the kernel affects the convolution dose calculation.

A.4.7 Investigating the equivalent fields concept away from the central axis

Off-axis kernels within the defined treatment field show a shape similar to the central axis kernel, being sharply peaked at the interaction point and falling off exponentially in the forward and backward directions. Outside the defined treatment field the 1D kernels become much less sharply peaked, with a significant decrease in total kernel energy, since contributions from points close to the interaction point become less significant than those farther away. While conservation of energy may be used to find an

equivalent field in off-axis situations, the kernel shape deviates significantly from the central axis equivalent kernel, and results in a significantly different scatter distribution with depth. Thus, whereas equivalent fields may be approximated for points within the treatment field, the approximation gets worse as the calculation point moves toward the beam edge, and points outside the treatment field give extremely poor results. This is demonstrated by examining several calculation points in and around a $15 \times 15 \text{ cm}^2$ field, for a cobalt-60 beam (Figure A.9). The actual kernels generated via Clarkson radial integration are presented along with their COE-equivalent square field kernels in Figure A.10(a) and (c). The rounding of the actual kernel as the calculation point leaves the treatment field is compared to the equivalent field kernel, which is always sharply peaked. The resulting scatter doses may be examined in Figure A.10(b) and (d). The shapes of the dose distributions calculated with the equivalent field kernels are significantly different than those generated by the actual kernels. This dramatically illustrates the breakdown of the single parameter equivalent field approximation as the calculation point moves further from the central axis.

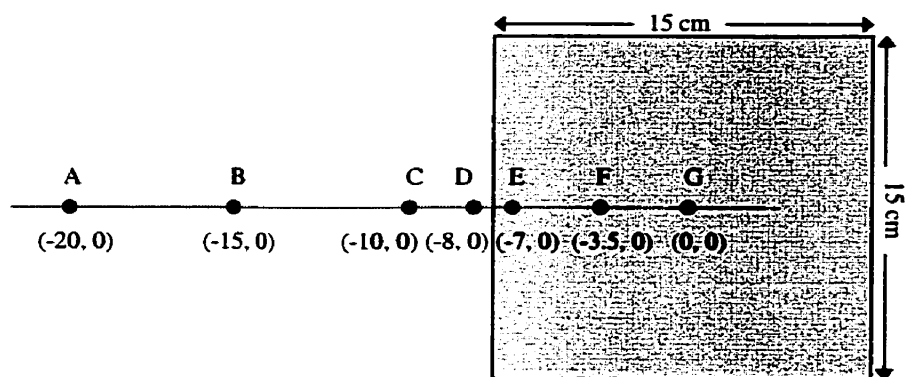


Figure A.9: Calculation points chosen to illustrate the change in 1D kernel shape and hence scatter dose distribution as the point moves away from the central axis, for a 15×15 cm^2 field. See Figure A.10.

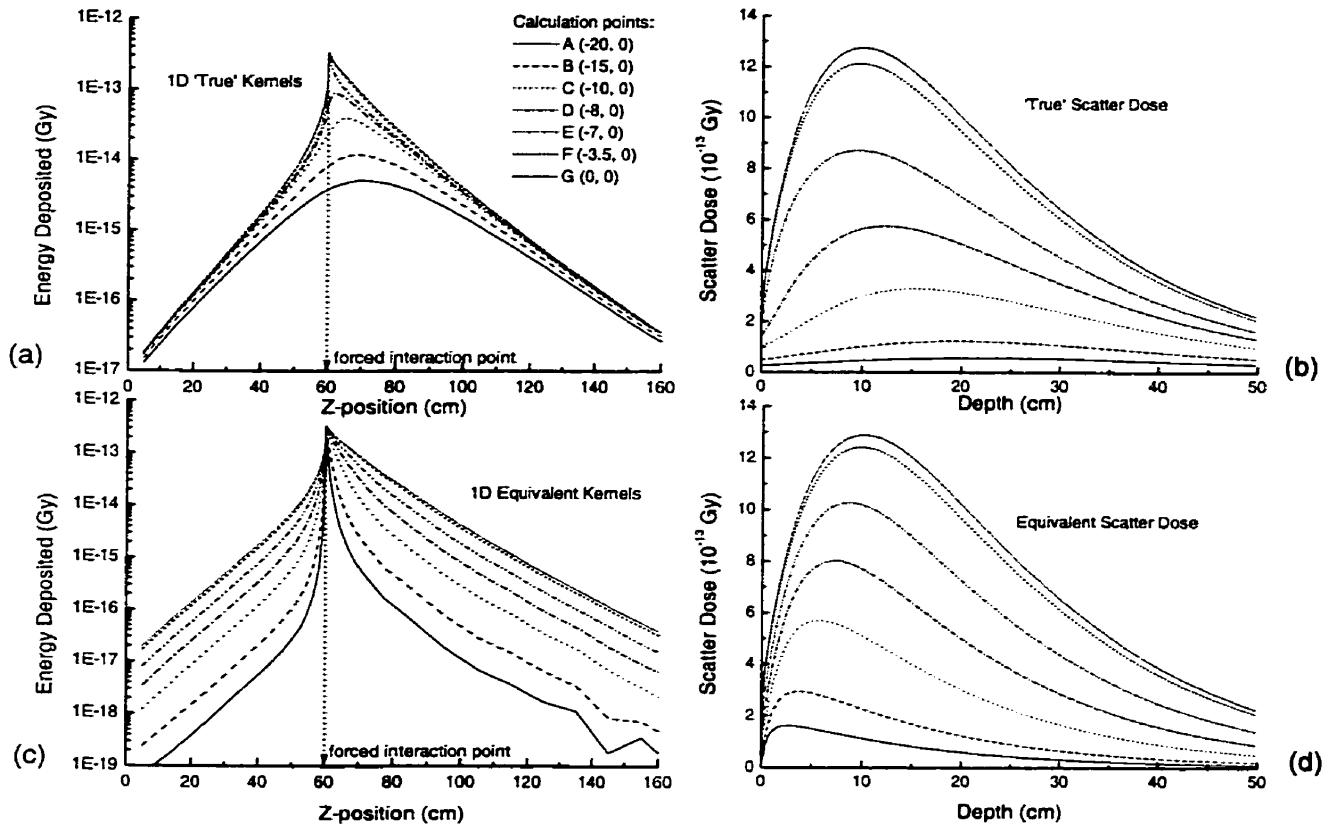


Figure A.10: Effect of moving off the central axis, while trying to maintain an equivalent field relationship, using calculation points illustrated in Figure A.9. (a) The accurate 1D kernels calculated via Clarkson integration. (b) The resulting scatter dose using the accurate kernels in (a). (c) The kernels associated with the COE-equivalent fields. (d) The resulting scatter dose using the equivalent kernels in (c).

A.5 Conclusions

The equivalent fields concept has been investigated through a variation of modern 3D convolution dose calculation methods. The validity of a 1D convolution in depth (of a pre-integrated scatter kernel) to determine dose is confirmed. Dose calculation results provide excellent agreement with independent 3D Monte Carlo simulation over an entire calculation plane, as well as with measured central axis TMRs and TARs, for a $15 \times 15 \text{ cm}^2$ field incident on a uniform water phantom using a variety of energy spectra.

Relationships describing in-phantom scatter energy deposited as a function of field size were developed for several incident energy spectra by integrating the Monte Carlo-generated scatter kernels over radius and utilizing reciprocity. These relationships were used to generate various equivalent field relationships, relating square, circular, and rectangular fields, which agree with BJR 25 data (mostly within 0.5 cm). Results support the use of a single circular, square, and rectangular equivalent fields relationship for all energies. The energy independence of equivalent field relationships was confirmed using a simple conservation of energy approach applied to phantom scatter only. The widely used equivalent fields concept has been demonstrated to be derivable within a modern 3D convolution calculation framework using Monte Carlo-generated scatter kernels.

The mathematics of convolution implies that the resulting function is affected by both the shape and area of the kernel. Therefore, treatment fields of different shape will be approximately equivalent when the scatter kernels are similar in shape and total energy content. This has been illustrated using an elongated rectangular field, showing that similarly shaped kernels with different total integrated energies predict the same shape of

dose distribution, with the area underneath the resulting dose distribution related to the integrated energy of the scatter kernel. Furthermore, it was shown that the equivalent field concept inevitably results in an optimal match with the actual percentage depth dose at a single depth only, with an overestimation in dose at shallower points and underestimation at deeper points. The validity of the equivalent fields concept at calculation points off of the central axis was investigated for a simple square field situation. Generalizing the findings, it is concluded that the single parameter equivalent field concept breaks down as the calculation point approaches the beam edge, and is extremely inaccurate outside the defined treatment field.

The application of modern convolution dose calculation techniques has provided an improved understanding of the equivalent fields concept. The continued use of the BJR 25-equivalent fields tables is recommended for all photon energies.

APPENDIX B

CONVERTING DIVERGENT BEAM SCATTER FRACTION DATA INTO A PARALLEL GEOMETRY

The scatter fraction data of Jaffray *et al.* [Ja94] was produced using an ideal point source, and a fixed source to phantom exit surface distance of 100 cm. To compare to scatter fraction data generated with an ideal pencil beam and assuming reciprocity (implying a parallel geometry), a conversion is performed which compensates for the inverse square fall-off of the primary. The general idea is to compare the geometries at field sizes that are defined in the depth-wise middle of the phantom (i.e. at a depth equal to half the phantom thickness), which assumes a similar scatter fluence production. This also requires a renormalization of the primary distribution in the diverging geometry to match the primary in the parallel geometry, at the exit surface of the phantom.

For a divergent beam assuming a source-to-exit surface distance of SAD (source to axis of rotation distance), the primary fluence at an air gap distance of a behind a phantom of thickness t , with the inverse square component normalized to the exit surface is:

$$P_z = \left(\frac{SAD}{SAD + a} \right)^2 \exp(-\bar{\mu}t) \quad (\text{B.1})$$

where $\bar{\mu}$ is the effective attenuation coefficient valid for a given incident energy spectrum and phantom material, and attenuation in air is neglected. For the parallel geometry, again ignoring attenuation in air, the primary fluence at a distance a behind the same phantom is:

$$P_{\parallel} = \exp(-\bar{\mu}r) \quad (\text{B.2})$$

Simultaneously normalizing both divergent and parallel primary fluences at the exit surface of the phantom by substituting (B.2) into (B.1) gives:

$$P_{\perp} = \left(\frac{SAD}{SAD + a} \right)^2 \cdot P_{\parallel} \quad (\text{B.3})$$

$$\frac{P_{\parallel}}{P_{\perp}} = \left(\frac{SAD + a}{SAD} \right)^2 \quad (\text{B.4})$$

Using the standard definition of scatter fraction of $SF = \frac{S}{S+P}$, where S is the scatter fluence and P is the primary fluence, rearranging and solving for the scatter gives

$$S = \frac{SF \cdot P}{1 - SF} \quad (\text{B.5})$$

Assuming the scatter fluence generated in a parallel geometry is similar to that generated in a diverging geometry for field sizes defined at $t/2$, the scatter contributions from the different geometries may be approximated:

$$\frac{SF_{\perp} \cdot P_{\perp}}{1 - SF_{\perp}} \approx \frac{SF_{\parallel} \cdot P_{\parallel}}{1 - SF_{\parallel}} \quad (\text{B.6})$$

Solving for the parallel geometry scatter fraction,

$$SF_{\parallel} \approx \frac{1}{1 + \frac{(1 - SF_{\perp}) \cdot P_{\parallel}}{SF_{\perp} \cdot P_{\perp}}} \quad (\text{B.7})$$

and substituting the ratio of primaries from above,

$$SF_{\parallel} \approx \frac{1}{1 + \frac{(1 - SF_{\perp})}{SF_{\perp}} \cdot \left(\frac{SAD + a}{SAD} \right)^2} \quad (\text{B.8})$$

which, after simplification yields,

$$SF_{\parallel} \approx \frac{1}{1 + \left(\frac{1}{SF_z} - 1\right)\left(\frac{SAD+a}{SAD}\right)^2} \quad (\text{B.9})$$

This conversion to a parallel geometry was made to Jaffray *et al.*'s [Ja94] data in chapter three, and plotted in Figures 3.6 (b) and (c), 3.7 (b) and (c) and 3.8 (b) and (c). The assumptions of this simple conversion lose validity for large field sizes, thick phantoms, and small air gaps, since the difference in shape of the scattering volume between the parallel and diverging geometries becomes significant in these situations.

APPENDIX C

ANALYTICAL PREDICTION OF FIRST SCATTER ENERGY FLUENCE INTO A PORTAL IMAGING DEVICE

C.1 Introduction

Several techniques for predicting the scatter contribution to a portal imaging device have been presented in the literature, and briefly described in chapter two. These are composed of 2D convolution/superposition style scatter fluence predictors [Ha97, Pa98a], or scatter dose prediction based on density scaling of 3D dose deposition kernels within a superposition framework [Mc96b]. Both of these approaches have certain disadvantages. The simpler 2D scatter fluence predictors do not take exact patient inhomogeneity into account, thus inherently limiting the accuracy of this approach. The validity of the 3D density scaling/superposition approach has not been investigated in high atomic number materials, which is of concern since many electronic portal imaging devices (EPID's) incorporate metal screen/phosphor (see section 2.3.2).

First scatter fluence has been shown to dominate scatter reaching the portal imaging plane over the therapeutic range of high energy photons [Ja94, Mc00a]. In this appendix, a purely analytical calculation of singly-scattered photon fluence into portal imaging devices is investigated. An overview of the implemented method is given, and comparisons of predicted fluence results to those of Monte Carlo simulation for a variety of inhomogeneous phantom configurations.

C.2 Materials and Methods

The method presented is based on the numerical integration of the analytical equations governing Compton scatter. By sampling over a lattice of ‘scatter source’ points within the volume defined by the intersection of patient and beam, first scatter fluence contributions to a point in the image plane may be calculated. Repeating this process for a grid of points in the image plane provides a map of first scatter fluence. By dividing the incident energy spectrum into bins and repeating the process for each energy bin, the first scatter fluence of a polyenergetic beam may be predicted. The attenuation along each ray line may be calculated exactly, using a fast recursive algorithm [Si85]. The probability of interaction is found using the Klein-Nishina differential cross section, whereas the energy of the scattered photon is established using Compton kinematics. Combining these effects, the equation to be evaluated is (see pp. 125-134 of [At86], and refer to Figure C.1):

$$\Phi(dA) = \int_V \int_E (\Phi_0 \exp(-I(E_0, \bar{r}_1, \bar{r}_2))) \cdot (\sigma(E_0, \phi, \bar{r}_2, \bar{r}_3)) \cdot (\exp(-I(E_1, \bar{r}_2, \bar{r}_3))) dEdV$$

where $I(E, \bar{r}_a, \bar{r}_b) = \int_0^{|\bar{r}_b - \bar{r}_a|} \left(\frac{\mu}{\rho}(E) \cdot \rho(\bar{r}_b - \bar{r}_a) \cdot \frac{d(|\bar{r}_b - \bar{r}_a|)}{|\bar{r}_b - \bar{r}_a|} \right)$ and $E_1 = \frac{E_0}{1 + (E_0/0.511) \cdot (1 - \cos \phi)}$

and $\sigma(E_0, \phi, \bar{r}_2, \bar{r}_3) = \frac{r_0^2}{2} \left(\frac{E_1}{E_0} \right)^2 \cdot \left(\frac{E_0}{E_1} + \frac{E_1}{E_0} - \sin^2 \phi \right) \cdot \left(\frac{dA \cos(\phi)}{|\bar{r}_3 - \bar{r}_2|^2} \right) \cdot (\rho_e(\bar{r}_2) \rho(\bar{r}_2))$

Here $I(E, r_a, r_b)$ is the integrated attenuation coefficient for energy E along the path $|r_b - r_a|$, E_0 is the incident photon energy, E_1 is the scattered photon energy, r_0 is the ‘classical electron radius’, and σ incorporates the Klein-Nishina differential cross section (cm^2). The first and third terms account for attenuation along the incident and outgoing rays. The second term scales the fluence by the probability of scattering through angle ϕ .

includes a divergence factor, and accounts for conversion to planar fluence. To generalize this equation to diverging geometries, an extra divergence factor for the incident ray may be incorporated.

In the current work, the scoring plane was $40 \times 40 \text{ cm}^2$ with $dA = 1.0 \text{ cm}^2$ and sampling throughout the phantom was performed at 0.5 cm^3 resolution. Calculations were performed for a variety of field sizes, phantom thicknesses, and heterogeneous configurations, with an incident energy spectrum typical for a 6 MV photon beam. Results were compared to EGS4 [Ne85] Monte Carlo simulations, which directly scored the first scatter fluence at a specified z -plane.

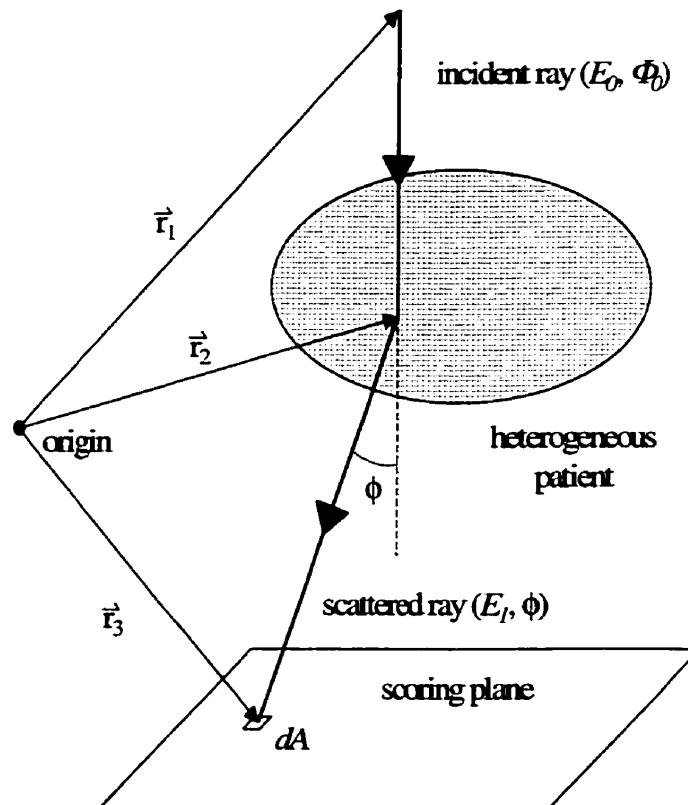


Figure C.1: Scoring geometry.

C.3 Results

The analytical model shows excellent agreement with Monte Carlo simulation in several simple homogeneous and inhomogeneous phantom situations (see Table C.1). Figure C.2 reports total fluence predicted in the scoring plane at selected points for an inhomogeneous, 20 cm thick lung/water slab (upper right inset, Figure C.2), with an incident $10 \times 10 \text{ cm}^2$ field and 30 cm air gap. The uncertainty estimate on the Monte Carlo-scored fluence accounts for most (87%) of the observed differences (upper left inset, Figure C.2).

Phantom	Basic Radiation Parameters of Singly Scattered Photons		
	Fluence	Mean Energy	Mean Angle
water slab	86.3	91.1	87.0
lung/water slabs	89.1	89.5	83.0
vertical slab	87.9	90.4	76.6
enclosed cube	87.6	90.8	83.7
lung slab	84.2	87.4	72.4
water/lung slabs	86.0	91.7	77.2
water/lung abutted	86.6	90.7	76.1

Table C.1: Percentage agreement between analytical model and Monte Carlo simulation for various simple phantoms.

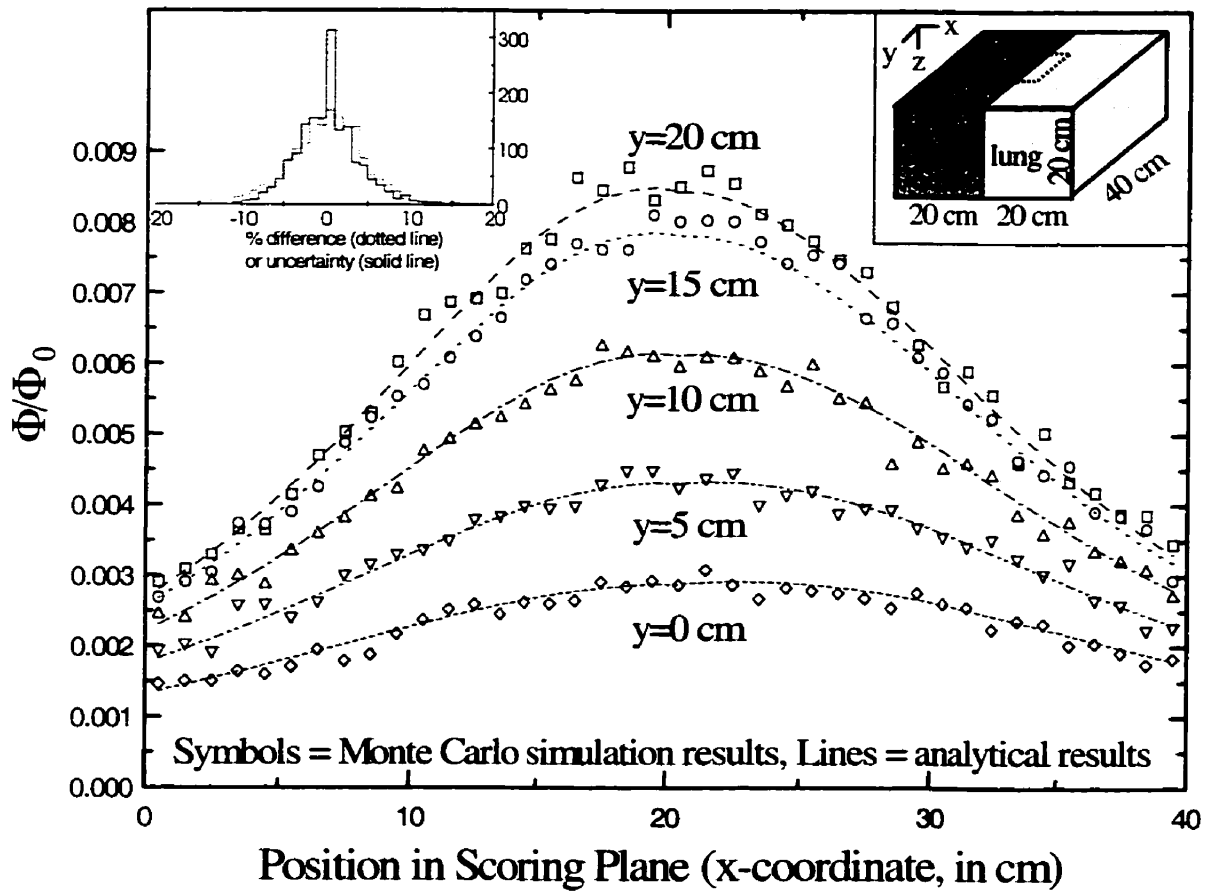


Figure C.2: Comparison of Monte Carlo-simulated first scatter fluence with analytical results.

C.4 Discussion and Conclusions

This appendix demonstrates the feasibility of employing an accurate method of predicting first scatter energy fluence into a portal imaging device, based on a first principles technique which takes into account patient heterogeneity. As expected, the technique agrees well with Monte Carlo simulations. This approach allows the output energy fluence to be coupled to a convolution style dose prediction algorithm specifically tailored to high Z materials (see chapters five and six), with a theoretical predicted portal image as the final outcome. Furthermore, this approach allows a compromise between speed and accuracy by scaling the sampling resolution within the phantom, as well as the sampling resolution of the scoring plane.

APPENDIX D:

UNCERTAINTY ESTIMATES

Every step of the portal dose prediction algorithm may introduce uncertainty into the final predicted dose image. In this section, the uncertainties involved are estimated along with the corresponding proportion of total execution time for the particular step. The uncertainties arise due to errors in a priori data used (including errors in Monte Carlo-generated kernels), and errors due to assumptions of the implemented algorithm. All contributing uncertainties are assumed to be independent, and are added in quadrature to estimate the overall uncertainty in the algorithm.

Errors in the *a priori* data include errors in the CT data (acquisition as well as the conversion to electron density), the incident beam fluence matrix, the dimensions of the flattening filter, physical parameters associated with the detector system (eg. densities, thicknesses, materials), and the incident energy spectra used. Errors in acquiring the CT data and converting to electron density are estimated at 1% [Th99]. Errors in the relative fluence matrix representing the incident beam are introduced by measurement error and also by fluctuations in electronics, and are estimated to be ~1%. Errors in the dimensions of the flattening filter and the physical parameters describing the detector should be very low (<0.5%), since accurate engineering schematics as well as material and density specifications are provided from the manufacturer. Statistical errors in the incident energy spectra used are <5% per bin [Mo85a], but these are random and should cancel out when averaged over the entire spectrum. However, since these distributions are calculated via Monte Carlo techniques, the systematic uncertainty may be estimated at 2-

5%, increasing with lower energies (up to 5% for <2 MeV). These uncertainties arise from the radiative stopping power distributions used [Ro90]. This implies that errors in the incident spectra will affect the final predicted dose image in a manner unique to the detector configuration being used. The response function of the detector will determine which energy bins will have greater contribution to the predicted dose image. However, assuming a constant response with energy (e.g. a photon counter), the overall uncertainty will be $\sim 3\%$. Detectors with higher response at energies below 2 MeV may exhibit uncertainties slightly higher than this in predicted dose images.

Two sets of Monte Carlo-generated kernels are used in the algorithm. The first represents scattered photon fluence data, the second characterises dose deposition within a specific detector configuration. The statistical uncertainty in each data set is $<3\%$ and $<5\%$, respectively, for the fluence and dose kernels. These statistical uncertainties will be averaged out over the convolution/superposition process. It is therefore the systematic errors which are important here. The error in photon cross section data for low Z materials at energies dominated by the Compton effect is $<1\%$. Since the scattered photon fluence kernels are generated using water slabs, and the Compton effect dominates over the energy range 0.003 MeV to above 50 MeV. Thus, the error estimate for these fluence kernels is 1%. The systematic errors in the dose kernels arise from cross section data representing photon interactions and mass stopping powers (both collisional and radiative), which govern the energy loss of electrons in a medium. The uncertainty in the mass collisional stopping powers is 1-2%. Mass radiative stopping power uncertainty ranges from $\sim 5\%$ below 2 MeV to 2-5% from 2 MeV to 50 MeV. It should be noted that the mass collisional stopping power dominates over the entire therapeutic energy regime

for low Z materials, and over a significant fraction of the energy regime for high Z materials (for example, 0-9 MeV for lead). Since detectors may include low and/or high Z materials, the worst case assumption of a high Z detector is used here to arrive at an uncertainty estimate of 3% for the mass collisional stopping powers. Again assuming a high Z detector, the uncertainty estimate for the photon interaction cross sections is ~2%.

The final factors contributing to uncertainty in predicted dose represent the effect of assumptions made throughout the implementation of the algorithm. These include assumptions such as the replacement of an inhomogeneous patient with an homogeneous phantom, assumption of semi-infinite slab geometry for fluence scatter kernels, sampling grid resolution of the incident beam, perpendicular orientation of fluence incident upon the detector, and the use of a mean energy spectrum for scattered photon fluence. Due to the complexity of many of these issues, the contributions to uncertainty are very difficult to estimate accurately. The worst case scenario estimates the combined uncertainty for the patient replacement and semi-infinite slab geometry assumption to be less than 3% (and decreasing rapidly with increasing air gap). The use of a 0.5 cm grid resolution for the incident beam introduces an error of <1%. These error estimates are described in a comprehensive study of uncertainty in the fluence prediction portion of the algorithm [Mc00b]. The error resulting from the assumption that the photon fluence is incident perpendicularly on the detector will vary, depending on the true angle of incidence. This angle will be quite small for primary photons (8° for a point 15 cm off axis), but will increase for scattered radiation. However, if adequate buildup is provided for the detector, the effect of this obliquity will be reduced, since the dose will be only slowly decreasing along the fluence ray line. It is estimated that the error introduced by this

effect (combining primary and scatter) is $<2\%$. The final uncertainty factor in this group results from the use of a mean energy fluence spectrum to represent the scatter dose kernel.

This analysis may be extended to examine the proportion of algorithm execution time corresponding to the specific calculation step where each uncertainty is introduced. This allows an objective evaluation in terms of both speed and accuracy, for every step of the algorithm. Therefore, this analysis may indicate where future effort should be expended to improve the algorithm's performance. The algorithm is broken into five main calculation steps, as described in Table D.1. Table D.2 provides a summary of the uncertainties and corresponding execution times. Examining Table D.2, the errors which may be assigned to a particular calculation step can be summed per step to give: 2.0% for C, 1.5% for E, 1.0% for A, and 0.5% for B and D. This indicates that more effort could be placed in parts C and E, which are the scatter fluence and scatter dose calculation, to improve accuracy. The primary fluence and dose calculation (B and D) are relatively accurate, but comprise the majority of the execution time. Methods of ray tracing, which are faster but less accurate, may be investigated to improve the overall balance of speed and accuracy. The calculation step A has $\sim 1\%$ error that cannot be avoided, since the CT conversion to electron density is required. This conversion is based on an electron density calibration curve, which is experimentally measured, and will have an inherent limit to its precision.

Section label	Calculation description	Percentage of total execution time
A	conversion of CT data to electron density	4.6
B	primary fluence calculation (including EHP calculation)	73.8
C	scatter fluence calculation	10.9
D	primary dose conversion	10.2
E	scatter dose conversion	0.5

Table D.1: Summary of percentage algorithm execution time as a function of calculation step.

Uncertainty Group	Specific Uncertainty	Worst Case Uncertainty Estimate	Practical Uncertainty Estimate	Calculation step in algorithm
<i>a priori</i> data	CT acquisition and conversion to electron density	1%	1%	A
	incident beam fluence matrix	1%	0.5%	n/a
	physical parameters of flattening filter, detector	0.5%	0.5%	n/a
	incident energy spectra	3%	2%	n/a
	fluence kernels	1%	1%	n/a
	dose kernels	$\sqrt{((2\%)^2 + (3\%)^2)} = 3.3\%$	$\sqrt{((1.5\%)^2 + (2\%)^2)} = 2.5\%$	n/a
assumptions in algorithm	replacement of patient with water, and semi-infinite slab assumption	3%	1%	B, C
	grid resolution of incident beam	1%	.5%	C
	perpendicularly incident fluence	2%	1%	D, E
	use of mean energy fluence spectrum for scatter dose calculation	2%	2%	C, E
TOTAL		6.4%	4.3%	

Table D.2: Uncertainty estimates and associated calculation section of the algorithm in which they are involved.

REFERENCES

- [AA98] American Association of Physicists in Medicine. *Quality Assurance for Clinical Radiotherapy Treatment Planning*. Report No. 62, (College Park, Maryland, USA, 1998).
- [Ah87] A. Ahnesjo, P. Andreo, and A. Brahme, "Calculation and application of point spread functions for treatment planning with high energy photon beams" *Acta Oncol.* **26 Fasc. 1**:49-56 (1987).
- [Ah89] A. Ahnesjo, "Collapsed cone convolution of radiant energy for photon dose calculation in heterogeneous media" *Med. Phys.* **16**:577-592 (1989).
- [An98] L. E. Antonuk, Y. El-Mohri, K. W. Jee, "Active matrix flat-panel imagers (AMFPIs) for electronic portal imaging" in *AAPM 1998 Summer School: Medical Physics Monograph #24*, Editors: J.D. Hazle, A.L. Boyer, (1998).
- [As80] L. W. Asp, "On equivalent square fields" *Br. J. Radiol.* **53**:485-487 (1980).
- [At86] F. H. Attix, *Introduction to Radiological Physics and Radiation Dosimetry*, (Wiley, New York, 1986).
- [Ba56] H. Batho, O. Theimer, and R. Theimer, "A consideration of the equivalent circle method of calculating depth doses for rectangular x-ray fields" *J. Can. Assoc. Radiol.* **7**:51-53 (1956).
- [Ba76] J. J. Battista, P. M. K. Leung, and W. B. Taylor, "Modified transit dosimeter system for ^{60}Co rotational therapy," *Med. Phys.* **3**(5): 335-339, (1976).
- [Ba80] J. J. Battista, W. D. Rider, and J. Van Dyk, "Computed tomography for radiotherapy planning," *Int. J. of Radiat. Oncol., Biol., Phys.* **6**:99-107, (1980).

- [Ba81] H.H. Barrett and W. Swindell, *Radiological Imaging: The Theory of Image Formation, Detection, and Processing*, Vol. 1 (Academic Press, New York, 1981), p.42.
- [Ba87] G. Barnea, and A. Ginzburg, "High energy x-ray film response and the intensifying action of metal screens," *IEEE Trans. Nucl. Sc.* **NS-34**, 1580-1585 (1987).
- [Ba91] G. Barnea, E. Navon, A.Ginzburg, J. Politch, H. Roehrig, C. E. Dick, and R. C. Placious, "Use of storage phosphor imaging plates in portal imaging and high-energy radiography: The intensifying effect of metallic screens on the sensitivity," *Med. Phys.* **18**:432-438 (1991).
- [Ba92] J. J. Battista, and M. Sharpe, "True Three-dimensional dose computations for megavoltage x-ray therapy: A role for the superposition principle", *Aust. Phys. Eng. Sci. Med.* **15**:159-178 (1992).
- [Ba97] J. J. Battista, M. Sharpe, E. Wong, and J. Van Dyk, "A New Classification Scheme for Photon Beam Dose Algorithms" *Proc. XIIth ICCR* ed D D Leavitt and G Starkschall (Salt Lake City, UT: Medical Physics Publishing), 39-42 (1997).
- [Be] M. J. Berger, J. H. Hubbell, S. M. Seltzer, J. S. Coursey, and D. S. Zucker, "XCOM: Photon cross sections database", Physics Laboratory, National Institute of Standards and Technology.
- [Bi87] A. F. Bielajew, and D. W. O. Rogers, "PRESTA - The Parameter Reduced Electron-Step Transport Algorithm for Electron Monte Carlo Transport," National Research Council of Canada Report No. PIRS-0042 (1987).

- [Bj88] B. E. Bjarngard, and P. L. Petti, "Description of the scatter component in photon-beam data" *Phys. Med. Biol.* **33**:21-32 (1988).
- [Bo88] A. L. Boyer, T. Schultheiss, "Effects of dosimetric and clinical uncertainty on complication free local tumor control", *Rad. Oncol.* **11**:65-71 (1988).
- [Bo92] A. L. Boyer, L. Antonuk, A. Fenster, M. van Herk, H. Meertens, P. Munro, L. E. Reinstein, and J. Wong, "A review of electronic portal imaging devices (EPIDs)," *Med. Phys.* **19**(1):1-16 (1992).
- [Bo97a] R. Boellaard, M. Van Herk, B. J. Mijnheer, "A convolution model to convert transmission dose images to exit dose distributions", *Med. Phys.* **24**(2):189-199 (1997).
- [Bo97b] R. Boellaard, M. Van Herk, H. Uiterwaal, B. J. Mijnheer, "Two dimensional exit dosimetry using a liquid filled electronic portal imaging device and a convolution model", *Rad. Oncol.* **44**:149-159 (1997).
- [Bo98a] R. Boellaard, M. Van Herk, H. Uiterwaal, B. J. Mijnheer, "First clinical tests using a liquid filled electronic portal imaging device and a convolution model for the verification of the midplane dose", *Rad. Oncol.* **47**:303-312 (1998).
- [Bo98b] R. Boellaard, M. Essers, M. Van Herk, B. J. Mijnheer, "New method to obtain the midplane dose using portal in vivo dosimetry", *Int. J. Radiat. Oncol. Biol. Phys.* **41**(2):465-474 (1998).
- [Br84] A. Brahme, "Dosimetric precision requirements in radiation therapy", *Acta Radiologica Oncology* **23 Fasc. 5**:379-391 (1984).

- [Ca93] R. Calandrino, G. M. Cattaneo, A. Del Vecchio, C. Fiorino, B. Longobardi, P. Signorotto, "Human errors in the calculation of monitor units in clinical radiotherapy practice", *Rad. Oncol.* **28**:86-88 (1993).
- [Ch96] C. Chui, S. Spiridon, and T. LoSasso, "Testing of dynamic multileaf collimation," *Med. Phys.* **23**:635-641 (1996).
- [Cu85] J. R. Cunningham, "Tissue inhomogeneity corrections in photon beam treatment planning," in *Progress in Modern Radiation Physics*, edited by C. G. Orton (Plenum Press, New York, 1985) pp 103-131.
- [Cu99] A. J. Curtin-Savard, E. B. Podgorsak, "Verification of segmented beam delivery using a commercial electronic portal imaging device", *Med. Phys.* **26**(5):737-742 (1999).
- [Da96] M. J. Day, and E. G. A. Aird, "The Equivalent Field Method for Dose Determination in Rectangular Fields" *Br. J. Radiol.* suppl 25 (London: BJR) pp 138-151 (1996).
- [De00] J. Deng, S. B. Jiang, A. Kapur, J. Li, T. Pawlicki, and C.-M. Ma, "Photon beam characterization and modelling for Monte Carlo treatment planning" *Phys. Med. Biol.* **45**: 411-427 (2000).
- [Du84] A. Dutreix, "When and how can we improve precision in radiotherapy?", *Rad. Oncol.* **2**:275-292 (1984).
- [El99] Y. El-Mohri, L. E. Antonuk, J. Yorkston, K.-W. Jee, M. Maolinbay, K. L. Lam, and J. H. Siewerdsen, "Relative dosimetry using active matrix flat-panel imager (AMFPI) technology" *Med. Phys.* **26**(8): 1530-1541 (1999).

- [Es96] M. Essers, R. Boellaard, M. van Herk, J. H. Lanson, and B. J. Mijnheer, "Transmission dosimetry with a liquid-filled electronic portal imaging device," *Int. J. Radiat. Oncol. Biol. Phys.* **34**: 931-941 (1996).
- [Fe57] S. O. Fedoruk, and H. E. Johns, "Transmission dose measurement for cobalt 60 radiation with special reference to rotation therapy," *Br. J. Radiol.* **30**:190-195 (1957).
- [Fi88] G. C. Field, "Dose Calculations for Megavoltage Photon Beams Using Convolution", *M.Sc. Thesis* University of Alberta (1988).
- [Fi93] C. Fiorino, A. del Vecchio, G. M. Cattaneo, M. Fusca, B. Longobardi, P. Signorotto, and R. Calandrino, "Exit dose measurements by portal film dosimetry," *Rad.Oncol.* **29**:336-340 (1993).
- [Fi96] C. Fiorino, C. Uleri, G. M. Cattaneo, R. Calandrino, "On-line exit dose profile measurements by a diode linear array," *Phys. Med. Biol.* **41**, 1291-1304 (1996).
- [Ha87] K. Han, D. Ballon, C. Chui, and R. Mohan, "Monte Carlo simulation of a cobalt-60 beam", *Med. Phys.* **14**:414-419 (1987).
- [Ha95] Hamamatsu Catalogue, "Characteristics and Use of Photodiodes", Hamamatsu Photonics K.K. Solid State Division, Hamamatsu, Japan, 1995.
- [Ha96] V. N. Hansen, P. M. Evans, and W. Swindell, "The application of transit dosimetry to precision radiotherapy," *Med. Phys.* **23**:713-721 (1996).
- [Ha97] V. N. Hansen, W. Swindell, and P. M. Evans, "Extraction of primary signal from EPIDs using only forward convolution," *Med. Phys.* **24**(9):1477-1484, (1997).
- [He95] B. J. M. Heijmen, K. L. Pasma, M. Kroonwijk, V. G. M. Althof, J. C. J. de Boer, A. G. Visser, and H. Huizenga, "Portal dose measurement in radiotherapy using

- an electronic portal imaging device (EPID)," *Phys. Med. Biol.* **40**:1943-1955 (1995).
- [Ho94] P. W. Hoban, D. C. Murray, and W. H. Round, "Photon beam convolution using polyenergetic energy deposition kernels", *Phys. Med. Biol.* **39**:669-685 (1994).
- [IC76] International Commission on Radiation Units and Measurements. *Determination of Absorbed Dose In a Patient Irradiated by Beams of X- or Gamma Rays In Radiotherapy Procedures*. Report No. 24, (Bethesda, Maryland, U.S.A., 1976).
- [IC84] International Commission on Radiation Units and Measurements. *Stopping Powers for Electrons and Positrons*. Report No. 37, (Washington D.C., 1984).
- [Iw85] A. Iwasaki, "A method of calculating high-energy photon primary absorbed dose in water using forward and backward spread dose-distribution functions", *Med. Phys.* **12**:731-737 (1985).
- [Iw90] A. Iwasaki, "Calculation of three-dimensional photon primary absorbed dose using forward and backward spread dose-distribution functions", *Med. Phys.* **17**:195-202 (1990).
- [Ja90] F. James, "A review of pseudorandom number generators", *Computer Physics Communications* **60**:329-344 (1990).
- [Ja93] S. Jani, *Handbook of dosimetry data for radiotherapy* (Boca Raton, Florida, USA: CRC Press, Inc. 1993).
- [Ja94] D. A. Jaffray, J. J. Battista, A. Fenster, and P. Munro, "X-ray scatter in megavoltage transmission radiography: physical characteristics and influence on image quality," *Med. Phys.* **21**:45-60 (1994).

- [Jo49] H. Johns, E. Darby, R. Haslam, L. Katz, and E. Harrington, "Depth Dose Data and Isodose Distributions for Radiation From a 22 MeV Betatron", *Br. J. Radiol.* **62**:257-268 (1949).
- [Jo83] H. E. Johns, and J. R. Cunningham, *The Physics of Radiology* 4th edn (Springfield, Illinois, USA: Charles C. Thomas,1983).
- [Ka99] C. Kausch, B. Schreiber, F. Kreuder, R. Schmidt, and O. Dössel, "Monte Carlo simulations of the imaging performance of metal plate/phosphor screens used in radiotherapy" *Med. Phys.* **26**(10):2113-2124 (1999).
- [Ki93] M. C. Kirby, and P. C. Williams, "Measurement possibilities using an electronic portal imaging device," *Rad. Oncol.* **29**:237-243 (1993).
- [Ki95] M. C. Kirby, and P. C. Williams, "The use of an electronic portal imaging device for exit dosimetry and quality control measurements," *Int. J. Radiat. Oncol. Biol. Phys.* **31**(3):593-603 (1995).
- [Kr98] M. Kroonwijk, K. L. Pasma, S. Quint, P. C. M. Koper, A. G. Visser, B. J. M. Heijmen, "In vivo dosimetry for prostate cancer patients using an electronic portal imaging device (EPID): detection of internal organ motion", *Rad. Oncol.* **49**:125-132 (1998).
- [La86] K. S. Lam, M. Partowmah, W. C. Lam, "An on-line electronic portal imaging system for external beam radiotherapy", *British J. Radiology* **59**:1007-1013 (1986).
- [Le86] J. Leong "Use of digital fluoroscopy as an on-line verification device in radiation therapy", *Phys. Med. Biol.* **31**:985-992 (1986).

- [Le92a] G. Leunens, J. Verstraete, A. Dutreix, E. van der Schueren "Assessment of dose inhomogeneity at target level by in vivo dosimetry: can the recommended 5% accuracy in the dose delivered to the target volume be fulfilled in daily practice?", *Rad. Oncol.* **25**:242-250 (1992).
- [Le92b] G. Leunens, J. Verstraete, W. Van den Bogaert, J. Van Dam, A. Dutreix, E. van der Schueren, "Human errors in data transfer during the preparation and delivery of radiation treatment affecting the final result: 'garbage in, garbage out' ", *Rad. Oncol.* **23**:217-222 (1992).
- [Ma85] T. R. Mackie, J. W. Scrimger, and J. J. Battista, "A convolution method of calculating dose for 15-MV x rays" *Med. Phys.* **12**:188-196 (1985).
- [Ma88] T. R. Mackie, A. F. Bielajew, D. W. O. Rogers, and J. J. Battista, 1988 "Generation of photon energy deposition kernels using the EGS Monte Carlo code," *Phys. Med. Biol.* **33**:1-20 (1988).
- [Ma90] G. Marsaglia, A. Zaman, W. W. Tsang, "Toward a universal random number generator," *Stat. Prob. Lett.* **9**:35-39 (1990).
- [Ma95] C. M. Ma, P. Reckwerdt, M. Holmes, D. W. O. Rogers, and B. Geiser, "DOSXYZ Users Manual", National Research Council of Canada, Report PIRS 509b (1995).
- [Ma97] L. Ma, P. B. Geis, A. L. Boyer "Quality assurance for dynamic multileaf collimator modulated fields using a fast beam imaging system", *Med. Phys.* **24**:1213-1220 (1997).

- [Ma99] T. R. Mackie, J. Balog, K. Ruchala, D. Shepard, S. Aldridge, E. Fitchard, P. Reckwerdt, G. Olivera, T. McNutt, M. Mehta, "Tomotherapy", *Semin. Radiat. Oncol.* **9**(1):108-117 (1999).
- [Mc96a] T. R. McNutt, T. R. Mackie, P. Reckwerdt, and B. Paliwal, "Modeling dose distributions from portal dose images using the convolution/superposition method," *Med. Phys.* **23**(8): 1381-1392 (1996).
- [Mc96b] T. R. McNutt, T. R. Mackie, P. Reckwerdt, and N. Papanikolaou, "Calculation of portal dose using the convolution/superposition method," *Med. Phys.* **23**(4): 527-535 (1996).
- [Mc98a] B. M. C. McCurdy, and S. Pistorius, "Analytical Prediction of First Scatter Energy Fluence into a Portal Imaging Device", 5th International Workshop on Electronic Portal Imaging, [abstract] (1998).
- [Mc98b] P. McDermott, "The physical basis for empirical rules used to determine equivalent fields for phantom scatter" *Med. Phys.* **25**:2215-2219 (1998).
- [Mc99] B. M. C. McCurdy, and S. Pistorius, "Determination of equivalent photon fields through integrated convolution kernels", *Phys. Med. Biol.*, **44**:2971-2985 (1999).
- [Mc00a] B. M. C. McCurdy, and S. Pistorius, "Photon scatter in portal images: Physical characteristics of pencil beam kernels generated using the EGS Monte Carlo code" *Med. Phys.* **27**(2):312-320 (2000).
- [Mc00b] B. M. C. McCurdy, and S. Pistorius, "Photon scatter in portal images: Accuracy of a fluence based pencil beam superposition algorithm" *Med. Phys.* **27**(5): 913-922 (2000).

- [Mc00c] B. M. C. McCurdy, and S. Pistorius, "A two step algorithm for predicting portal dose images in arbitrary detectors" *Med. Phy.* **27(9)**:2109-2116 (2000).
- [Mi87] B. J. Mijnheer, J. J. Battermann., A. Wambersie, "What degree of accuracy is required and can be achieved in photon and neutron therapy?", *Rad. Oncol.* **8**:237-252 (1987).
- [Mi88] R. W. Miller, J. van de Geijn, "The use of a bar code scanner to improve the utility and flexibility of record and verify systems used in radiation therapy," *Med. Phys.* **15(4)**:611-613 (1988).
- [Mi91] C. Mitine, G. Leunens, J. Verstraete, N. Blanckaert, J. Van Dam, A. Dutreix, E. van der Schueren, "Is it necessary to repeat quality control procedures for head and neck patients?", *Rad. Oncol.* **21**:201-210 (1991).
- [Mo85a] R. Mohan, C. Chui, and L. Lidofsky, "Energy and angular distributions of photons from medical linear accelerators," *Med. Phys.* **12**:592-597 (1985).
- [Mo85b] R. Mohan, K. C. Podmaniczky, R. Caley, A. Lapidus, and J. S. Laughlin, "A computerized record and verify system for radiation treatments", *Int. J. Radiat. Oncol. Biol. Phys.* **10**:1975-1985 (1985).
- [Mo86] R. Mohan, and C. Chui, " Differential pencil beam dose computation model for photons," *Med. Phys.* **13(1)**:64-72 (1986).
- [Mo91] E. J. Morton, W. Swindell, D. G. Lewis, P. M. Evans, "A linear array, scintillation crystal-photodiode detector for megavoltage imaging", *Med. Phys.* **18(4)**:681-691 (1991).
- [Mu91] R. Muller-Runkel, S. Watkins, "Introducing a computerized record and verify system: Its impact on treatment errors", *Med. Dosimetry* **16**:19-22 (1991).

- [Mu95] P. Munro, "Portal Imaging Technology: Past, Present, and Future," *Semin. Radiat. Oncol.* **5**(2):115-133 (1995).
- [Mu98a] P. Munro, and D. C. Bouius, "X-ray quantum limited portal imaging using amorphous silicon flat-panel arrays" *Med. Phys.* **25**(5):689-702 (1998).
- [Mu98b] P. Munro, D. C. Bouius, J. Moseley, L. Martin, Y. Zhang, and D. A. Jaffray, "Glaring errors in transit dosimetry" Proceedings of the 5th International Workshop on Electronic Portal Imaging, 128-129 (1998).
- [Na00] National Cancer Institute of Canada, "Canadian Cancer Statistics 2000", web site: <http://www.cancer.ca/stats2000/currente.htm>
- [Ne85] W. R. Nelson, H. Hirayama, and D. W. O. Rogers, *The EGS4 Code System*. (Springfield, Virginia, USA: National Technical Information Service, 1985).
- [Ni88] B. Nilsson, B. I. Ruden, B. Sorcini, "Characteristics of silicon diodes as patient dosementers in external radiation therapy", *Rad. Oncol.* **11**:279-288 (1988).
- [No95] A. Noel, P. Aletti, P. Bey, L. Malissard, "Detection of errors in individual patients in radiotherapy by systematic in vivo dosimetry", *Rad. Oncol.* **34**:144-151 (1995).
- [NRa] National Research Council of Canada, Ionising Radiation Standards Group, web page: <http://www.irs.inms.nrc.ca/inms/irs/papers/egs.biblio/egs.biblio.html>
- [NRb] National Research Council of Canada, Ionising Radiation Standards Group, web site: <http://www.irs.inms.nrc.ca/inms/irs/irs.html>
- [OI98] M. Oldham, I. Baustert, C. Lord, T. A. Smith, M. McJury, A. P. Warrington, M. O. Leach, S. Webb, "An investigation into the dosimetry of a nine-field

- tomotherapy irradiation using BANG-gel dosimetry," *Phys. Med. Biol.* **43**(5): 1113-1132 (1998).
- [Pa93] N. Papanikolaou, T. Mackie, C. Meger-Wells, M. Gehring, and P. Reckwerdt, "Investigation of the convolution method for polyenergetic spectra", *Med. Phys.* **20**:1327-1336 (1993).
- [Pa98a] K. L. Pasma, B. J. M. Heijmen, M. Kroonwijk, and A. G. Visser, "Portal dose image (PDI) prediction for dosimetric treatment verification in radiotherapy. I. An algorithm for open beams," *Med. Phys.* **25**(6):830-840, (1998).
- [Pa98b] K. L. Pasma, M. Kroonwijk, J. C. J. de Boer, A. G. Visser, and B. J. M. Heijmen, "Accurate portal dose measurement with a fluoroscopic electronic portal imaging device (EPID) for open and wedged beams and dynamic multileaf collimation," *Phys. Med. Biol.* **43**:2047-2060 (1998).
- [Pa99a] M. Partridge, P. M. Evans, and J. R. N. Symonds-Tayler, "Optical scattering in camera-based electronic portal imaging" *Phys. Med. Biol.* **44**:2381-2396 (1999).
- [Pa99b] K. L. Pasma, M. L. P. Dirkx, M. Kroonwijk, A. G. Visser, B. J. M. Heijmen, "Dosimetric verification of intensity modulated beams produced with dynamic multileaf collimation using an electronic portal imaging device", *Med. Phys.* **26**(11):2373-2378 (1999).
- [Pa99c] K. L. Pasma, M. Kroonwijk, S. Quint, A. G. Visser, B. J. M. Heijmen, "Transit dosimetry with an electronic portal imaging device (EPID) for 115 prostate cancer patients", *Int. J. Radiat. Oncol. Biol. Phys.* **45**(5):1297-1303 (1999).

- [Pa99d] K. L. Pasma, M. Kroonwijk, E. B. van Dieren, A. G. Visser, and B. J. M. Heijmen, "Verification of compensator thicknesses using a fluoroscopic electronic portal imaging device," *Med. Phys.* **26**(8):1524-1529 (1999).
- [Pa00] M. Partridge, P. M. Evans, M. van Herk, L. S. Ploeger, G. J. Budgell, H. V. James, "Leaf position verification during dynamic beam delivery: A comparison of three applications using electronic portal imaging," *Med. Phys.* **27**(7): 1601-1609 (2000).
- [Po85] K. C. Podmaniczky, R. Mohan, G. J. Kutcher, C. Kestler, B. Vikram, "Clinical experience with a computerized record and verify system", *Int. J. Radiat. Oncol. Biol. Phys.* **11**:1529-1537 (1985).
- [Ra93] T. Radcliffe, G. Barnea, B. Wowk, R. Rajapakshe, S. Shalev, "Monte Carlo optimization of metal/phosphor screens at megavoltage energies", *Med. Phys.* **20**(4): 1161-1169 (1993).
- [Ri90] R. Rice, and M. Lee, "Monte Carlo calculations of scatter to primary ratios for normalisation of primary and scatter dose" *Phys. Med. Biol.* **35**:333-338 (1990).
- [Ro84] D. W. O. Rogers, "Low energy electron transport with EGS", *Nuc. Instrum. Methods Phys. Res., Sect. A* **227**: 535-548 (1984).
- [Ro90] D. W. O. Rogers and A. F. Bielajew, "Monte Carlo techniques of electron and photon transport for radiation dosimetry," in *The Dosimetry of Ionizing Radiation*, Vol. III, edited by K. R. Kase, B.E. Bjarngard, and F.H. Attix (Academic Press, New York, 1990), pp. 427-539.
- [Sa95] O. A. Sauer, "Calculation of dose distributions in the vicinity of high-Z interfaces for photon beams," *Med. Phys.* **22**(10):1685-1690 (1995).

- [Sh93] M. B. Sharpe, and J. J. Battista, "Dose calculations using convolution and superposition principles: the orientation of dose spread kernels in divergent x-ray beams", *Med. Phys.* **20**:1685-1694 (1993).
- [Sh96a] S. Shalev, "Megavoltage Portal Imaging," in *Teletherapy: Present and Future*, edited by J. Palta, and T. Mackie (Advanced Medical Publishing, Madison, USA, 1996), pp. 445-469.
- [Sh96b] S. Shalev, "On-Line Portal Imaging: Contributions and Limitations in Clinical Practice" in *Frontiers of Radiation Therapy and Oncology* 29:156-167, 1996.
- [Si85] R. Siddon, "Fast calculation of the exact radiological path for a three-dimensional CT array," *Med. Phys.* **12**(2):252-255 (1985).
- [Sp00a] L. Spies, "On scatter in megavoltage X-ray transmission imaging", *Ph.D. Thesis Ruprecht-Karls University, Heidelberg, Germany* (2000).
- [Sp00b] L. Spies, P. M. Evans, M. Partridge, V. N. Hansen, T. Bortfeld "Direct measurement and analytical modeling of scatter in portal imaging", *Med. Phys.* **27**(3):462-471 (2000).
- [Sv84] H. Svensson, "Quality assurance in radiation therapy: Physical aspects", *Int. J. Radiat. Oncol. Biol. Phys.* **10 Sup. 1**:59-65 (1984).
- [Sw91] W. Swindell, E. J. Morton, P. M. Evans, and D. G. Lewis, "The design of megavoltage projection imaging systems: Some theoretical aspects," *Med. Phys.* **18**:855-866 (1991).
- [Sw96] W. Swindell, and P. M. Evans, "Scattered radiation in portal images: a Monte Carlo simulation and a simple physical model," *Med. Phys.* **23**, 63-73 (1996).

- [Ta93] M. Tatcher, and B. Bjarngard, "Equivalent squares of irregular photon fields", *Med. Phys.* **20**:1229-1232 (1993).
- [Va88] M. Van Herk, H. Meertens, "A matrix ionisation chamber imaging device for on-line patient setup verification during radiotherapy", *Rad. Oncol.* **11**:369-378 (1988).
- [Va92] J. van Dam, C. Vaerman, N. Blanckaert, G. Leunens, A. Dutreix, and E. van der Schueren, "Are port films reliable for in vivo exit dose measurements?," *Rad. Oncol.* **25**:67-72 (1992).
- [Va93] J. Van Dyk, R. B. Barnett, J. E. Cygler, P. C. Scragge, "Commissioning and quality assurance of treatment planning computers", *Int. J. Radiat. Oncol. Biol. Phys.* **26**:261-273 (1993).
- [Ve97] J. L. M. Venselaar, S. Heukelom, H. N. Jager, B. J. Mijnheer, J. J. M. van Gasteren, H. J. van Kleffens, R. van der Laarse, and C. F. Westermann, "Is there a need for a revised table of equivalent square fields for the determination of phantom scatter correction factors?" *Phys. Med. Biol.* **42**:2369-2381 (1997).
- [We93] S. Webb, "The Physics of Three-dimensional Radiation Therapy: Conformal Radiotherapy, Radiosurgery, and Treatment Planning", IOP Publishing Ltd., Bristol, UK pp1-373 (1993).
- [Wo83] J. W. Wong, and R. M. Henkelman, "A new approach to CT pixel-based photon dose calculations in heterogeneous media", *Med. Phys.* **10**(2):199-208.
- [Wo90a] J. W. Wong, E. D. Slessinger, R. E. Hermes, C. J. Offutt, T. Roy, and M. W. Vannier, "Portal dose images I: quantitative treatment plan verification," *Int. J. of Radiat. Oncol. Biol. Phys.* **18**:1455-1463 (1990).

- [Wo90b] M. K. Woo, J. R. Cunningham "The validity of the density scaling method in primary electron transport for photon and electron beams", *Med. Phys.* **17**:187-194 (1990).
- [Wo92] J. W. Wong, and J. A. Purdy, "Review of methods of inhomogeneity corrections," in *Medical Physics Monograph No. 19*, edited by J. A. Purdy (American Institute of Physics, Inc., 1992) pp 887-899.
- [Wo94] M. K. Woo "Analysis of photon beam exit dose using photon point kernels", *Phys. Med. Biol.* **39**:687-702 (1994).
- [Ye97] C. Yeboah, "Analysis of the physical factors influencing portal imaging exit dosimetry using Monte Carlo modeling", *M.Sc. Thesis, University of Manitoba, Winnipeg, Canada* (1997).
- [Ye00] C. Yeboah and S. Pistorius, "Monte Carlo studies of the exit photon spectra and dose to a metal/phosphor portal imaging screen", *Med. Phys.* **27**(2): 330-339 (2000).
- [Yi90] X. Ying, L. Y. Geer, and J. W. Wong, "Portal dose images II: patient dose estimation," *Int.J.Radiat. Oncol. Biol.Phys.* **18**:1465-1475 (1990).
- [Zh95] Y. Zhu, X. Q. Jiang, and J. Van Dyk, "Portal dosimetry using a liquid ion chamber matrix: dose response studies," *Med. Phys.* **22**:1101-1106 (1995).